Université Paris Diderot (Paris 7)
Service de Physiques des Particules de l'IRFU du CEA de Saclay
École Doctorale: Particules, Noyaux et Cosmos (ED 517)

Thèse
pour obtenir le grade de
Docteur ès Sciences

Mesure des dibosons WZ avec le détecteur ATLAS auprès du LHC et Etude des performances des Micromegas resistif en vue de leur application auprès du HL-LHC

par
Joany Manjarrés Ramos

Commission d'examen:

U.	Bassler	Président du Jury
D.	Bloch	Rapporteur
S.	Hassani	Encadrante
F.	Jeanneau	Examinateur
S.	Lavignac	Examinateur
G.	Mikenberg	Examinateur
C.	Petridou	Rapporteur
Ph.	Schune	Directeur de thèse

Soutenue le 8 Juillet 2013

University Paris Diderot (Paris 7)
"Service de Physiques des Particules de l'IRFU du CEA de Saclay"
Doctoral school: "Particules, Noyaux et Cosmos" (ED 517)

Thesis
to obtain the degree of
"Docteur ès Sciences"
(Doctor of Philosophy)

WZ diboson measurements with the ATLAS experiment at the LHC and Performance of resistive Micromegas in view of HL-LHC applications

by
Joany Manjarrés Ramos

Examination Committee:

U.	Bassler	President of the jury
D.	Bloch	Referee
S.	Hassani	Thesis advisor
F.	Jeanneau	
S.	Lavignac	
G.	Mikenberg	
C.	Petridou	Referee
Ph.	Schune	Thesis advisor

Presented on July 8th, 2013

A mis padres,
a mis hermanas
y a Heberth

Résumé

Cette thèse comporte deux parties: la première porte sur la mesure de la production des paires de deux bosons de jauge $W^{\pm}Z$ en utilisant les données collectées par le détecteur ATLAS auprès du grand collisionneur de proton-proton (LHC) au CERN. La deuxième partie de la thèse est dédiée à l'étude des propriétés des Micromegas résistives, en vue de leur installation dans la partie avant du spectromètre à muons du détecteur ATLAS, durant la première phase de haute luminosité du LHC (HL-LHC).

La mesure de production des paires $W^{\pm}Z$ permet de tester le secteur électrofaible du Modèle Standard à haute énergie et de rechercher de la nouvelle physique au-delà du Modèle Standard. Toute déviation par rapport aux prédictions du Modèle Standard serait l'indication de nouvelle physique. L'étude présentée dans cette thèse est basée sur les données des collisions proton-proton à une énergie de centre de masse de 7 et 8 TeV. Elles correspondent à une luminosité intégrée de 4.8 et 13 fb^{-1} enregistrées respectivement durant l'année 2011 et durant le premier semestre de 2012. Les états finals de paires $W^{\pm}Z$ se désintégrant en électrons, muons et énergie transverse manquante, sont sélectionnés. Les bruits de fond $t\bar{t}$ et Z+jets sont estimés à partir des données avec des méthodes développées dans le cadre de cette thèse. La section efficace fiducielle et totale de production des paires $W^{\pm}Z$ sont calculées et les limites sur les couplages à trois bosons de jauge WWZ en sont extraites.

La deuxième partie de cette thèse est dédiée à l'amélioration du spectromètre à muons d'ATLAS en vue de son fonctionnement à haute luminosité auprès du HL-LHC. La très haute luminosité atteinte à l'horizon 2018 impose de prévoir des modifications substantielles sur l'ensemble des sous-détecteurs constituant ATLAS. L'efficacité, la résolution

et la robustesse de Micromegas résistives sont étudiées dans le cadre d'un projet de R&D visant à la construction de chambres à muons vers l'avant à l'aide de la technologie Micromegas résistives.

Abstract

During the past two years, the CERN Large Hadron Collider (LHC) has performed exceptionally. The data collected by ATLAS made possible the first Standard Model physics measurements and produced a number of important experimental results. In the first part of this document the measurement of the $W^{\pm}Z$ production with the ATLAS detector is presented and the second part is devoted to the study of resistive Micromegas properties, in view of the installation in the ATLAS spectrometer forward regions for the first phase of High Luminosity LHC (HL-LHC).

The measurement of the $W^{\pm}Z$ production probes the electroweak sector of the Standard Model at high energies and allows for generic tests for New Physics beyond the Standard Model. Two datasets of LHC proton-proton collisions were analyzed, 4.8 fb^{-1} of integrated luminosity at center-of-mass energy of $\sqrt{s} = 7$ TeV, and 13 fb^{-1} at $\sqrt{s} = 8$ TeV, collected in 2011 and the first half of 2012 respectively. Fully leptonic decay events are selected with electrons, muons and missing transverse momentum in the final state. Different data-driven estimates of the background were developed in the context of this analysis. The fiducial and total cross section of $W^{\pm}Z$ production are measured and limits on anomalous triple gauge boson couplings are set.

The second part of the document is devoted to the upgrade of the ATLAS detector. The conditions at the High Luminosity LHC calls for detectors capable of operating in a flux of collisions and background particles approximately ten times larger compared to today's conditions. The efficiency, resolution and robustness of resistive Micromegas were studied, as part of the R&D project aimed at the construction of large-area spark-resistant muon chambers using the micromegas technology.

Resumen

Esta tesis consta de dos partes: la primera está dedicada a la medida de la producción de pares de bosones de calibre $W^{\pm}Z$ a partir de datos recogidos por el detector ATLAS en el Gran Colisionador protón-protón (LHC) en el CERN. La segunda parte, presenta el estudio de las propiedades de Micromegas resistivos, para su instalación en la parte frontal del espectrómetro de muones del detector ATLAS durante la primera fase de alta luminosidad del LHC (HL-LHC).

La medida de la producción de pares $W^{\pm}Z$ permite estudiar el sector electrodébil del Modelo Estándar a altas energías y la búsqueda de nueva física más allá del Modelo Estándar. Cualquier desviación con respecto a las predicciones del Modelo Estándar podría ser considerado un indicio de nueva física. El estudio presentado en esta tesis se basa en los datos de colisiones protón-protón con una energía en el centro de masa de 7 y 8 TeV. Estos datos corresponden a una luminosidad integrada de 4.8 y 13 fb^{-1}, respectivamente, registrados durante 2011 y el primer semestre de 2012.

Para este estudio se utilizaron los estados finales de pares $W^{\pm}Z$ desintegrándose en electrones, muones y energía transversa faltante. La estimación del ruido de fondo $t\bar{t}$ y Z+jets se realiza a partir de los datos, utilizando métodos desarrollados en el contexto de este análisis. Por último, la sección eficaz fiducial y total de la producción de pares $W^{\pm}Z$ es medida y se extraen límites sobre los acoplamientos de tres bosones de calibre WWZ.

La segunda parte de esta tesis está dedicada a las mejoras necesarias del detector ATLAS para su adecuado funcionamiento a la alta luminosidad del HL-LHC. Las condiciones de alta luminosidad esperadas en 2018 requieren cambios sustanciales en todos los sub-detectores que constituyen ATLAS. La eficiencia, la resolución y la solidez de los Mi-

cromegas resistivos son estudiadas en el marco de un proyecto destinado a la construcción de cámaras de muones con la tecnología de Micromegas resistivos.

Contents

Introduction

After about two years of operation, the excellent performance of the LHC and the ATLAS detector made possible, a number of important experimental results, including precision test of the Standard Model and the discovery of a new scalar particle compatible with the Higgs boson.

The physics potential of the LHC is closely related to the amount of data available. In order to continue scientific progress and to explore the LHC's full potential, the High Luminosity LHC project proposes an increase of the instantaneous luminosity by a factor of ten. Plans are already advancing and, in view of their operation at high luminosity, detector upgrades will be needed.

During my PhD studies, I have worked in the ATLAS experiment. In my first year, I was involved in the Muon Spectrometer detector upgrade. The idea to use Micromegas detectors for muon triggering and tracking was proposed a few years earlier, and by the time I joined the group, studies on resistive Micromegas were carried on. I participated in performance studies such as the measurements of efficiency, resolution and an assessment of the robustness of different type of resistive Micromegas detectors using test beam data. In particular, I have shown, that Micromegas with resistive strips have the best response parameters.

By the end of 2011, the LHC had collected about ~ 5 fb^{-1} of data at 7 TeV, and at this time I joined the $W^{\pm}Z$ diboson group. I participated to the analysis by providing a cross section measurement and limits in anomalous triple gauge couplings [1]. I also cross-checked the origin of the excess observed in the W transverse mass. In 2012 the center-of-mass energy of the collisions was increased to 8 TeV and by the end of the year ~ 20 fb^{-1} of data were collected. I participated in a second round of the $W^{\pm}Z$ analysis using a subset of 13 fb^{-1} of that data; this time with more experience, I was the main analyzer and I participated in all the different steps of the measurement, cut optimization, new data driven background estimation and cross section extraction. The effort ended with the publication of a conference note in March 2013 [2].

These three years have been a very exciting period for research in the field of high energy physics. The work presented here summarizes my activities during my PhD and is organized in seven chapters, the first four are dedicated to presenting the physics context and previous measurements, the detector as well as general concepts on the reconstruction

of physics objects. The studies I performed on the Micromegas detector and $W^{\pm}Z$ diboson measurements are detailed in the last three chapters.

Chapter 1 begins with the description of the basic elements of the Standard Model, with a focus on the electro-weak interactions. The $W^{\pm}Z$ production mechanism, and the effective Lagrangian predicting the anomalous triple gauge boson couplings and previous experimental results are also exposed.

Descriptions of the LHC and the ATLAS experiment are given in chapters 2 and 3. The reconstruction algorithms used to build the objects in this analysis are presented in chapter 4. Chapters 5 and 6 are devoted to the study of the $W^{\pm}Z$ production cross section and anomalous triple gauge couplings (aTGCs), using two ATLAS datasets with collisions at 7 and 8 TeV.

This thesis work has laid to a solid foundation for further measurements of the $W^{\pm}Z$ production with the full ~ 20 fb^{-1} integrated luminosity at 8 TeV recorded during 2012, which will further improve the precision and yield more stringent limits on aTGCs.

The last part of the thesis, chapter 7, is dedicated to the performance study of Micromegas detectors in view of their installation in the ATLAS muon spectrometer. Concluding remarks and perspectives are discussed at the end of the thesis.

Chapter 1

Theory Elements

"What is matter?" Democritus the greek philosopher was the first to propose that matter consists of tiny "indivisibles" which he called "atoms". Democritus was on the right direction. Today we know that atoms are not the smallest building blocks of matter; but there exists a whole world of particles more fundamental than atoms (quarks, leptons, and force carrier particles). Through experimentation and theory, the Standard Model (SM) of particle physics has been created, which reflects our understanding of elementary particles and their fundamental interactions.

Huge progress was made in the field after the middle of the 20th century. The first step towards the Standard Model was in 1960 when Steven Weinberg, Sheldon Glashow and Abdus Salam created the electro-weak theory, combining the electromagnetic and weak nuclear force into one single model (they win the Nobel prize in 1979). In this field theory the objects of study are not particles and forces, but quantum fields and their symmetries. The basic equations of the unified theory correctly describe the electro-weak force and its associated force-carrying particles, the photon, the W and Z bosons, except for a major problem. All of these particles emerge without a mass. While this is true for the photon, the W and Z have mass.

Robert Brout, François Englert [3] and Peter Higgs [4] made a proposal to solve this problem. They showed that when a gauge theory is combined with an additional field that spontaneously breaks the symmetry, the bosons can consistently acquire a finite mass. The so called Higgs mechanism was used to break the electroweak symmetry resulting in the actual electroweak theory [5–10]. After the neutral weak currents caused by Z boson exchange were discovered at CERN in 1973, the electroweak theory became widely accepted. The W and Z bosons were discovered experimentally in 1981, and their masses were found to be as the predicted values.

In the early 1970s the quantum chromodynamics formalism was proposed by David Politzer, Frank Wilczek and David Gross (they were awarded with the 2004 Nobel Prize). The theory of the strong interactions [11–13], acquired its modern form around 1973-74, when experiments confirmed that the hadrons were composed of fractionally charged

quarks. These theories form what became the Standard Model of particle physics.

As seen developments in this field have always been closely related to the observations. Technical progress and the interest to produce particle collisions in a controlled environment motivated the construction of particle accelerators: devices with increasing size, capable of attaining higher energies were built throughout the last decades. The goal for the high energy physics experiments in the past years, have been to test the description predicted by the SM, and search for deviations from its predictions.

Most of the experimental observations are in agreement with the SM predictions, but there are still some intriguing questions that lie outside our current understanding provided by the SM.

Given the vast scope of the SM, this thesis will only provide a brief introduction to some aspects of the theory. In this chapter, the context of the $W^{\pm}Z$ diboson measurement is presented. First, the SM is briefly introduced, with focus on the electro-weak sector. Then, the $W^{\pm}Z$ production process is described and motivations for its study are given. In particular, its importance, both within the context of the Standard Model, and scenarios beyond the SM predictions are stressed. The experimental results, available at the beginning of this thesis are also presented on this chapter.

1.1 The Standard Model

The Standard Model of Particle Physics [5, 14] explains how the basic building blocks of matter interact, through the fundamental forces. This model is the result of theories and discoveries of thousands of physicists since the 1930s. It has successfully explained almost all experimental results and precisely predicted a wide variety of phenomena. Over time and through many experiments, the SM has become a well-tested physics theory.

The existence of hundreds of particles and their complex interactions, can be explained by the SM with only six *quarks*, six *leptons* and five force carrier particles. Figure 1.1 shows the particle's mass, charge, color charge and spin. These particles are called elementary particles because they don't seem to be made from combinations of smaller particles. The elementary particles can be classified on the basis of conserved quantities, called quantum numbers (a quantified representation of the particle's interaction properties). Quarks and leptons have a spin equal to 1/2, they obey to Fermi-Dirac statistics and are called *Fermions*. The force mediators have an integer spin, they follow the Bose-Einstein statistics and are called *Bosons*. An antiparticle is associated with each of the elementary particles, although some are their own antiparticle.

Among leptons, the electrons (e), muons (μ) and taus (τ) are electrically charged, whereas the corresponding neutrinos (ν_e, ν_μ and ν_τ) are neutral. The quarks carry a fractional charge, and they also have a color charge (leptons are colorless). Every quark appears in three different color states: "red", "blue", and "green". This is relevant for their strong interaction, which binds them together inside colorless particles called hadrons

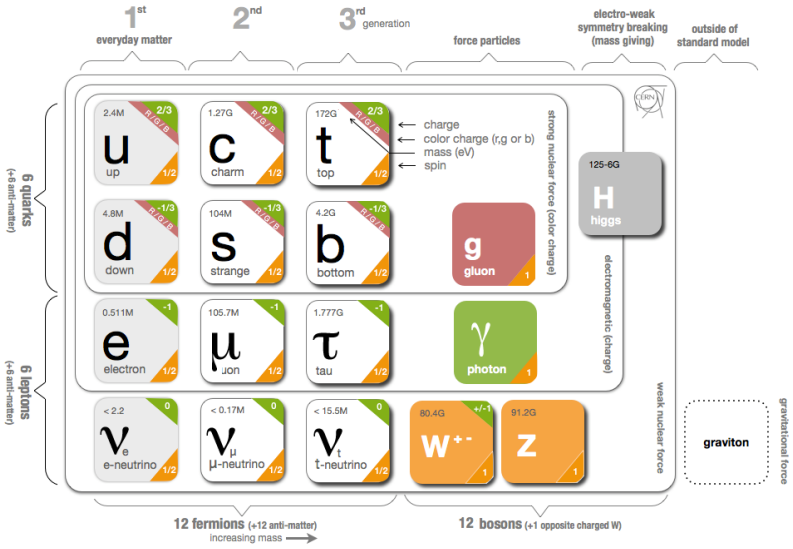

Figure 1.1: The Standard Model particles and some of their properties: charge, color charge, mass and spin. The quarks, leptons, bosons and the three generations of fermions are pointed. The particles that interact through strong nuclear, electromagnetic and weak nuclear forces are shown. The graviton mediator of the gravitational force, is also shown even though it is not part of the Standard Model.

(like the protons).

The fermions (quarks and leptons) can be classified into three generations of identical structure and differing only by the particle mass, which comprise a total of six flavors of quarks and six flavors of leptons. The mass increases from the first generation to the next. Everything we see around us in everyday life is made of the quarks and leptons from the first generation. The second and third generations of charged leptons (μ and τ) are unstable and decay to other particles.

The bosons are the mediators of the fundamental forces of physics: strong, electromagnetic, weak and gravitational. Each fundamental force has its own corresponding boson: the strong force is carried by gluons (g), the electromagnetic force is carried by the photon (γ), and the $W^{\pm}$ and Z bosons are responsible for the weak force. Although not yet found, the graviton, a spin-2 boson, should be the corresponding force-carrying particle of gravity. The Standard Model includes the electromagnetic, strong and weak forces and all their carrier particles, and explains well how these forces act on all of the matter particles. Efforts to include gravity into the formalism of quantum mechanics to unify all four interactions have failed so far. However, the Standard Model describes properly their interaction, since the gravitation strength is too small to affect the interactions at the particle level.

The SM is a relativistic quantum field theory built from the principles that physics should be invariant under local symmetry transformations (gauge invariance). It describes the electromagnetic, weak and strong interactions based on a combination of local gauge

symmetry groups $\mathrm{U}(1)_Y \times \mathrm{SU}(2)_L \times \mathrm{SU}(3)_C$. The indices refer to the conserved quantity in each transformation: weak hyper-charge (Y), color (C) and for SU(2), L indicates that only left handed fields are involved, and the conserved quantity is the weak isospin (I). The two components of the SM are Quantum Chromodynamics (QCD), the theory of the strong force, and the Electroweak (EWK) theory, a single theory which unifies the Quantum Electrodynamics (QED) description of electromagnetism with the weak force.

1.1.1 The Electroweak theory

The Electroweak theory (EWK) is a unified theory of Quantum Electrodynamics (QED), which describes the electromagnetic force in terms of the exchange of a photon, and the weak force, which is described in terms of the exchange of the $W^{\pm}$ and Z bosons and is responsible for weak nuclear decay. The electroweak theory was developed by Glashow, Salam, and Weinberg in the 1960s [5] and is based on the $\mathrm{SU}(2)_L \times \mathrm{U}(1)_Y$ gauge symmetry which is spontaneously broken down to the observable $\mathrm{U}(1)_{EM}$ symmetry by the Higgs mechanism.

Weak interactions govern a variety of phenomena like beta decay, and explain why the observed lifetimes of the pion and the muon are longer than the ones of particles decaying either through strong or electromagnetic interactions. The strength and the distance of an interaction depends the mass of the force carrier. The difference between the observed strengths of the weak and electromagnetic interactions, is due to the huge difference in mass between the $W^{\pm}$ ($m_{W^{\pm}} \sim 80$ GeV [15]) and Z particles ($m_Z \sim 91$ GeV [15]) and the photon, which is massless.

The fundamental couplings between the EWK gauge bosons and the SM matter constituents are shown in Fig. 1.2. Quarks and charged leptons interact electromagnetically by the exchange of a photon as seen in the Feynman diagram of Fig. 1.2a, while all the fermions interact weakly by the exchange of charged ($W^{\pm}$) or neutral (Z) bosons, as shown in the Feynman diagrams in Fig. 1.2b,c.

Therefore the weak interactions involve both charged and neutral currents. Charged currents are responsible for the flavor transitions between up-type and down-type quarks or leptons whereas neutral currents conserve flavor. Fermions are grouped into left-handed fields, ψ_L

$$\begin{pmatrix} u \\ d \end{pmatrix}_L, \begin{pmatrix} \nu_e \\ e \end{pmatrix}_L, \qquad \begin{pmatrix} c \\ s \end{pmatrix}_L, \begin{pmatrix} \nu_\mu \\ \mu \end{pmatrix}_L, \qquad \begin{pmatrix} t \\ b \end{pmatrix}_L, \begin{pmatrix} \nu_\tau \\ \tau \end{pmatrix}_L. \tag{1.1}$$

and the right-handed fiels, ψ_R

$$u_R, d_R, e_R, \qquad c_R, s_R, \mu_R, \qquad t_R, b_R, \tau_R \tag{1.2}$$

The doublet structure illustrated in Equation 1.1 accommodates the left-handed chiral

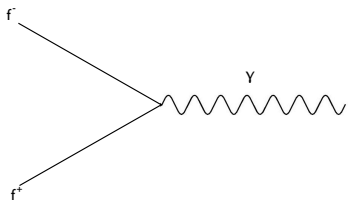

(a) γ coupling to fermions.

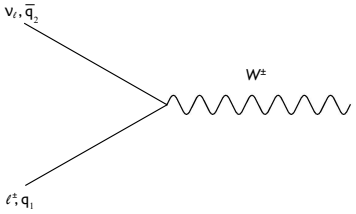

(b) $W^{\pm}$ coupling to fermions.

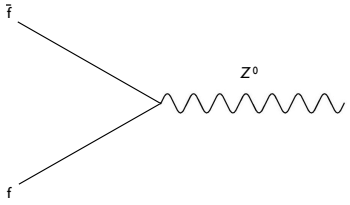

(c) Z coupling to fermions.

Figure 1.2: Fundamental couplings of electroweak gauge bosons to the Standard Model matter content.

fields, while the right-handed partners transform as singlets under $SU(2)_L$. Right-handed neutrinos do not exist in the minimal version of the theory, only charged leptons, up and down-type quarks exist.

The interactions among the particles can be derived from the gauge principle. The gauge symmetry implies the existence of two coupling constants, denoted g for the SU(2) and g' for the U(1) coupling, and four gauge fields: W_μ^a (with $a = 1, 2, 3$) and B_μ. Taking for instance a quark family given by:

$$\psi_1(x) = \begin{pmatrix} u \\ d \end{pmatrix}_L , \qquad \psi_2(x) = u_R \, , \qquad \psi_3(x) = d_R \, , \tag{1.3}$$

the associated Lagrangian can be written under the form:

$$\mathscr{L}_{EWK} = \sum_{j=1}^{3} i\bar{\psi}_j(x)\gamma^\mu D_\mu \psi_j(x) - \frac{1}{4} W^a_{\mu\nu} W_a^{\mu\nu} - \frac{1}{4} B^{\mu\nu} B_{\mu\nu} \, , \tag{1.4}$$

the covariant derivative D_μ is defined like:

$$D_\mu \, \psi_j(x) = \left[\partial_\mu - ig \frac{\sigma_a}{2} W^a_\mu \delta_{kj} - ig' \frac{Y_j}{2} B_\mu \right] \psi_j(x) \, . \tag{1.5}$$

where g is the SU(2) and g' the U(1) coupling constants, Y_j is the hyper-charge, $\delta_{kj} = 1$ for $k = j$ and 0 otherwise and σ_a are the Pauli matrices. The second term, transforms

only left-handed fields (ψ_1) and is associated with $SU(2)$ while the last term corresponds to $U(1)$, and acts on both chiralities. Then :

$$W_a^{\mu\nu} = \partial^\mu W_a^\nu - \partial^\nu W_a^\mu + g\,\epsilon_{abc}\,W_b^\mu\,W_c^\nu\,, \tag{1.6}$$

$$B^{\mu\nu} = \partial^\mu B^\nu - \partial^\nu B^\mu\,. \tag{1.7}$$

The last term in Equation 1.6 represents the self-interactions of the gauge fields. The combinations of the first two components of W_μ^i are associated with the two charged vector bosons:

$$W_\mu = W_\mu^\dagger, W_\mu^\pm = \frac{1}{\sqrt{2}}\left(W_\mu^1 \mp i W_\mu^2\right)\,. \tag{1.8}$$

The W_μ^3 mixes with B_μ via the Weinberg angle θ_W in such a way to form two neutral bosons: the photon and the Z.

$$\begin{pmatrix} W_\mu^3 \\ B_\mu \end{pmatrix} = \begin{pmatrix} \cos\theta_W & \sin\theta_W \\ -\sin\theta_W & \cos\theta_W \end{pmatrix} \begin{pmatrix} Z_\mu \\ A_\mu \end{pmatrix}\,. \tag{1.9}$$

The non-abelian group symmetry predicts the existence of interactions between the gauge bosons. There are triple gauge couplings and vertices involving four bosons, always with the presence of a W pair. The theory is capable of describing charged and neutral interactions associated with weak decays, and also incorporates QED and self-interactions between the gauge bosons. However at this level there is an important disagreement with experimental facts. The $W^\pm$, the Z and the fermions are massive objects, and mass terms for any of these particles violate explicitly the gauge symmetry.

1.1.2 Spontaneous Symmetry Breaking

One remaining problem with electro-weak theory is the origin of the gauge boson masses. Experimentally, the W and Z gauge bosons are known to be massive, with $m_{W^\pm} \sim 80$ GeV [15] and $m_Z \sim 91$ GeV [15]. Generating a massive gauge boson field requires an additional term in the Lagrangian

$$\mathscr{L}_h = -\frac{1}{4} V_{\mu\nu}^\dagger V^{\mu\nu} + m_V^2 V_\mu^\dagger V^\mu \tag{1.10}$$

where $V = Z, W$ and $V_{\mu\nu} = \partial_\mu V_\nu - \partial_\nu V_\mu$. The mass term $m_V^2 V_\mu^\dagger V^\mu$, however is forbidden by gauge invariance. One way to solve this problem is to consider the case where a symmetry of the Lagrangian is not a symmetry of the vacuum, a mechanism known as spontaneous symmetry breaking. This is done by introducing a complex scalar field ϕ, with Lagrangian,

$$\mathscr{L} = (\partial^\mu \phi^\dagger)(\partial_\mu \phi) - \mu^2 \phi^\dagger \phi - \lambda(\phi^\dagger \phi)^2, \tag{1.11}$$

which can interact with massless real vector fields. the mass parameter is μ, if this symmetry is now broken ($\mu^2 < 0$), a massive gauge field is recovered. A real scalar field is

also predicted, with an associated massive boson known as the Higgs boson, which was recently observed by the LHC experiments [16, 17].

To summarize, the unified electro-weak theory has been successfully developed through the 20^{th} century, considering the electromagnetism and the weak interactions as different aspects of the electroweak interaction unified at the high energy scale. The Standard Model is completed by the strong interaction, an SU(3) gauge theory describing color interactions between quarks and gluons. The combination of the strong and electro-weak gauge theories and the Higgs mechanism allowed the building of a solid SM theory.

1.1.3 Gauge Boson Self-Couplings

Terms of the form $g\epsilon_{abc}W_b^\mu W_c^\nu$ in Equation 1.6 are a consequence of the non-abelian nature of the theory, and is the origin of self-interactions between the gauge bosons, with both triple and quartic couplings. The gauge boson self-interactions and couplings are in consequence completely fixed by the structure of the non-abelian symmetry. The triple gauge coupling (TGC) vertex takes the form:

$$-\frac{1}{2}\epsilon_{jkl}(\partial_\mu W_j^\nu - \partial_\nu W_j^\mu)W_{k\mu}W_{l\nu}, \tag{1.12}$$

where the factor ϵ_{jkl} only allows interactions involving three different types of bosons. Figure 1.3 shows the fundamental TGC interactions of the SM. The two possible vertices are $WW\gamma$ and WWZ, with coupling constants of $g_{WW\gamma} = -e$ and $g_{WWZ} = -e\cot(\theta_W)$ respectively where θ_W is the weak mixing angle ($\cos\theta_W = m_W/m_Z$). In addition, the coupling strength of these interactions have a momentum dependence. The momentum dependence implies that the coupling strength of the TGC vertices will have a non-trivial dependence on the gauge-boson momentum.

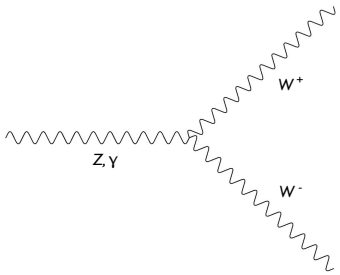

Figure 1.3: Feynman diagram of the WWZ and $WW\gamma$ triple gauge boson interaction.

The Z pair and $Z\gamma$ production via a triple gauge vertex is forbidden in the SM at tree level. Anomalous interactions between three neutral gauge bosons, however, may arise as a result of New Physics beyond the SM.

A good understanding of the diboson production in high energy experiments is an effective and important way to verify the SM theory, especially its high energy behavior

in electroweak interactions. Precision measurements of diboson production are probing the triple gauge-boson vertices WWZ and $WW\gamma$. New Physics may potentially manifest itself by modifying the vector boson self-interactions.

1.2 The $W^{\pm}Z$ diboson production

The $W^{\pm}Z$ final state which is the subject of this thesis can only be accessed through charged initial state processes. The primary production mechanism at hadron colliders is through quark-antiquark interactions. The leading-order (LO) Feynman diagrams for the $q\bar{q} \to W^{\pm}Z$ process in the Standard Model are shown in Fig. 1.4. For the t-channel and u-channel diagrams, the $W^{\pm}$ and Z bosons are emitted from the quark lines. The only LO diagram which contains the TGC vertex is the s-channel, where a $q\bar{q}$ pair annihilate to an off-shell W which then decays to the $W^{\pm}Z$ pair.

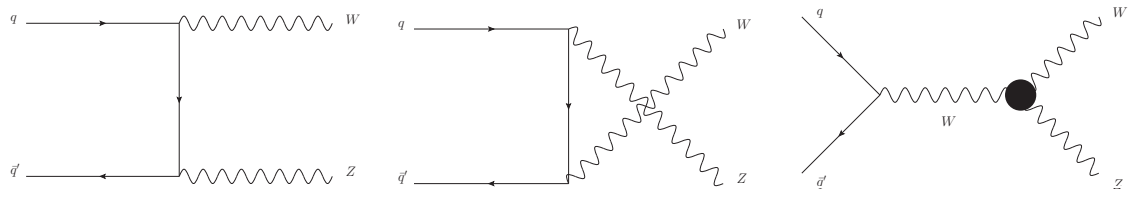

(a) t-channel (b) u-channel (c) s-channel

Figure 1.4: The SM tree-level Feynman diagrams for $W^{\pm}Z$ production through the $q\bar{q}'$ initial state in proton-proton collisions. The s-channel diagram, on the right, contains the WWZ TGC vertex.

Next-to-leading order (NLO) contributions from quark-gluon or antiquark-gluon processes can be seen in the Feynman diagrams of Figures 1.5(a)-(c), and 1.5(f)-(g). These $gq(\bar{q})$ processes result in an additional quark being present in the final state. Additional NLO corrections include $q\bar{q}$ initiated interactions with gluon bremsstrahlung in the final state (diagrams in Figures 1.5(d), and 1.5(e)), as well as $q\bar{q}$ interactions with virtual corrections (diagrams Fig. 1.5(h)-(k)). In the gluon-gluon processes by charge conservation the $W^{\pm}Z$ need to be accompanied with at least two jets, this next-to-next-to-leading order (NNLO) process have a very small contribution (1%).

The production cross-section of $W^{+}Z$ and $W^{-}Z$ is expected to be the same at the Tevatron. However since the LHC is a proton-proton machine, the $W^{+}Z$ and $W^{-}Z$ cross sections are not equal,

$$\sigma(W^{+}Z) \propto \text{pdf(u)} \cdot \text{pdf}(\bar{\text{d}}) \tag{1.13}$$

$$\sigma(W^{-}Z) \propto \text{pdf}(\bar{\text{u}}) \cdot \text{pdf(d)} \tag{1.14}$$

with the ratio $\sigma^{NLO}(W^{-}Z)/\sigma^{NLO}(W^{+}Z)$ varying between 0.56 (for $\sqrt{s} = 7$ TeV) and 0.65 (at 14 TeV). Table 1.1 shows the total cross section of $W^{\pm}Z$ production at LO and NLO at the LHC [18], and for different centre of mass energies.

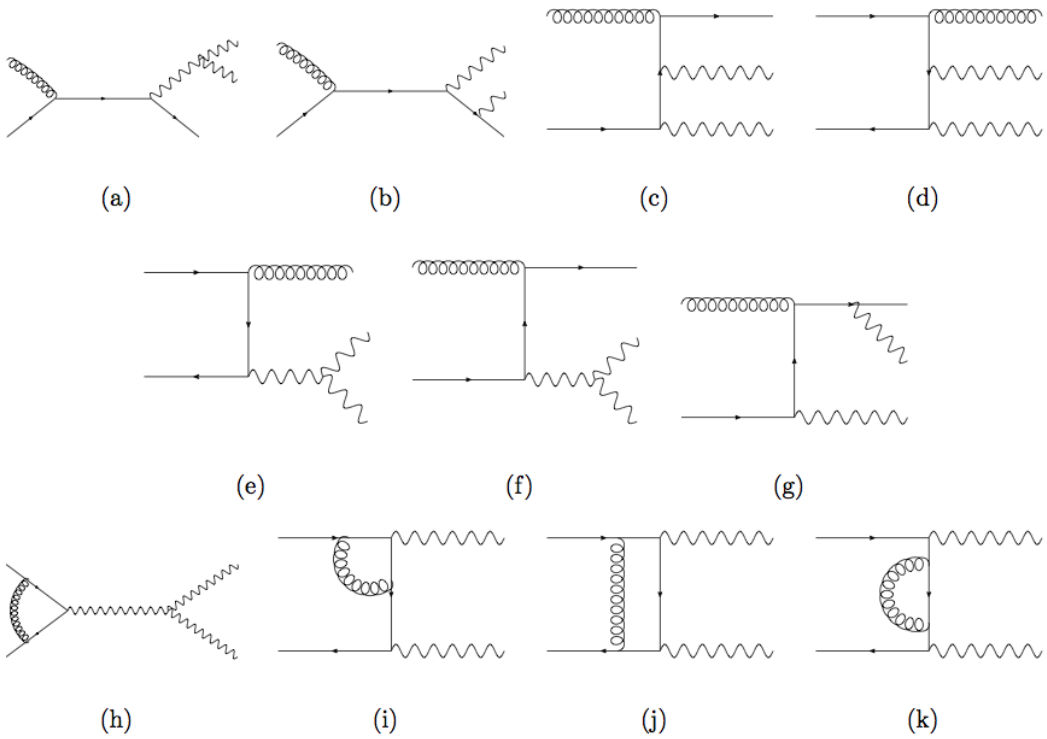

Figure 1.5: QCD NLO corrections to $W^{\pm}Z$ production. Figures 1.5(a)-1.5(g) are the real contributions with additional quarks or gluons in the final state. Figures 1.5(h)-1.5(k) are the virtual contributions with internal gluon loops.

The $W^{\pm}Z$ production can be measured using the fully leptonic ($l\nu + ll$), semi-leptonic ($jj + ll$, or $l\nu + jj$) or pure hadronic final state ($jj + jj$). Due to the decay branching ratios of Zs and Ws, a search limited to a fully leptonic final state corresponds to only 1.2% of the inclusive cross section (using electrons and muons). But the advantage of using this channel is that it provides a clean signature, and low background. With this channel, it is possible to discriminate between the signal and the hadronic/multi-jet backgrounds, which dominate the production cross-section at the LHC. The analysis presented in this thesis was performed using the $W^{\pm}Z$ fully leptonic decays.

1.3 Beyond the Standard Model

Even though the Standard Model provides currently the best description of phenomena observed by experiments, it is still an incomplete theory. The theory incorporates only three out of the four fundamental forces, omitting gravity. It does not provide an explanation for dark matter and dark energy nor for Charge Parity (CP) violation, responsible for the matter-antimatter asymmetry observed in our universe. Furthermore the existence of exactly three generations of quarks and leptons with such a different mass scale, and

$\sqrt{s}$ [TeV]	$\sigma^{LO}(W^+Z)$ [pb]	$\sigma^{NLO}(W^+Z)$ [pb]	$\sigma^{LO}(W^-Z)$ [pb]	$\sigma^{NLO}(W^-Z)$ [pb]
7	6.93	$11.88^{+5.5\%}_{-4.2\%}$	3.77	$6.69^{+5.6\%}_{-4.3\%}$
8	8.29	$14.48^{+5.2\%}_{-4.0\%}$	4.65	$8.40^{+5.4\%}_{-4.1\%}$
14	16.98	$31.50^{+3.9\%}_{-3.0\%}$	10.57	$20.32^{+3.9\%}_{-3.1\%}$

Table 1.1: Total cross sections for $W^{\pm}Z$ production at the LHC as a function of energy. Renormalization and factorization scales are set equal to the average mass of the W and Z i.e. $\mu_R = \mu_F = (M_W + M_Z)/2$. Upper and lower percentage deviations are obtained by varying the scales around the central scale by a factor of two. The vector bosons are kept on-shell, with no decays included [18].

the evidence for neutrinos masses, provided by the observed oscillations patterns, have no explanation within the SM.

Even if the Standard Model accurately describes the phenomena within its domain, it is still incomplete. The SM can be considered as an effective theory, at low energy limit (at the electroweak scale $\sim 10^2$ GeV) of another more fundamental theory (at the Planck scale $\sim 10^{19}$ GeV). Perhaps it is only a part of a bigger picture that includes New Physics. The so called "Beyond the Standard Model" (BSM) theories, wich are considered, must be in agreement with the current experimental data and extend the SM, providing solutions to some of the raised puzzles [19].

Concerning the WZ channel, some examples of common BSM theories affecting its production are:

- Supersymmetry, with multi-lepton final states. The specific case of Minimal Supersymmetric Standard Model (MSSM) [20].

- Exotic WZ resonances [21, 22] can appear besides the SM Higgs boson, as new states such as a technirho and other technimesons in Technicolor models [23], or as a new heavy gauge boson in composite Higgs models [24], or Little Higgs models [25]. A simple benchmark model conventionally used is the extended gauge model (EGM) [26] where a W' has the same fermionic couplings as the W boson of the SM but the triple gauge coupling $W'WZ$ is suppressed with respect to that of the SM.

If these theories do exist in nature, they may leave measurable traces in collisions at the LHC. The evidence of New Physics can be observed through both indirect and direct searches. As mentioned before, some models predict the existence of new particles which could be observed directly in their decays to $W^{\pm}Z$ diboson.

In the case of indirect measurements, these new particles appear as virtual particles in loop diagrams. The production cross-section, the kinematics distributions and the direct TGCs measurement could be affected and reveal the presence of New Physics as deviations from the SM predictions.

The indirect searches allows to be sensitive to production of any massive particle which could decay to WZ dibosons, avoiding to be focused on one specific model.

The sensitivity to the effects from new particles, allows indirect measurements to access higher scales, beyond the reach of direct searches. This means in practice that it is possible that we would observe new particles in loop diagrams before we would find them in direct searches.

1.4 Anomalous Triple Gauge Couplings (aTGC)

Less restrictive theories than the SM can be built using the model-independent method of effective Lagrangians. This method is used by indirect searches to parameterize the non-SM physics contributing to $W^{\pm}Z$ production within the existing experimental constraints.

Since no signals of New Physics have been directly observed, the scale of the high energy New Physics (Λ), must be above the energies accessible by current experiments.

If Λ is much larger than the interaction energies and SM particle masses, our measurements will only be sensitive to virtual effects, that can be summarized by a series expansion in powers of $1/\Lambda$ of effective vertices. The most general effective Lagrangian can be written as:

$$\mathcal{L}_{\text{eff}} = \sum_i g^i_{\text{eff}} \mathcal{O}_i(\phi) \qquad \text{with} \qquad g^i_{\text{eff}} = \frac{g^i}{\Lambda^{d_i-4}} \tag{1.15}$$

The operators $\mathcal{O}_i(\phi)$ are of dimension d_i, they are local functions of the SM particles represented by the fields ϕ and affected by the coupling constant g^i_{eff}.

If the particle momentum and masses lie significantly below the scale Λ, the high order terms in the expansion become extremely small. Equation 1.15 can be expanded using a finite number of terms. However, if the energies approach to Λ the fields associated with New Physics become real, all terms of the Lagrangian expansion become important and this approach will fail.

The main advantage of using an effective Lagrangian approach is its independence from models predicting New Physics. Expressions of the most general effective Lagrangian with two charged and one neutral vector boson can be found in [27] and [28]. If only terms that separately conserve charge C and parity P are considered then the Lagrangian reduces for the $WW\gamma$ and WWZ to

$$\begin{aligned}\mathcal{L}_{WWV} = ig_{WWV}[g_1^V(W^\dagger_{\mu\nu}W^\mu V^\nu - W_{\mu\nu}W^{\dagger\mu}V^\nu) &+ \kappa^V W^\dagger_\mu W_\nu V^{\mu\nu} \\ &+ \frac{\lambda^V}{m_W^2} W^\dagger_{\rho\mu} W^\mu_\nu V^{\nu\rho}]\end{aligned} \tag{1.16}$$

and the Lagrangian for $ZZ\gamma$ and ZZZ to

$$\mathcal{L}_{VZZ} = -\frac{e}{M_Z^2}\left[f_4^V(\partial_\mu V^{\mu\beta})Z_\alpha(\partial^\alpha Z_\beta) + f_5^V(\partial^\sigma V_{\sigma\mu})\tilde{Z^{\mu\beta}}Z_\beta\right] \tag{1.17}$$

where $g_{WWV} = -e\cot\theta_W$, θ_W is the weak mixing angle, and g_1^V, κ^V, λ^V, f_4^V and f_5^V are the new coupling parameters. In the SM, all these couplings are 0 except $g_1^V = \kappa^V = 1$. We define the anomalous triple gauge couplings (aTGC) as the deviation from the SM, i.e $\Delta g_1^V = g_1^V - 1$, $\Delta\kappa^V = \kappa^V - 1$, λ^V, f_4^V and f_5^V.

In the case of the WWZ vertices, which are the subject of this work, the couplings involved are g_1^Z, κ^Z and λ^Z. Those couplings are dimensionless parameters and multiply dimension 4 and dimension 6 operators. The higher dimension operators have been cut off in this expansion, which is justified if Λ is large and thus the effect of aTGCs is small. As mentioned before the expected size of the aTGCs is $\mathcal{O}(\frac{m_W^2}{\Lambda^2})$ and thus aTGCs of $\mathcal{O}(10^{-2})$ are expected for Λ= 1 TeV, the deviations decrease with increasing Λ.

The dependence of the anomalous interaction amplitudes on the total energy ($\sqrt{\hat{s}}$) at the TGC vertex (equivalent to the diboson invariant mass) is non-trivial. In $W^\pm Z$ production Δg_1^Z and λ^Z are proportional to $\hat{s}$, whereas $\Delta\kappa^Z$ is proportional to $\sqrt{\hat{s}}$. The fact that the anomalous contributions for the $\Delta\kappa^Z$ parameters grow as $\sqrt{\hat{s}}$, while the other contributions grow as $\hat{s}$, implies that the limits on coupling sizes will be least stringent for $\Delta\kappa^Z$ at a fixed energy.

1.4.1 Unitarity Violation

As mentioned before the effective Lagrangian cannot properly describe interactions at energies close to Λ. Unitarity violation is one of the consequences, since it arises when radiative corrections from the effective Lagrangian are bigger than the tree-level contributions. This means that the fields involved in this model are not able to reproduce the SM in the low-energy limit [29]. In order to avoid unitarity violation near Λ, the anomalous couplings must vanish when $\sqrt{\hat{s}} \to \infty$. An arbitrary cut-off or form factor is introduced

$$\alpha(\hat{s}) = \frac{\alpha_0}{(1 + \hat{s}/\Lambda^2)^2} \tag{1.18}$$

where α stands for Δg_1^Z, $\Delta\kappa^Z$ or λ^Z, the anomalous couplings with respect to the SM values, and α_0 is the value of the anomalous coupling at low energy. This approach is model-dependent, in contradiction with the general model-independent approach of the effective Lagrangian. Nevertheless introducing form factors in the model requires relatively fewer assumptions about the BSM high energy physics than other models.

A dipole form factor was used and Λ was arbitrary chosen to be 2 TeV at the Tevatron. ATLAS and CMS have agreed that aTGC limits should be presented without a form factor: this means that the value of Λ is set to infinity. But in order to compare with Tevatron, results with $\Lambda = 2$ TeV are also produced.

In addition to affecting the total $W^\pm Z$ production cross-section, the presence of aTGCs also has an important impact on the expected behavior of measured observables. Due to the $\sqrt{\hat{s}}$ dependence of the aTGCs, observables that are sensitive to $\sqrt{\hat{s}}$, such as the

mass of the $W^{\pm}Z$ system, will be sensitive to the presence of aTGCs. The presence of a derivative in the couplings in the effective Lagrangian translates to a gauge boson momentum dependence on the values of the aTGC parameters.

1.4.2 Impact of aTGC on Physical Observables

The cross section, $W^{\pm}Z$ mass and the Z transverse momentum distributions are sensitive to the presences of aTGCs. This distributions from simulation are shown in Fig. 1.6 for different values of aTGC parameters (Δg, $\Delta\kappa$, and λ), and compared to the SM predictions. The kinematic distributions have been normalized to the same area; only shape comparisons can be made. The presence of non-zero aTGC parameters will modify the total number of events produced, and the $W^{\pm}Z$ cross section has a quadratic dependence on the aTGCs. The mass of the WZ system, and the Z boson p_T distributions all show large deviations from the Standard Model distributions at high mass or momentum. If the effect of the aTGCs on the cross-section is also included, the distribution of these observables can be considerably more sensitive to the presence of aTGCs than the cross-section alone.

So different approaches can be taken by the analyses to evaluate the presence of aTGCs depending on the available data. The WZ mass distribution for example, suffers from our inability to directly reconstruct the W boson momentum (neutrinos pass through detectors without being measured).

The p_T^Z distribution, however, is built directly from the measurement of leptons. In the case of non-zero aTGC parameters, the Z boson momentum distribution shows the largest shape differences for positive and negative values of the aTGC parameters, as can be observed in Fig. 1.6. Thus, if aTGCs are actually measured, the transverse momentum of the Z boson could be sensitive to the sign of the parameter.

1.5 Existing experimental results

Experimental measurements of the $W^{\pm}Z$ production cross-section as well as aTGCs limits have previously been performed by CDF [30] and D0 [31, 32] using the proton-antiproton collisions at the Tevatron at $\sqrt{s} = 1.96$ TeV. These were the first experiments to observe $W^{\pm}Z$ production and to use the measurement to set direct limits on aTGCs. Prior to the Tevatron direct measurements of the WWZ vertex were made, indirect limits on aTGCs using the WW final state were set by the LEP collaborations [33]. After the LHC started operating, several publications reported the results of analyzes with the large amount of data from ATLAS [1, 2, 34] and CMS [35].

The available results at the begining of this thesis on the triple gauge couplings measured through the exclusive $W^{\pm}Z$ production are reported in Table 1.2. The results present the 95% C.L. intervals for the measured aTGCs and were obtained by varying

one of the couplings, while fixing the remaining ones to the SM values. The limits on aTGCs at the Tevatron were derived using a form factor $\Lambda = 2$ TeV and using the Z boson transverse momentum spectrum to search for the presence of aTGCs and calculate

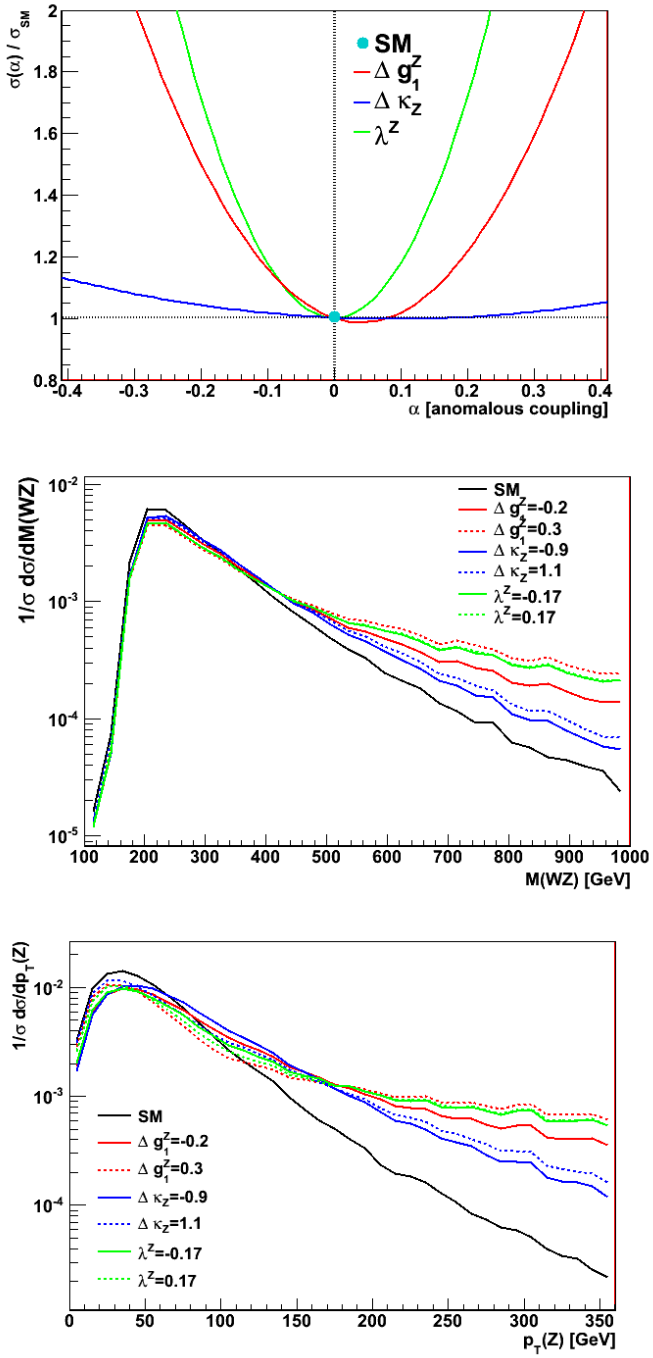

Figure 1.6: The impact of aTGCs on the truth distributions of physical observables in simulation, cross section in the top, $W^{\pm}Z$ mass on the middle and p_T^Z on the bottom. A form factor with $\Lambda = 2$ TeV is used in these distributions. The kinematic distributions have been normalized to the same area; only shape comparisons are shown here.

limits. ATLAS provided limits using $\Lambda = 2$ TeV and ∞. The limits on the anomalous triple gauge couplings Δg_1^Z, $\Delta\kappa^Z$ and λ^Z reported by all the experiments are consistent with zero, as expected from the SM. The latest limits provided by ATLAS [1] are the subject of this thesis work and will be discussed at the end of Chapter 5.

Experiment	Δg_1^Z	$\Delta\kappa^Z$	λ^Z	$\mathcal{L}$ [fb^{-1}]	Λ [TeV]
D0 [31]	[-0.053,0.156]	[-0.376,0.686]	[-0.075,0.093]	4.1	2.0
CDF [30]	[-0.08,0.20]	[-0.39,0.90]	[-0.08,0.10]	7.1	2.0
ATLAS [34]	[-0.20,0.30]	[-0.9,1.1]	[-0.17,0.17]	1.02	2.0
ATLAS [34]	[-0.9,1.1]	[-0.8,1.0]	[-0.14,0.14]	1.02	∞

Table 1.2: Summary of the observed 95% C.I. for the anomalous couplings Δg_1^Z, $\Delta\kappa^Z$ and λ^Z obtained from direct measurement of the WWZ vertex, from D0 [31], CDF [30] and ATLAS [34].

For the cross-section measurement of the $W^{\pm}Z$ production, the results from D0 [32], CDF [30], ATLAS [34] and CMS [35] are summarized in Table 1.3. The total cross-sections are in all cases in good agreement with the SM expectation. The ATLAS latest cross-section results [1, 2] are part of this thesis work and are discussed in detail in Chapters 5 and 6.

Experiment	Mesured σ_{total} [pb]	Theoretical σ^{NLO} [pb]	Z mass window [GeV]	$\mathcal{L}$ [fb^{-1}]	$\sqrt{s}$ [TeV]
D0 [32]	4.50 ± 0.61 (stat) $^{+0.16}_{-0.25}$ (sys)	3.21 ± 0.19	$60 < m_{ll} < 120$	8.6	1.96
CDF [30]	$3.93\ ^{+0.60}_{-0.53}$ (stat) $^{+0.59}_{-0.46}$ (sys)	3.50 ± 0.21	$66 < m_{ll} < 116$	7.1	1.96
ATLAS [34]	$20.5\ ^{+3.1}_{-2.8}$ (stat) $^{+1.4}_{-1.3}$ (sys) $^{+0.9}_{-0.8}$ (lumi)	$17.3\ ^{+1.3}_{-0.8}$	$66 < m_{ll} < 116$	1.02	7.0
CMS [35]	17.0 ± 2.4(stat) ± 1.1(sys) ± 1.0(lumi)	19.790 ± 0.088	$60 < m_{ll} < 120$	1.1	7.0

Table 1.3: Summary of the $W^{\pm}Z$ production cross section measurements from D0 [32], CDF [30], ATLAS [34] and CMS [35].

Chapter 2

The Large Hadron Collider

The Large Hadron Collider (LHC) [36] is a proton-proton circular accelerator. The superconducting hadron accelerator and collider was installed in the existing Large Electron-Positron (LEP) accelerator tunnel. It is capable of accelerating counter-rotating proton beams to a center of mass energy ($\sqrt{s}$) $\sim$ 14 TeV, and also lead ions (Pb) to 2.8 TeV per nucleon.

To reach these high unexplored energies and since the LHC was installed in LEP accelerator tunnel, using hadrons was a better option than using leptons/electrons. The energy loss through synchrotron radiation in circular accelerators is proportional to $1/\mathrm{m}^4$, where m is the mass of the accelerated particle, since protons are $\sim$ 2000 times heavier than electrons, they loose $\sim 10^{-13}$ less energy than electrons.

Even though the LHC is operated with a fixed beam energy, the collisions actually provide interactions in a wide energy range. At these energies when proton collisions occur, the interactions are between the proton constituents, quarks and gluons, rather than between the protons as a whole. The quarks and gluons inside the proton carry an unknown fraction of the proton energy. The accessible energy domain for new particle searches is from $\sim$ 100 GeV to few TeV.

A set of linear and circular accelerators are used to accelerate protons or heavy ions before their injection into the LHC. The chain is illustrated in Fig. 2.1. Most of these accelerators already existed at CERN before the LHC construction, and were upgraded to satisfy LHC requirements.

A hydrogen bottle, at the beginning of the process, provides the protons to be extracted. Then protons reach 50 MeV of energy in a linear accelerator (LINAC), which is followed by a circular booster (PSB) where the beam reaches 1.4 GeV. In the last two steps it reaches 25 GeV in the Proton Synchrotron (PS) and 450 GeV in the Super Proton Synchrotron before being transferred to the LHC. It is injected in both directions, clockwise and anti-clockwise and there, protons are accelerated up to the nominal energy and they collide at four different interaction points.

All four interaction points are instrumented with detectors. There are six detectors

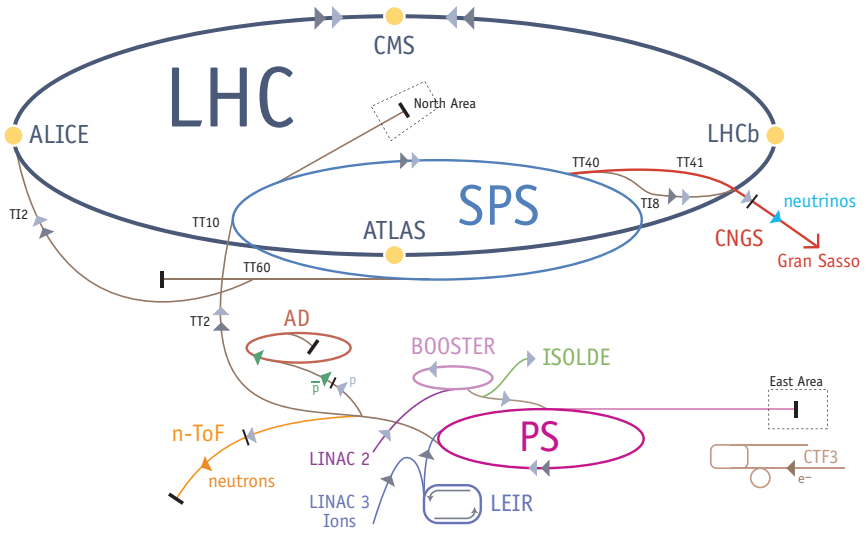

Figure 2.1: Illustration of the CERN accelerator complex. The LHC experiments are indicated with yellow circles. The LHC is the last ring (dark grey line) in a chain of particle accelerators. The smaller machines are used in a chain to help boost the particles to their final energies.

installed at the LHC, four of them installed in each one of the collision points ATLAS (A Toroidal LHC ApparatuS), CMS (Compact Muon Solenoid), ALICE (A Large Ion Collider Experiment) and LHCb (Large Hadron Collider beauty). The two others TOTEM (Total elastic and diffractive cross-section measurement) and LHCf (Large Hadron Collider forward) are positioned near CMS and ATLAS.

ATLAS [37] and CMS [38] are general purpose experiments detectors. Designed to explore the widest possible range of physics in proton-proton and heavy ion collisions. The study of the Standard Model and the search for new phenomena in proton-proton collisions are among their main objectives, and involve detection of very rare processes. The associated cross sections are many orders of magnitude below the total proton-proton cross section, dominated by Quantum Chromodynamics effects. Their dependence with the center of mass energy is shown in Fig. 2.2. A more detailed description of ATLAS and its physics programs will be given in the next chapters.

ALICE [39] is dedicated to heavy ion collisions. It is designed to address the physics of strongly interacting matter and the quark-gluon plasma at extreme values of energy density and temperature in nucleus-nucleus collisions.

LHCb [40] is dedicated to precision measurements of CP violation and rare decays of B hadrons. The TOTEM and LHCf experiments are positioned near CMS and ATLAS, respectively. These two detectors were designed to focus on particles which are scattered in the very forward region. TOTEM [41] measures the total proton-proton cross-section and studies elastic and diffractive scattering.

LHCf [42] is dedicated to the measurement of neutral particles emitted in the very forward region. The physics goal is to provide data for calibrating the hadron interaction models which are used in the study of Extremely High-Energy Cosmic-Rays.

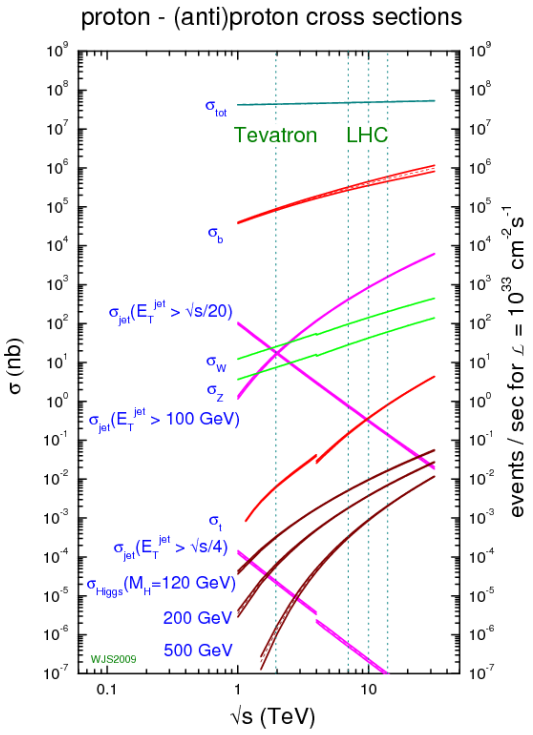

Figure 2.2: Cross sections of various physics processes in proton-proton (or proton anti-proton) collisions as a function of the center of mass energy $\sqrt{s}$. The discontinuity is due to the Tevatron being a proton-antiproton collider while the LHC is a proton-proton collider. The scale on the right-hand side shows the event rate with the LHC design luminosity. The vertical bands correspond to the center of mass energies at the Tevatron (1.96 TeV) and for the LHC (7 TeV, 10 TeV and 14 TeV) [43].

2.1 Design and Luminosity

Since the LHC is a same charge particle-particle accelerator, two separate beam lines are used for the counter-rotating beams. Due to space restrictions, "two-in-one" superconducting magnets were designed. In order to reach the design energies, the 26.7 km of circumference of the tunnel is equiped with about 1200 dipoles magnets each providing a field of $\sim$ 8.3 T. The acceleration is performed by radio-frequency (RF) cavities. A 400 MHz superconducting cavity increases the beam energy by 485 keV at each turn until it reaches the desired value. The limiting factor for the LHC to go at higher center-of-mass energy is not the acceleration power itself but the bending power of the dipole magnets.

The event rate, i.e the number of collisions events per second, generated in the collisions, depends on the event cross section (σ_{event}) and the machine luminosity ($\mathcal{L}$). The

luminosity depends on the beam parameters through the equation:

$$\mathcal{L} = \frac{N_b^2 n_b f_r \gamma_r}{4\pi\epsilon_n \beta^*} F \,, \tag{2.1}$$

where N_b is the number of particles per bunch, n_b is the number of bunches per beam, f_r is the revolution frequency, γ_r the relativistic gamma factor, ϵ_n the normalized transverse beam emittance, related to the beam size, β^* is the beta function at the collision point, related to the beam focusing, F is the geometric luminosity reduction factor if the beams do not collide head-on.

Nominal design values for some of these beam parameters are quoted in the last column of Table 2.1. The LHC should be able to reach a luminosity of $10^{34}\text{cm}^{-2}\text{s}^{-1}$ for proton-proton and $10^{27}\text{cm}^{-2}\text{s}^{-1}$ for heavy ion collisions. The luminosity at the LHC is not constant during collisions, decreases due to the degradation of the beam intensity. The luminosity decreases by a factor of 2 within 10 h, after which a new injection into LHC takes place.

Parameter	2010	2011	2012	Nominal
$\sqrt{s}$ [TeV]	7	7	8	14
N_b				1.15×10^{11}
n_b	368	1380	1380	2808
Δt [ns]	150	50	50	25
ϵ_n [μm rad]				3.75
β^* [m]	3.5	1.0	0.60	0.55
L [$\text{cm}^{-2}\text{s}^{-1}$]	2.07×10^{32}	3.65×10^{33}	7.73×10^{33}	10^{34}
Int. lumi. per year [fb^{-1}]	0.0481	5.61	21.7	80

Table 2.1: Parameters of the LHC proton-proton collisions for the data-taking periods: 2010, 2011 and 2012 [44, 45], and the design values [36]. The quoted parameters are: the center-of-mass energy $\sqrt{s}$, the number of protons per bunch N_b, the number of bunches per beam n_b, the bunch-to-bunch time spacing Δt, the normalized transverse beam emittance ϵ_n, the instantaneous peak luminosity L and integrated luminosity per year. Each value quoted corresponds to the best performance achieved during the year.

2.2 Startup and physics run

The first beams circulated in the LHC in September, 2008 [46]. Nine days later an accident caused by a faulty electrical connection between two magnets delayed the operations by about a year. After the repairs and consolidation work, the LHC started to collide protons by the end of 2009. These firsts collisions were performed at a center-of-mass energy of $\sqrt{s} = 900$ GeV, and later at $\sqrt{s} = 2.36$ TeV. After the winter shutdown, the LHC restarted in march 2010, and quickly increased the center-of-mass energy collision to 7 TeV, achieving an integrated luminosity ($\int \mathcal{L}\text{d}t$) of approximately 50 pb^{-1} per experiment at the end of the year. After this period of proton-proton collisions, the LHC performed heavy ion collisions for a few weeks.

In 2011, the LHC continued colliding protons at a center-of-mass energy of 7 TeV, instantaneous luminosities of 3.65×10^{33} cm^{-2}s^{-1} were reached, allowing a total integrated luminosity of about ~ 6 fb^{-1}, by the end of the year. The proton-proton run was followed by a few weeks of heavy ion collisions.

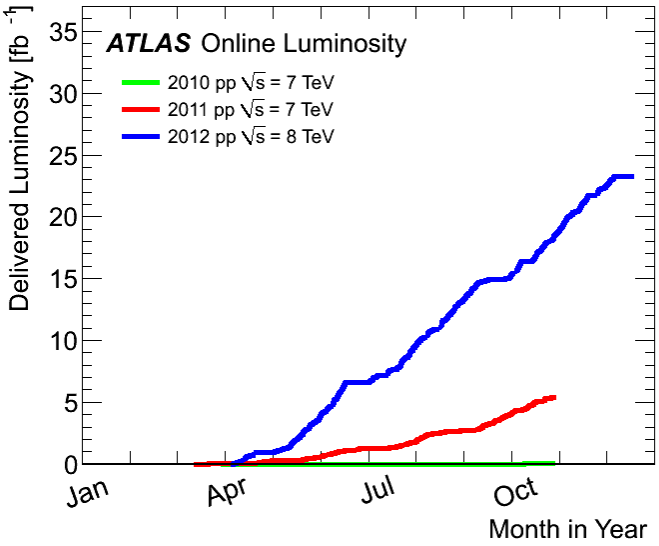

Figure 2.3: Cumulative luminosity versus month delivered to ATLAS during stable beams for proton-proton collisions, is shown for 2010 (green), 2011 (red) and 2012 (blue) running.

During 2012, the center-of-mass energy was increased to 8 TeV, ATLAS recorded a total of 21.7 fb^{-1} of data, reaching an instantaneous luminosity of 7.73×10^{33} cm^{-2}s^{-1}. At the beginning of 2013, a few weeks of heavy ion collisions were taken, and a long shutdown started, which is expected to last about two years. During this period the machine will be prepared to reach an energy of $\sqrt{s} \sim 13$ TeV, with the repair of all the welds between superconducting magnets. The repair of all these connections is crucial since it was such a failure that led to the accident of 2008 and only half of them was repaired. The four big LHC experiments will take the opportunity to perform upgrades and routine repairs.

Figure 2.3 shows the cumulative luminosity delivered to ATLAS, during stable beams for proton-proton collisions and for each year of operation.

Chapter 3

The ATLAS experiment

ATLAS is a general purpose detector designed to explore a wide range of physical processes using the proton-proton and heavy ion collisions at the LHC. ATLAS is made of several sub-detectors in an onion structure that are able to measure the particles traveling in all directions from the interaction point after the collisions. These secondary particles carry information about the physics processes involved in the collisions. They are composed of electrons, muons, neutrinos, photons, neutral and charged hadrons, and maybe still unknown particles. They are either direct products of the hard processes (called *prompt* particles), or products of secondary processes. Prompt particles usually travel isolated from other particles. There are also groups of particles assembled in objects called *jets*. Jets are the product of quark or gluon hadronization and subsequent decays of unstable hadronic particles; jet direction and energy are associated with the direction and energy of the original quark or gluon. The task of the detector, is to measure the direction of flight and momentum (or kinetic energy) of these different particles and jets, and to identify them.

ATLAS has a cylindrical shape, as shown in Fig. 3.1. It was designed for the proton collisions to take place at its center. The detector dimensions are roughly: 44 m long, 21 m high and 21 m wide, with a weight of 7000 *tons*. The collaboration includes more than 2800 physicists from 32 countries. These characteristics make ATLAS the largest LHC experiment at CERN.

ATLAS was designed to exploit the full physics potential of the LHC [47], which ranges from electroweak precision measurements and b-quark physics to the study of top-quark properties, the search for the Higgs boson and for physics beyond the Standard Model. A few physics examples are given here:

- The Standard Model, has been very successful in describing the currently available experimental data. Nevertheless we continue to test it through precision studies of the electroweak bosons, W and Z, and their properties. An interesting test of the Standard Model and the main subject of this thesis is the measurement of diboson production and the study of Triple Gauge Coupling (TGC) vertices, this kind of

vertices being completely constrained by the electroweak gauge structure. Their precise measurement will test the high energy behavior of electroweak interactions and search for possible new physics in the bosonic sector.

The $W^{\pm}$ and Z boson leptonic decays will result in high p_T leptons and missing energy (if a neutrino is involved). So that these measurements require a high-resolution lepton measurement, charge identification and good missing energy resolution.

- The top quark also plays an important role in constraining new physics phenomena. The LHC production rates enables precise measurements of the top quark mass and its couplings. A good performance in the tagging of b jets, lepton measurement and missing energy resolution is required.

- With a good performance in tagging b jets, the b-quark physics is also feasible where B-hadrons properties and their decays, including some rare processes, can be studied, as well as CP violation.

- Standard Model Higgs boson discovery or exclusion was one of the main goals of the LHC physics program. This is reflected in the performance and requirements of the ATLAS detector.

  For example the $H \to \gamma\gamma$ channel calls for excellent electromagnetic calorimetry. The $H \to ZZ^{(*)} \to 4l$ channel requires efficient lepton identification and precise determination of their momentum, direction and production point. Higgs boson searches were successful with the discovery of a new particle compatible with the Standard Model Higgs boson. The collaboration's efforts are now focused on the study of its properties, like mass, spin, and couplings.

- Supersymmetry and physics beyond the Standard Model is also an important search program, there is a large variety of phenomena and models beyond the Standard Model that can be tested with LHC data. Supersymmetry is one of the theoretically favored candidates for physics beyond the Standard Model postulating invariance of the theory under a symmetry which transforms fermions into bosons and viceversa.

  The models based on extra-dimensions usually include heavy gauge bosons like W' and Z'. Measurement of these bosons will be accessible at the LHC for masses up to 6 TeV through their decay to high p_T leptons, and leptoquarks which are colored bosons carrying both lepton and quark quantum numbers.

With such a physics program and considering the difficult conditions at the LHC, like the collision rate, overlapping events (pileup) and high particle fluxes, the ATLAS design needed to address stringent demands on the detector capabilities, including electronics, and the trigger system for all its subsystems.

Before detailing detector requirements (in the following sections) I will briefly describe some of the main features of the ATLAS detector.

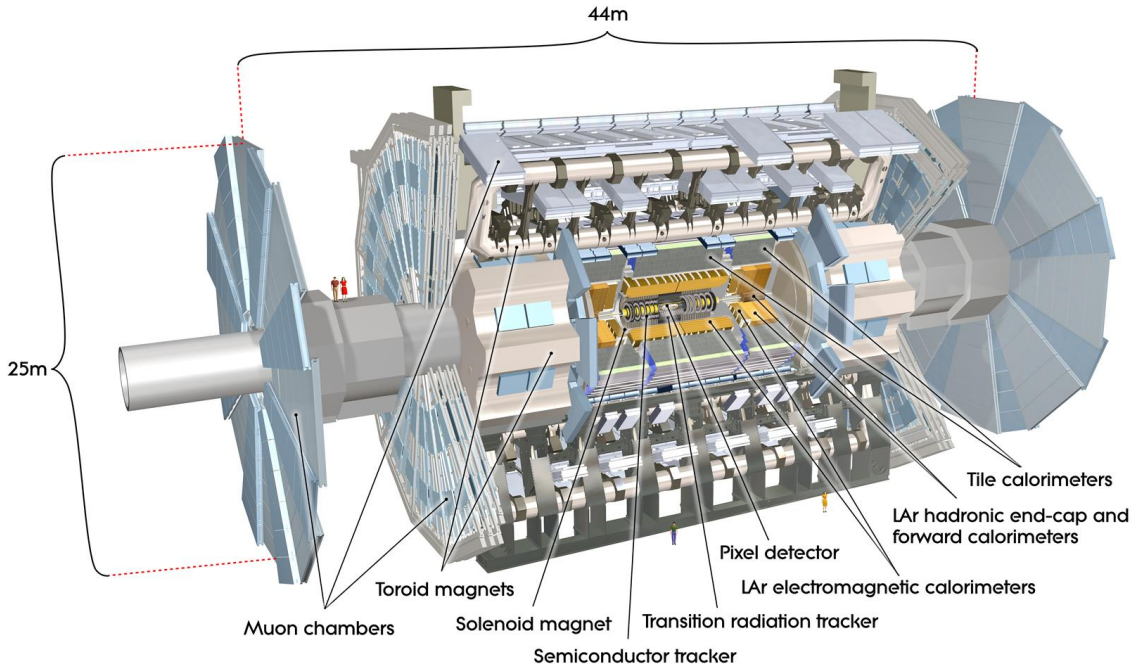

Figure 3.1: Cut-away view of the ATLAS detector, with the different sub-systems identified.

- A high granularity and quick response is essential to handle the particle fluxes and to reduce the effect of pileup.
- For all detectors and their associated electronics, radiation hardness is required to tolerate the large particle fluxes without loss in performance or important ageing effects.
- Excellent tracking capability with precise momentum determination over a wide range of momenta - from hundreds of MeV to a few TeV.
- Large pseudo-rapidity acceptance with almost full azimuthal coverage in the whole detector.
- Efficient and precise vertex identification of charged particles and good performance in tagging of b jets and τ-leptons through secondary vertex reconstruction.
- An important requirement for ATLAS calorimetry is hermeticity, required for missing transverse energy (MET) measurements. The electromagnetic (EM) calorimeter must provide good identification and measurement of electrons and photons. Hadronic calorimetry must provide accurate jet measurements.
- Efficient muon identification and good momentum resolution over three orders of magnitude in momentum; from 1 GeV to a few TeV.

- Finally, highly efficient triggering on low transverse-momentum objects with sufficient background rejection. It is important to achieve an acceptable trigger rate for most physics processes of interest and to reduce background levels for efficient storage.

In order to achieve all these requirements, the detector is composed of four sub detectors: the closest to the beam line is the Inner Detector (ID) which measures charged particle tracks wich are bended by the 2 T solenoidal magnetic field. The inner detector is followed by electromagnetic and hadronic calorimeters, surrounded by the large Muon Spectrometer (MS) mounted inside a large magnetic volume produced by air-core toroids.

The magnet system configuration has driven the design of the detector, as we can see in Fig. 3.1.

Before giving an overview of the sub-systems, including the trigger, I present a few definitions and conventions which will be used throughout the text.

Geometry and coordinate system

ATLAS has a cylindrical shape and uses a right-handed coordinate system, illustrated in Fig. 3.2. The center of the detector corresponds to the interaction point and is defined as the origin of the coordinate system. The beam direction defines the z-axis and the x-y plane perpendicular to the beam direction, is called the transverse plane. The x-axis points towards the center of LHC ring and the y-axis points upwards in the vertical direction. Detector side A is the one with positive z and side C the one with negative z.

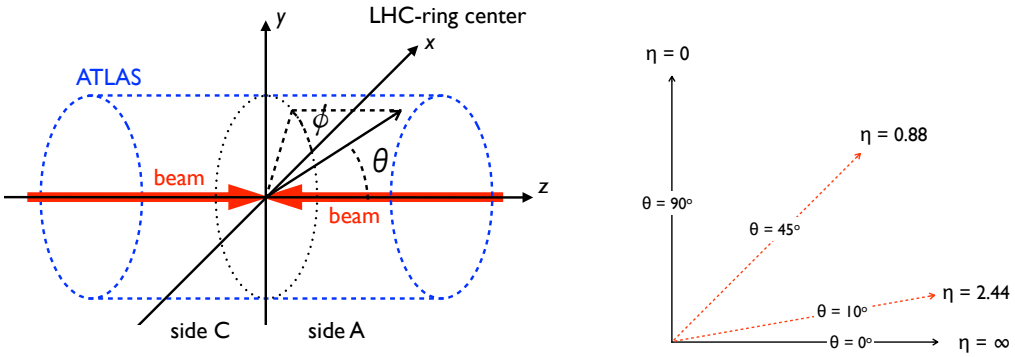

Figure 3.2: Left: Coordinate system used in ATLAS. Right: Correspondence between the pseudorapidity η and the polar angle θ for some specific values.

A polar system is frequently used, and defined by the radial vector R, the azimuthal angle ϕ, and the polar angle θ. The ϕ angle is measured from the x-axis, and runs from $-\pi$ to π, while θ is comprised between 0 and π, and R starts at the origin of the system. As

illustrated in Fig. 3.2, the polar angle can be expressed as a function of the pseudo-rapidity, η, defined by:

$$\eta \equiv -\ln\left(\tan\frac{\theta}{2}\right) . \tag{3.1}$$

The advantage of this particular unit is that differences in pseudo-rapidity are invariant under boosts along the beam axis. The pseudorapidity is preferred over the polar angle θ because, loosely speaking, particle production is constant as a function of rapidity. One speaks of the "forward" direction as regions of the detector that are close to the beam axis, at high η.

In ATLAS several quantities are expressed in the transverse plane, such as the transverse momentum and the transverse energy. Since the LHC is a proton collider, the portion of the proton energy carried by any parton is unknown. Therefore it is not possible to know the initial energies and momenta of the two partons, but the partons have very small transverse components. As a consequence the initial transverse momentum for primary collisions is taken as zero, and it is possible to use the conservation of momentum and energy in this plane. The transverse momentum (P_T) and the transverse energy (E_T), can be defined as:

$$P_T = P\,\sin(\theta)\ , \quad \text{and} \quad E_T^2 = m^2 + p_T^2 \tag{3.2}$$

Boosts along the beam axis do not affect the ϕ angle, and thus it is useful to measure distances in the azimuthal – pseudo-rapidity plane. The distance ΔR is defined as:

$$\Delta R = \sqrt{(\Delta\eta)^2 + (\Delta\phi)^2}\,. \tag{3.3}$$

3.1 The Inner Detector

The Inner Detector (ID) is used to reconstruct charged particle trajectories; it has been designed to provide hermetic and robust pattern recognition, excellent momentum resolution and both primary and secondary vertex measurements within the pseudo-rapidity range of $|\eta| < 2.5$. Details can be found in [48].

The ID located at the innermost part of ATLAS, is surrounded by a central solenoid that generates a uniform axial magnetic field with a strength of 2 T. Charged particles are bent by the solenoid magnetic field and the different ID layers allow a precise measurement of the charged particle trajectory. The combination of the high bending power and fine granularity allows us to determine the charge and momentum of the traversing particles.

To achieve the resolution requirements, the ID is made of three independent and complementary systems. The detectors closest to the beam line are the precision silicon detectors (pixels and strips) while the outer part is made of straw-tube trackers with the capability to generate and detect transition radiation. As illustrated in Fig. 3.3 the three

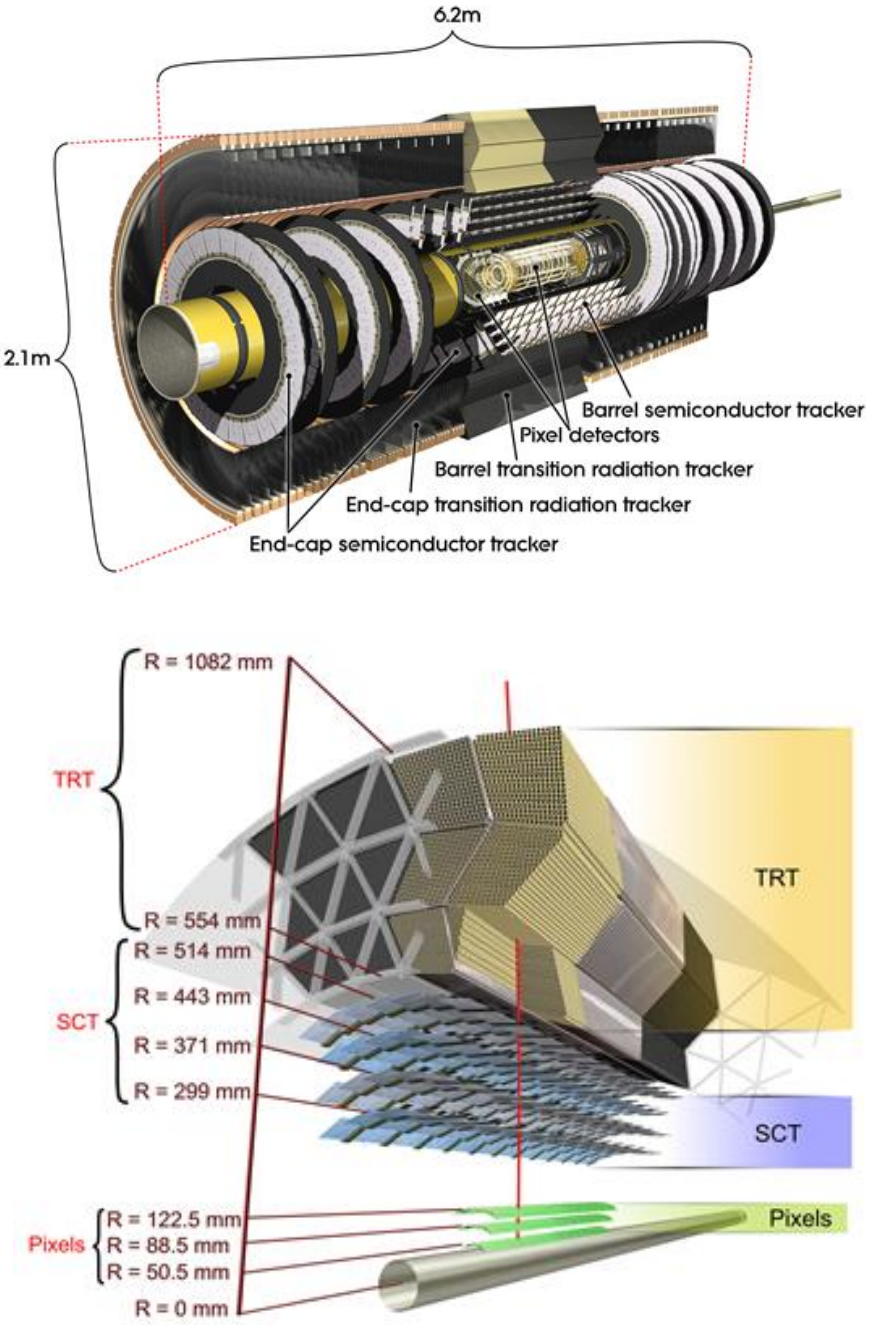

Figure 3.3: Illustration of the Inner Detector structural elements and sensors with their respective position, traversed by a track in the barrel region.

layers of detectors are arranged in concentric cylinders around the beam axis, in the barrel, and on disks perpendicular to the beam axis, in the end-caps.

The high-radiation environment and the occupancy impose important constrains on

the design of all the Inner Detector sensors, electronics, mechanical structure and services. Even though, the innermost layer of the pixels will need to be replaced after 2021.

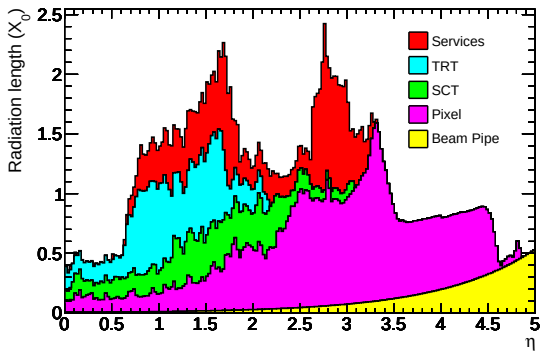

Figure 3.4: Material distribution between the interaction point and the Inner Detector envelope as a function of $|\eta|$ (averaged over ϕ).

Another important issue on the ID design was the material budget. The amount of material that particles cross needs to be minimized, in order to avoid the deterioration of the resolution in both tracking and calorimetry. In Fig. 3.4 the material distribution, in radiation lengths (X_0) is given, along with the contributions from detector elements, the beam-pipe and external services. Even though the amount of material was minimized, it varies from 0.5 to 2.5 radiation lengths mainly due to the services and supports. As a consequence $\sim 40\%$ of the photons convert into electron-positron pairs and electrons loose a small fraction of their energy through bremsstrahlung before reaching the electromagnetic calorimeter.

3.1.1 Silicon Pixel Detector

The pixel detector is the detector closest to the interaction point, where the high particle density around the vertex region requires fine detector granularity. The pixel layers are arranged in three concentric cylinders around the beam axis in the barrel (Fig. 3.3), and three disks perpendicular to this axis in the forward regions, for a cover that extends up to $|\eta| < 2.5$. The location of the layers are indicated in Fig. 3.3 radial positions in the barrel (z position in the end-caps).

The pixels are made of crystals of a silicon semiconductor material submitted to a voltage. When charged particles pass through the semiconductor they create electron-hole pairs. Then, the electrons are collected by electrodes and generate a current that is measured. The hit position is determined through charge interpolation over adjacent pixels. The pixel sensors are segmented in the transverse plane ($R-\phi$) and in the longitudinal plane (z), with intrinsic accuracies of 10 μm in $R-\phi$ and 115 μm in z. This provides the required accurancy in the $(R-\phi)$ bending plane for charged particles trajectories. There are approximately 80.4 million readout channels.

Since this sub-detector is the closest to the beam, there are strict requirements on the radiation hardness, occupancy and precision. The pixel detector needs to be kept at low temperatures (approximately -5 to -10°C) in order to minimize the damage caused by radiation.

An additional sensor layer will be inserted in the current shut-down (2013); it will be even closer to the beam axis than the current silicon pixel detector. This will improve the vertex reconstruction precision, and therefore the capability to disentangle multiple vertices very close to each other, in high pileup conditions.

3.1.2 Semi-Conductor Tracker (SCT)

The Semi-Conductor Tracker (SCT) follows the pixel detectors. It is made of layers of silicon strips. The silicon strip sensors themselves provide information in only one direction at the sensor plane (the electrodes are "strips"). Therefore, the sensor modules are arranged in 2-by-2 structures forming double sensor layers, with a small stereo angle of 40 mrad between them. In this way, they create a grid and provide the required two-dimensional information.

The silicon strip detector should satisfy radiation hardness and precision requirements similar to those of the pixels since it is placed 299 mm away from the interaction point in the radial direction. The strip sensors have a width which can vary from 56.9 μm to 94.2 μm.

The resolution is 17 μm in the bending plane and 580 μm along the z direction. The SCT operates at the same conditions as the pixels, since they share the same thermal enclosure. They have a total of about 6.3 million readout channels.

3.1.3 The Transition Radiation Tracker (TRT)

The transition radiation tracker (TRT) is made of layers of gaseous straw tubes inserted in transition radiation material. The TRT measurements complement the silicon sensor for the transverse momentum estimation, providing a large number of $(R-\phi)$ measurements per track, typically 36.

The TRT is located on the outer part of the Inner Detector, and extends radially from 56 to 107 cm over $|\eta| < 2.0$. The TRT does not provide information in the η direction. It only gives $(R-\phi)$ information in the barrel and $(z-\phi)$ in the end-cap. It has an intrinsic accuracy of 130 μm per straw. In the barrel region, the straws of diameter 4 mm and length 144 cm are disposed parallel to the beam axis, with their wires cut around $\eta = 0$. In the end-cap region, the 37 cm long straws are arranged radially in wheels. The total number of TRT readout channels is approximately 351 000.

The straws are filled with a non-flammable xenon-based gas mixture of 70% Xe, 27% CO_2 and 3% O_2. The gas is ionized whenever charged particles pass through. Each straw has a wire in the center, and between the wire and the straw's inner wall a voltage

is applied. The ions drift to the straw's wall, while the electrons are drawn to the central wire generating a current, which is measured.

In addition, the straws are surrounded by polypropylene fibers. When the charged particles pass through, they may radiate $X - ray$ photons that will also ionize the gas, making the signal stronger. Typically, between seven to ten strong wire signals (called high-threshold hits) from transition radiation are expected for electrons with energies above 2 GeV. This capability is illustrated in Fig. 3.5. Since electrons radiate more photons than charged hadrons like pions (because electrons are lighter than hadrons), the TRT has also electron identification capabilities.

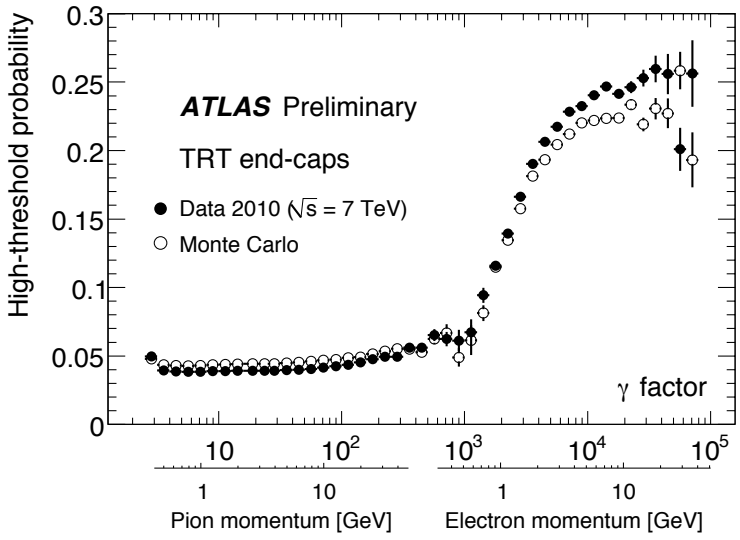

Figure 3.5: Probability of a transition radiation high-threshold hit in the TRT end-caps as a function of the Lorentz Factor. Measurements from 2010 LHC collision events are compared to predictions from Monte Carlo simulations.

As explained above, the precision silicon trackers close to the beam line are complemented by straw tubes providing many space point measurements with a longer lever arm. This results in a reconstruction efficiency above 98% for muons with transverse momenta above 5 GeV, as shown in Fig. 3.6a. The efficiency for reconstructing pions and electrons around 5 GeV is expected to go down to $\sim 80\%$ at large rapidities, becoming larger and more uniform as a function of $|\eta|$ at higher momenta. Multiple scattering, hadronic interactions in the case of pions and bremsstrahlung effects in the case of electrons are behind such inefficiencies.

By design, the tracking system is expected to provide a transverse momentum resolution of $\sigma_{P_T}/P_T = 0.05\%\, P_T(\mathrm{GeV}) \oplus 1\%$. The low-$P_T$ tracking is limited by the amount of material in the detector, while for large pseudo-rapidities the absence of the TRT implies a degradation of the momentum resolution. The expected momentum resolution for muons as a function of $|\eta|$ is given in Fig. 3.6b.

The expected resolution for the impact parameter (the point of closest approach with

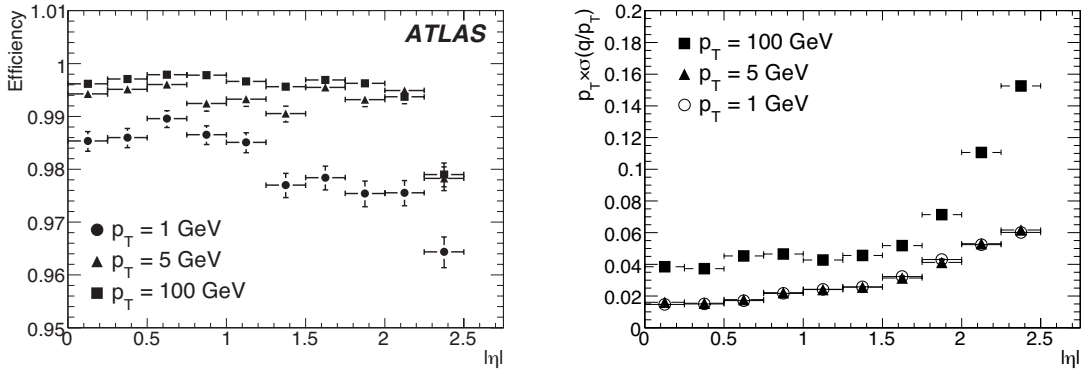

(a) (b)

Figure 3.6: Expected tracking performance in terms of (a) reconstruction efficiency and (b) relative transverse momentum resolution as a function of $|\eta|$ for muons of $P_T = 1$ GeV, 5 GeV and 100 GeV.

respect to the beam line) is a few hundred microns for the modified longitudinal impact parameter ($z_0 \times \sin\theta$), while in the transverse plane (d_0) it goes down to 10 μm for high momentum tracks. Low momentum particles are more subject to multiple scattering effects, which limits the resolution. The results obtained with full simulations for pions of $P_T = 1$, 5 and 100 GeV are shown in Fig. 3.7.

The fine granularity of the silicon detectors ensures low occupancy rates ($< 4\%$) up to 100 collisions per bunch crossing, which corresponds to a luminosity of 4×10^{34} cm^{-2} s^{-1} [49]. Only the momentum resolution may be worsened due to the high occupancy of the TRT (up to 60%), with degradations up to a factor of two.

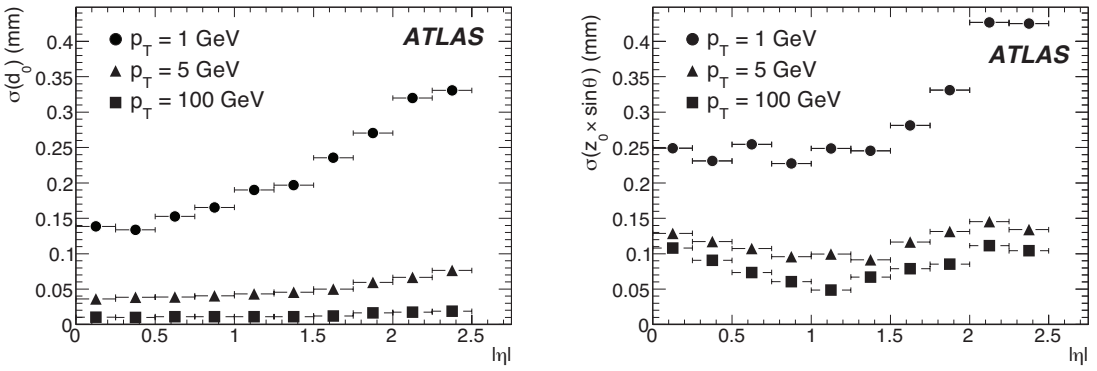

(a) (b)

Figure 3.7: Expected resolution on (a) transverse and (b) modified longitudinal impact parameters (d_0 and $z_0 \times \sin\theta$, respectively) as a function of $|\eta|$ for pions of $P_T = 1$ GeV, 5 GeV and 100 GeV.

3.2 The Calorimeters

The calorimeter measures the energies carried by charged and neutral particles. It consists of a dense absorber material, to develop a shower and fully absorb incident particles, and sensing material to produce an integrated output signal proportional to the particle energy. Interactions in the absorbers transform the incident particle energy into secondary particles with lower energy, that further interact with the material and generate more of them, thus creating a "shower".

The shower of particles are detected by the sensing materials. Photons and electrons interact electromagnetically with the electrons and nuclei in the matter, while hadrons have mainly strong interactions with the nuclei. As a consequence, the amounts of matter necessary for the development of an electromagnetic and a hadronic shower are different. The characteristic amount of matter for the electromagnetic interactions at high energy, X_0 (radiation length), is typically one order of magnitude smaller than the equivalent quantity for the hadronic interactions λ_I (nuclear interaction length). This interaction difference makes it possible to measure separately the energy of electrons or photons, and hadrons, in different calorimeter sections.

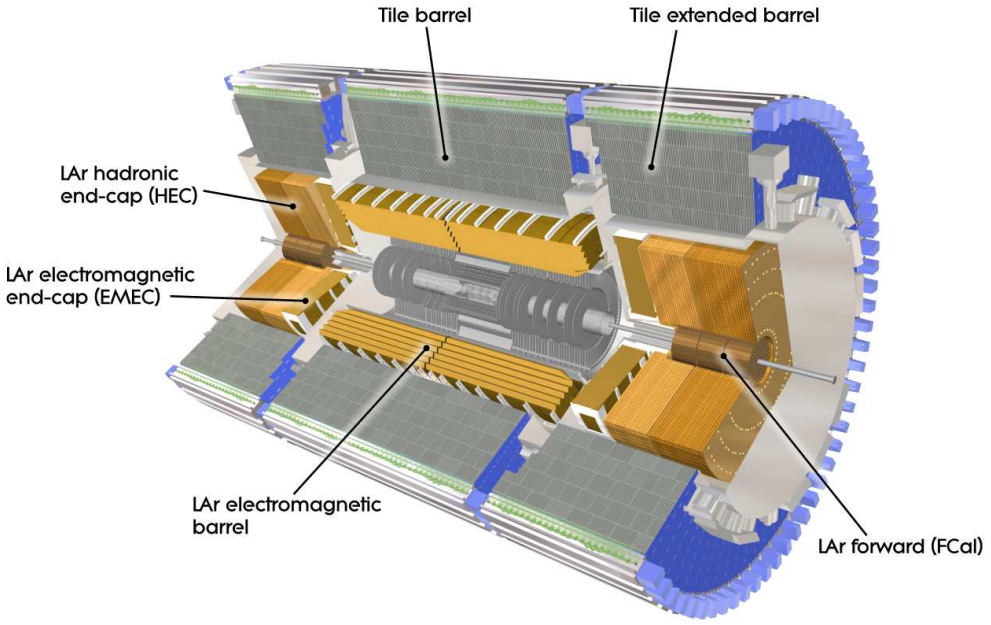

Figure 3.8: Cut-away view of the ATLAS calorimeter system.

The ATLAS calorimeter is composed of electromagnetic (EM) and hadronic sampling detectors, as presented in Fig. 3.8. In the inner sections of the calorimeter, the sensing element is liquid argon. The showers in the argon liberate electrons that are collected and recorded. In the outer sections, the sensors are tiles of scintillating plastic. The showers cause the sensitive component in the plastic to emit light which is detected and

recorded. The calorimetric system covers all the region $|\eta| < 4.9$. This η coverage gives large acceptance for electrons, photons and jets and given the full azimuthal coverage and good hermeticity of the detectors also information about missing transverse energy (caused by non-interacting particles escaping detection, such as neutrinos). The electromagnetic and hadronic calorimeters are described in detail in the following sections.

A layout of the ATLAS calorimeters is presented in Fig. 3.8 and the segmentation of each part is summarized in Table 3.1. Each sub-calorimeter is described in the following subsections and their performance is also discussed.

Calorimeter	**Coverage**		**Granularity ($\Delta\eta \times \Delta\phi$)**
EM calorimeter	**barrel**	**end-cap**	
Presampler	$\|\eta\| < 1.54$	$1.5 < \|\eta\| < 1.8$	0.025×0.1
Sampling 1	$\|\eta\| < 1.475$	$1.375 < \|\eta\| < 3.2$	0.003×0.1 ($\|\eta\| < 1.4$) 0.025×0.025 ($1.4 < \|\eta\| < 1.475$) 0.003 - 0.025×0.1 ($1.375 < \|\eta\| < 2.5$) 0.1×0.1 ($2.5 < \|\eta\| < 3.2$)
Sampling 2	$\|\eta\| < 1.475$	$1.375 < \|\eta\| < 3.2$	0.025×0.025 0.075×0.025 ($1.4 < \|\eta\| < 1.475$) 0.1×0.1 ($2.5 < \|\eta\| < 3.2$)
Sampling 3	$\|\eta\| < 1.35$	$1.5 < \|\eta\| < 2.5$	0.05×0.025
Tile calorimeter	**barrel**	**extended barrel**	
Sampling 1 Sampling 2	$\|\eta\| < 1.0$	$0.8 < \|\eta\| < 1.7$	0.1×0.1
Sampling 3			0.2×0.1
Hadronic end-cap calorimeter			
Samplings 1-4	$1.5 < \|\eta\| < 3.2$		0.1×0.1 ($1.5 < \|\eta\| < 2.5$) 0.2×0.2 ($2.5 < \|\eta\| < 3.2$)
Forward calorimeter			
Samplings 1-3	$3.1 < \|\eta\| < 4.9$		0.2×0.2

Table 3.1: Pseudo-rapidity coverage, longitudinal segmentation and granularity of the ATLAS calorimeters. The full numbers can be found in [50].

3.2.1 The electromagnetic calorimeter

The electromagnetic calorimeter detects and identifies electrons and photons, and measures their energy. In the electromagnetic calorimeter the absorbers are made of lead, the detection medium is liquid argon (LAr) and the electrodes are made of kapton, the absorbers and electrodes have an accordion shape. The space filled with liquid argon is under an electric field (2000 V over 2 *mm*), the kapton electrodes are surrounded by thin copper plates and thus readout is performed via capacitive coupling. Since the gaps between electrodes and absorber plates are 2 *mm* this implies a drift time of 450 ns.

The interactions of an incident particle through the lead generate an electromagnetic

shower. The resulting low energy particles, mainly electrons and positrons, ionize the liquid argon. The electrons produced in the ionization are collected on the copper electrodes, generating a current that is measured. The number of particles ionizing the argon is proportional to the energy of the incident particle, and so is the measured charge and maximum current. The signal derived from this electron current is amplified, shaped, digitized and recorded.

The EM calorimeter accordion shape geometry, represented in Fig. 3.9, provides full azimuthal coverage without cracks, allows fast signal extraction and segmentation of the active layers in depth. The EM calorimetric depth is approximately constant over η.

The EM calorimeter has a fine granularity in η and ϕ in the region covered by the inner detector ($0 < |\eta| < 2.5$), and a coarser granularity in the rest of the end-caps. Energy losses by particles crossing the material in front of the calorimeters introduce an uncertainty in the energy measurements. To overcome this difficulty, there is a thin LAr layer with electrodes before the other layers; it is called pre-sampler and covers the region $|\eta| < 1.8$. The η coverage and granularity of each layer are quoted in Table 3.1. Figure 3.9 shows a sketch of the different layers in the barrel, with the granularity details.

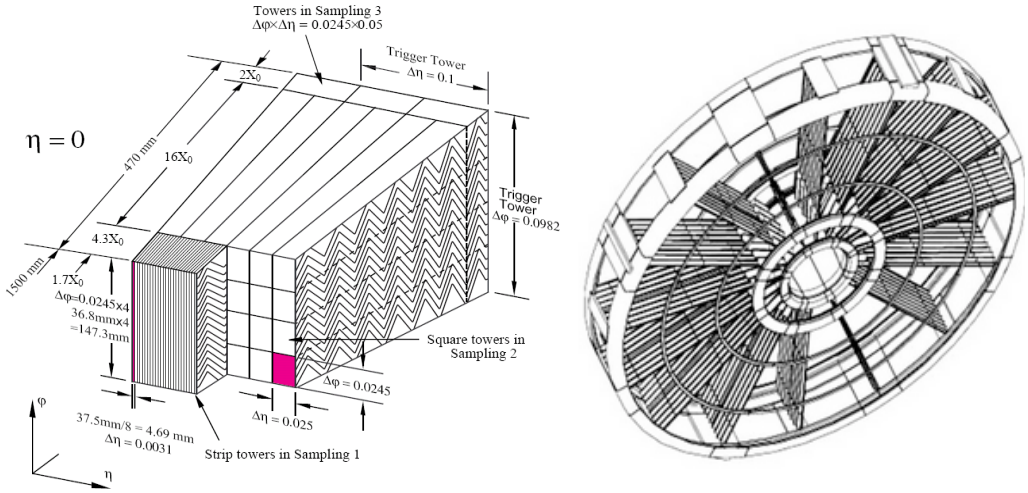

Figure 3.9: Sketch of a electromagnetic calorimeter barrel module. The cell granularity in η and ϕ each of the three layers are shown.

3.2.2 The hadronic calorimeters

The hadronic calorimeter is used to measure the energy of hadrons. Unlike electrons or photons contained in the EM calorimeter, hadrons traverse the EM calorimeter without loosing much energy. Two different active materials are used in the hadronic calorimeters, the end-caps ($1.5 < |\eta| < 3.2$) use the radiation hard liquid argon technology and the barrel

($|\eta| < 1.7$) scintillating tiles. Their main features are presented here, and their pseudo-rapidity coverage, longitudinal segmentation and granularity are quoted in Table 3.1.

In the barrel the hadronic activity is measured by the tile calorimeter (TileCal), which is placed directly outside the EM calorimeter envelope. Steel absorbers are used to generate the hadronic shower and scintillating tiles as active material, they are placed to form alternate layers of steel and scintillating material. When the particle shower particles pass through the scintillating tiles, they emit light in an amount proportional to the incident energy. The two sides of the scintillators are connected to wavelength shifting fibers that carry the light to the photomultiplier tubes.

The TileCal is divided into a 5.8 m long barrel, covering the region up to $|\eta| < 1.0$ and two extended barrels in the range $0.8 < |\eta| < 1.7$ with 2.6 m in length, see Fig. 3.8.

The hadronic end-cap calorimeter (HEC) uses liquid argon as active material and is based in the same principle used in the EM calorimeter. But in this case, copper is used as absorber and the structure geometry is different. It provides coverage for hadronic showers in the range $1.5 < |\eta| < 3.2$, and is located behind the electromagnetic end-caps. The HEC is formed by two wheels divided into two segments in depth, with a total of four compartments per end-cap. Each wheel is built from 32 identical wedge-shaped modules, providing projective geometry in the ϕ direction but only "pseudo-projectivity" in η.

The thickness of the hadronic calorimeter layers are optimized to fully contain the hadronic showers and provide adequate longitudinal sampling for shower shape development analysis. The granularity of the layers are optimized to allow jet direction measurements and to provide adequate measurements of the shower profile in η and ϕ.

3.2.3 The forward calorimeter

The forward calorimeter (FCal) has been designed to cope with the high particle flux and energy densities in the forward direction. It is located from $|\eta| = 3.1$ to $|\eta| = 4.9$. The FCal provides both electromagnetic and hadronic energy measurements. The primary purpose of this detector is to help in the calculation of the missing transverse energy and measure the properties of forward jets.

The FCal is made of three modules in each end-cap. The first one uses copper as absorber and is optimized for electromagnetic measurements, while the other two use tungsten and measure mainly the hadronic energy. The electrode structure consists of concentric rods and tubes parallel to the beam axis, and they use also liquid argon as active material.

3.3 The Muon Spectrometer

Muons penetrate through the calorimeters without being stopped and reach the outermost part of ATLAS, known as the muon spectrometer. The muon spectrometer surrounds the

calorimeters and measures muon trajectories, momenta and charge.

This happens inside a volume of magnetic field produced by superconducting toroid magnets. The detection elements (the muon chambers) are made of gaseous detectors of various kinds. All of them are based on the same principle: as a charged particle passes through, the detector gas is ionized, it leaves a trail of electrically charged ions and electrons which drift to the anode electrodes and generate a current. By measuring these localizated charges drift time, it is possible to determine the position of the muon as it passes through. The momentum can be estimated from the muon trajectory curvature caused by the magnetic field provided by the toroidal magnets. A view of this sub-detector is shown in Fig. 3.10. It covers the region $|\eta| < 2.7$.

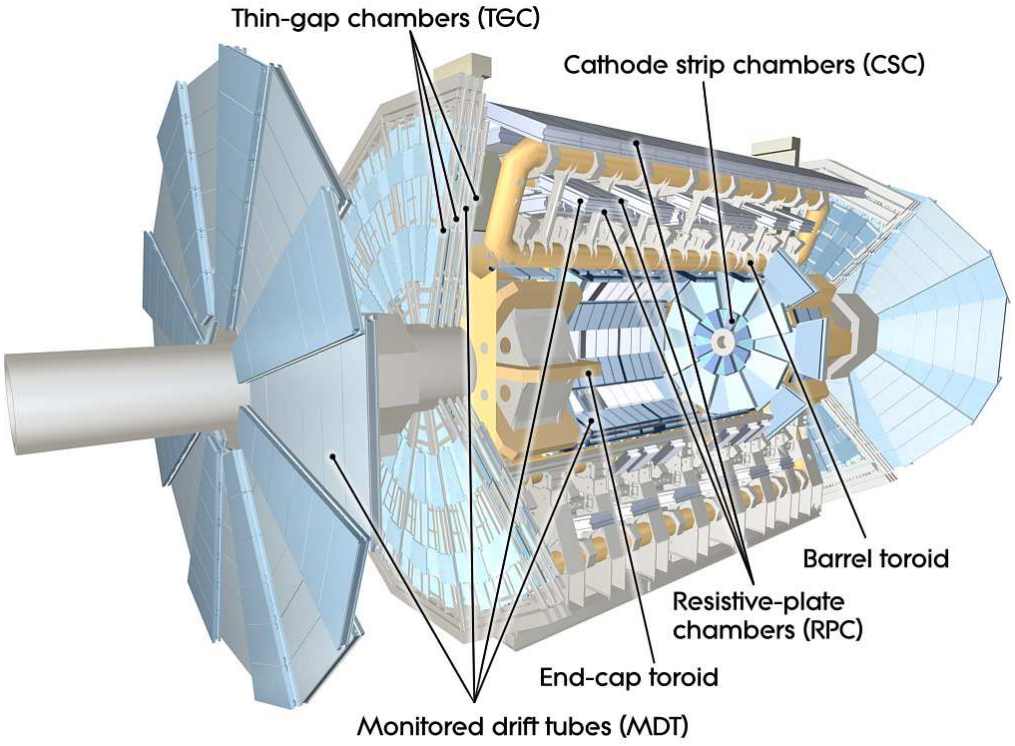

Figure 3.10: A schematic of the ATLAS muon spectrometer [50].

Different gaseous detectors are used to satisfy different requirements. Some detectors provide precision measurements of the track coordinate in the principal muon bending direction (η), and some others provide prompt information for the trigger system. The detectors providing precision measurements in η are: Monitored Drift Tubes (MDT) in the barrel and the external part of the end-caps ($|\eta| < 2.7$) and Cathode Strip Chambers (CSC) in the forward inner region ($2.0 < |\eta| < 2.7$). The detectors providing fast information to the trigger are: Resistive Plate Chambers (RPC) in the barrel, and Thin Gap Chambers (TGC) in the end-caps. These detectors also complement the MDTs measurements by providing information in both directions, η and ϕ. A summary of the expected individual

chamber resolution and number of elements of each technology is given in table 3.2.

Type	Chamber resolution			Measurements/track	
	z/R	ϕ	time	barrel	end-cap
MDT	35 μm	–	–	20	20
CSC	40 μm (R)	5 mm	7 ns	–	4 + 4
RPC	10 mm (z)	10 mm	1.5 ns	6	–
TGC	2-6 mm (R)	3-7 mm	4 ns	–	9

Table 3.2: Parameters of the four chamber technologies used in the muon system: expected individual chamber intrinsic resolutions, maximum number of measurements per track.

A high momentum 1 TeV muon has a track curvature of 500 μm in the barrel spectrometer. In order to achieve the required transverse momentum relative resolution of about 10% for a 1 TeV muon, the track curvature (sagitta) must be known with an accuracy of 50 μm. Those requirements are fulfilled with precise knowledge of the magnetic field and chamber positioning. An optical alignment system is used to infer the chambers positions within 30 μm, as well as the chamber deformation. A brief description of the different components of the muon system and the obtained performance are given in the following subsections. The reader is referred to [47, 48, 50, 51] for more information.

3.3.1 Geometry and chamber types

The muon chambers are arranged in three layers following a cylindrical shape around the beam axis in the barrel ($|\eta| < 1.05$). There is a gap at $z = 0$ for services. In the end-cap ($1.05 < |\eta| < 2.7$), the chambers are arranged in three planes, each called wheels, that are perpendicular to the beam axis. The first two end-cap layers are built on movable wheels, while the outermost layer is attached to the cavern support structure. The three layers are denoted inner (I), middle (M), and outer (O) layers, both in the barrel and end-cap (in the end-cap the Inner wheel is called small wheel), and the layers of a given sector build a projective tower.

The chambers are also arranged to follow the eight-fold symmetry of the toroid magnets, as illustrated in figure 3.11. The sectors alternate between large (in between toroid coils) and small (around toroid coils) chambers, with overlaps between sectors to minimize azimuthal gaps in detector coverage.

The precise momentum measurement is performed by determining the track coordinate in the bending plane. A brief description of the technologies used to built the muon chambers follows.

Monitored drift tubes (MDTs)

The Monitored Drift Tubes chambers cover both the barrel and the end-cap regions. Each chamber is made of three or four layers of aluminium tubes of 30 mm in diameter, filled

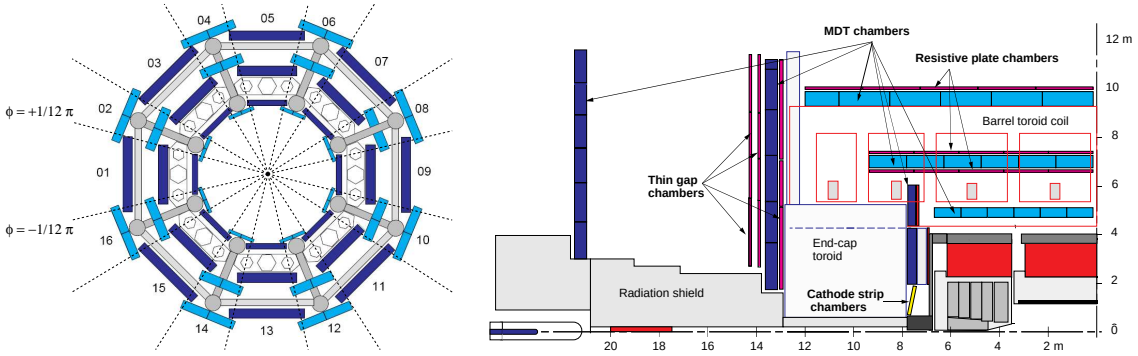

(a) $R - \phi$ view of the barrel muon spectrometer, illustrating large sectors (dark blue), small sectors (light blue) and the magnet coils (dark grey).

(b) $R - z$ view of the muon spectrometer showing the different technologies and stations.

Figure 3.11: Illustration of the muon system in $R - \phi$ and $R - z$ projections.

with gas and equiped with a central wire set at high voltage ($\sim$3 kV) with respect to the tube wall. As illustrated in Fig. 3.12a when a muon passes through these tubes, it leaves a trail of electrons which drift to the anode wire under the influence of the electric field. In the vicinity of the wire, an avalanche process takes place inducing a voltage drop on the wire and this is the primary signal of the MDT tube, called a hit. The time between the hit and the last charges of the signal pulse is read out and digitized. An amplifier / shaper / discriminator chip including a charge analog-to-digital converter (ADC) feeds the pulses to a time-to-digital converter (TDC).

The hit time is a measure of the time of arrival of electrons created by the muon at the closest distance of the wire. The drift time depends on the distance of the muon track to the wire (Fig. 3.12a) and has a maximum value of $\sim$700 ns. Single hit resolutions of the order of 80 μm are achieved, with an efficiency around 96%. The chamber resolution, since they contain several layers of MDTs, is of the order of 35 μm.

The tubes operate with Ar/CO_2 gas (93% / 7%) at three bars, selected for its excellent aging properties. In the center of each tube, a 50 μm tungsten-rhenium wire is kept at 3080 V, generating a radial electric field. Each MDT chamber is built with two multilayers of three tube layers, except in the inner most layers where four tube layers are used in order to aid pattern recognition in the face of high particle fluxes. There are from 30 to 72 tubes in each layer, depending on the chamber location, and the tubes of adjacent layers are staggered by half a tube (Fig. 3.12b). Since the tubes are oriented along the ϕ direction, each tube gives essentially no information on this second coordinate. The chambers are held together with a support structure which contains an optical alignment system that is used to monitor the chambers for deformations and to monitor the inter-chamber alignment. In addition, each chamber is outfitted with sensors to monitor the local magnetic field and temperature.

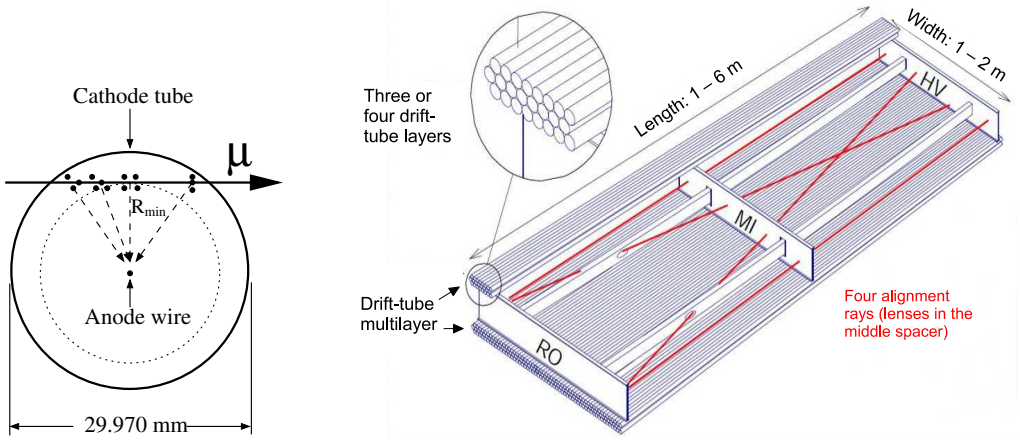

(a) Cross section of a MDT tube.

(b) Sketch of a MDT chamber. The alignment rays, shown in red, allow for the monitoring of chamber deformations.

Figure 3.12: Illustration of (a) a Monitored Drift Tube (MDT) and (b) the corresponding chamber.

Cathode Strip Chambers (CSCs)

In the very forward region ($2 < |\eta| < 2.7$) the flux of muons is higher, the MDT have been replaced by CSC which combine high spatial and time resolutions with high-rate capability. CSCs are multi-wire proportional chambers filled with a Ar / CO_2 (80% / 20%) gas mixture with radial anode wires and cathode planes segmented into orthogonal strips. The wires are 30 μm in diameter and operate at 1900 V. This results in drift times of less than 40 ns, with an associated precision of $\sim$7 ns.

When a muon traverses the chamber, the gas is ionized and an electron avalanche is formed on the anode wire. The avalanche induces a charge on the strips, which is read out as the signal. A single avalanche can induce signals on multiple strips, and interpolating the charges on neighboring strips allows for a hit resolution of 40 μm in R; in the ϕ coordinate the avalanche falls only on one strip so that the hit resolution is 5 mm.

The cathode-to-wire distance is 2.54 mm. A single chamber combines four such anode/cathode layers, thus providing four precision and four second-coordinate measurements per track.

Resistive Plate Chambers (RPCs)

Resistive Plate Chambers provide the trigger and second coordinate measurement in the barrel. RPCs are gaseous parallel-plate detectors, with a 2 mm gap created by insulating spacers between the electrodes. The RPCs are filled with a mixture of $C_2H_2F_4$ / Iso-C_4H_10/SF_6 (94.7/5/0.3), the electric field between the plates is about 4.9 kV/mm. The RPC chamber layout is shown in Fig. 3.13a.

Signals are generated when a muon traverses the gaps and ionizes the gas. The primary ionization causes an avalanche that is read out capacitively by metallic strips mounted on

the plates. The strips on either side of the gap are perpendicular, thus allowing for measurements of both the η and ϕ coordinate. The strip pitch is approximately 30 *mm*, thus giving a spacial resolution of around 10 *mm* for both coordinates, with timing resolutions below 7 *ns*, which allows for accurate bunch crossing identification.

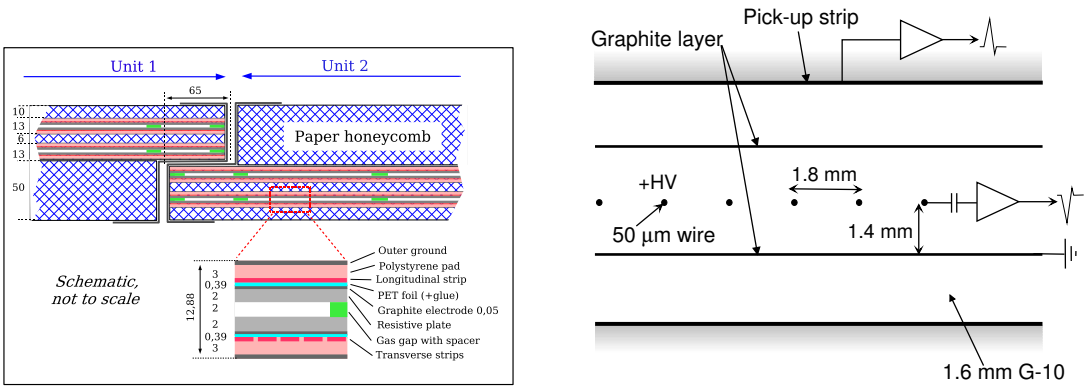

(a) (b)

Figure 3.13: Structure of (a) Resistive Plate Chambers (RPC) and (b) Thin Gap Chambers (TGC).

Thin Gap Chambers (TGCs)

The TGC chambers provide the triggering and second-coordinate measurements in the end-cap region ($1.05 < \eta < 2.7$ with triggering out to $\eta = 2.4$). They were preferred to the RPCs because of their higher granularity and higher rate capabilities needed to operate in the high flux environment of the end-caps. Each chamber is a multi-wire proportional chamber filled with a highly quenching gas mixture of CO_2 and n-pentane. The TGCs have two layers of graphite cathodes separated by 2.8 *mm* and a series of 50 μm diameter anode wires running in the middle of the gap between cathodes. One side of the cathodes is segmented into read-out strips. The structure of a TGC chamber is illustrated in Fig. 3.13b. The wires are oriented in the ϕ direction to measure the η coordinate, while the strips are oriented radially and measure ϕ. A voltage of 2.9 kV is applied on the anode wires. Including the variation of the propagation time on wires and strips, signals arrive with 99 % probability inside a time window of 25 *ns*.

The chambers used for triggering are located around the end-cap middle wheel, with two layers of chambers on the inside of the wheel and one on the outside. Additional chambers used for second coordinate measurements are located on the small wheel.

3.4 The Magnets

The ATLAS detector has a superconducting magnet system in order to provide the bending power needed for charged particles momentum measurement, in a light and open structure,

for minimizing scattering effects.

The magnet system consists of two sub-systems: the solenoid magnet surrounding the inner detector and the toroid magnet system inside the muon spectrometer. The toroidal-shape magnet system is actually one of the main features which gives ATLAS its name: "A Toroidal LHC ApparatuS".

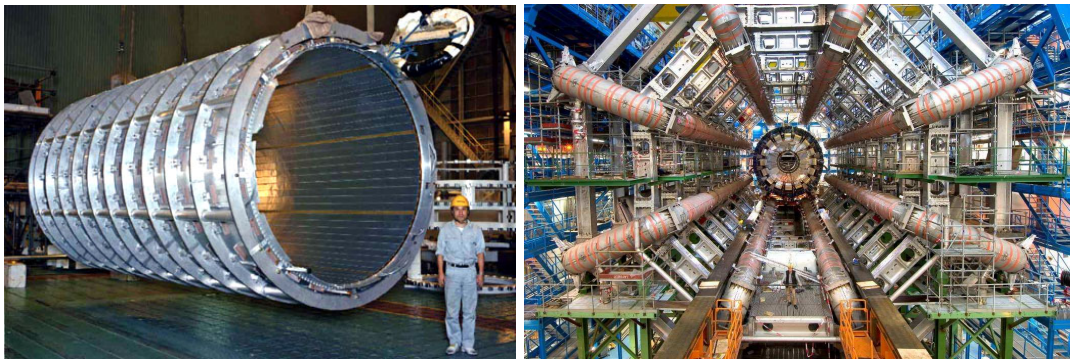

(a) (b)

Figure 3.14: Pictures of the ATLAS magnets. (a) The solenoid magnet provides the magnetic field required for the inner detector momentum measurements and (b) the picture of the barrel toroid magnet installed in the ATLAS cavern, consisting of 8 coils in the barrel and coils regions.

The solenoid magnet, shown in Fig. 3.14a, is aligned with the beam axis, surrounds the inner detector and produces a 2 T magnetic field in the z-direction. Therefore the charged particles are bent in the $x-y$ plane, changing their ϕ direction of flight. The solenoid was designed to keep a small amount of material in front of the electromagnetic calorimeter. Therefore, the solenoid is made of a single-layer coil wound with a high-strength aluminium-stabilized niobium-titanium (NbTi) conductor inside a 12 *mm* thick support cylinder, that produces the high magnetic field while keeping the solenoid thin. It is housed in a cryostat which is shared with the calorimeter, in order to avoid additional dead material between the two components.

Three air-core toroid magnets, one in the barrel and one in each end-cap, provide magnetic fields for the muon spectrometer of approximately 0.5 T and 1 T, in the barrel and end-cap respectively. The toroidal configuration provides a field which is mostly orthogonal to the muon trajectories over a large volume. The magnet coils are not placed in iron, which would increase the magnetic field strength, but are surrounded by air to minimize the amount of material in the measurement regions, minimizing the degradation of the resolution due to multiple scattering. The magnets are cooled down to 4.5 °K by liquid helium and operate at a nominal current of 20.5 kA. Figure 3.14b shows a picture of the barrel toroid system during the ATLAS installation period.

Ideally, the magnetic field lines make big circles around the beam axis, and so the muons are bent changing their η direction. Nevertheless, due to the finite number of coils, the field configuration is not perfectly toroidal. The field in the transition region

is also affected creating a small region with degraded momentum resolution. The B-field integral shown as a function of η in Fig. 3.15 is far from being uniform. The magnetic toroidal field is continuously monitored with a system of about 1800 Hall sensors. Their information is used to derivate the superconductors positions (with a *mm* precision). Using this information it is possible to calculate the B-field map in the muon spectrometer volume.

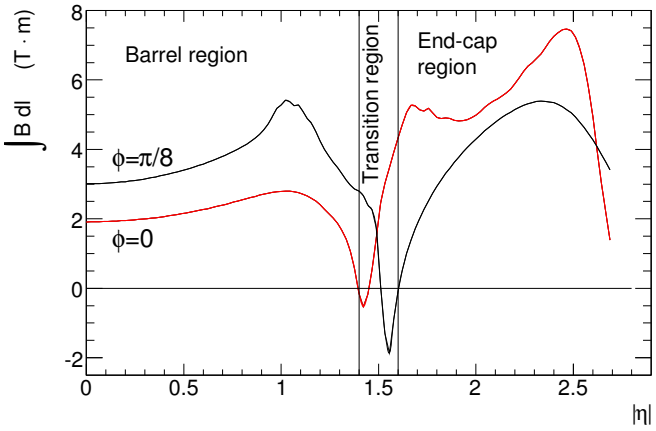

Figure 3.15: Predicted field integral as a function of $|\eta|$ inside the muon spectrometer. The field integral in the transition region is low resulting in a degraded momentum resolution.

3.5 The trigger system

The trigger system at the LHC is the first step of the event selection process and represents a very challenging task. It has a crucial role, given the enormous range of production cross sections for the benchmark phenomena to be studied.

The trigger system is basically a filter that must provide a huge reduction factor and at the same time must maintain high efficiency for retaining the few interesting events among millions of background events. It has to decrease the event rate from the nominal bunch crossing rate of 40 MHz to a rate of about 400 *Hz*, a rate at which data can be written to permanent storage. The trigger is provided by the combined action of three different levels, called level 1 (L1), level 2 (L2) and event filter (EF). Each trigger level refines the decisions made at the previous level and, where necessary, applies additional selection criteria.

The first trigger level (L1), which is hardware based, uses a limited amount of the detector information from the calorimeters and the muon trigger chambers to make a decision in less than $2.5\mu s$, reducing the rate to about 75kHz. The L1 trigger searches for objects with high transverse momentum, muons, electrons, photons and jets, as well as large missing and total transverse energy. The trigger relies on the RPC and TGC for muon triggers and the calorimeter for triggering on EM clusters, jets, taus, and missing

energy. The L1 trigger also identifies the so-called Regions of Interest (RoI).

The level-2 trigger is software-based and uses the Regions-of-Interest (RoI) identified by the L1 trigger, which corresponds to only a subset of the detector information. Fast reconstruction algorithms are performed on the data in the RoI to allow for more precise trigger decisions. The L2 reduces the trigger rate to approximately 3.5 *kHz*, with an event processing time of about 40 *ms*.

The Event Filter is also software based, events are reconstructed completely, using algorithms similar to the ones used in the offline analysis. It is designed to reduce the rate to the final ∼400 *Hz* with an average event size of ∼1.3 *Mbyte*. The events passing the EF are then recorded for further analysis.

The information used by the different trigger levels can be organized in different trigger menus. These trigger menus serve to classify events into physics channels and store them separately. For example, there is a trigger menu that requires at least one muon or one electron to satisfy the trigger criteria. To perform the $W^{\pm}Z \to \ell\nu\ell\ell$ analysis reported in this thesis, it was enough to process events triggered by the muon and electron menus. The criteria used in these menus are optimized as the luminosity increases, to satisfy the output rate limits. One can, for example, increase the momentum threshold for triggering, or require two leptons in the trigger menu.

3.6 LHC environment and background

The high center of mass energy and luminosity of the LHC generate important levels of secondary radiation in the detector and in the ATLAS experimental hall. This is one major concern for ATLAS and a large effort has been made since the early phase to design an effective shielding.The background radiation can produce:

- An increase in the detector occupancy. In tracking detectors this can lead to inefficiencies, deteriorated resolutions and fake tracks. In calorimeters, the increased pileup fluctuations degrade energy resolution. Also, an increase in the rates of random triggers.
- Radiation damage of silicon detectors and electronics.
- Wire detectors can experience “aging” (reduced efficiency) due to polymerised deposits on the wires caused by radiation interacting with organic additives in the detector gas.
- Nuclear interactions in dense materials lead to the creation of residual radionuclides.

The background is studied in some detail in this section, as it is of great importance at the high luminosities encountered at the LHC upgrade.

There are three major sources of radiation at the LHC: particle production in the interaction region, local beam losses, and beam-gas interactions. The total beam loss around the ring should not exceed 10^7 protons s^{-1}, to remain small compared to the

proton-proton collision rate of $\sim 10^9\ s^{-1}$ per collision point. Beam gas interactions are estimated to be $\sim 10^2\ m^{-1}s^{-1}$ in the interaction region. Therefore, the dominant radiation source is due to particles produced in the proton-proton collisions in the interaction region [52].

Most of the collision products are absorbed in the calorimeters, and in the shielding. However there are remaining neutrons, traveling long distances, losing their energy gradually. Nuclear capture, in particular of thermal neutrons, frequently results in the production of photons via (n,γ) reactions; photons also result from excited-state decay via evaporation from spallation products. The typical γ energy from these processes are between 100 keV up to several MeV. Photons produced deep inside the material are quickly absorbed; those observed in the detectors are usually produced in the outermost centimeters of the materials. These photons in turn, can produce electrons and positrons, thus giving rise to most of the low-energy electron background. As these neutrons, photons and electrons are produced in a lengthy showering process, they form a background with essentially no time structure. Neutrons, and to a smaller extent photons, are scattered many times before being captured giving rise to a relatively uniform and isotropic "gas" of low-energy background particles, this type of background is the *uncorrelated* background. Figure 3.16 shows the fluences in the muon chambers at a luminosity of $10^{34}cm^{-2}s^{-1}$. The neutron and γ fluences are in units of kHz/cm^2 and the μ and proton fluences in Hz/cm^2.

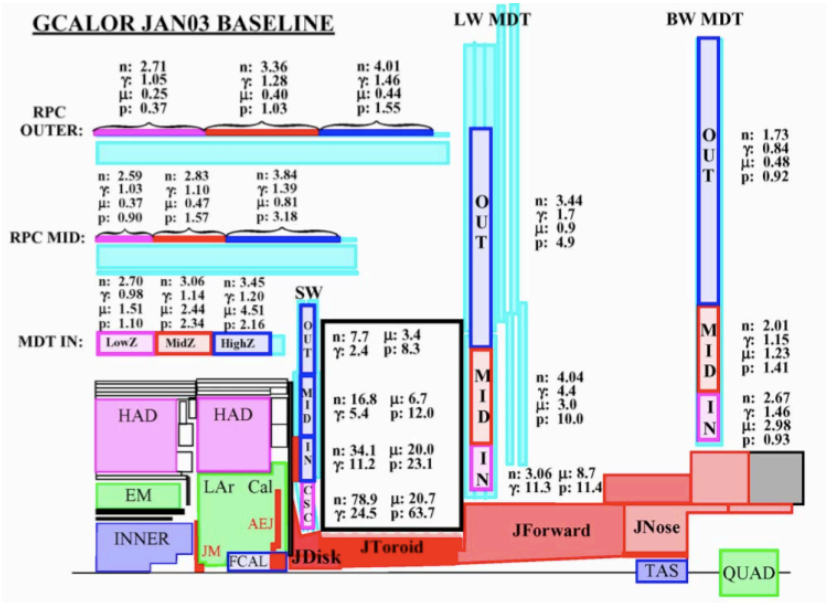

Figure 3.16: Fluences in the muon chamber location a luminosity of $10^{34}cm^{-2}s^{-1}$. The neutron and γ fluences are in units of kHz/cm^2 and the μ and proton fluences in Hz/cm^2. The figure represents the projection on the $(R-z)$ plane for $z>0$

3.6.1 Shielding Strategies

Even though the ATLAS detector has been designed to support large amounts of radiation, it contains several shieldings protecting its different subdetectors. The shielding strategy extensively used in ATLAS consists in using dense materials wherever possible to develop hadronic and electromagnetic showers, and to range out their particles. Ideally, the material should be thick enough to absorb all charged particles (with muons being typically the exception).

The remaining neutrals are mostly neutrons, which can travel long distances, losing their energy gradually by collision, and lead to further photon production. So for shielding to be efficient, most of these neutrons and gammas should be confined to the shielding volume surrounding the beam pipe. In the ATLAS detector, most of the energy from primaries is dumped into the forward calorimeter. The thickness of the forward calorimeter has been chosen to contain and absorb the electromagnetic and hadronic showers, so they serve as shielding for the muon spectrometer. Nevertheless there can be neutrals and some secondary particles that escape the calorimeters to become sources of secondary radiation. The beam vacuum system on the other hand spans all the length of the experiment and is in the forward region a major source of radiation backgrounds.

There are also several regions where the shielding design is particularly weak (see Fig. 3.17). As mentioned before, the calorimeters themselves are the primary shield protecting the muon system (evidently no shielding matter can be put in front of them). But between barrel and endcap there is a gap of approximately 50 cm in width, running radially to the outside, filled with lightweight cryostat structures, electronics, and services. This gap puts a serious radiation into the barrel muon system, but the effect seems to be small compared to the radiation in the barrel region [53].

Another potential weak area is the endcap calorimeter, particularly in the very forward region where the CSC muon detectors are placed. For this reason, three shielding plugs of copper alloy have been placed inside and at the back of each endcap cryostat to increase the total absorption lengths. The effect of all these shielding optimizations is that the overall rates in the CSC/TGC region behind the endcap calorimeter are acceptable for operation of the muon system.

There is not always enough space to accommodate an ideal shielding. The shielding design in the limited space of the ATLAS detectors involved judgments about the relative seriousness of the radiation effects and within some margin the shield design was tuned accordingly. The critical fluxes that should be monitored are neutrons (below and above 100 keV), photons, hadrons (above 20 MeV), and pions in the inner detector and penetrating particle rates in the muon chambers.

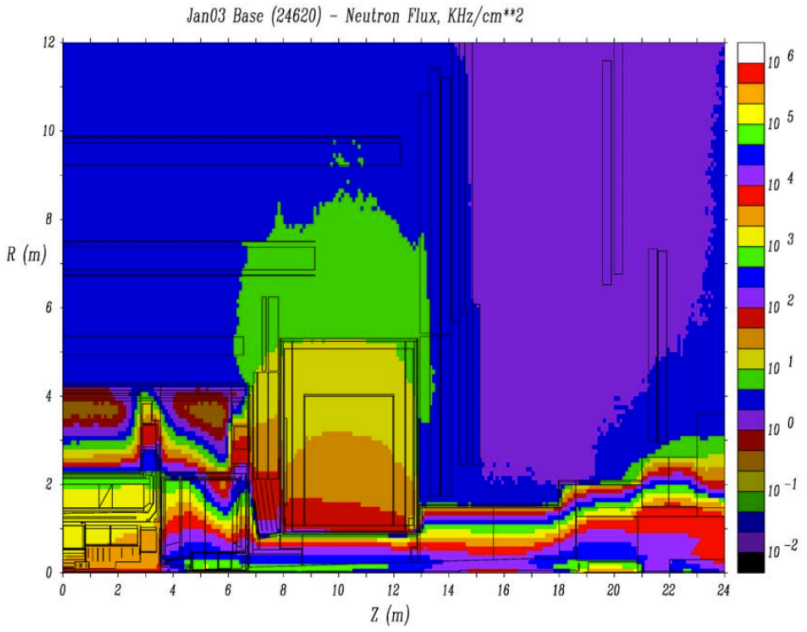

Figure 3.17: Neutron flux simulation. The regions where the shielding design is particularly weak can be seen. One of them is the gap of 50 cm between barrel and endcap area. Another potential weak area is the endcap calorimeter, particularly in the very forward region.

3.6.2 The background in the ATLAS muon chambers

The anticipated high level of particles fluxes has played an important role in the choice of the detectors and have a major impact on the spectrometer design. They influence parameters such as the rate capability of chambers, the aging of the detector components, the granularity and redundancy of the trigger instrumentation, the pattern recognition efficiency, or the momentum resolution tails induced by incorrect hit association [50].

Fluxes of background particles tend to be isotropic in the barrel, while in the endcap a substantial fraction of the particles comes from the interaction region. They are two broad classes of background hits: *i*) primary collision products, called *correlated* background, such as prompt muons from heavy particle decays and hadronic debris of calorimeter showers or additional hits to the muon track like δ-rays. *ii*) the very low-energy secondaries from radiation background make the so called *uncorrelated* background.

The photon and neutron background interactions with the detectors are studied in more detail below:

- **Neutron background:**

  Neutron-induced background hits in the detectors are due to a large variety of reactions. First of all the neutrons contribute to the photon spectrum via (n, γ) reactions. Also the when they are finally thermal the neutron capture ($E \sim 0.025\ eV$ [54]) creates background hits in the tubes due to β-decay following the neutron capture (in

the gas or in the tube wall). For example in MDT chambers, there is a background constant in time produced by neutron activation of different elements of the tube material. The main contribution to this process is the production of ^{28}Al and ^{41}Ar in the reaction of neutron absorption by ^{27}Al (in the tube) and ^{40}Ar (in the gas) respectively, followed by the β decay of the nucleus [55]. The electrons produced in ^{28}Al decay ($E_{max} \sim 2.8\ MeV$) can eventually pass through the tube walls and induce a signal in adjacent tubes. In addition, the presence of any material in the vicinity can also increase the tube count rate induced by thermal neutrons [55].

For neutrons in the energy range 100 keV - 1 MeV, it is the recoil of gas nuclei with its associated ionization that produces the signal. At higher energies ($>$ 1 MeV prompt spallation signal), the neutrons can make charged secondaries, mainly protons from quasi-elastic scattering in the chamber wall or surrounding material, hence their rate may vary locally (e.g an important source of protons are the endcap toroid coils because they are exposed to a flux of hard neutrons).

The efficiency for neutrons in different chamber types is shown in Fig. 3.18; three ranges of neutron energies can be seen. The important differences between the detectors at energies $10^{-2} - 10$ MeV are mainly due to the different gas composition with which chambers are filled. The fact that the gas in the CSC contains no hydrogen, combined with the small gap, explains the low sensitivity to neutrons in these ranges of energies. When a chamber is irradiated by neutrons, the counting rate of one specific tube is the combination from the counting rate induced by particles originated in the tube itself and the counting rate induced by particles originated in the surrounding tubes.

- **Gamma background:**

  In the neutron background, the main source of gammas are due to the remaining neutrons. Gammas result from excited-state decays of spallation products, from fast neutron interaction with atomic nuclei and by the process of nuclear capture. Because of the high photon energies, the main background in the tubes is Compton scattering on the electrons in either the counting gas or the tube walls. The magnetic field curl the tracks of these Compton electrons but eventually they will be energetic enough to go out of the tube and fire a RPC or TGC doublet and fulfill the trigger logic. In addition, the scattered photon may continue, unhampered by the magnetic field, reach the next station and produce a second electron. That effect (called "Double-Compton") has been considered in the latest trigger rate estimates [53]. A critical element is the angular distribution of the photons that must be taken into account.

  Calculations, made from simulations of the detector [53], show that in the barrel region typically 10% of the electrons produced by Compton scattering have enough

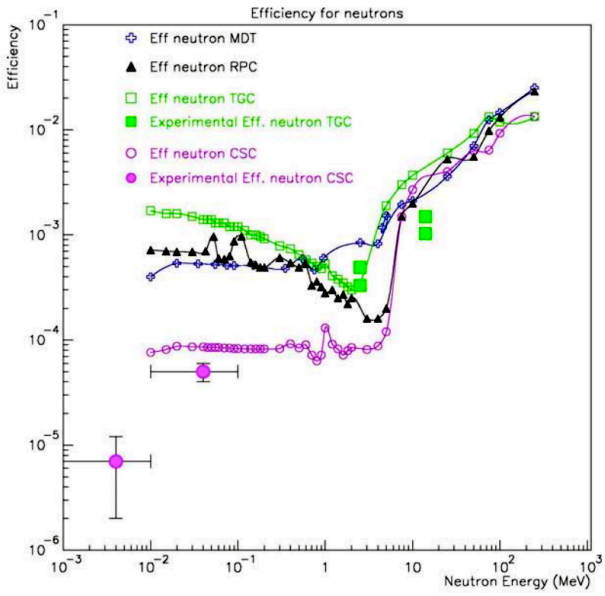

Figure 3.18: The efficiency for neutrons for the different chamber types as calculated with the simulation Geant3. Experimental measurements are show for CSC and TGC. [53]

energy (> 5 MeV) to fire a doublet, and in the forward region some 10% to 20% [53]. The contributions of pair production can be neglected because this process dominates only when photon energies are more than 10 MeV.

- **Ionizing particle background:**

  Protons (and pions) with energies above 20 MeV can fire one or two of RPC planes with a 100% probability [53]. These protons are produced mainly by interaction of energetic neutrons in the material and hence their rate may vary locally. One of the important sources of protons are the endcap toroid coils that are exposed to a flux of hard neutrons. It is not the case for the barrel region where the neutron energy spectrum is softer.

So the background affects the muon system in two ways: by generating uncorrelated noise hits, and by producing penetrating particles. The uncorrelated noise hits in the chambers may affect the pattern recognition and aging. On the other hand penetrating particles are an important component of the background for the trigger. RPC and TGC chambers provide transverse measurements and they are used by the trigger to reject muons with p_T below a given threshold. The penetrating particles background can increase the rates of false triggers. Also, the increased occupancies can increase the rates of random triggers.

Taking into account chambers efficencies the fluences in the muon chambers at high luminosity ($10^{34} cm^{-2} s^{-1}$) are shown in Fig. 3.16. The counting rates in the barrel are

of the order of $10 - 12$ Hz/cm^2 both for MDTs and RPCs. They are dominated by the photon contribution ($\sim$ 80 %) followed by neutron and protons ($\sim$ 10% each). In the inner barrel, the contribution from punchthrough muons raises to about 15 % and from pions to a few %, pions being produced mainly by interaction of energetic neutrons in the material. In the forward region, photons contribute somewhat less to the counting rate. In the CSC for example, photons account for about half of the rate while muons account for 30 % and protons for 10 %. The average single plane and penetrating counting rates (Hz/cm^2) at the design luminosity and the measured in the 7 TeV data to simulation ratio in the various scoring regions are shown in Fig. 3.19.

Finally another effect of the radiation rate appears in the wire detectors. They can experience aging due to polymerised deposits on the wires caused by radiation interacting with organic additives in the detector gas.

In the future the upgrade plans of the LHC foresees a luminosity increase by a factor 10 compared to the nominal LHC of 10^{34} $\mathrm{cm}^{-2}\mathrm{s}^{-1}$. The luminosity increase will mean ten times higher particle rates than for the LHC detectors. While in most of the ATLAS muon system the detectors have enough safety margin to handle these rates [53], this is not the case for the first forward station (Small Wheel). And upgrade of the Small Wheel is expected, during the LHC shutdown planned for 2018.

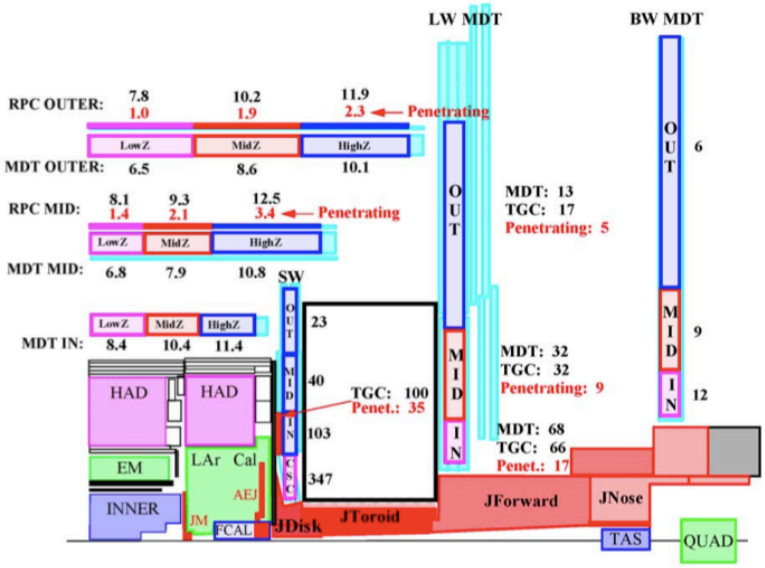

(a)

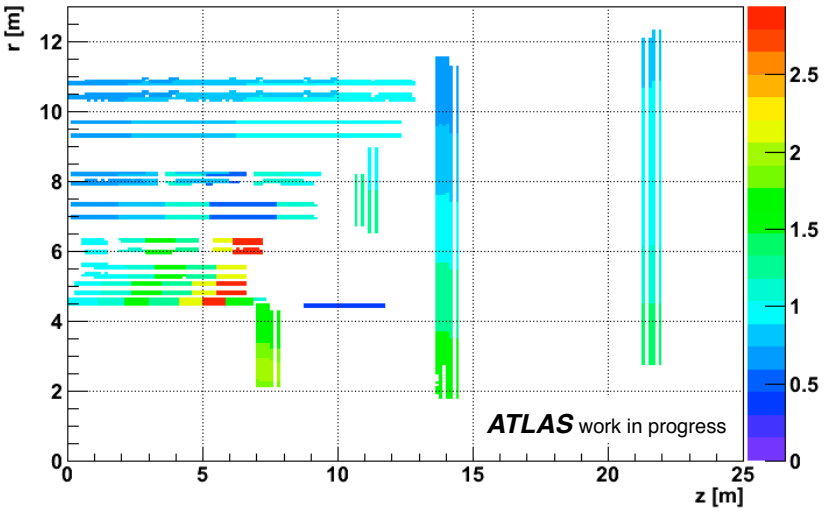

(b)

Figure 3.19: (a) Simulation of the average single plane and penetrating counting rates (Hz/cm^2) at a luminosity of $10^{34} cm^{-2} s^{-1}$ in the various scoring regions. (b) 7 TeV data to simulation ratio.

Chapter 4

Physics Objects : Electrons, Muons and Missing Energy

For the $W^{\pm}Z \to \ell\nu\ell\ell$ cross section measurement the objects involved are muons, electrons and missing transverse energy (to account for the neutrino). In order to perform this analysis the identification, reconstruction, energy measurement and direction of those objects is required. This chapter explains how this is done in ATLAS.

As discussed in the previous chapter, particles produced in collisions travel through the different layers of ATLAS sub-detectors, leaving hits or energy deposits depending of the nature of the particle. Collecting all this information from different parts of the detector and using reconstruction algorithms, is possible to identify and measure the passing particle. With this procedure, physics objects are obtained which are used in the physics analyses.

The reconstruction of electrons and muons, used extensively in this analysis, is described in Section 4.1 and Section 4.2, respectively. The reconstruction of the transverse missing energy associated with particles escaping detection (i.e. neutrinos) is described in Section 4.3.

4.1 Electron reconstruction and Identification

The electrons leave a clear signature in the ATLAS detector: a track measured by the Inner Detector and a shower in the Electromagnetic Calorimeter, providing two independent measurements. These two measurements are the main ingredients to electron reconstruction.

ATLAS uses three reconstruction algorithms for electrons:

- The main one starts with a cluster in the electromagnetic calorimeter.
- The second one is track based, the starting point for the electron reconstruction being a track in the Inner Detector. This algorithm has been developed mainly for

electrons at low transverse momentum, and for electrons inside jets. The electrons reconstructed with this algorithm are called *soft electrons*.

- Finally the third algorithm, is used for electron reconstruction in the forward regions, when the electrons fall outside the acceptance of the Inner Detector. For this algorithm no track matching is possible.

The shower generated by an electron in the electromagnetic calorimeter spans through several cells. The main algorithm for reconstruction starts with the clustering of neighboring calorimeter cells, around the area into which a certain amount of energy was deposited. The algorithm used for this clustering procedure is called "sliding-window", and is described in [56]. It looks for regions in $\Delta\eta \times \Delta\phi = 0.075 \times 0.125$, where the the sum of the transverse energy deposited in the cells exceed 2.5 GeV and defines the cluster position in a way which maximazes the energy inside the $\eta \times \phi$ window. This cluster is called a *seed-cluster*.

The seed-clusters are then matched to ID tracks in the vecinity. The track is required to have a rough position matching within $\Delta\eta \times \Delta\phi = 0.05 \times 0.10$, between the cluster position and the track extrapolated to the Calorimeter. If a good matching candidate is found the object is flagged as an electron, otherwise it is a photon.

In the next step, a cluster is built and the window size is redefined according to the region of the calorimeter and the type of particle being reconstructed. In the barrel, electrons need larger clusters than photons due to the bending in the magnetic field, which leads to soft photon radiation, so a window of $\Delta\eta \times \Delta\phi = 0.075 \times 0.175$ is used for electrons. In the end-caps, the effect of the magnetic field being smaller, a window of $\Delta\eta \times \Delta\phi = 0.125 \times 0.125$ is used.

Once the object is flagged as an electron, a classification of its reconstruction quality takes place. The reconstruction of electrons is not immune against background processes in which fake-electron objects are reconstructed. Actually, often a high fraction of fake electrons is found among the reconstructed candidates. In order to separate the true electrons from background, a set of identification cuts are applied. The characteristic properties of electrons such as the amounts of energy deposited in the electromagnetic and the hadronic calorimeters, can be exploited in the selection for example:

- Since the electrons deposit most of their energy in the electromagnetic calorimeter, this property is a powerful discriminant against jets.
- The lateral and longitudinal shower extensions in the Electromagnetic Calorimeter, the shower width, is expected to be narrow for electrons due to the small lateral leakage.
- The fine granularity of the first layer of the EM calorimeter can be exploited, because the electron shower is expected to be narrow in pseudo-rapidity with no second maximum, while jets contain several particles that can possibly cause a second maximum.

- The presence of a good quality Inner Detector track consistent with the EM cluster is also important.

The electron candidates are required to pass a certain number of those identification criteria, which have been optimized in η and E_T. In ATLAS there are three levels of criteria, with increasing background rejection power, also called working points and labeled *loose++*, *medium++* and *tight++* [57–59].

- At *loose++* level, shower shape variables, leakage fraction in the hadronic calorimeter, number of hits associated to the track and track-cluster matching following η, are used to select electrons with a 93-95 % effciency.
- The *medium++* selection, combines the previous shower cuts with tighter cluster-track matching in η and with a loose cut on the TRT signal. For $|\eta| > 2.01$ stricter requirements are applied to the shower shapes and track hits. These cuts allow to achieve an identification efficiency of ∼85 %.
- Finally the *tight++* selection introduced an asymetric cut on the cluster-track match variable following ϕ and stronger cuts on TRT variables, so that the efficiency to electrons becomes better than for the *medium++* selection.

This three working points can be used depending on the particular requirements of each physics analysis.

4.2 Muon reconstruction and Identification

Muons are the only charged particles that can travel through the entire ATLAS detector. Since muons are charged, they leave a track in the inner detector. Muons can also pass through the calorimeters almost without any energy loss, and are detected again by the muon spectrometer in the outermost layer of the ATLAS detector. Since muons are the only known charged particles that the calorimeters do not stop, their identification relies primarily on the muon spectrometer measurement.

In ATLAS there are two independent reconstruction algorithms `Muonboy` [60] and `MOORE`. Both are based on reconstructing trajectories first locally, at the level of individual chambers, and then at the level of the muon spectrometer. The reconstruction starts by building track segments in the muon chambers. For this purpose, a straight line is fitted across the measurements, due to the small effect of the bending over the depth of a single chamber, and then the segments are combined within multiple chambers, considering the effect of the magnetic field, in order to form full Muon Spectrometer (MS) tracks.

The independent measurements provided by the inner detector and the calorimeters, can also be used in the muon reconstruction. Depending on the information to be used, four muon categories can be defined :

1. **Stand-alone reconstruction (SA):** In regions inside the muon spectrometer acceptance ($|\eta| < 2.7$), the muon track can be reconstructed and extrapolated to the beam axis, using only the muon spectrometer information, and taking into account the multiple scattering and energy losses for the extrapolation. This capability is especially usefull in high pseudorapidity regions ($2.5 < |\eta| < 2.7$) where the spectrometer coverage exceeds the inner detector coverage, and only the MS measurement can be used.

2. **Combined reconstruction (CB):** When a muon is inside the inner detector acceptance ($|\eta| < 2.5$), it will leave a track in both the inner detector and the muon spectrometer. An independent track reconstruction is performed for both, and then the two are combined into a single track. The combination of a muon spectrometer track with the inner detector information improves the momentum resolution and ensures very low fake rates. The combined tracks using `MOORE` and `Muonboy` MS tracks are known as `MuID` and `STACO` respectively. `MuID` is a global refit, whereas `STACO` is a statistical combination.

3. **Segment Tagged (ST):** refers to the combination of an inner detector track with a muon spectrometer segment, the segment being typically in an inner muon station. This category of muons is useful to reconstruct muons with a transverse momentun below $P_T = 4$ GeV. Those low p_T muons in the barrel do not reach the middle and outer stations, due to the energy loss upstream the MS and the bending in the toroidal field. Segment tagging also recovers muons in the low efficiency regions of the muon system, at $\eta \approx 0$ and in the transition region ($|\eta| \approx 1.2$).

4. **Calorimeter Tagged Muons (CT):** In regions inside the inner detector coverage ($|\eta| < 2.5$), the ID provides an independent measurement of the muon track. The ID track can be identified as a muon candidate by matching the track with the energy deposited in the calorimeters if it is consistent with minimum ionizing particles. These types of muons are expected to improve the muon identification efficiency in the region $|\eta| < 0.1$, where there is an incomplete coverage in the muon spectrometer.

Combined, segment-tagged and calorimeter-tagged muons have associated inner detector tracks. The momentum measurement in the inner detector is more precise than in the MS for muons with $p_T \lesssim 40$ GeV. Because the solenoid field is strong enough to significantly bend the track and since there is relatively little material for causing energy loss, the ID track resolution is excellent. For muons with $p_T \gtrsim 100$ GeV, the MS tracking resolution is excellent because of the long MS lever arm. The Combined muons have the lowest fake rates and the best resolution of the reconstruction algorithms [47].

For the $W^{\pm}Z$ analysis `STACO` muons, either Combined or Segment Tagged with $|\eta| < 2.5$, are used.

4.3 Missing Energy

The Missing Transverse Energy ($E_{\mathrm{T}}^{\mathrm{miss}}$) is the main physics quantity used to infer the presence of non-detectable particles. In hadron colliders, the initial momentum of the colliding partons along the beam axis is not known[1], so the momentum conservation for each event can only be exploited projected in the plane transverse of the colliding beams.

When particles escape the detector without being detected, they cause an imbalance in the event transverse energy, which is otherwise expected to be small due to the detector hermeticity. Such imbalance is generally attributed to neutral particles such as neutrinos, mis-reconstructed particles or particles not detected because they fall outside the detector acceptance. Large amounts of $E_{\mathrm{T}}^{\mathrm{miss}}$ are also expected to be a signature of many new physics events.

The measurement of $E_{\mathrm{T}}^{\mathrm{miss}}$ in ATLAS, makes use of the full event reconstruction, including contributions from energy deposits in the calorimeters and muons reconstructed in the muon spectrometer. The calorimeter cells associated with a reconstructed and identified physics object (electrons, photons, hadronically decaying τ leptons, jets and muons) are calibrated as part of these physics objects. Cells not associated with any of such objects are summed together and also added in the $E_{\mathrm{T}}^{\mathrm{miss}}$calculation, this is called the *CellOut* term. The missing transverse energy is defined as

$$E_T^{\mathrm{miss}} = \sqrt{(E_x^{\mathrm{miss}})^2 + (E_y^{\mathrm{miss}})^2} \tag{4.1}$$

and is calculated using the information from energy depositions in the calorimeter cells and from reconstructed muons

$$E_{x(y)}^{\mathrm{miss}} = E_{x(y)}^{\mathrm{miss,\ calo}} + E_{x(y)}^{\mathrm{miss,\ }\mu}. \tag{4.2}$$

The callorimeter cells are calibrated to the appropriate physics object, and the $E_{x(y)}^{\mathrm{miss,\ calo}}$ term is calculated by summing over the cells using the following equations

$$E_x^{\mathrm{miss,\ calo}} = -\sum_{i=1}^{\mathrm{N_{cell}}} E_i \sin\theta_i \cos\phi_i, \tag{4.3}$$

$$E_y^{\mathrm{miss,\ calo}} = -\sum_{i=1}^{\mathrm{N_{cell}}} E_i \sin\theta_i \sin\phi_i. \tag{4.4}$$

where E_i, θ_i and ϕ_i are the cell calibrated energy, polar angle and azimuthal angle respectively.

The $E_{x(y)}^{\mathrm{miss,\ }\mu}$ term is calculated from the momentum of muons, in the region covered

[1]The energy of the partons in the tranverse plane is not known, but supposed to be small

by the muon spectrometer $|\eta| < 2.7$

$$E_{x(y)}^{\text{miss},\,\mu} = -\sum_{i=1}^{\text{N° muons}} p_{x(y)}^{\mu_i}. \tag{4.5}$$

For this the muon momentum is extrapolated though the calorimeter taking into account energy loss. Since muons eventually leave energy depositions in the calorimeter, those cells are subtracted from the calorimeter cell summation to avoid double counting.

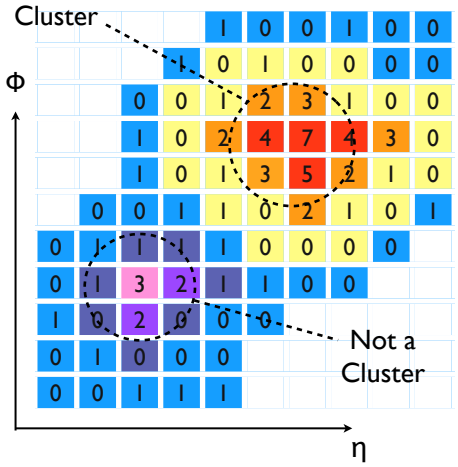

Figure 4.1: Example of how topological clusters are built. Cells with $|E_{\text{cell}}| > 4\sigma_{\text{noise}}$ seed the cluster. Then neighboring cells with $|E_{\text{cell}}| > 2\sigma_{\text{noise}}$ are added iteratively, and finally a single layer of neighboring cells is added.

$E_{\text{T}}^{\text{miss}}$ used in the $W^{\pm}Z$ analysis is called `MET RefFinal`. For this $E_{\text{T}}^{\text{miss}}$ calculation, the calorimeter term is measured, using the sum of the transverse energy of calibrated topological clusters. The topological clusters are built from a seed as shown in Fig. 4.1, the cluster grows from calorimeter cells with an energy deposition greater than four times the standard cell noise. From there, all the neighbouring cells, with energy deposition greater than twice the standard cell noise, are added. And finally all neighbouring cells are included regardless the energy deposition. The η coverage of topological clustering goes up to 4.9 allowing nearly all the transverse energy in an event to be recorded in calibrated topological clusters.

Chapter 5

$W^{\pm}Z$ Analysis at 7 TeV

The $W^{\pm}Z$ production cross-section and the coupling at triple gauge boson vertices are completely fixed by the electroweak gauge structure of the Standard Model, as explained in chapter 1. The measurement provides a test of the high energy behavior of electroweak interactions and probes for possible New Physics (NP) in the bosonic sector. Any deviation from the SM predictions and in particular an enhancement of the production cross-section can be interpreted as sign of New Physics, like the anomalous gauge boson couplings, some supersymmetric models with an extended Higgs sector (charged Higgs) as well as models with extra vector bosons (e.g. W') [61].

As dicussed in Section 1.2, the $W^{\pm}Z$ pairs at the LHC are produced mainly from quark-antiquark interaction and also, but to a lesser extent from quark-gluon or antiquark-gluon. The process $(\bar{q})q - g$ result in an additional quark being present in the final state. The gluon-gluon fusion is strongly supressed by charge conservation. Figure 5.1 shows the leading-order Feynman diagrams for $W^{\pm}Z$ production with $q\bar{q}'$ initial states.

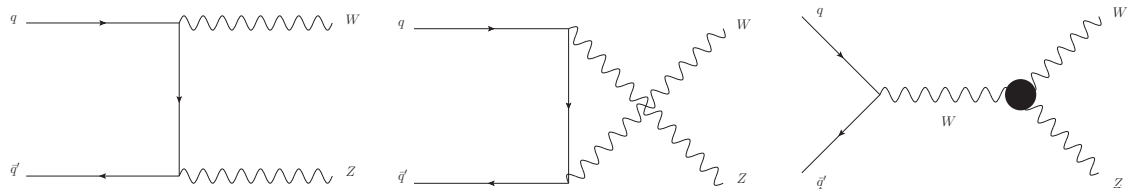

(a) t-channel (b) u-channel (c) s-channel

Figure 5.1: The SM tree-level Feynman diagrams for $W^{\pm}Z$ production through the $q\bar{q'}$ initial state in proton-proton collisions. The s-channel diagram, on the right, contains the WWZ TGC vertex.

The full 5 fb^{-1} of 7 TeV data sample of the LHC proton-pronton collisions taken by ATLAS in 2011, have been used for this analysis. The fully leptonic decay of $W^{\pm}Z \to \ell\nu\ell\ell$ is considered, and analyzed in the four possible channels: $e\nu ee$, $\mu\nu ee$, $e\nu\mu\mu$ or $\mu\nu\mu\mu$. The experimental signature will then be events containing three high transverse momentum (p_{T}) isolated leptons and missing transverse energy ($E_{\mathrm{T}}^{\mathrm{miss}}$) in the final state. Additional selection criteria are required for the dilepton mass of the Z candidate and the transverse

mass of the W candidate in order to ensure the presence of the Z and W bosons. For this analysis a cut-based approach is chosen with a simple set of cuts.

Several background processes can mimic this signature, as it will be discussed in Section 5.4. The main background contributions are: W/Z+jets, ZZ, $W/Z+\gamma$, and top-quark production (including $t\bar{t}$, single top and $t\bar{t}+V$ with $V = W^{\pm}, Z$). The background that arises from Z+jets and top-quark events is estimated using data driven methods and cross-checked with Monte Carlo (MC) predictions, while the background from ZZ and $W/Z+\gamma$ is estimated using simulations.

The cross section was calculated using a maximum likelihood technique to fit the observed number of events in each of the four decay channels, anomalous Triple Gauge Couplings (aTGC) limits have also been extracted. For this measurement, the selection acceptance and efficiency are modeled using MC simulations of the signal. Several corrections are applied to this simulation in order to account for observed discrepancies between the MC simulations and the data.

Experimental measurements of the $W^{\pm}Z$ production cross-section as well as aTGCs limits have been performed by CDF [30] and D0 [32] at the Tevatron using proton-antiproton collisions at $\sqrt{s} = 1.96$ TeV. After the LHC started operating, results have been published reporting the analyses of the large amount of data collected by ATLAS [1, 2, 34] and by CMS [35].

This Chapter is organized as follows: Section 5.1 list data as well as signal and background Monte Carlo (MC) samples used for this analysis; Section 5.2 defines the important physics objects needed for the event selection, Section 5.3 presents the results for the selection acceptance. Section 5.4 explains in details how the backgrounds are estimated. The signal and background contributions expected from the data are mainly modeled with MC simulation corrected with data-driven measurements. Systematics related to each reconstructed physics object are discussed in Section 5.5. Final event yields and cross-section results are presented in Sections 5.6 and 5.7, respectively. Finally review of aTGCs as well as explanations of reweighting and limit extraction techniques are given in Section 5.8.

5.1 Data and MC simulation samples

5.1.1 Data samples

The full data sample of 5 fb^{-1} taken by ATLAS in 2011 during the proton-proton collisions at $\sqrt{s} = 7$ TeV has been used. During the data taking, the instantaneous luminosity varied from about 10^{32} cm^{-2}s^{-1} to 6.8×10^{33} cm^{-2}s^{-1}. The bunch-to-bunch time spacing was 50 ns.

The data is subject to a set of quality criteria, based on the proper functioning of the inner detector, calorimeters, muon spectrometer, magnets, luminosity detectors, trigger, data acquisition system and beam quality. These requirements are applied to small sets

of data corresponding to short data taking periods, of about one minute called luminosity block [62]. The quality of the data per luminosity block is stored in a Good Run List (GRL).

With these data-quality conditions, the integrated luminosity on the 7 TeV sample is estimated to be 4.64 fb^{-1}, with a relative uncertainty of 1.8% [63]. The integrated luminosity is calculated for a given GRL using the ATLAS luminosity calculation tool [64]; details on the luminosity calculation can be found in [63], while the uncertainty on the luminosity calculation is derived following the methodology detailed in [65]. Depending on the event trigger, the data can be recorded in two streams: "physics Muons" when a muon triggered the event and "physics Egamma" when an electron or a photon triggered. If an event is observed to be both muon and electron triggered (and thus present in both streams), the event is removed from the electron stream. The threshold of trigger chains which were used varied during the year, in order to cope with the data taking conditions.

The data format is D3PD ntuple which are essentially ROOT ntuples [66]. The reconstruction has been performed with Athena [67], release 17.0.

5.1.2 Monte Carlo samples

The simulated signal and backgrounds were produced with different Monte Carlo (MC) event generators and then simulated through a detailed detector simulation based on Geant4 [68]. The simulated signals are digitized and reconstructed using the Athena [67] offline reconstruction software. The simulation includes detectors, as well as trigger efficiencies and resolutions.

The $W^{\pm}Z$ production processes and subsequent pure leptonic decays were modeled by the MC@NLO 4.0 [69]. The MC@NLO MC generator uses a parton density function (PDF) set CT10 [70], which incorporates the next-to-leading-order (NLO) QCD matrix elements into the parton shower by interfacing to the Herwig/Jimmy [71] program. The $W^{\pm}Z$ decays into τ leptons are included in dedicated MC samples and these τ leptons decay to all known final states.

Two sets of $W^{\pm}Z$ MC samples were generated, one with the SM couplings and the other one with anomalous coupling with $\Delta g = 0$, $\Delta\kappa = 0$, $\lambda = 0.13$. The SM samples are used in the cross section analysis to calculate the acceptance and efficiency of the selection, while the samples including anomalous couplings are used in the aTGC analysis. The major backgrounds come from jets associated with a Z gauge boson, these processes being modeled using Alpgen [72]. The W+jets is simulated with Alpgen/Jimmy [73]. MadGraph [74] and MC@NLO [69] are used to model the $t\bar{t}+V$, $t\bar{t}$ and single top events; the diboson processes WW, ZZ are modeled with Herwig [71] and Pythia [75] respectively. The $W/Z+\gamma$ is modeled with Sherpa [76]. Table 5.1 lists the MC samples and generators used in the 7 TeV analysis. In Appendix A the list of MC samples including the generator names, the total number of MC events produced, the k-factor (the ratio of

the NLO to LO cross section for a given process), the generator level filter efficiencies and the corresponding cross sections, are presented.

Process	Generator
$W^{\pm}Z \to \ell\nu\ell\ell$	MC@NLO
aTGC $W^{\pm}Z \to \ell\nu\ell\ell$	MC@NLO
Z+jets	Alpgen
Z+bb	Alpgen/Jimmy
Z+jets filter 10< $m_{\ell\ell}$ <40 GeV, Z p_T >20 GeV	Alpgen/Jimmy
$W^{\pm}$+jets	Alpgen
WW	Herwig
ZZ	Pythia
$Z\gamma$+jets	Sherpa
$W^{\pm}\gamma$+jets	Sherpa
$t\bar{t} + W^{\pm}$	MadGraph
$t\bar{t} + Z$	MadGraph
$t\bar{t}$	MC@NLO
single top	MC@NLO
Wt	MC@NLO

Table 5.1: MC samples/processes used to model signal and backgrounds in the 7 TeV analysis. For each process the corresponding generator names are listed.

While the MC simulation is seen to perform very well, small differences between the data and MC simulations have been observed. These differences come primarily from the modeling of the pileup, the efficiency and the resolution.

The pileup is simulated by adding in each event a variable number of MC inelastic proton-proton collisions, and taking into account the structure of the beam bunch train at the LHC. Since the MC simulations are generally produced before the end of the data taking, the pileup conditions in the MC are not identical to those of the data. The difference in pileup conditions between the data and the MC can cause discrepancies in the calorimeter energy modeling, which translates into discrepancies of the modeling of physics objects such as the missing energy, and the calorimeter and track isolation. Thus, the MC distribution of the mean number of interactions per bunch crossing is corrected using event weights to match the distribution of real data. This reweighting procedure is called pileup reweighting, and Pythia [77] generator is used to model it.

The simulation of the reconstruction and trigger efficiencies for electrons and muons are not identical to the data efficiencies. These efficiency differences can cause incorrect predictions of the number of expected $W^{\pm}Z$ events and their kinematic distributions, and thus must be corrected in order to accurately measure cross sections and set limits on aTGCs. As such, the efficiencies in both data and MC are measured, and the MC efficiencies are corrected with respect to the data by using scale factors (data/MC ratio).

The resolutions in the MC simulations of the electron and muon p_T are not the same as in the data. The MC resolution is corrected by adding resolution smearing to the electrons and muons using the Z mass as a constraint for electrons and muons.

By including all these corrections into the MC, we make sure that the simulations correctly describe our data.

5.2 $W^{\pm}Z$ selection

Since we concentrate on the fully leptonic decay of the $W^{\pm}Z$ boson pairs, all final states with electrons and muons for $W^{\pm}Z$ events are considered : $\mu^+\mu^-\mu^{\pm}\nu$, $\mu^+\mu^-e^{\pm}\nu$, $e^+e^-\mu^{\pm}\nu$, $e^+e^-e^{\pm}\nu$. The criteria used to select events and the physics objects of interest, essentially electrons, muons and missing transverse energy, are of fundamental importance for a performant cut-based analysis.

The selection of $W^{\pm}Z$ events starts at the trigger level. Then event candidates are retained if they have a reconstructed primary vertex with at least three tracks. In these events the reconstructed electron and muon objects are further selected on the basis of a few discriminating variables (identification quality, p_T, isolation etc.). Taking into account the presence of the neutrino, events are required to have large $E_{\mathrm{T}}^{\mathrm{miss}}$. Additional selection criteria are imposed on the dilepton mass of the Z candidate and the transverse mass of the W candidate, in order to ensure the presence of the Z and W bosons and to reject most of the reducible background processes. These requirements are detailed in the following sections.

5.2.1 Data Quality

Events must be in the Good Run List (GRL), reflecting luminosity blocks with fully functional sub-detectors during data taking. The GRL is meant to ensure that the given collision data are of adequate quality in terms of the condition or performance of each of the detector subsystems during the data-taking.

5.2.2 Trigger

The ATLAS trigger system was described in Section 3.5. Considering that the $W^{\pm}Z$ analysis contains three high p_T leptons in the final state, and that each of them has a high probability of passing the trigger threshold, single muon (electron) triggers are used in this analysis without significant loss of signal events.

The instantaneous luminosity was ramping during the 7 TeV collisions, and so the trigger and acquisition rates. In order to cope with the increasing luminosity conditions, the p_T (E_T) thresholds for the single muon (electron) triggers were raised, according to the conditions of each data-taking period. For the single electron trigger, three different E_T threshold were required $E_T > 20$ GeV, $E_T > 22$ GeV and $E_T > 45$ GeV. The last one is called higher level trigger and hadronic leakage and dead material corrections were applied. In the case of single muon trigger, the same event threshold was kept during the full data-taking and events were required to have a muon with a $p_T > 18$ GeV.

The trigger efficiencies determined with the $W^{\pm}Z$ signal MC sample after all selection cuts, except the trigger requirement, are all close to or above 99% in all channels.

5.2.3 Lepton selection

Special attention must be given to lepton reconstruction, since the precision of this analysis is highly dependent on the efficiencies and fake rates for both electrons and muons. Details about the reconstruction algorithms were described in Chapter 4 and here only the main ideas are re-discussed and some additional selection criteria for muons and electrons are introduced.

Muon Selection

Muons are identified by tracks (or track segments) reconstructed in the muon spectrometer and matched to tracks reconstructed in the inner detector, as described in Section 4.2. The muons used in this analysis are required to be reconstructed either as Combined (CB) or Segment-Tagged (ST), and also to be inside the acceptance of the inner detector $|\eta| < 2.5$ and they must have p_T >15 GeV.

The inner detector plays an important role in the track parameter calculation for Combined tracks, and solely determines the track parameters for the Segment-Tagged muons. Additional quality criteria are required for the inner detector tracks, in order to ensure their accurate reconstruction and also to reject decay in flight backgrounds (like pions or kaons). A minimum number of hits in each silicon sub-detector is required for each track [78]. The hit requirements for the 7 TeV analysis are:

- at least 1 pixel B-layer hit, unless the track passes from an un-instrumented or dead area of the B-layer,
- at least 2 hits in the pixels including the B-layer hit. If the track crosses a known pixel dead channel then it is counted as containing a hit,
- at least 6 hits in the SCT including the number of crossed dead sensors,
- less than 3 holes (no hit in a layer crossed by the track) in all silicon layers (Pixel and SCT).
- For $|\eta| < 1.9$, one requires TRT hits + outliers $\geqslant 6$ and outliers/(outliers+hits) < 0.9.
- For $|\eta| > 1.9$, if the TRT hits + outliers > 6, requires outliers/(outliers+hits) < 0.9.

To ensure that the candidates come from the primary vertex, the transverse impact parameter significance (the transverse impact parameter, $|d_0|$, divided by its error) with respect to the primary vertex must be less than 3 and the absolute distance in the $z-$direction, $|z_0|$, must be less than 1 *mm* to the primary vertex.

Finally we ask for the inner detector track used by the muon to be isolated from other tracks to reject secondary muons from hadronic jets. The muon tracking isolation parameters (called $\frac{p_T Cone30}{p_T}$), is computed as the scalar sum of the transverse momentum of the tracks with $p_T > 400$ MeV reconstructed around the muon candidate (excluding the candidate track), with the distance (ΔR) between each track and the muon candidate

direction below 0.3. This quantity divided by the muon candidate track momentum, must be less than 0.15. The tracks to be considered in the sum are required to originate from the primary vertex, which greatly reduces the contribution to the isolation parameter from pileup. Calorimeter isolation was not used in this analysis for muons, studies having shown that using calorimeter isolation on top of tracking isolation, does not increase the background rejection and will add another systematic bias to our selection.

The muon reconstruction efficiency has been measured with data by using a tag-and-probe method with dimuon decays of the Z as described in [79]. The event weights of MC samples are scaled to match the measured efficiency for each CB and ST muon. Associated systematics are taken into account (Section 5.5.2).

Electron Selection

Electrons are identified by large deposits in the electromagnetic calorimeter, associated with tracks measured in the inner detector. For this analysis the electrons are required to pass the egamma "$loose++$" [57, 58] electron identification requirements. The energy of the electron candidates is taken from the calorimeter measurement, while the η and ϕ are taken from the track. Using the transverse momentum defined in this way, electron candidates are required to have $E_{\mathrm{T}} > 15$ GeV.

To avoid problems with the front-end boards of the liquid argon calorimeter or other data quality issues, the electron candidates are required to pass the object quality (OQ) cut. The OQ cuts test if the electron cluster is affected by at least one of the following problems: the presence of a dead front-end board in the first or second EM calorimeter sampling layer, a dead region affecting the three EM calorimeter samplings or a masked cell in the calorimeter.

In addition, the electron candidate is required to be inside the inner detector tracking coverage and outside the transition region between the barrel and end-cap calorimeters where the energy is not well measured, the electrons must be reconstructed using a cluster with $|\eta| < 1.37$ or $1.52 < |\eta| < 2.47$ in the absolute detector coordinate system.

The electrons must also come from a primary vertex, this is achived by requiring the longitudinal distance with respect to the primary vertex $|z_0|$ to be less than 1 mm and the transverse impact parameter significance $|d_0|$ less than 10.

The final electron requirement applied is a relative isolation condition. The hadronic activity around the electrons inside jets can be quantified with the tracks reconstructed in the inner detector and the transverse energy deposits in the calorimeters. Although the quantities are correlated, the measurements take place in different sub-systems, and thus carry some independent informations.

Both calorimetric and track-based isolation were applied as discriminants. The transverse energy or momenta deposited in a cone of size ΔR around the electron candidate was used, excluding the contribution of the electron under consideration. The performance for

different cone sizes was evaluated, a $\Delta R = 0.3$ was chosen.

The track-based isolation must be less than 0.13 of the electron candidate p_{T}, while the calorimeter isolation must be less than 0.14 of the electron candidate E_{T}.

In order to match the resolution observed for electrons in W and Z data events, the energy of electrons in MC simulation is smeared with the egamma Energy Rescaler Tool [80], keeping the electron direction fixed.

Missing Transverse Energy

The missing transverse energy ($E_{\mathrm{T}}^{\mathrm{miss}}$) is reconstructed from the energies deposited in the calorimeters and the muon momenta measured by the muon spectrometer and inner detector. The $E_{\mathrm{T}}^{\mathrm{miss}}$ used in this analysis is called MET_RefFinal [81, 82]. It is built using the sum of the transverse energy of calibrated topological clusters, measured in the calorimeters, see Section 4.3.

5.2.4 Primary vertex

The primary vertex (vertex with largest Σp_T^2) is required to be reconstructed with at least three good associated tracks, so as to make sure that the selected events correspond to a hard-scattering proton-proton collision.

5.2.5 Overlap removal

Some of the reconstructed objects may result from the same measurement. This "overlap" appears when two lepton candidates are sharing the same inner detector track. Therefore, an "overlap removal" prescription is introduced in order to avoid double-counted measurements for: μ/e, e/e and lepton/jet. Objects are removed from the event using ΔR overlap criteria:

- when an electron shares the same track with a selected muon, remove electrons within $\Delta R < 0.1$ of the muon;
- if two selected electrons overlap within $\Delta R < 0.1$, remove the lower-p_{T} electron;
- remove jets within $\Delta R < 0.3$ of any selected muon or electron. $W^{\pm}Z$ analysis is independent of jets.

No events are removed at this stage, only objects.

5.2.6 Event cleaning

In order to eliminate events which are affected by some problematic physics objects badly measured by the detector, the following event cleaning strategies are introduced:

- $E_{\mathrm{T}}^{\mathrm{miss}}$ ***cleaning :*** a jet with badly measured energy and directions will affect the resolution of the $E_{\mathrm{T}}^{\mathrm{miss}}$reconstruction. Hence, a dedicated "looser bad" criteria [83]

is defined to spot those jets that need to be removed, since they come either from background events (non-collision background and cosmics) or are caused by detector effects (like problematic calorimeter regions, noise spikes or coherent noise). Jets with $p_{\mathrm{T}} > 20$ GeV which do not overlap (whithin $\Delta R > 0.3$) with a selected lepton are tested for the "looser bad" jet criteria. If any of the aforementioned jets is tagged as "bad", the entire event is rejected.

- ***LAr/Tile noise and corrupted events***: events with Liquid Argon or Tile Calorimeter data integrity errors are vetoed by checking a particular data quality flag.

5.2.7 Z candidate

The event must have two selected leptons of the same flavor and of opposite charge. The dilepton pair is required to have an invariant mass (m_{ll}) close to the Z mass, within $|m_{ll} - M_Z^{PDG}| < 10$ GeV ($M_Z^{PDG} = 91.1876$ GeV).

If more than one pair of leptons form a Z candidate, as it can be the case in the $\mu\mu\mu$ and eee channels, the candidate with invariant mass closest to the PDG mass is taken. The physics argument for this choice comes from the Breit-Wigner distribution: the Z is more likely to be found near the pole mass and this method selects the correct candidate in more than 90% of the cases.

5.2.8 WZ candidate

The event must have at least three leptons passing the selection criteria, and coming from the primary vertex. Between those leptons two of them have already been associated with the Z boson, and the third lepton will be associated to the W. There can be more than three leptons in the event, in which case we choose the lepton with the highest p_T.

- **Third lepton:** since for the W boson the mass cannot be fully reconstructed due to the neutrino, there is no a strong constraint such as the Z mass. The lepton requirements are then tightened, in order to avoid fake leptons. The W lepton must satisfy the combined ($tight++$ [57, 58]) quality definition for muons (electrons) and must have $p_{\mathrm{T}} > 20$ GeV, for the event to be selected.

- **Missing Transverse Energy:** to take into account the neutrino contribution, the missing transverse energy in the event must be larger than 25 GeV.

- **The $W^{\pm}$ transverse mass:** The tranverse mass of the system M_T (lepton identified as coming from $W^{\pm}$and $E_{\mathrm{T}}^{\mathrm{miss}}$) defined by $M_T^2 = 2E_{\mathrm{T}}^{\ell}E_{\mathrm{T}}^{\nu} - 2\mathbf{p}_{\mathrm{T}}^{\ell}\mathbf{p}_{\mathrm{T}}^{\nu}$ must be larger than 20 GeV.

5.2.9 Trigger matching

Finally we ask that one of the offline reconstructed muons (electrons) in the event associated with the W or Z decay must match the online reconstructed muon (electron) that triggered the event within $\Delta R < 0.1$ (0.15). The lepton matched to the trigger must have $p_{\mathrm{T}} > 20$ (25) GeV for muons (electrons). Due to the presence of three leptons with large p_T, the trigger matching efficiencies for $W^{\pm}Z$ events is close to 99%.

5.3 Selection Acceptance

Using the set of cuts described above, the expected number of events in the 7 TeV sample ($\mathcal{L} = 4.64$ fb^{-1}) selected after each cut for the $W^{\pm}Z$ MC signal, with all corrections applied are summarized in Tables 5.2. At each step, the number of events is shown for each channel. In addition the relative acceptance of each is given in Table 5.3.

Cutflow 7 TeV	Events			
	eee	$ee\mu$	$\mu\mu e$	$\mu\mu\mu$
All	1202.26			
Muon or electron trigger	1120.78			
Primary vertex	1117.91			
$E_{\mathrm{T}}^{\mathrm{miss}}$ cleaning	1116.16			
Z cut	218.88		317.37	
Three leptons	51.22	70.55	74.82	106.55
$E_{\mathrm{T}}^{\mathrm{miss}}$ cut	40.50	57.00	59.17	86.44
$W^{\pm}M_T$ cut	38.07	54.05	55.67	81.85
Trigger match	38.04	53.99	55.29	81.67
Scale factors	37.24	51.77	54.20	78.32

Table 5.2: Expected number of MC events after each cut for $W^{\pm}Z \to \ell\nu\ell'\ell'$ for $\mathcal{L} = 4.64$ fb^{-1} at 7 TeV.

Cutflow 7 TeV	Acceptance (%)			
	eee	$ee\mu$	$\mu\mu e$	$\mu\mu\mu$
All	100			
Muon or electron trigger	93.22			
Primary vertex	99.74			
$E_{\mathrm{T}}^{\mathrm{miss}}$ cleaning	99.84			
Z cut	19.61		28.43	
Three leptons	23.40	32.23	23.57	33.57
$E_{\mathrm{T}}^{\mathrm{miss}}$ cut	79.07	80.80	79.09	81.12
$W^{\pm}M_T$ cut	93.99	94.82	94.08	94.70
Trigger match	99.93	99.90	99.31	99.78
Scale factors	97.89	95.89	98.04	95.89

Table 5.3: Relative acceptance of MC events after each cut for $W^{\pm}Z \to \ell\nu\ell'\ell'$ for $\mathcal{L} = 4.64$ fb^{-1} at 7 TeV. Each acceptance is given with respect to events remaining after the previous cut. At the stage of the Z cut the maximum value is the 50%, since the Z is separated in the two decays channels.

As expected the absolute acceptance increases with the number of muons in the final state because the reconstruction efficiency for muons is higher than for electrons. The contribution from $W^{\pm}Z \to \ell\nu\ell'\ell'$, where at least ℓ or ℓ' is tau, is dominated by events

Cutflow 7 TeV	Events			
	eee	$ee\mu$	$\mu\mu e$	$\mu\mu\mu$
All	1502.83			
Muon or electron trigger	950.01			
Primary vertex	947.66			
$E_{\mathrm{T}}^{\mathrm{miss}}$ cleaning	942.34			
Z cut	107.07		152.36	
Three leptons	2.98	4.02	4.39	5.62
$E_{\mathrm{T}}^{\mathrm{miss}}$ cut	2.42	3.12	3.44	4.44
$W^{\pm}M_T$ cut	1.77	2.38	2.46	3.49
Trigger match	1.76	2.38	2.44	3.50
Scale factors	1.71	2.28	2.37	3.35

Table 5.4: Expected number of MC events after each cut for $W^{\pm}Z \to \ell\nu\ell'\ell'$, where at least ℓ or ℓ' is a τ going to μ or e, for $\mathcal{L} = 4.64$ fb^{-1}.

$W^{\pm}Z \to \tau\nu\ell'\ell'$, where the τ decays into an electron or a muon. This contribution amounts to 4% and is added to the signal for the cross-section extraction; the cutflow for this MC sample is shown in Table 5.4.

5.4 Background Estimation

The same final state particles can also come from other physics processes which are background sources for the $W^{\pm}Z$ trilepton events. The WZ signal events contain leptons from vector-boson decay. Background events can contain two leptons from vector-boson decay an a third "fake" lepton from other sources, e.g. muons from in-flight decays of pions and kaons, or heavy-flavor quark (b or c) decays. The significant backgrounds for the $W^{\pm}Z$ signal after the event selection are Z+jets, ZZ, top-quark ($t\bar{t}$ and single top) and $W/Z+\gamma$.

The backgrounds can be organized in two categories:

- backgrounds containing real leptons from Z or W decays, and
- backgrounds containing at least one "fake" lepton.

Backgrounds containing one or more "fake leptons" are estimated using Data-Driven (DD) methods. Backgrounds containing only real leptons are estimated using MC.

This is the case for ZZ, $Z+\gamma$, $W+\gamma$, $t\bar{t}+Z$ and $t\bar{t}+W$. The leptonic final states in particular are generated with processes well tested in the MC generation and can be safely exploited. Background with three real leptons, coming from ZZ events or $t\bar{t}+W/Z$, and background from $W/Z+\gamma$ events, in which the photon produces an electron via conversion, are estimated using MC simulation, as will be explained in Section 5.4.1.

In the case of Z+jets and top-quark events, both contain two real leptons as well as a third "fake" lepton. In the first case, the fake leptons arise either from decays of hadrons with b or c-quark content or from misidentified light jets. In the second case, each top quark decays mainly to a W boson and a b quark. These fake leptons are produced in the jet fragmentation process and thus will be spatially correlated with jets. The jet

fragmentation is extremely difficult to model, and since we are looking at the tail of the distributions, we don't expect them to be well simulated by MC. The Z+jets and top-quark ($t\bar{t}$ and single top) backgrounds have been estimated using DD methods, where control regions in data are used to model the background, and transfer factors to extrapolate from the control regions into the signal region as will be discussed in Section 5.4.2.

The WW events also enter into this category of background, since their leptonic decay will give two real leptons, plus possibly one fake. However, the total WW cross section is much smaller than Z+jets and top, and if we include the probability for producing a fake lepton, this makes this contribution negligible. This is confirmed by MC simulation where no events passed our selection criteria and thus WW is neglected in our final background estimate. Finally, there could be additional backgrounds which contain more than one fake leptons, such as W+jets, single top production, or QCD dijet production. These backgrounds are expected to be very small since the probability of producing more than one fake lepton is extremely small. For completeness, the small contribution of these "double fake" backgrounds are accounted for in the Z+jets and top DD estimate.

The control and the estimation of the background contributions is essential in order to achieve a precise cross section measurement and aTGC limits.

5.4.1 MC-based Estimations

Using the previously described selection criteria (Section 5.2) to the ZZ, $t\bar{t}+W/Z$ and $Z/W+\gamma$ generated MC samples, the expected event yields from MC estimations are obtained.

ZZ Background

The fully leptonic decay of ZZ events, is a major background in all four $W^{\pm}Z$ decay channels. Since the ZZ events need to pass the full $W^{\pm}Z$ selection, the $E_{\mathrm{T}}^{\mathrm{miss}}$ requirement plays a crucial role for this background rejection. Although transverse energy should be well balanced in a ZZ event, there are several sources of "fake" $E_{\mathrm{T}}^{\mathrm{miss}}$:

- When a lepton is outside of the detector acceptance, three of the four leptons are reconstructed in the detector. The fourth lepton is considered missing and is a source of $E_{\mathrm{T}}^{\mathrm{miss}}$. In particular for muons whose momentum is not fully measured by the calorimeter and the muon spectrometer coverage stops at $|\eta| = 2.7$. In the case of electrons this contribution should be smaller since the coverage is provided up to $|\eta| = 4.9$ by the electromagnetic and hadronic calorimeters. This background is considered at some point irreducible.
- Mismeasured jets, from the tail of the $E_{\mathrm{T}}^{\mathrm{miss}}$ distribution. In this case the four leptons are reconstructed in the detector.

$W^{\pm}/Z+\gamma$ Background

The leptonic decays of Z boson produced in association with photons can mimic the trilepton signature when a photon undergoes a conversion into an electron-positron pair upon interaction with the material of the detector. Such a final state is different from those in the data-driven method for "lepton-like" jets described below. $Z + \gamma$ is then estimated using MC simulations. The $W^{\pm} + \gamma$ background contribution for this analysis is negligible.

$t\bar{t} + V$ $(V = W, Z)$ Background

The $t\bar{t} + W^{\pm}$ and $t\bar{t} + Z$ can produce three or more real leptons in the final state, two from the $t\bar{t}$ decay plus the ones coming from the W or Z leptonic decay. Since this background doesn't contain a "fake" lepton is estimated using a dedicated MC sample that include weak boson radiation.

The $t\bar{t} + W^{\pm}$ events have an additional prompt lepton which increases their probability to pass selection cuts, but just like $t\bar{t}$ they are rejected by the dilepton invariant mass cut. Their final yield is thus much smaller than $t\bar{t} + Z$. The $t\bar{t} + W^{\pm}W^{\pm}$ and $t\bar{t}t\bar{t}$ samples have also been considered, but due to even lower production cross-sections they do not give any significant event yield after selections.

Table 5.5 summarizes the expected event yields from MC estimations, at the end of the cut flow. The yields were normalized to a luminosity of 4.64 fb^{-1}. The first error on the yields is statistical and the second error is the systematic. The systematic error includes the uncertainties on theoretical cross-sections used to normalize the MC samples, given in Table 5.9, and the uncertainties for each object used in the event reconstruction are summarized in Section 5.5. These values, with the corresponding uncertainties, are included in the background estimation for the cross-section calculation.

7 TeV MC Sample	Events			
	eee	$ee\mu$	$e\mu\mu$	$\mu\mu\mu$
$W/Z + \gamma$	1.4±0.7±0.1	–	2.3±0.9±0.1	–
ZZ	3.2±0.1±0.2	4.9±0.1±0.2	5.0±0.1±0.1	7.9±0.1±0.2
$t\bar{t} + W^{\pm}$	0.1±0.02	0.1±0.02	0.1±0.03	0.1±0.03
$t\bar{t} + Z$	0.6±0.1	1.1±0.1	1.2±0.1	1.5±0.1

Table 5.5: Expected number of events passing all 7 TeV selection cuts for background MC samples, normalized to an integrated luminosity of $\mathcal{L} = 4.64$ fb^{-1}. The first error is statistical while the second is systematic.

5.4.2 Data-Driven Estimations

WZ signal events contain leptons from vector-boson decay. Background events can contain two leptons from vector-boson decay an a third "fake" lepton from other sources, e.g.

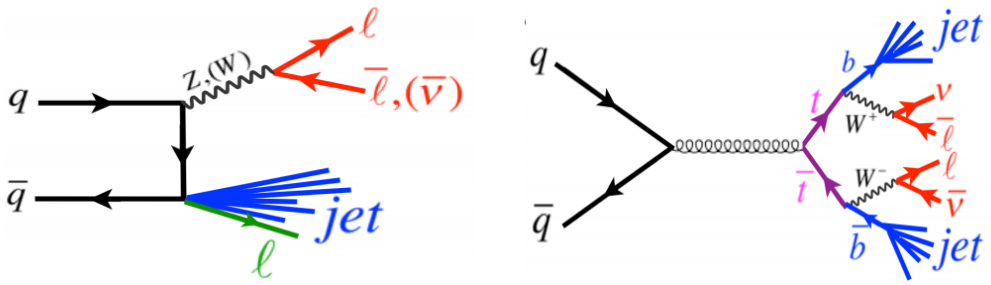

Figure 5.2: Feynmann diagrams for the Z+jets (left) and $t\bar{t}$ (right) backgrounds. These two backgrounds can include leptons from jet fragmentation or misidentified jets and are estimated using Data Driven methods.

muons from in-flight decays of pions and kaons, or heavy-flavor quark (b or c) decays. This is the case for the Z+jets as well as $t\bar{t}$ events as illustrated in Fig. 5.2, because the top quark is heavy enough to decay to a real W. While leptons from the decay of W or Z bosons are primarily isolated, "fake" leptons from b or c decays tend to be spatially correlated with jets. There are also cases where the jet is misidentified as an electron. The majority of these "fake" leptons will fail the isolation or the IP significance requirements and the residual background is estimated using data driven techniques. The "fake" lepton being either a muon or an electron, different control regions have been defined to estimate the amount of Z+jet and top backgrounds.

The following sections describe the data driven method used and the different control-regions in the data.

Top-quark background ($t\bar{t}$ and single top)

Backgrounds including top quarks decays ($t\bar{t}$ and single top), have the potential of producing multiple real leptons, through subsequent leptonic decays of the W boson and semi-leptonic decays of the b quark. Particles within jets produced in hadronic decays of the W boson can also be identified as electrons by depositing energy in the electromagnetic calorimeter.

An important part of this background is eliminated by the isolation and impact parameter cuts of the selection.

A control region for this data driven estimation, is obtained by only modifying the charge requirement in the Z lepton pair selection: same-sign pairs are required. Since $t\bar{t}$ events do not contain an actual Z boson, they should therefore behave similarly to the regular opposite-charge selection. On the contrary, processes with a real Z boson will be strongly rejected by this requirement; additionally only the channels where reconstructed Z and W lepton flavors are different are considered, in order to eliminate events combining a lepton from the Z with the W lepton.

The $E_{\mathrm{T}}^{\mathrm{miss}}$ distribution in the control region is shown in Fig. 5.3. The Control region

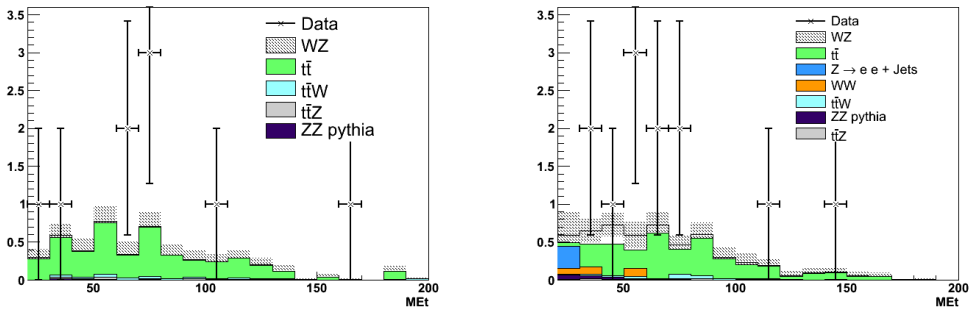

Figure 5.3: Missing transverse energy in events passing all selection cuts, but requiring Z lepton pair to have same charge instead of opposite; (left): $e\mu\mu$ channel, (right): $ee\mu$ channel.

Channel	eee	$ee\mu$	$e\mu\mu$	$\mu\mu\mu$
$t\bar{t}$	0.4±0.3±0.2	1.7±0.5±0.8	2.3±0.5±1.0	2.4±0.5±1.1

Table 5.6: $t\bar{t}$ background predictions per decay channel. $t\bar{t}$ numbers are obtained by Monte Carlo, and rescaled to data by a factor 2.2; their uncertainties are split in two terms, the first statistical in nature, the second are derived from the uncertainty on the rescaling method.

is dominated by the $t\bar{t}$ contribution, with a purity of 88.8% in the $e\mu\mu$ channel and 61.6% in the $ee\mu$ channel when the missing transverse energy is lower than 200 GeV. The purity is enhanced to 80.5% in events with a missing transverse energy above 60 GeV in the $ee\mu$ channel, and only those are considered in the following. A clear deficit of MC compared to data can be seen; the ratio of data to MC in those samples is respectively 2.06 ± 0.77 and 2.32 ± 1.13. Therefore a rescaling factor of 2.2 is defined for MC $t\bar{t}$ events, with an uncertainty of 1.0.

The final estimates for the $t\bar{t}$ background are given in Table 5.6.

Original numbers per channel are given by simulation, then corrected with the factor 2.2 calculated above. The first uncertainty is the original statistical error from Monte Carlo, multiplied by the rescaling factor, named "statistical" in the following. The second term is the original MC estimate, multiplied by the uncertainty on the rescaling factor, will be the "systematic".

W/Z+jets background : Fake Factor Method

The Fake Factor method also known as ABCD method relies on the assumption that the background distribution can be decomposed in a (x, y) plane, where x and y are two uncorrelated variables. The method is illustrated in Fig. 5.4. Neglecting the signal leakage in regions B, C and D, and assuming that variables x and y are uncorrelated, the number of events in the signal region (N_A) can be evaluated using the number of events in the other regions as :

$$\frac{N_A}{N_B} = \frac{N_D}{N_C} \tag{5.1}$$

$$N_A = N_B \times \frac{N_D}{N_C} \tag{5.2}$$

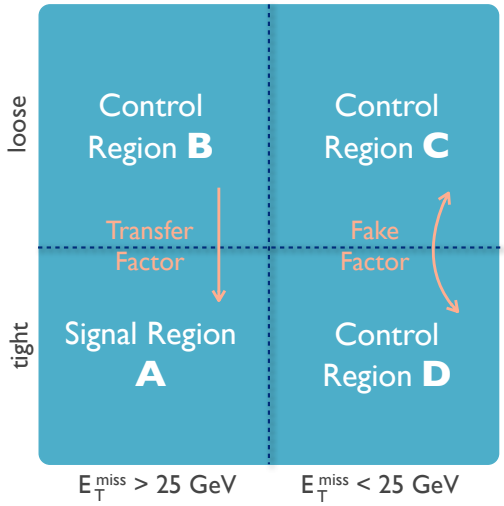

Figure 5.4: Control region definition for the Fake Factor method. The regions are defined using the missing energy cut $E_{\mathrm{T}}^{\mathrm{miss}} < 25$ GeV and the extra muon or electron is required to pass either a "tight" or a "loose" object definition. The Fake Factor is calculated in the low $E_{\mathrm{T}}^{\mathrm{miss}}$region (D/C), and the loose+tight $E_{\mathrm{T}}^{\mathrm{miss}}$region (B) is used to extrapolate to the signal region.

In our case to define a x variable that explicitly excludes our signal region, we require the background sample to fail the $E_{\mathrm{T}}^{\mathrm{miss}}$ selection. For the y variable the muon or electron associated with the W on the event is required to pass either a "tight" or a "loose" object definition. A "loose" object is one that fails a specific lepton cut, where the cut is chosen to maximize the separation between leptons from jets and leptons from boson decay, while keeping the correlation with x small. The "loose" and "tight" definition are different for electrons and muons. For muons, a tight muon passes all cuts including isolation, while a loose muon fails the isolation requirement. A tight electron passes all selection, while a loose electron fails either the loose++ quality or the isolation requirements.

The low $E_{\mathrm{T}}^{\mathrm{miss}}$sample is used to measure the electron and the muon fake factors. The so called "fake factor" is measured by counting the number of lepton candidates in the low $E_{\mathrm{T}}^{\mathrm{miss}}$sample passing the tight requirements and dividing it by the number of "lepton-like" jets.

$$f_{lepton} = \frac{N_{\text{tight lepton}}}{N_{\text{loose lepton}}} = \frac{N_D}{N_C} \tag{5.3}$$

The fake factor is then applied to the "loose" plus high $E_{\mathrm{T}}^{\mathrm{miss}}$ region (region B) to obtain a data driven measurement of the backgrounds from fake leptons. This method can be applied in principle without relying on Monte Carlo information.

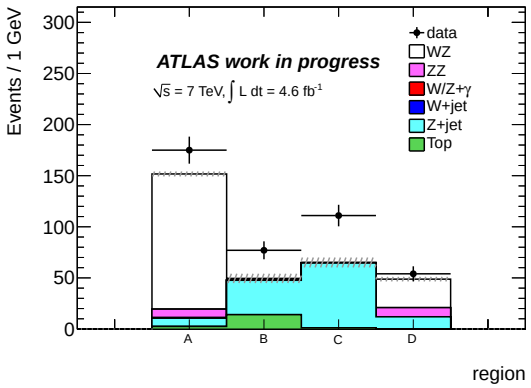

Figure 5.5: Control region composition for the fake factor method for $ee\mu$ and $\mu\mu\mu$ channels. The regions are defined using the missing energy cut and the isolation of the W muon daughter. The region A corresponds to the signal region passing all selection requirements, for region B the W muon is asked to fail the isolation requirement, for regions D and C the $E_{\mathrm{T}}^{\mathrm{miss}}$ cut is reversed and the isolation cut applied or reversed respectively.

Contaminations of signal and other backgrounds in the control regions need to be carefully estimated and subtracted using MC simulation. In our case, contamination from processes which produce three real leptons can contribute to all control regions, an example for the muon case can be seen in Fig. 5.5. The contamination contributions are estimated from MC and subtracted. The correction is a less than 1% to the control region C, but up to 60% to the D control region (essentially Z+jets and WZ), for both electrons and muons.

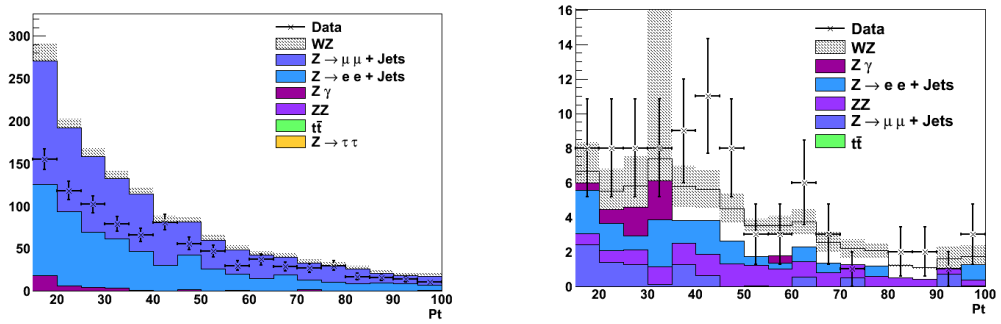

Figure 5.6: Number of electron candidates of a) fakeable and b) tight quality as a function of p_{T} in events with a Z and an extra object which fail the $E_{\mathrm{T}}^{\mathrm{miss}}$ cut. The MC expectations are shown as histograms. Note that fakeable electrons are those that failed the loose++ quality requirement or the electron isolation requirements.

The number of loose and tight electrons as a function of p_{T}, for the low $E_{\mathrm{T}}^{\mathrm{miss}}$ region is shown in Fig. 5.6. The number of non isolated and isolated combined muons as a function of p_{T} are shown in Fig. 5.7, also for the low $E_{\mathrm{T}}^{\mathrm{miss}}$ region. The fake factor is calculated using these distributions and Equation 5.3. Contributions from sources other than Z+jets are subtracted using MC.

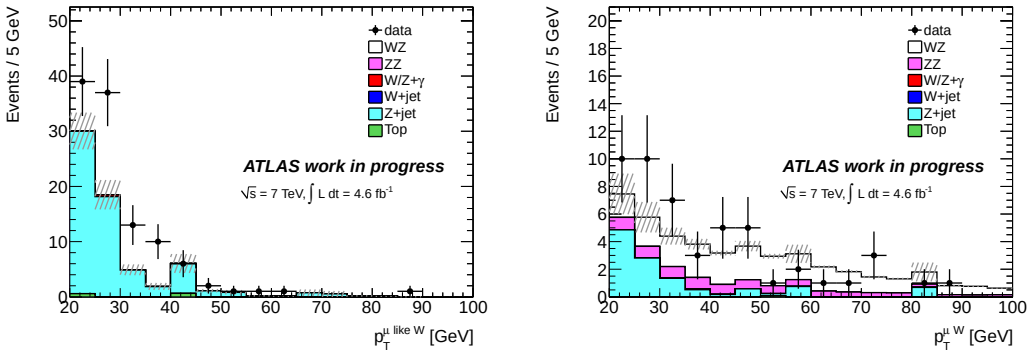

Figure 5.7: Number of non isolated (left) and isolated (right) muon candidates as a function of p_{T} in events with a Z and an extra object which fail the $E_{\mathrm{T}}^{\mathrm{miss}}$ cut. The MC expectations are shown as histograms.

In the $\mu\nu\mu\mu$ and $e\nu ee$ channels, the "fake" lepton may not be associated with the W lepton, but rather mis-associated with the Z boson. Since the loose and tight control regions are built using criteria on the W lepton, the mis-pairing can bias the control region composition. While the mis-pairing from real WZ events is expected to be very small (percent level), it is larger for Z+jets. The reason is that the p_T spectrum of jets is sharply falling from 15 to 20 GeV, so there are more possible "fake" leptons at 15 GeV than at 20 GeV. The percentage of mis-pairing is estimated and a systematic uncertainty is assigned to account for the effect on the control region composition. The percentage of mis-pairing in data for the $e\nu ee$ channel, was found to be 10% and added as a correction to the final yield. For the $\mu\nu\mu\mu$ channel, the loose region has an important contribution from $t\bar{t}$, so it is not possible to estimate the mis-pairing from data; therefore, 8% correction obtained from MC was applied. For the $\mu\nu ee$ and $e\nu\mu\mu$ channels, no correction is needed because the Z lepton assignment is unambiguous.

In the systematic uncertainty of the measurement a possible correlation between $E_{\mathrm{T}}^{\mathrm{miss}}$ and the fake factor is considered. The systematic is taken as the deviation from unity of the ratio between the fake factor in the high $E_{\mathrm{T}}^{\mathrm{miss}}$ region to the low $E_{\mathrm{T}}^{\mathrm{miss}}$ region calculated in the Z+jets Monte Carlo. For the muon fake factor, this uncertainty is 35%. For the electron fake factor, it is 20%.

An additional systematic uncertainty comes from the subtraction of the contamination from non Z+jets samples to the control regions. These samples include $W^{\pm}Z$, ZZ and $t\bar{t}$ simulation. To estimate the uncertainty that this subtraction has on the final estimate of the Z+jets background, the WZ and ZZ samples are variated by the theoretical uncertainty on the cross sections used to normalize the MC samples. The theoretical uncertainties are listed in Table 5.9. The $t\bar{t}$ cross section is varied by 100%, since the $t\bar{t}$ contribution to these samples includes $t\bar{t}$ events in which the third lepton is a fake, and this contribution is not necessarily well modeled by the simulation. The uncertainty is taken as half of the difference between the data driven estimate with the varied MC sample and

the data driven estimate with the nominal MC samples.

The systematic uncertainties due to the contamination subtraction are dominant on this DD estimation. This method was used on the 7 TeV dataset due to the low statistics available, but will need to be improuved for the 8 TeV analysis with larger statistics.

Final estimates obtained with this method are given in Table 5.7.

Table 5.7: Z+jets data driven background predictions per decay channel. Their uncertainties are split in two terms, the first statistical in nature, the second are derived from the systematics affecting the data driven method.

Final State	eee	$ee\mu$	$e\mu\mu$	$\mu\mu\mu$
W/Z+jets	$8.8\pm0.7^{+1.9}_{-1.9}$	$3.7\pm0.5^{+1.6}_{-1.6}$	$10.2\pm0.8^{+2.2}_{-2.2}$	$9.1\pm1.1^{+3.9}_{-3.9}$

For the aTGC limit extraction the p_{T}^{Z} distribution is used, the data driven methods are then performed bin by bin. Final estimates obtained for top and Z+jets background are given in Table 5.8. For the differential (i.e binned) fake factor estimation, the method is the same as for the inclusive estimate, except the sample is divided by bins of p_{T}^{Z}. For the top estimation original numbers per $p_T(Z)$ range are given by simulation, then corrected with the factor 2.2 calculated above in Section 5.4.2.

Table 5.8: Summary of data driven estimated background contributions in different $p_{\mathrm{T}}(Z)$ ranges used for anomalous Triple Gauge Coupling limit setting. The first error is statistical while the second is systematic.

Z p_{T} [GeV]	[0-30]	[30-60]	[60-90]	[90-120]	[120-150]	[150-180]	[180-2000]
W/Z+jets	$12.2\pm2.8^{+2.6}_{-2.6}$	$11.5\pm1.2^{+2.1}_{-2.1}$	$3.3\pm0.4^{+0.6}_{-0.6}$	$1.5\pm0.3^{+0.3}_{-0.3}$	$0.5\pm0.2^{+0.2}_{-0.2}$	$0.4\pm0.2^{+0.1}_{-0.1}$	$0.6\pm0.3^{+0.2}_{-0.2}$
Top	$1.4\pm0.4\pm0.5$	$2.9\pm0.5\pm0.9$	$2.9\pm0.4\pm0.9$	$1.8\pm0.4\pm0.5$	$0.9\pm0.2\pm0.2$	$0.4\pm0.1\pm0.04$	$1.1\pm0.1\pm0.1$

5.5 Systematic Uncertainties

The systematic uncertainties in this analysis are either theoretical or experimental. The theoretical uncertainty is related to the cross sections used in the normalization of signal and background MC, whereas the experimental uncertainty has contributions from reconstruction efficiencies and resolutions for each object, from the luminosity calculation and from the various data driven methods used.

All the systematic uncertainties taken into account in the $W^{\pm}Z$ cross section measurement are summarized in Table 5.13 and discussed below. The uncertainties on the data driven background estimates were discussed in Section 5.4.2.

For all systematics, the uncertainties of different channels resulting from the variation of the same underlying source are treated as fully correlated. The same relative uncertainties calculated using the signal MC samples have been assigned to the background processes whose estimation is MC based.

5.5.1 Theoretical uncertainties

The systematic uncertainties on the theoretical cross-sections concern both signal and background processes and are estimated using MC [84–87]. In the case of the backgrounds the uncertainties will affect the cross-sections used to the overall normalizations of MC predictions. For the signal, since this is a cross-section measurement, the theoretical uncertainties on the cross-section will not enter directly. Nevertheless the detector coverage is limited and the MC signal is needed to extrapolate from the fiducial volume cross-section to the full phase space, so the theoretical uncertainties on the signal will affect the acceptance calculation.

The theoretical uncertainties on the cross-sections are summarized in Table 5.9. The Parton Distribution Functions (PDF) uncertainties are considered for the theoretical cross section uncertainty and in the acceptance calculation.

Sample	Uncertainty (%)
WZ	$^{+7.5}_{-4.6}$
WW	$^{+5.5}_{-4.5}$
ZZ	$^{+5.0}_{-4.1}$
$Z+\gamma$	± 5.0
$t\bar{t}$	$^{+7.0}_{-9.6}$

Table 5.9: Uncertainties on theoretical cross-sections for MC samples used in the analysis [84–87].

PDF, Scale and Generator

The momentum distribution functions of the partons within the proton allows one to know the energy scale of the collisions. Systematics uncertainties due to mismodeling of PDF, renormalization (μ_r) and factorization (μ_f) scales as well as differences arising from different MC generators must be considered.

As mentioned before, these theoretical systematics will affect the calculation of the fiducial acceptance A_{WZ}. The central value of A_{WZ}, is calculated based on events generated with MC@NLO using a CT10 NLO PDF and the corresponding ATLAS MC11 tune. The uncertainty within CT10 PDF set is obtained by following a standard procedure described in the CTEQ manual [70]. Each one of the parameters is variated by $\pm\sigma$ and the symmetric uncertainty is evaluated by averaging positive and negative uncertainties. The uncertainty between different PDF sets is estimated by comparing CT10 to the MSTW2008 NLO PDF set. The uncertainty calculated from CT10 error eigenvectors is about 0.3%, and the central value deviation from MSTW2008 NLO is around 1.6%. The uncertainty due to the statistics of the sample is about 0.2%. The combined systematic uncertainty with the quadratic sum is 1.6%, which is the PDF uncertainty for A_{WZ}.

To determine the uncertainty on A_{WZ} due to μ_r and μ_f scales, various MC@NLO samples were produced in which the scale was varied by a factor of 2 and a factor 0.5. The difference between the change in the expected number of events in the fiducial volume and the change in cross section is 0.9%, the scale uncertainty. The A_{WZ} generator dependence was cross checked using `POWHEG BOX` [88], differences were found to be $\sim 1.2\%$. Table 5.13 summarizes the scale and generator uncertainties for the acceptance A_{WZ}.

For aTGC extraction the signal cross-section is fixed to the SM values, and limits are calculated for the aTGC couplings, so in this case the theoretical uncertainties in the cross-section will need to be considered. The scale uncertainty on the total WZ cross section is thereby found to be about 4.7%. The effect of the PDF choice on the theoretical cross section is provided by CT10 and is about 3.5%. The uncertainties are also given in bin of $p_{\mathrm{T}}(\mathrm{Z})$, and summarised in Table 5.14. In this case the generator and scale uncertainties account for differences in shape of the $p_{\mathrm{T}}(\mathrm{Z})$ spectrum. For the generator uncertainty, the cross sections predicted by MC@NLO and `POWHEG BOX` are normalized so to account only for shape differences, and not differences in cross section predictions.

5.5.2 Experimental uncertainties

The experimental systematic uncertainties concern the calculation of the integrated luminosity which affects the MC normalization and the physics objects (like the reconstruction efficiencies and resolutions, trigger efficiencies, etc.). The systematics for each physics object used in the event reconstruction are calculated separately using the signal samples, but they are also used for background uncertainty estimation when no data-driven method is used, the reason being the insufficient MC background statistics available. The systematic uncertainties on the predicted $W^{\pm}Z$ signal are calculated varying the systematic uncertainty of the underlying source in signal MC and taking the fractional difference between the predicted nominal number of events and the number of events predicted with the systematic variation. All the sources of systematic uncertainties, and how they are estimated are discussed below.

Luminosity

The overall normalization uncertainty of the integrated luminosity is 1.8% [65]. This uncertainty is also applied to MC samples for which the normalization is obtained using the calculated luminosity of data. This systematic is assumed to be correlated across the samples.

Muons

The primary sources of uncertainty related to muons come from reconstruction efficiency, and momentum resolution. A systematic uncertainty on the muon isolation and impact parameter cut efficiency has also been considered. The contributions are quantified by

Uncertainty per channel (%)		μee	$\mu\mu e$	$\mu\mu\mu$
Reconstruction efficiency		0.27	0.53	0.8
p_{T} smearing	ID	0.03	0.01	0.04
	MS	0.02	0.05	0.04
	combination	0.04	0.05	0.06
Isolation & Impact Parameter Efficiency		0.2	0.43	0.62
Total		0.34	0.68	1.01

Table 5.10: Detailed list of systematic uncertainties on the expected event yields for muon objects in MC signal samples, tau channels included. Each contribution is used separately in cross-section estimations; indicative total values are shown for each channel. The reconstruction efficiency uncertainty is dominant.

varying each systematic source within its associated uncertainty and observing the fractional change in the number of events passing the selection. Systematic uncertainties coming from muon objects are summarized in Table 5.10. And the different sources are commented below:

- *Reconstruction efficiency*: The reconstruction efficiencies are measured from data using a tag-and-probe method with di-muon decays of the Z [79]. The differences between data and MC are taken into account by weighting the simulation with scale factors (SF).
- *Momentum resolution (p_{T} Smearing)*: The muon momentum resolution affects the muons selection efficiency, as well as some of the event selection cuts, like the Z mass requirement, or the W lepton p_T. Momentum corrections were obtained by comparing the di-muon mass resolution measured in data and in MC. The event yields are computed by varying the p_{T} correction of the muons in the muon spectrometer (MS) and inner detector (ID), according to the uncertainty on the p_{T} scale and resolution observed in data. The final value used is the sum in quadrature of the ID, MS and scale systematic uncertainties.
- *Muon Isolation, Impact Parameter* : The efficiencies for isolation and impact parameter cuts have also been measured with data. The isolation-Impact Parameter scale factor is an overall factor applied per muon, and it depends on the muon p_{T} .

Electrons

In the electron channel, the primary sources of systematics are related to the uncertainties in electron reconstruction and identification efficiency, energy scale, energy smearing, and calorimeter isolation. The contributions are quantified by varying each parameter within its associated uncertainty and observing the fractional change in the number of events passing the selection. The uncertainties used are those provided by the Egamma performance group [89]. The systematic uncertainties on the expected event yields are listed in Table 5.11 and were estimated as follows:

Source	eee	$ee\mu$	$e\mu\mu$
Energy scale	0.5	0.3	0.3
Energy smearing	0.1	0.1	0.0
Reconstruction Efficiency	2.5	1.7	0.8
Identification Efficiency	3.5	2.3	1.2
Isolation & Impact Parameter Efficiency	1.5	1.1	0.4
Total	4.5	3.1	1.5

Table 5.11: Summary of electron systematic uncertainties on the expected event yields in MC signal samples.(%).

- *Reconstruction and Identification Efficiency*: The differences observed in the reconstruction and identification efficiencies between the data and MC are corrected by weighting the simulation. The electron identification efficiency scale factors and their uncertainties are determined from W, Z, and J/ψ electron measurements as a function of η and E_T. The uncertainties of the η and E_T dependent scale factors are added in quadrature to obtain the combined electron identification uncertainty.
- *Energy Scale*: The electron energy scale is calibrated and checked in data and MC using $Z \rightarrow ee$ events.The dominant uncertainties on the energy scale come from the modeling of the material in ATLAS and the calibration of the EM calorimeter pre-sampler energy scale, as well as several other smaller contributions.
- *Energy Smearing*: As in the muon case, the electron resolution is corrected in MC in order to match the observed data.
- *Isolation and Impact Parameters:* Includes differences between data and MC when measuring the isolation efficiency using the Z tag-and-probe method.

Missing Transverse Energy

The missing transverse energy used in this analysis is built using the information of the reconstructed objects in the event and also includes the cells outside of any object, as described in Section 4.3. The uncertainties affecting the reconstructed objects must be then propagated to the missing energy [81]. Therefore the $E_{\mathrm{T}}^{\mathrm{miss}}$ systematic uncertainties are 100% correlated with the leptons and jet energy uncertainties. The $E_{\mathrm{T}}^{\mathrm{miss}}$ uncertainties will affect the efficiency of the W transverse mass and $E_{\mathrm{T}}^{\mathrm{miss}}$ cuts. Thus contributing to the uncertainty on the signal selection efficiency and the background normalizations. The main sources of $E_{\mathrm{T}}^{\mathrm{miss}}$ systematic uncertainty are: the topocluster energy scale, the muon and electron energy scale and resolution, the jet energy scale and the pileup description by the MC.

A standard ATLAS procedure was used to estimate the uncertainty on the topocluster energy scale [90]. The uncertainties from propagating the muon and electron scale and resolution uncertainties are already included in the muon and electron uncertainties, and not considered again here. The uncertainty due to pileup events (estimated to be 6.6% on

Source	eee	$ee\mu$	$e\mu\mu$	$\mu\mu\mu$
Topocluster energy scale	0.40	0.17	0.57	0.18
Jet energy scale	0.11	0.08	0.10	0.08
Jet energy resolution	0.28	0.30	0.39	0.25
Pileup	0.32	0.11	0.32	0.13

Table 5.12: Summary of systematic uncertainties on the expected event yields (%) for $E_{\mathrm{T}}^{\mathrm{miss}}$in MC signal samples.

the calorimeter terms of $E_{\mathrm{T}}^{\mathrm{miss}}$) is provided by the jet/MET group.Table 5.12 summarizes the systematic uncertainties from the sources considered.

5.5.3 Summary of Systematic Uncertainties

A summary of the acceptance corrections systematic uncertainties previously computed is presented by decay channel in Table 5.13 and for all the channels in Z p_T bins in Table 5.14. These systematics are used as input for the cross-section measurement, used for aTGC limits setting.

Source	$\mu\mu\mu$	$e\mu\mu$	$ee\mu$	eee
μ reconstruction efficiency	0.8	0.53	0.27	-
μ p_{T} scale & resolution	0.06	0.05	0.04	-
μ isolation & impact parameter efficiency	0.62	0.43	0.2	-
e reconstruction efficiency	-	0.8	1.7	2.5
e identification efficiency	-	1.2	2.3	3.5
e isolation & impact parameter efficiency	-	0.4	1.1	1.5
e energy scale	-	0.3	0.3	0.5
e energy resolution	-	0.0	0.1	0.1
$E_{\mathrm{T}}^{\mathrm{miss}}$ cluster energy scale	0.18	0.57	0.17	0.40
$E_{\mathrm{T}}^{\mathrm{miss}}$ jet energy scale	0.08	0.10	0.08	0.11
$E_{\mathrm{T}}^{\mathrm{miss}}$ jet energy resolution	0.25	0.39	0.30	0.28
$E_{\mathrm{T}}^{\mathrm{miss}}$ pileup	0.13	0.32	0.11	0.32
Trigger - μ	0.29	0.15	0.07	-
Trigger - e	-	<0.05	<0.05	<0.05
Generator	0.4	0.4	0.4	0.4
PDF	1.2	1.2	1.2	1.2
Scale	0.4	0.4	0.4	0.4
Luminosity	1.8	1.8	1.8	1.8

Table 5.13: Summary of all relative acceptance uncertainties (%) in the cross-section calculation.

5.6 Observed and Expected Events

The number of expected and observed events after applying all selection cuts are shown by decay channel in Table 5.15 and in Z p_T bins in Table 5.16, with both statistical and systematic uncertainties. The W/Z+jets background and top quark production were estimated using data-driven methods, and the other predictions come from MC simulation.

For each channel or $p_{\mathrm{T}}(Z)$ range and each process, the fractional systematic uncertain-

	Z p_T [GeV]						
Source	[0-30]	[30-60]	[60-90]	[90-120]	[120-150]	[150-180]	[180-2000]
μ reconstruction efficiency	0.55	0.56	0.57	0.58	0.59	0.61	0.63
μ p_{T} scale &resolution	0.07	0.03	0.07	0.18	0.35	0.15	0.25
μ isolation & impact parameter efficiency	0.32	0.43	0.49	0.53	0.55	0.57	0.55
e reconstruction efficiency	0.97	0.97	1.19	1.03	1.06	0.10	1.13
e identification efficiency	1.35	1.44	0.94	1.44	1.37	0.55	1.30
e isolation & impact parameter efficiency	0.41	0.56	0.79	0.70	0.70	0.03	0.73
e energy scale	-0.16	0.16	0.10	0.38	0.40	-0.43	1.10
e energy resolution	0.05	0.02	-0.28	-0.07	0.09	0.51	-0.14
$E_{\mathrm{T}}^{\mathrm{miss}}$ cluster energy scale	-0.00	0.20	0.41	0.47	0.19	0.06	-0.12
$E_{\mathrm{T}}^{\mathrm{miss}}$ jet energy scale	-0.07	-0.09	-0.23	0.04	-0.16	0.35	0.04
$E_{\mathrm{T}}^{\mathrm{miss}}$ jet energy resolution	-0.01	0.01	0.27	0.36	-0.07	0.05	0.61
$E_{\mathrm{T}}^{\mathrm{miss}}$ pileup	0.04	0.10	0.35	0.36	0.08	0.04	-0.21
Trigger - μ	0.14	0.16	0.16	0.16	0.15	0.14	0.14
Trigger - e	0.02	0.03	0.03	0.03	0.02	0.02	0.02
Generator	-0.58	-2.97	3.90	1.11	1.10	4.28	-1.45
PDF	4.28	4.19	4.09	4.00	4.16	4.02	4.24
Scale	2.60	2.60	4.80	8.70	6.70	7.30	8.00
Luminosity	1.8	1.8	1.8	1.8	1.8	1.8	1.8

Table 5.14: Summary of all relative acceptance uncertainties (%) in different $\mathrm{p}_T(Z)$ ranges used for anomalous Triple Gauge Coupling limit setting, and combined.

ties are calculated by combining different sources (Tables 5.13 and 5.14) in quadrature and then applying to the central value of MC-based estimates. The uncertainty in the cross sections used to normalize the MC samples (see Table 5.9) is also included as a systematic uncertainty. The uncertainty on the rescaling method used for the top background estimate is added in quadrature to that systematic uncertainty. For W/Z+jets background, the systematic uncertainties are the ones from the data-driven method.

A total of 317 $W^{\pm}Z$ candidates in data were observed with 231.2 signal and 68.1 background events expected.

Note that the systematic uncertainties listed in Table 5.15 are not used in the cross-section fit. The fit procedure accounts for the full granularity and correlation of systematic sources across the different channels (see Section 5.7).

5.6.1 Kinematic Distributions

For the events selected at the stage of the three lepton cut, the $E_{\mathrm{T}}^{\mathrm{miss}}$ distributions are shown in Fig. 5.8 Where data are compared to the Monte Carlo. Figure 5.9 shows the kinematic distributions for inclusive $W^{\pm}Z$ candidate events. The W transverse mass distribution shows an excess around ~ 75 GeV. Figure 5.10 shows the W transverse mass in the four different decay channels, for events passing all selection cuts. Further studies were performed in order to investigate the origin of the excess and are discussed in Section 5.6.3. Finally, the di-lepton mass for events passing all selection cuts are presented in Fig. 5.11.

5.6.2 $W^{\pm}Z$ Mass definition

An important factor in the behavior of $W^{\pm}Z$ invariant mass is expected come from the presence of New Physics. In the case of the aTGCs, large deviations from the Standard

Final State	eee	$ee\mu$	$e\mu\mu$	$\mu\mu\mu$	Combined (all channels)
Observed	56	75	78	108	317
ZZ	3.2±0.1±0.2	4.9±0.1±0.2	5.0±0.1±0.1	7.9±0.1±0.2	21.0±0.2±0.7
W/Z+jets	$8.8\pm0.7^{+1.9}_{-1.9}$	$3.7\pm0.5^{+1.6}_{-1.6}$	$10.2\pm0.8^{+2.2}_{-2.2}$	$9.1\pm1.1^{+3.9}_{-3.9}$	$31.9\pm1.6^{+7.5}_{-7.5}$
Top	1.1±0.3±0.2	2.9±0.5±0.8	3.5±0.5±1.0	4.0±0.5±1.1	11.5±0.9±3.4
$W/Z+\gamma$	1.4±0.7±0.1	–	2.3±0.9±0.1	–	3.7±1.1±0.1
Bkg (total)	$14.5\pm1.0^{+1.9}_{-1.9}$	$11.5\pm0.7^{+1.8}_{-1.8}$	$21.0\pm1.3^{+2.4}_{-2.4}$	$21.0\pm1.2^{+4.0}_{-4.0}$	$68.1\pm2.1^{+8.2}_{-8.2}$
Expected signal	38.9±0.5±2.0	54.0±0.5±2.1	56.6±0.6±1.6	81.7±0.7±2.0	231.2±1.1±7.8
Expected S/B	2.7	4.7	2.7	3.9	3.4

Table 5.15: Summary of observed events and expected signal and background contributions in the four tri-lepton channels. The first error is statistical while the second is systematic. The W/Z+jets and top background were estimated using data-driven methods. The systematics for the W/Z+jets estimates for the fake muon are correlated in both channels. The same applies to the estimates in the channels with a fake electron. The two sets of W/Z+jets systematic uncertainties are then summed in quadrature, since the uncertainties associated with fake electrons and fake muons are uncorrelated. The systematics for the MC estimates are added linearly since they are correlated across channels. These are summed in quadrature with the systematics from the W/Z+jets background.

Z p_{T} [GeV]	[0-30]	[30-60]	[60-90]	[90-120]	[120-150]	[150-180]	[180-2000]	Combined
Observed	73	111	69	24	14	13	13	317
ZZ	4.8±0.1±0.3	7.4±0.1±0.5	4.3±0.1±0.3	2.1±0.1±0.2	1.0±0.0±0.1	0.6±0.0±0.1	0.8±0.0±0.1	21.0±0.2±0.7
W/Z+jets	$12.2\pm2.8^{+2.6}_{-2.6}$	$11.5\pm1.2^{+2.1}_{-2.1}$	$3.3\pm0.4^{+0.6}_{-0.6}$	$1.5\pm0.3^{+0.3}_{-0.3}$	$0.5\pm0.2^{+0.2}_{-0.2}$	$0.4\pm0.2^{+0.1}_{-0.1}$	$0.6\pm0.3^{+0.2}_{-0.2}$	$30.0\pm3.2^{+7.5}_{-7.5}$
Top	1.4±0.4±0.5	2.9±0.5±0.9	2.9±0.4±0.9	1.8±0.4±0.5	0.9±0.2±0.2	0.4±0.1±0.04	1.1±0.1±0.1	11.5±0.9±3.4
$W/Z+\gamma$	0.4±0.4±0.0	2.0±0.8±0.1	0.3±0.3±0.0	1.0±0.6±0.1	0.0±0.0±0.0	0.0±0.0±0.0	0.0±0.0±0.0	3.7±1.1±0.1
Bkg (total)	$18.7\pm2.9^{+2.6}_{-2.6}$	$23.8\pm1.4^{+2.4}_{-2.4}$	$10.8\pm0.6^{+1.2}_{-1.2}$	$6.4\pm0.7^{+0.6}_{-0.6}$	$2.4\pm0.3^{+0.3}_{-0.3}$	$1.5\pm0.3^{+0.2}_{-0.2}$	$2.5\pm0.3^{+0.2}_{-0.2}$	$68.1\pm2.1^{+8.2}_{-8.2}$
Expected signal	52.1±0.6±3.0	76.3±0.7±4.8	49.4±0.5±3.9	24.7±0.4±2.5	12.0±0.3±1.0	7.2±0.2±0.7	9.4±0.2±0.9	231.2±1.1±7.8
Expected S/B	2.8	3.2	4.6	3.8	4.9	4.9	3.8	3.4

Table 5.16: Summary of observed events and expected signal and background contributions in different $p_{\mathrm{T}}(Z)$ ranges used for anomalous Triple Gauge Coupling limit setting and combined. The first error is statistical while the second is systematic.

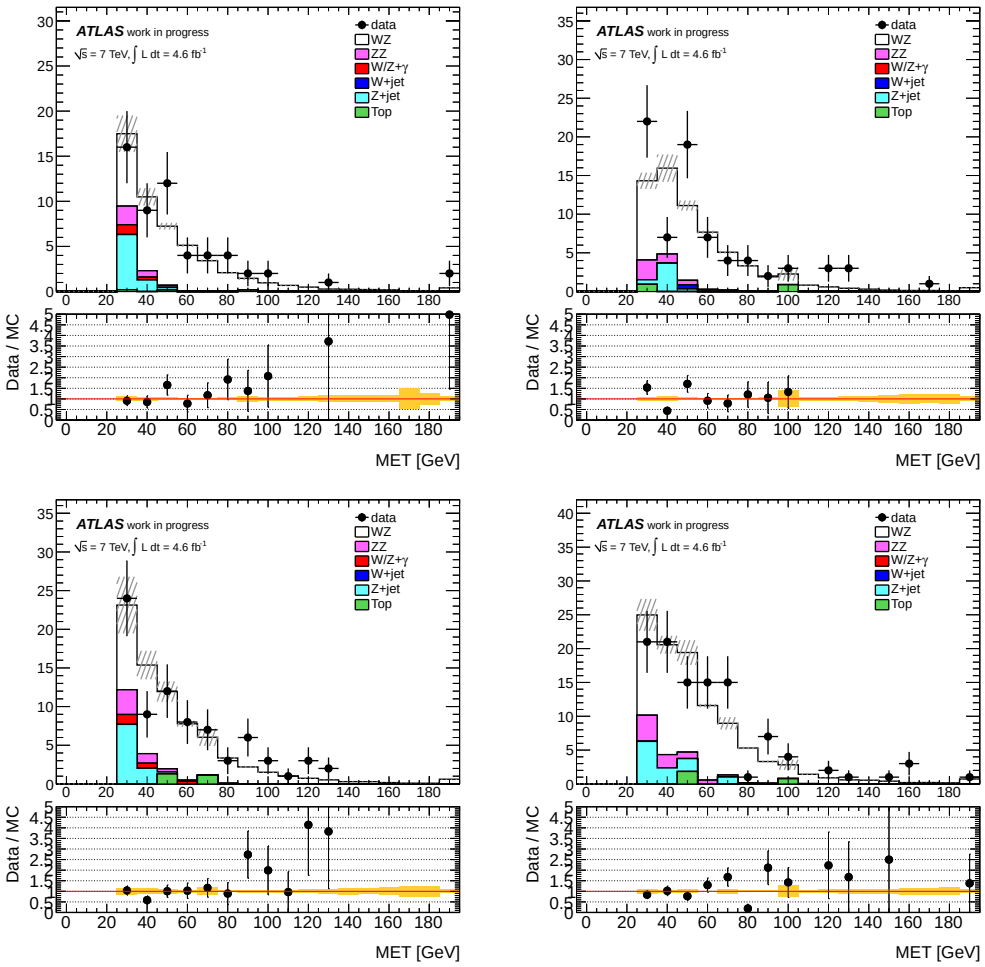

Figure 5.8: $E_{\mathrm{T}}^{\mathrm{miss}}$ distribution of eee (top left), $ee\mu$ (top right), $e\mu\mu$ (bottom left) and $\mu\mu\mu$ (bottom right) events.

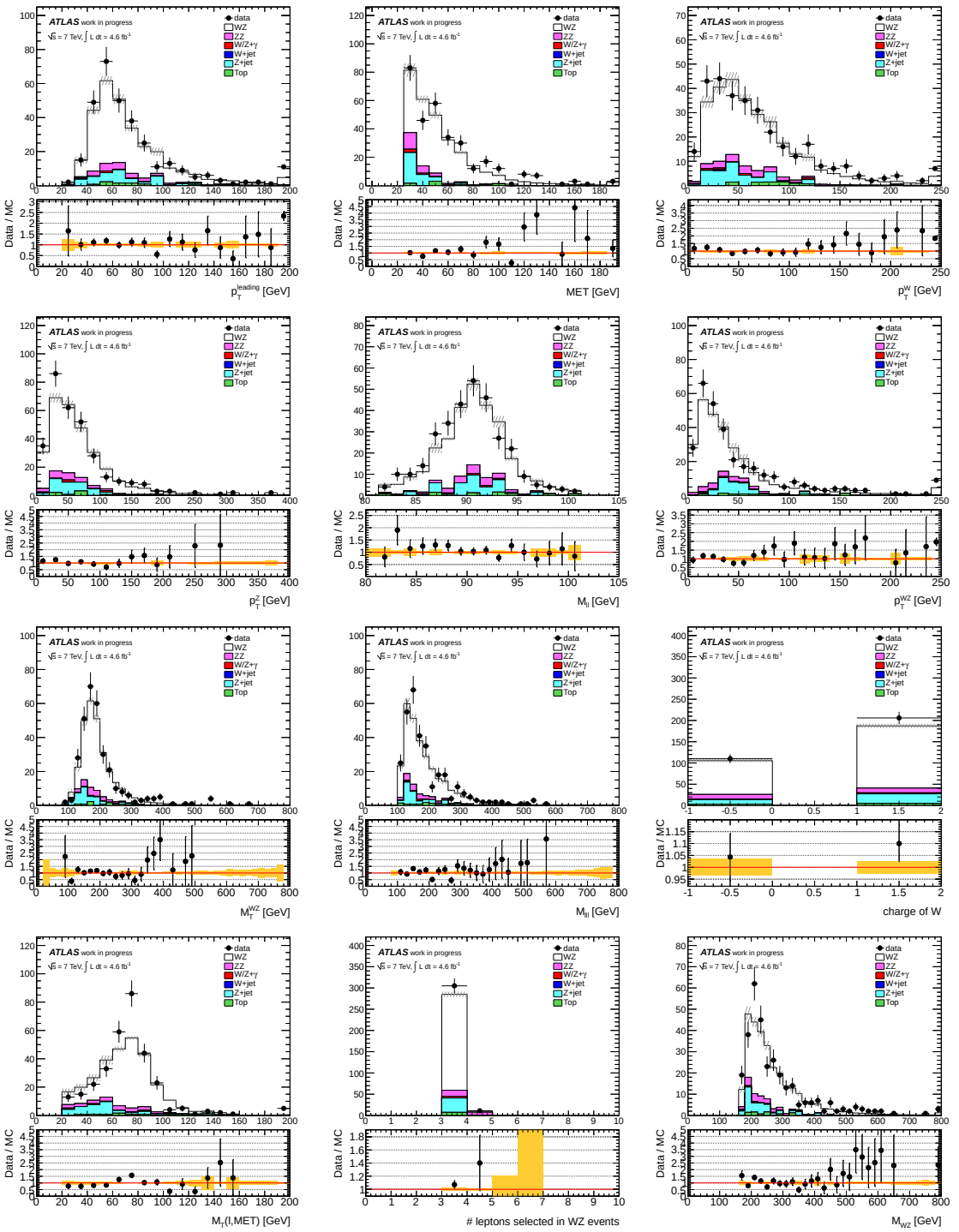

Figure 5.9: Kinematic distributions after all cuts for WZ candidates including p_{T} of the leading lepton, $E_{\mathrm{T}}^{\mathrm{miss}}$ and p_{T} of W in the top row, p_{T} of Z, invariant mass of Z and p_{T} of WZ in the second row, transverse mass of WZ, invariant mass of 3-lepton system and W charge in the third row and the W transverse mass, the number of leptons and the invariant mass of the $W^{\pm}Z$ diboson system in the last row. The last bin is the overflow bin. The shaded bands indicate the total statistical and systematic uncertainties of the MC prediction. Prediction distributions come from MC; but for top and Z+jets, the yields are scaled up according to data-driven estimation.

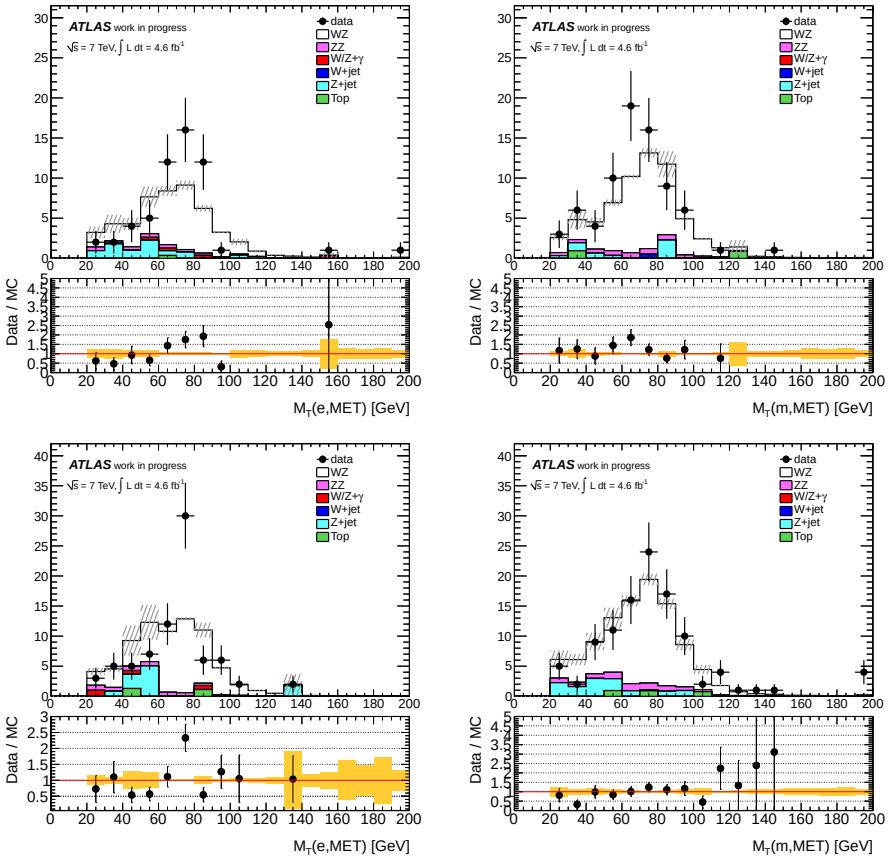

Figure 5.10: W transverse mass distribution of eee (top left), $ee\mu$ (top right), $e\mu\mu$ (bottom left), $\mu\mu\mu$ (bottom right) events after $E_{\mathrm{T}}^{\mathrm{miss}}$ cut.

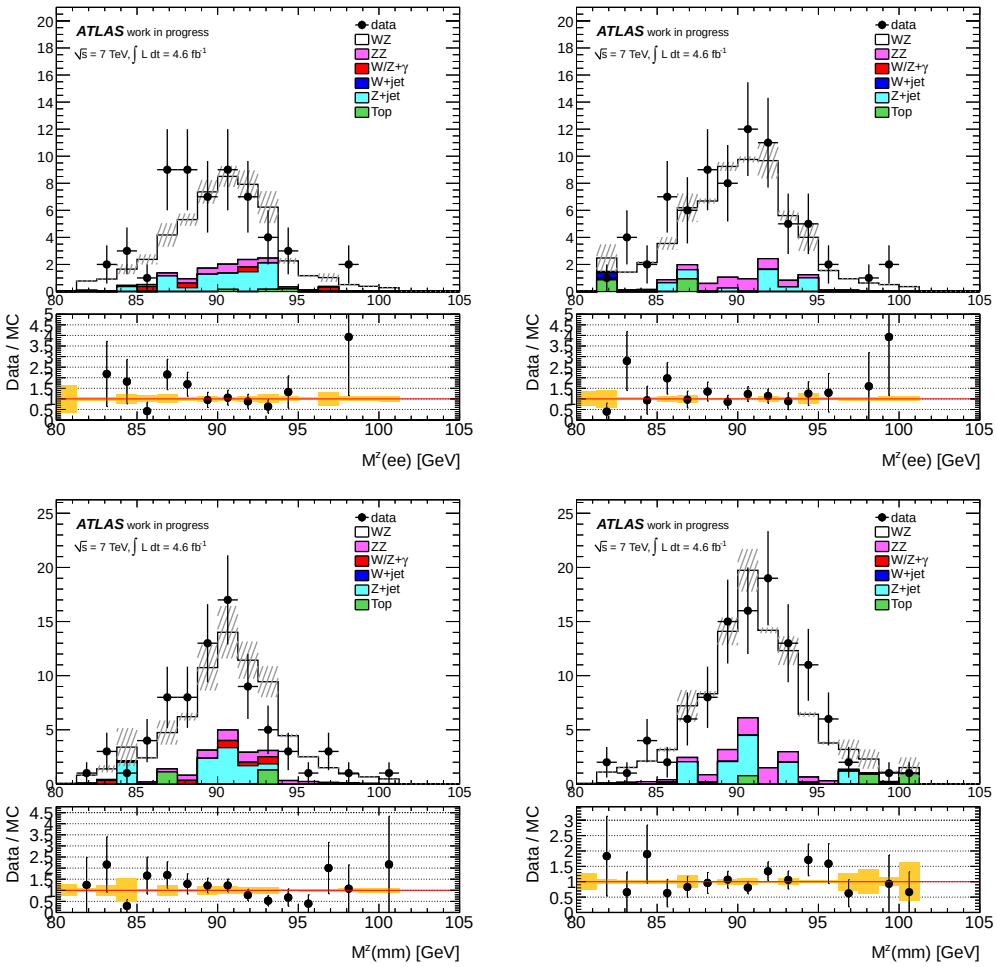

Figure 5.11: Dilepton mass distribution of events in eee, $ee\mu$, $e\mu\mu$ and $\mu\mu\mu$ channels that passed all selection cuts.

Model distributions at high mass are expected. If the effect of the aTGCs on the cross-section is also included, the $W^{\pm}Z$ invariant mass distribution can be considerably more sensitive to the presence of aTGCs than the cross-section alone. The $W^{\pm}Z$ invariant mass distribution will also be affected in the case of new resonances decaying into $W^{\pm}Z$ final state.

When computing the WZ invariant mass there is an ambiguity due to the incomplete knowledge of the neutrino. The measured $E_{\mathrm{T}}^{\mathrm{miss}}$ vector is assumed to be the neutrino p_T^{ν}, so the x and y components of $E_{\mathrm{T}}^{\mathrm{miss}}$ can be written as:

$$p_x^{\nu} = p_T^{\nu} \times \cos\phi^{\nu} \qquad \text{and} \qquad p_y^{\nu} = p_T^{\nu} \times \sin\phi^{\nu} \quad , \tag{5.4}$$

and the longitudinal momentum p_z^{ν} can then be obtained by solving the quadratic equation which results when requiring the invariant mass of the third charged lepton and the neutrino to be the mass of the W boson (PDG mass 80.4 GeV [15]):

$$m_W = \sqrt{(p_\nu + p_l)^2} = 80.4 \text{ GeV} \tag{5.5}$$

since $p_\nu^2 = m_\nu^2 = 0$ and assuming that the lepton mass is ≈ 0 ($p_l^2 = m_l^2 \approx 0$), the m_W can be written as

$$m_W^2 = 2p_\nu p_l \Leftrightarrow \frac{m_W^2}{2} = E_\nu E_l - \overrightarrow{p_\nu}\overrightarrow{p_l} \quad , \tag{5.6}$$

where $\overrightarrow{p_\nu}\overrightarrow{p_l}$ and $E_\nu E_l$ are

$$\overrightarrow{p_\nu}\overrightarrow{p_l} = p_T^{\nu} p_T^{l}.(\cos\phi^{\nu}\cos\phi^{l} + \sin\phi^{\nu}\sin\phi^{l}) + p_z^{\nu} p_z^{l} \quad , \tag{5.7}$$

$$E_\nu E_l = \sqrt{(p_T^{\nu})^2 + (p_z^{\nu})^2} E_l = \frac{m_W^2}{2} + p_T^{\nu} p_T^{l}\cos(\phi^{\nu} - \phi^{l}) + p_z^{\nu} p_z^{l} \quad . \tag{5.8}$$

If we define $X = \frac{m_W^2}{2} + p_T^{\nu} p_T^{l}\cos(\phi^{\nu} - \phi^{l})$, we can write :

$$(E_l^2 - (p_z^l)^2).(p_z^{\nu})^2 - 2Xp_z^l p_z^{\nu} + (E_l^2 (p_T^{\nu})^2 - X^2) = 0. \tag{5.9}$$

Finally, the neutrino p_z^{ν} can be estimated using the following equation

$$p_z^{\nu} = \frac{Xp_z^l \pm E_l\sqrt{X^2 + (p_T^{\nu})^2((p_z^l)^2 - E_l^2)}}{(E_l^2 - (p_z^l)^2)}. \tag{5.10}$$

When Equation 5.10 is solved, two p_z^{ν} solutions are obtained. If the determinant for the p_z^{ν} calculation is negative only the real part of the solution is kept. Using these solutions, the WZ mass can be computed. The agreement between the different possible solutions and the truth WZ mass distribution have been studied.

Figure 5.12 shows the WZ mass truth distribution, compared to the reconstructed solutions. The plot on the left compares the WZ mass computed using the solution with

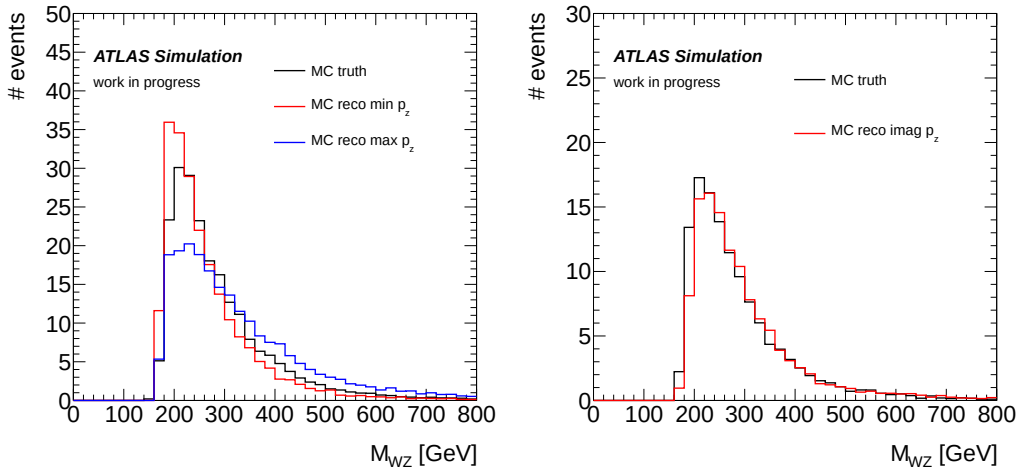

Figure 5.12: WZ mass Monte Carlo distributions. The plot on the left simulation shows in black the truth WZ mass, the red (blue) curves show the reconstructed WZ mass when the minimum (maximum) neutrino p_z^ν solution is chosen. The plot on the right shows the cases when an imaginary solution for the p_z^ν is found, in those cases the truth MC is drawn in black and the real part of the p_z^ν solution is kept to calculate the reconstructed WZ mass shown in red.

the smallest and highest $|p_z^\nu|$ when two real solutions are found. The plot on the right compares the truth WZ mass distribution, with the one calculated using the real part of the p_z^ν solution, when the solution is imaginary. The differences between the reconstructed solutions and the truth WZ mass are shown in Fig. 5.13. The solution with the smallest $|p_z^\nu|$ gives a better agreement with the truth, so it is selected as baseline for the WZ mass calculation and if the determinant for the p_z^ν calculation is negative the real part is used.

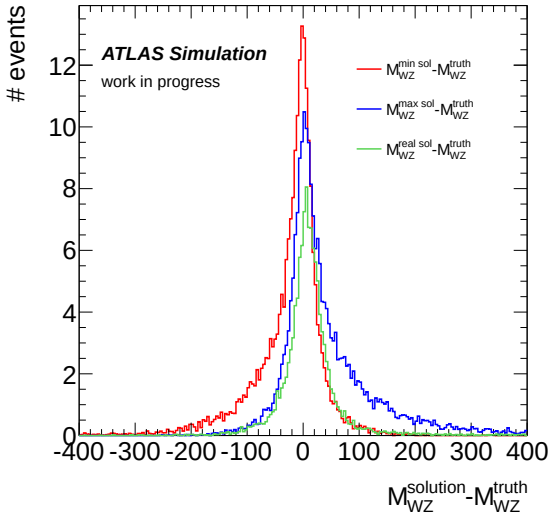

Figure 5.13: Difference between the reconstructed solutions and the truth WZ mass. The red and blue lines show the reconstructed WZ mass using the smallest and highest p_z^ν solution respectively, the green line shows the cases when an imaginary solution is found and the real part is kept.

5.6.3 Investigation of the excess in the W transverse mass

After all cuts for WZ candidates, the W transverse mass distribution in Fig. 5.9 (bottom left) shows an excess in the bin around 75 GeV. In order to see if the excess is due to a particular channel, the W transverse mass for the four channels is plotted separately in Fig. 5.10. The excess in this bin is mainly seen in the $e\mu\mu$ channel, while the eee channel shows a smaller and broader excess spread on three bins.

Several selections were tried, the distributions in Fig. 5.14 show the W transverse mass on the top row after raising the E_T^{miss} requirement to 30 GeV, 35 GeV and 40 GeV, and on the bottom row the same distributions after raising the p_{T} requirement on the W lepton to 25 GeV, 30 GeV and 35 GeV. The excess remains in all cases.

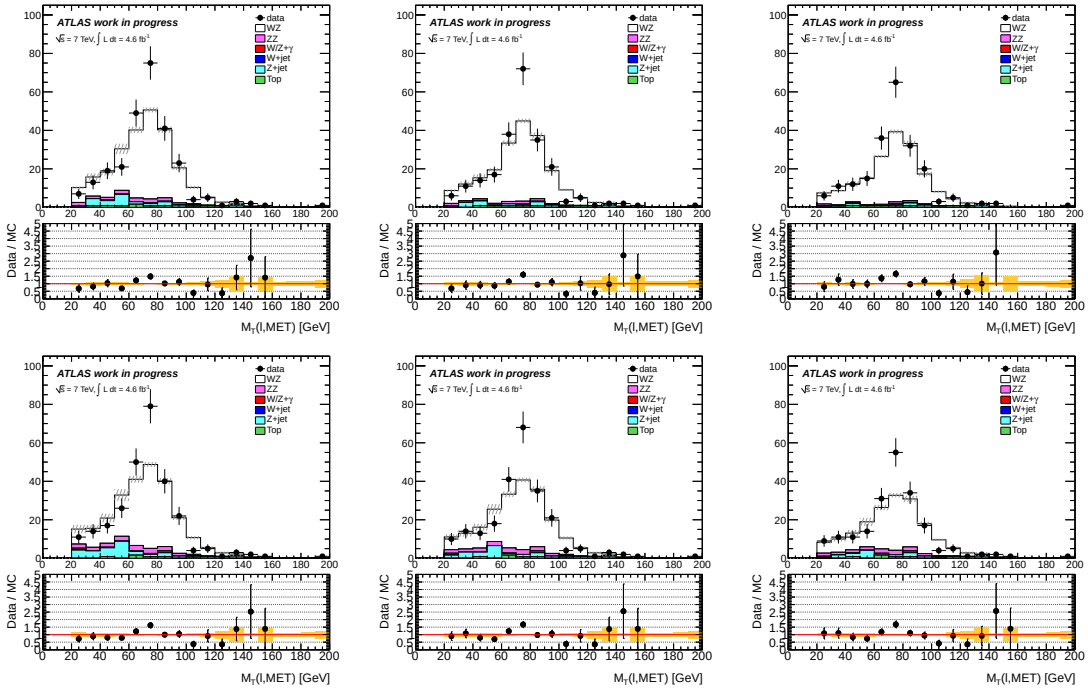

Figure 5.14: The top row shows the $W^{\pm}$ transverse mass distribution after raising the E_T^{miss} requirement to 30 GeV (left), 35 GeV (center) and 40 GeV (right). The bottom row shows the $W^{\pm}$ transverse mass distribution after raising the p_T requirement on the W lepton to 25 GeV (left), 30 GeV (center) and 35 GeV (right).

In order to see if the excess was localized in a specific detector region, in Fig. 5.15 the W transverse mass for positive and negative values of η and Φ is plotted. The excess seems to span the fiducial volume (i.e. it is not a localized effect). The events in the excess are not from a particular period of data taking, which indicates that it is not a problem concerning the data quality of a particular run or an effect of pileup.

To check if the excess is caused by a fake E_T^{miss} due to badly reconstructed jets, Fig. 5.16 shows the $\Delta\Phi$ between the E_T^{miss} and the nearest jet with $p_T > 25$ GeV for the four channels. The distribution is flat and compatible with the expectations, so the excess

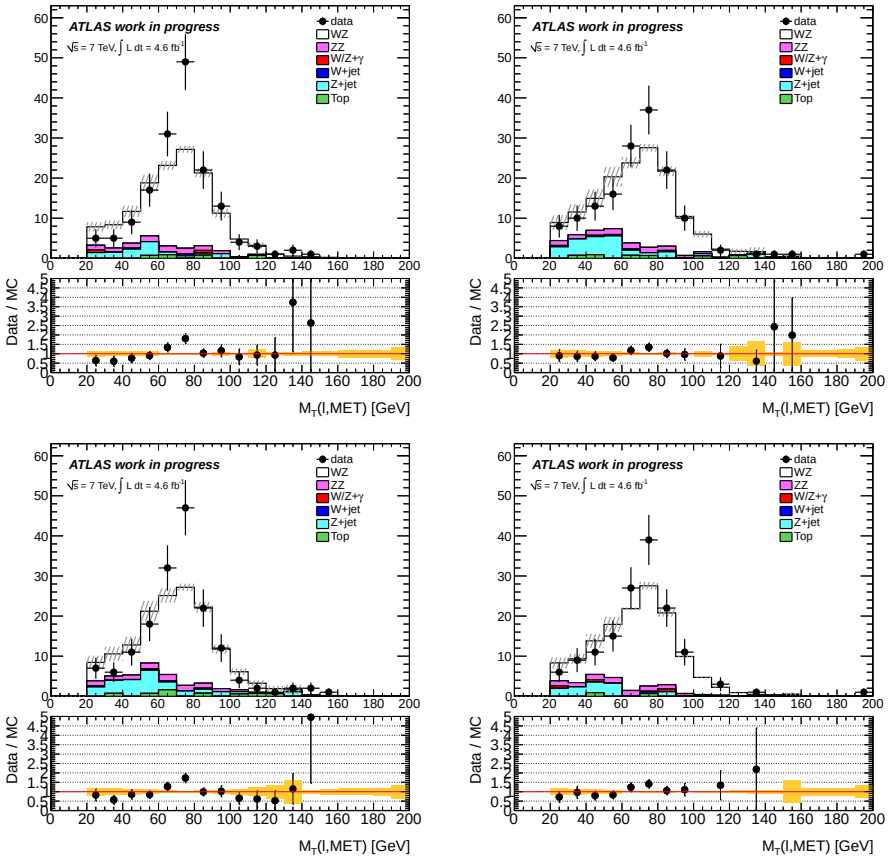

Figure 5.15: W transverse mass for positive η (top left), negative η (top right), positive Φ (bottom left) and negative Φ (bottom right).

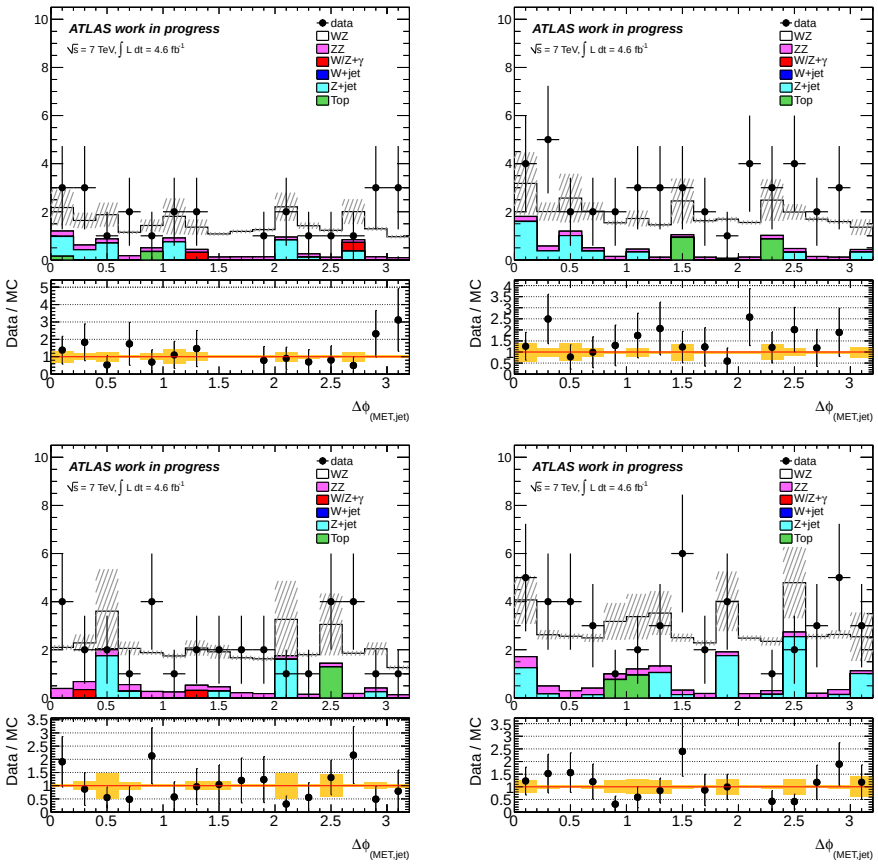

Figure 5.16: $\Delta\Phi$ between E_T^{miss} and the closest jet with pt >25 GeV eee (top left), $ee\mu$ (top right), $e\mu\mu$ (bottom left), $\mu\mu\mu$ (bottom right) events.

does not appear to come from fake E_T^{miss} due to badly reconstructed jets.

Finally, a statistical test of compatibility in shape between the data and the Monte-Carlo histograms of the W transverse mass, using the Kolmogorov test [91] was performed. The W m_T cumulative distribution by channel shown in Fig. 5.17, was used to perform the test. The cumulative distributions were obtained by calculating the integral bin by bin of the plots in Fig. 5.10. For the predicted MC, the MC signal plus the total backgrounds were added. In the case of data driven backgrounds, the MC shape was kept and the plot was scaled to the data driven estimates.

Channel	Prob
eee	0.51
$ee\mu$	0.25
$\mu\mu e$	0.15
$\mu\mu\mu$	0.40
total	0.03

Table 5.17: Kolmogorov test results for the W transverse mass histograms.

The probabilities that the data and MC histograms describe the same distribution obtained using the Kolmogorov test are listed in Table 5.17. These numbers are expected to be flat between 0 and 1 if the two distributions agree, and the smallest the maximal difference between the two integrated distribution the nearest towards 1. So the distributions between data and expected number of events tested are compatible. All the checks performed seem to support the idea that the excess is likely a statistical fluctuation. This conclusion is intuitive when considering the cumulative distributions in Fig. 5.17.

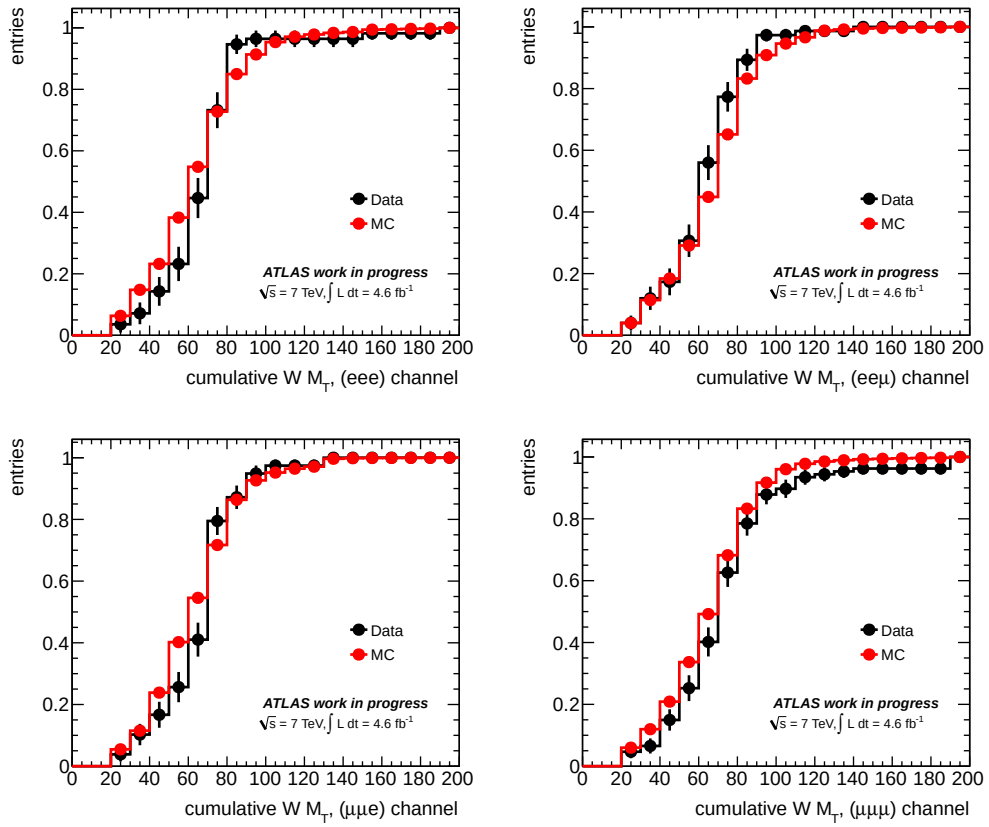

Figure 5.17: Cumulative plot for the W transverse mass distribution, for eee (top left), $ee\mu$ (top right), $e\mu\mu$ (bottom left), $\mu\mu\mu$ (bottom right) events.

5.7 Cross Section Extraction

The main ingredients for the cross section measurement have been presented. Those are the number of observed and expected events, as well as the number of background events for each one of the $W^{\pm}Z$ channels and the uncertainties affecting those measurements. Since electrons and muons have different detector acceptances, a common phase space region for the channels need to be defined, in which a combined fiducial cross section can be extracted. The fiducial volume is defined by the limited coverage of our detector (η cut), and it is even more reduced by the reconstruction efficiency and the selection cuts (leptons

p_T, $\Delta R(l, l')$ etc). To account for the detector efficiency (probability of reconstructing an event, inside the fiducial volume of our detector) the efficiency correction term C_{WZ} is included in the cross section calculation.

To estimate the total cross-section, an extrapolation must be made from the measurement within the detector acceptance, to the total volume. The detector total acceptance (A_{WZ}) is calculated to do this extrapolation using Monte Carlo and implies theoretical uncertainties. So, both a fiducial cross-section without the full extrapolation and therefore with reduced uncertainties, and a total cross section were calculated. The fiducial volume definition, the calculation of the total acceptance A_{WZ} and efficiency correction term C_{WZ}, as well as the techniques used to extract the fiducial and total cross section, are presented in detail in the following sections.

5.7.1 Fiducial Acceptance

The ATLAS detector has a limited phase space coverage, which is even more reduced when we apply our selection cuts. The selection for electrons and muons is different, so the fiducial volume exactly corresponding to our selection cuts for each $W^{\pm}Z$ channel will also be different. A common fiducial volume across the channels need to be defined in order to calculate a combined fiducial cross-section. The common fiducial volume is defined as:

- $p_T^{\ell} > 15\,\text{GeV}$ for the two charged leptons from the Z decay
- $p_T^{\ell} > 20\,\text{GeV}$ for the charged lepton from the W decay
- $|\eta^{\ell}| < 2.5$ for the three charged leptons
- $p_T^{\nu} > 25\,\text{GeV}$ for the neutrino
- $|m_{\ell\ell} - m_Z| < 10\,\text{GeV}$ for the Z candidate
- $m_T^W > 20\,\text{GeV}$ for the W candidate
- $\Delta R(l, l') > 0.3$ for all leptons

The selected events are the ones reconstructed by the detector inside the common volume, so a cross section calculated with those events will give a reconstructed level cross-section. To correct the reconstructed level cross-section to a truth level cross-section defined in the fiducial volume, the efficiency correction term C_{WZ} is used.

The C_{WZ} correction essentially gives us the probability of reconstructing an event, given that all the objects in the event would have been in the detector and passed our selection level cuts. It can be defined as the fraction of the $W^{\pm}Z$ events decaying into electron and muon final states, reconstructed and passing all the selection cuts, over the total number of events generated in the fiducial volume (truth events). It should be noted that for the selection of truth objects, we are using "dressed" final state leptons (electrons and muons). A dressed final state lepton has all photons within $\Delta R < 0.1$ added to the Lorentz vector of the lepton.

C_{WZ} can be calculated by applying the necessary MC to data corrections to the MC signal $W^{\pm}Z \to l\nu ll$ (all the scale factors (SF) such as trigger efficiency, smearing, pileup re-weighting, z-vertex position re-weighting, reconstruction scale factors, etc.) and by finding the ratio of the number of events which pass the reconstruction level cuts to the number of events which pass the fiducial volume cuts at the generator level. Thus,

$$C_{WZ\to l\nu ll} = \frac{\sum \mathrm{Evts}^{\text{MC Pass All Cuts}}_{\text{Reconstructed WZ}\to l\nu ll} \times \mathrm{SF}}{\sum \mathrm{Evts}^{\text{MC Fiducial Volume}}_{\text{Generated WZ}\to l\nu ll}} \tag{5.11}$$

The SF as already mentioned, include all the corrections applied to MC to correct for discrepancies with the data, and is defined as

$$SF = \frac{\epsilon^{data}_{trig}}{\epsilon^{MC}_{trig}} \cdot \frac{\epsilon^{data}_{reco}}{\epsilon^{MC}_{reco}} \tag{5.12}$$

with $\epsilon_{reco} = \epsilon_{lep} \times \epsilon_{event}$. This fiducial acceptance must be calculated for each $W^{\pm}Z \to l\nu ll$ decay channel separately. Branching ratios will be needed for each channel to obtain a combined cross-section.

5.7.2 Total Acceptance

The total cross section is determined by extrapolating the $W^{\pm}Z$ fiducial cross section to the full phase-space, correcting for the $Z \to ll$ and the $W \to l\nu$ branching ratios and the acceptance of the fiducial cuts. The total cross section measured here requires the Z boson to have a mass between 66 GeV and 116 GeV. This is performed by applying a correction from truth level fiducial volume to the full phase space of truth. This correction is defined as the ratio of the number of events generated in the fiducial volume to the total number of events generated:

$$A_{WZ\to l\nu ll} = \frac{N^{\text{MC Fiducial Volume}}_{\text{Generated } WZ\to l\nu ll}}{N^{\text{MC All}}_{\text{Generated } WZ\to l\nu ll}} \tag{5.13}$$

and is calculated for each channel separately. The value of $A_{WZ\to l\nu ll}$ is affected by the PDF and other theoretical uncertainties, which only lead to small uncertainties on $C_{WZ\to l\nu ll}$. The total acceptance correction will be the product $A_{WZ\to l\nu ll} \times C_{WZ\to l\nu ll}$.

5.7.3 Acceptance Values

The calculated A_{WZ} and $C_{WZ\to l\nu ll}$ are summarized in Table 5.18. The A_{WZ} values have been cross checked with the `POWHEG BOX` generator [88] and differences were found to be 0.4%, which are taken as a generator uncertainty.

	$\mu\mu\mu$	$e\mu\mu$	$ee\mu$	eee
A_{WZ}	0.338	0.333	0.332	0.330
C_{WZ}	0.780	0.548	0.525	0.380
$A_{WZ} \times C_{WZ}$	0.263	0.182	0.174	0.125

Table 5.18: Fiducial and total acceptance corrections per channel.

5.7.4 Cross-Section Calculation

The WZ cross-section measurement is obtained as the combination of the different decay channels, and assuming that the probability for our expected number of signal and background events, to produce the observed number of events in data, follow a Poisson distribution. The Poisson law can be written for each channel i (were $i = \mu\nu\mu\mu$, $e\nu\mu\mu$, $\mu\nu ee$, $e\nu ee$)

$$P\left(\frac{N^i_{obs}}{N^i_s + N^i_b}\right) = \frac{e^{-(N^i_s+N^i_b)} \times (N^i_s + N^i_b)^{N^i_{obs}}}{(N^i_{obs})!} \tag{5.14}$$

were N^i_s is the expected number of $W^{\pm}Z$ signal predicted using MC, N^i_b is the number of background events estimated using either MC or data driven methods, and N^i_{obs} is the number of observed events in data after the full selection. This assumption is particularly usefull when dealing with small statistical samples, whose fluctuations are well described by a Poisson distribution.

The systematics errors of the measurement can affect signal and background estimations, to account for this, N^i_s and N^i_b can be written as

$$N^i_s(\{x_k\}) = N^i_s(1 + \sum_{k=1}^{n} x_k S^i_k) \quad \text{and} \quad N^i_b(\{x_k\}) = N^i_b(1 + \sum_{k=1}^{n} x_k B^i_k) \tag{5.15}$$

The parameters S^i_k and B^i_k are the standard deviation representing the systematic uncertainty (the nuisance parameter) in channel i, and n is the number of uncertainty types. All the systematic uncertainties, are assumed to follow a normal distribution with zero mean and unit variance ($x_k \sim N(0,1)$).

The number of signal events can also be expressed as a function of the fiducial cross section, $\sigma \equiv \sigma^{fid}_{WZ\to l\nu ll}$

$$N^i_s(\sigma^{fid}_{WZ\to l\nu ll}, \{x_k\}) = \frac{\sigma^{fid}_{WZ\to l\nu ll}}{\sigma^{tot}_{MC,\ WZ\to l\nu ll} \times A_{WZ\to l\nu ll}} \times \left(N^{MC}_{WZ\to l\nu ll} + N^{MC}_{WZ\to \tau+X}\right) \times (1 + \sum_{k=1}^{n} x_k S^i_k) \tag{5.16}$$

where $\sigma^{tot}_{MC,\ WZ\to l\nu ll}$ is the theoretical total cross-section, or as a function of the total cross section measurement $\sigma \equiv \sigma^{tot}_{WZ}$

$$N^i_s(\sigma^{tot}_{WZ}, \{x_k\}) = \frac{\sigma^{tot}_{WZ}}{\sigma^{tot}_{MC,\ WZ}} \times \left(N^{MC}_{WZ\to l\nu ll} + N^{MC}_{WZ\to \tau+X}\right) \times (1 + \sum_{k=1}^{n} x_k S^i_k) \tag{5.17}$$

In the two equations 5.16 and 5.17, the MC is used to determine the number of expected

signal events in a given channel. This number is scaled by the ratio of the measured cross-section to the MC generator cross-section used to produce the MC expectations. In this way, the data is driving our measurement to find the best rescaling of the expected signal contributions, and thus allows us to extract a cross-section.

The cross section is calculated using a negative log-likelihood function and determining the cross section which minimizes the function. With this method the estimates from the different decays channels can be combined; each channel is treated as a measurement of the cross section and the total likelihood is the product of the individual channel probabilities. In practice, the negative log-likelihood function is defined as

$$-\ln L(\sigma,\{x_k\}) = \sum_{i=1}^{4} -\ln\left(\frac{e^{-(N_s^i(\sigma,\{x_k\})+N_b^i(\{x_k\}))}\times(N_s^i(\sigma,\{x_k\})+N_b^i(\{x_k\}))^{N_{obs}^i}}{(N_{obs}^i)!}\right)+\sum_{k=1}^{n}\frac{x_k^2}{2} \quad (5.18)$$

the expression inside the log is essentially the Poisson probability that our expected number of signal and background events produce our observed number of events, as shown in Equation 5.14.

The last term in the likelihood equation is the log of the product of the Gaussian constraints on the nuisance parameters x_k. The systematic uncertainties can be easily incorporated in the likelihood using nuisance parameters. When a systematic is correlated across the channels, the same single random variable x_k is used over all channels in signal and background. However if a systematic k^* is affecting a single channel, only the $S_{k^*}^i$ or $B_{k^*}^i$ which are effected by systematic k^* are non-zero.

To find the cross section value (fiducial or total) the log-likelihood function is minimized simultaneously over σ and all the nuisance parameters x_k. To calculate the errors the likelihood function is minimized over the nuisance parameters for different values of σ, i.e. the profile likelihood function. This calculation is performed both in the positive and negative directions. The points where the log-likelihood is 0.5 units above the minimum are chosen as errors, and this may be different positive and negative errors. The nuisance parameters account for the systematic errors on our measurement, this error is the combined statistical and systematic uncertainty on our measurement. The minimization and error calculation is performed with the Minuit package [92].

To calculate the cross section (fiducial or total) in only a single channel i, we take only the Poisson probability in channel i rather than the product over all channels. The Gaussian constraint terms are unchanged. Note that the fiducial cross section result does not include the contribution from taus decaying to leptons. The tau contribution from the $W^{\pm}Z$ decays as predicted by the MC simulation is taken into account as background in the fiducial cross section fit.

5.7.5 Calculation of Systematic Uncertainties on the Cross-Section

The likelihood function with nuisance parameters automatically take into account all the systematic errors and propagate them to the final uncertainty. To understand the individ-

ual contribution of a systematic, each systematic uncertainty can be propagated by hand to the final cross-section. To do this in addition to the main fit where all parameters are free, a series of fits where each nuisance parameter is in turn fixed and shifted from its value in the main fit by ± 1 standart deviations is made. The change on the cross-section with respect to its value in the main fit is taken as systematic uncertainty from this source.

This procedure is used for the systematic uncertainties on the fiducial and total cross-sections. The results for each source of systematic uncertainty for each channel, and for the combined measurement are summarized in Tables 5.19 and 5.20. All systematic uncertainties are added in quadrature to yield the total uncertainty (Total (no lumi)), excluding the uncertainty in luminosity.

Source	$\mu\mu\mu$	$e\mu\mu$	$ee\mu$	eee	Combined
μ - Rec. efficiency	$^{+0.88}_{-0.87}$	$^{+0.57}_{-0.56}$	$^{+0.32}_{-0.32}$	$^{+0.00}_{-0.00}$	$^{+0.52}_{-0.53}$
μ -p_T smearing	$^{+0.11}_{-0.11}$	$^{+0.11}_{-0.11}$	$^{+0.00}_{-0.00}$	$^{+0.00}_{-0.00}$	$^{+0.07}_{-0.07}$
μ - isolation & IP efficiency	$^{+0.66}_{-0.65}$	$^{+0.45}_{-0.45}$	$^{+0.22}_{-0.22}$	$^{+0.00}_{-0.00}$	$^{+0.39}_{-0.40}$
e - Rec. Efficiency	$^{+0.00}_{-0.00}$	$^{+0.91}_{-0.90}$	$^{+1.86}_{-1.80}$	$^{+2.84}_{-2.71}$	$^{+1.12}_{-1.11}$
e - Id. Efficiency	$^{+0.00}_{-0.00}$	$^{+1.37}_{-1.34}$	$^{+2.53}_{-2.42}$	$^{+4.02}_{-3.76}$	$^{+1.61}_{-1.57}$
e - Energy Smearing	$^{+0.00}_{-0.00}$	$^{+0.00}_{-0.00}$	$^{+0.11}_{-0.11}$	$^{+0.11}_{-0.11}$	$^{+0.04}_{-0.04}$
e - Energy Scale	$^{+0.00}_{-0.00}$	$^{+0.34}_{-0.34}$	$^{+0.32}_{-0.32}$	$^{+0.56}_{-0.55}$	$^{+0.25}_{-0.25}$
e - iso IP	$^{+0.00}_{-0.00}$	$^{+0.34}_{-0.34}$	$^{+1.20}_{-1.17}$	$^{+1.58}_{-1.53}$	$^{+0.62}_{-0.63}$
$E_{\mathrm{T}}^{\mathrm{miss}}$ - jes	$^{+0.11}_{-0.11}$	$^{+0.11}_{-0.11}$	$^{+0.11}_{-0.11}$	$^{+0.11}_{-0.11}$	$^{+0.11}_{-0.11}$
$E_{\mathrm{T}}^{\mathrm{miss}}$ - jer	$^{+0.22}_{-0.22}$	$^{+0.45}_{-0.45}$	$^{+0.32}_{-0.32}$	$^{+0.33}_{-0.33}$	$^{+0.32}_{-0.32}$
$E_{\mathrm{T}}^{\mathrm{miss}}$ - cluster	$^{+0.22}_{-0.22}$	$^{+0.68}_{-0.67}$	$^{+0.22}_{-0.22}$	$^{+0.45}_{-0.44}$	$^{+0.36}_{-0.37}$
$E_{\mathrm{T}}^{\mathrm{miss}}$ - pileUp	$^{+0.11}_{-0.11}$	$^{+0.34}_{-0.34}$	$^{+0.11}_{-0.11}$	$^{+0.33}_{-0.33}$	$^{+0.20}_{-0.20}$
μ - Trigger	$^{+0.33}_{-0.33}$	$^{+0.23}_{-0.23}$	$^{+0.11}_{-0.11}$	$^{+0.00}_{-0.00}$	$^{+0.20}_{-0.20}$
Signal stat. (MC)	$^{+0.86}_{-0.85}$	$^{+1.07}_{-1.05}$	$^{+0.93}_{-0.92}$	$^{+1.30}_{-1.27}$	$^{+0.50}_{-0.51}$
Bkg stat. (MC)	$^{+0.11}_{-0.11}$	$^{+1.59}_{-1.59}$	$^{+0.16}_{-0.16}$	$^{+1.70}_{-1.70}$	$^{+0.43}_{-0.42}$
Bkg stat. (data driven)	$^{+4.52}_{-4.52}$	$^{+4.30}_{-4.30}$	$^{+2.79}_{-2.79}$	$^{+5.12}_{-5.12}$	$^{+2.30}_{-2.23}$
Data driven method - Z+jets	$^{+4.43}_{-4.44}$	$^{+3.85}_{-3.86}$	$^{+2.46}_{-2.47}$	$^{+4.59}_{-4.57}$	$^{+3.05}_{-3.04}$
Data driven method - top	$^{+1.26}_{-1.26}$	$^{+1.75}_{-1.75}$	$^{+1.26}_{-1.26}$	$^{+0.48}_{-0.48}$	$^{+1.26}_{-1.26}$
Total (no lumi)	$^{+6.63}_{-6.64}$	$^{+6.68}_{-6.67}$	$^{+5.31}_{-5.24}$	$^{+8.93}_{-8.75}$	$^{+4.67}_{-4.62}$

Table 5.19: Relative systematic uncertainties (%) on the fiducial cross-section for each channel.

5.7.6 Cross-Section Results

The results of the fiducial and total cross section measurement are shown in Tables 5.21 and 5.22, first for each individual channel and in the last row the combined one. The systematic uncertainties include all sources except luminosity, which is listed separately.

Source	$\mu\mu\mu$	$e\mu\mu$	$ee\mu$	eee	Combined
μ - Rec. efficiency	$^{+0.88}_{-0.88}$	$^{+0.57}_{-0.56}$	$^{+0.32}_{-0.32}$	$^{+0.00}_{-0.00}$	$^{+0.53}_{-0.53}$
μ -p_T smearing	$^{+0.10}_{-0.12}$	$^{+0.11}_{-0.11}$	$^{+0.00}_{-0.00}$	$^{+0.00}_{-0.00}$	$^{+0.07}_{-0.07}$
μ - isolation & IP efficiency	$^{+0.65}_{-0.66}$	$^{+0.45}_{-0.45}$	$^{+0.22}_{-0.21}$	$^{+0.00}_{-0.00}$	$^{+0.40}_{-0.40}$
e - Rec. Efficiency	$^{+0.00}_{-0.00}$	$^{+0.91}_{-0.89}$	$^{+1.86}_{-1.79}$	$^{+2.87}_{-2.72}$	$^{+1.10}_{-1.09}$
e - Id. Efficiency	$^{+0.00}_{-0.00}$	$^{+1.37}_{-1.34}$	$^{+2.53}_{-2.41}$	$^{+4.06}_{-3.77}$	$^{+1.57}_{-1.55}$
e - Energy Smearing	$^{+0.00}_{-0.00}$	$^{+0.00}_{-0.00}$	$^{+0.11}_{-0.11}$	$^{+0.11}_{-0.12}$	$^{+0.04}_{-0.04}$
e - Energy Scale	$^{+0.00}_{-0.00}$	$^{+0.34}_{-0.34}$	$^{+0.32}_{-0.32}$	$^{+0.56}_{-0.56}$	$^{+0.24}_{-0.24}$
e - iso IP	$^{+0.00}_{-0.00}$	$^{+0.34}_{-0.34}$	$^{+1.19}_{-1.17}$	$^{+1.58}_{-1.54}$	$^{+0.61}_{-0.60}$
$E_{\mathrm{T}}^{\mathrm{miss}}$ - jes	$^{+0.10}_{-0.12}$	$^{+0.11}_{-0.11}$	$^{+0.11}_{-0.11}$	$^{+0.11}_{-0.12}$	$^{+0.11}_{-0.11}$
$E_{\mathrm{T}}^{\mathrm{miss}}$ - jer	$^{+0.21}_{-0.23}$	$^{+0.45}_{-0.45}$	$^{+0.32}_{-0.32}$	$^{+0.33}_{-0.34}$	$^{+0.32}_{-0.32}$
$E_{\mathrm{T}}^{\mathrm{miss}}$ - cluster	$^{+0.21}_{-0.23}$	$^{+0.68}_{-0.67}$	$^{+0.22}_{-0.21}$	$^{+0.44}_{-0.45}$	$^{+0.36}_{-0.36}$
$E_{\mathrm{T}}^{\mathrm{miss}}$ - pileUp	$^{+0.10}_{-0.12}$	$^{+0.34}_{-0.34}$	$^{+0.11}_{-0.11}$	$^{+0.33}_{-0.34}$	$^{+0.20}_{-0.20}$
μ - Trigger	$^{+0.32}_{-0.34}$	$^{+0.23}_{-0.23}$	$^{+0.11}_{-0.11}$	$^{+0.00}_{-0.00}$	$^{+0.20}_{-0.20}$
Generator	$^{+0.40}_{-0.41}$	$^{+0.40}_{-0.40}$	$^{+0.40}_{-0.40}$	$^{+0.40}_{-0.40}$	$^{+0.40}_{-0.40}$
PDF	$^{+1.22}_{-1.20}$	$^{+1.21}_{-1.18}$	$^{+1.21}_{-1.18}$	$^{+1.22}_{-1.20}$	$^{+1.21}_{-1.18}$
Scale	$^{+0.40}_{-0.41}$	$^{+0.40}_{-0.40}$	$^{+0.40}_{-0.40}$	$^{+0.40}_{-0.40}$	$^{+0.40}_{-0.40}$
Signal stat. (MC)	$^{+0.86}_{-0.86}$	$^{+1.07}_{-1.05}$	$^{+0.93}_{-0.91}$	$^{+1.31}_{-1.28}$	$^{+0.50}_{-0.50}$
Bkg stat. (MC)	$^{+0.11}_{-0.12}$	$^{+1.59}_{-1.59}$	$^{+0.16}_{-0.16}$	$^{+1.70}_{-1.71}$	$^{+0.43}_{-0.42}$
Bkg stat. (data driven)	$^{+4.52}_{-4.51}$	$^{+4.30}_{-4.29}$	$^{+2.78}_{-2.78}$	$^{+5.06}_{-5.11}$	$^{+2.31}_{-2.21}$
Data driven method - Z+jets	$^{+4.42}_{-4.44}$	$^{+3.85}_{-3.85}$	$^{+2.46}_{-2.46}$	$^{+4.54}_{-4.57}$	$^{+3.06}_{-3.02}$
Data driven method - top	$^{+1.26}_{-1.27}$	$^{+1.75}_{-1.75}$	$^{+1.25}_{-1.25}$	$^{+0.48}_{-0.49}$	$^{+1.26}_{-1.25}$
Total (no lumi)	$^{+6.76}_{-6.77}$	$^{+6.81}_{-6.78}$	$^{+5.47}_{-5.37}$	$^{+9.00}_{-8.86}$	$^{+4.85}_{-4.76}$

Table 5.20: Relative systematic uncertainties (%) on the total cross-section for each channel.

Channel	Cross-Section [fb]
$\mu\mu\mu$	$23.03^{+2.84}_{-2.66}(\mathrm{stat})\ ^{+1.53}_{-1.53}(\mathrm{syst})\ ^{+0.46}_{-0.45}(\mathrm{lumi})$
$e\mu\mu$	$21.46^{+3.46}_{-3.20}(\mathrm{stat})\ ^{+1.43}_{-1.43}(\mathrm{syst})\ ^{+0.44}_{-0.43}(\mathrm{lumi})$
$ee\mu$	$24.98^{+3.57}_{-3.25}(\mathrm{stat})\ ^{+1.33}_{-1.31}(\mathrm{syst})\ ^{+0.49}_{-0.48}(\mathrm{lumi})$
eee	$22.53^{+4.29}_{-3.85}(\mathrm{stat})\ ^{+2.01}_{-1.97}(\mathrm{syst})\ ^{+0.46}_{-0.44}(\mathrm{lumi})$
All channels	$92.31^{+6.66}_{-6.33}(\mathrm{stat})\ ^{+4.31}_{-4.26}(\mathrm{syst})\ ^{+1.85}_{-1.79}(\mathrm{lumi})$

Table 5.21: Measured fiducial cross-sections for each channel and combined.

Channel	Cross-Section [pb]
$\mu\mu\mu$	$18.74^{+2.31}_{-2.17}(\text{stat})\ ^{+1.27}_{-1.27}(\text{syst})\ ^{+0.38}_{-0.36}(\text{lumi})$
$e\mu\mu$	$17.72^{+2.86}_{-2.64}(\text{stat})\ ^{+1.21}_{-1.20}(\text{syst})\ ^{+0.37}_{-0.35}(\text{lumi})$
$ee\mu$	$20.69^{+2.97}_{-2.69}(\text{stat})\ ^{+1.13}_{-1.11}(\text{syst})\ ^{+0.41}_{-0.39}(\text{lumi})$
eee	$18.78^{+3.58}_{-3.20}(\text{stat})\ ^{+1.69}_{-1.66}(\text{syst})\ ^{+0.38}_{-0.37}(\text{lumi})$
Combined	$19.00^{+1.38}_{-1.30}(\text{stat})\ ^{+0.92}_{-0.90}(\text{syst})\ ^{+0.38}_{-0.37}(\text{lumi})$

Table 5.22: Measured total cross-sections for each channel and combined.

5.8 Anomalous Triple Gauge Couplings Analysis

The effective lagrangian that predicts the presence of anomalous triple gauge couplings was described in Section 1.4. The presence of aTGCs can modify the $W^{\pm}Z$ production cross sections and the kinematic distributions. For the aTGC study the objects and event level selection are the same used for the fiducial cross-section measurement, which is described in Section 5.2. The kinematic distributions sensitive to the presence of aTGCs, were divided into a few bins. Figure 5.18 shows Z tranverse momentum and $W^{\pm}Z$ mass, MC distributions after the $W^{\pm}Z$ selection. The black dots corresponds to the SM WZ Monte Carlo and the red dots to the MC generated with aTGC parameters ($\Delta g = 0$, $\Delta\kappa = 0$, $\lambda = 0.13$). Since aTGC dependence is largest at high momentum or high mass, the sensitivity to the presence of aTGCs depends strongly on the ratio of SM/aTGC events in the last bin, which in turn depends on the number of expected SM events in the last bin.

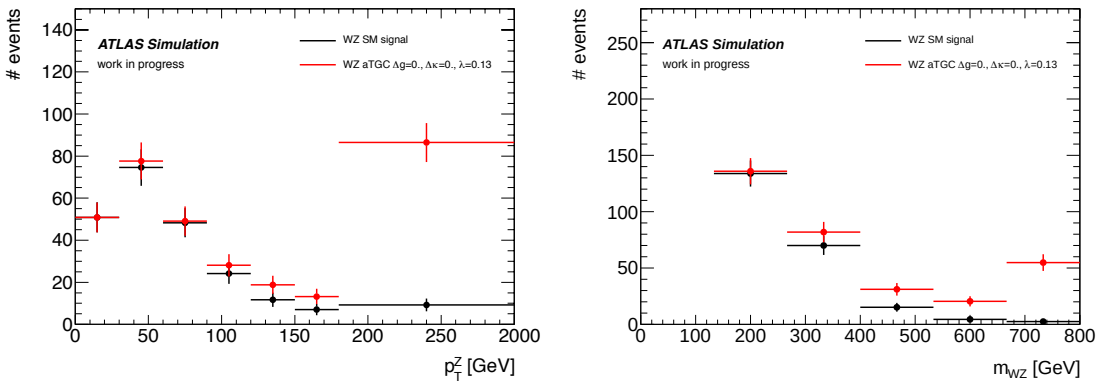

Figure 5.18: After the full selection WZ mass (right) and Z transverse momentum distribution (left), for the SM WZ Monte Carlo (black curve) and for the MC generated with aTGC parameters $\Delta g = 0$, $\Delta\kappa = 0$, $\lambda = 0.13$ (red curve). The bins at hight Z p_T or m_{WZ} are the most sensitives to the aTGC presence.

The reconstructed WZ mass suffers from our inability to directly reconstruct the W boson momentum. The W momentum is reconstructed by solving for the z component of the momentum as seen in Section 5.6.2. In this way, information is lost in reconstructing

the WZ mass. The p_T^Z distribution, however, is built directly from the measurement of leptons. As mentioned in Section 1.4.2, in the case that there are non-zero aTGC, the p_T^Z distribution also has the advantage to be sensitive to the sign of the parameter.

As can be seen in Fig. 5.18, the largest deviation from the SM predictions in the case of non-zero aTGC parameters appears at high p_T^Z. The expected number of events from the SM and aTGC events varies as the binning of the p_T^Z distribution changes. To chose a binning for the extraction of aTGC limits, the sensitivity to differential distributions was tested, for different p_T^Z bins using a profile log-likelihood method, with statistical uncertainties only. For each aTGC parameter and for each observable, the width of the 95% confidence interval was calculated.

The analysis was initially optimized using four bins. However, adding additional bins was found to increase the expected sensitivity. Seven bins was found to be an optimum between expected sensitivity, visual presentation, ability to do data-driven background estimates and keeping systematic uncertainties under control. Therefore, a final binning of [0,30,60,90,120,150,180,2000] GeV was chosen.

With this binning the p_T^Z distribution is used to check consistency between the observed data and MC predictions including aTGCs. The measurement is done by determining the set of aTGC parameters that could reproduce the observed data at the 95% confidence interval. The confidence interval is found using a likelihood function that depends on the aTGC parameters. The likelihood function used is the same as those for the cross section measurement, but the predicted number of events is written as a function of the aTGC parameters rather than as a function of the cross section. The predicted number of events for any anomalous couplings value is estimated using a reweighting procedure. The reweighting procedure and the TGC limits extraction, will be described in the following sections.

5.8.1 aTGC Reweighting

The effective Lagrangian used to describe the effect of non-SM processes on TGCs depends on a number of parameters. The most general amplitude for this process can be written as follows [61, 69]:

$$\mathcal{A} = \mathcal{A}_0 + \Delta g_1^Z \mathcal{A}_{\Delta g_1^Z} + \Delta\kappa^Z \mathcal{A}_{\Delta\kappa^Z} + \lambda^Z \mathcal{A}_{\lambda^Z} \tag{5.19}$$

with $\mathcal{A}_0$ the SM amplitude and $\mathcal{A}_{\Delta g_1^Z,\Delta\kappa^Z,\lambda^Z}$ the amplitudes containing the anomalous vertices associated with the Δg_1^Z, $\Delta\kappa^Z$, λ^Z parameters respectively. Setting these three variables to zero produces the SM results. This factorization also implies that the amplitudes on the right hand side of equation 5.19 can be calculated for each event without any aTGC dependence and thus the total amplitude for each event with any aTGC parameters is a simple linear combination of precomputed amplitudes.

A reweighting procedure is then used to predict the numbers of expected events as a function of the parameter being studied. In the MC@NLO generator [69] the $W^{\pm}Z$ events

can be simulated with any aTGC parameter $(\Delta g_1^Z, \Delta\kappa^Z, \lambda^Z)$, event weights are determined by the cross section, which is in turn are calculated using the square amplitudes. The weight at a new point is given by

$$\begin{aligned} w(\Delta g_1^Z, \Delta\kappa^Z, \lambda^Z) = w_0 &+ (\Delta g_1^Z)^2 w_1 + (\Delta\kappa^Z)^2 w_2 + (\lambda^Z)^2 w_3 \\ &+ 2\Delta g_1^Z w_4 + 2\Delta\kappa^Z w_5 + 2\lambda^Z w_6 \\ &+ 2\Delta g_1^Z \Delta\kappa^Z w_7 + 2\Delta g_1^Z \lambda^Z w_8 + 2\Delta\kappa^Z \lambda^Z w_9. \end{aligned} \quad (5.20)$$

were w_0 is the SM weight while the others come from anomalous vertices. All the weights w_i are independent of the anomalous couplings and depend only on the initial and final particle kinematics. Each event is associated with a vector of 10 weights $\{w_0 \dots w_9\}$ which can be reweighted to another aTGC phase space point, by multiplying them by the appropriate anomalous couplings using equation 5.20.

The events in the MC signal samples with aTGCs were generated with a cutoff scale $\Lambda = 100$ TeV. In order to remove the form factor, we multiply the aTGC parameters Δg_1^Z, $\Delta\kappa^Z$, and λ^Z by $(1 + \hat{s}/\Lambda^2)^2$ where $\hat{s}$ is the center of mass energy. This is equivalent to adjusting the event weights $\{w_0 \dots w_9\}$ as

$$w_i \to \begin{cases} w_i & \text{for } i = 0 \\ w_i(1 + \hat{s}/\Lambda^2)^2 & \text{for } i = 4, 5, 6 \\ w_i(1 + \hat{s}/\Lambda^2)^4 & \text{for } i = 1, 2, 3, 7, 8, 9 \end{cases} \quad (5.21)$$

to remove the form factor completely, the new cutoff scale is set to infinity, which implies $(1 + \hat{s}/(\Lambda)^2)^2 \to 1$.

To calculate the expected number of signal events after reconstruction and selection, it is necessary to apply some additional corrections to the MC samples. The same corrections applied for the cross section extraction are applied to the MC sample (MC generator weights, pile-up weights, trigger and reconstruction scale factors.

The expected number of signal events N_s^i is the sum of the event weights for the MC signal events that pass the selection, after applying these factors. The accumulation of the event weights after the full selection $\{W_j^i\}$ allows us to write the expected number of signal events N_s^i in our data sample in the following form

$$\begin{aligned} N_s^i(\Delta g_1^Z, \Delta\kappa^Z, \lambda^Z) = W_0^i &+ (\Delta g_1^Z)^2 W_1^i + (\Delta\kappa^Z)^2 W_2^i + (\lambda^Z)^2 W_3^i \\ &+ 2\Delta g_1^Z W_4^i + 2\Delta\kappa^Z W_5^i + 2\lambda^Z W_6^i \\ &+ 2\Delta g_1^Z \Delta\kappa^Z W_7^i + 2\Delta g_1^Z \lambda^Z W_8^i + 2\Delta\kappa^Z \lambda^Z W_9^i \end{aligned} \quad (5.22)$$

for each bin of p_T^Z. These coefficients $\{W_j^i\}$ go into the aTGC limit setting procedure described next.

5.8.2 Limit Setting Procedure

The likelihood function used in the cross section extraction, translates the fitted cross section into an expected number of events. It calculates the Poisson probability, for our expected number of signal and background events, to produce the observed number of events. The same likelihood function can be used for the aTGC analysis by replacing only the formula for the expected number of signal events. The new equation for the expected number of signal events in each p_T^Z bin i is given by:

$$N_s^i(\Delta g_1^Z, \Delta\kappa^Z, \lambda^Z, \{x_k\}) = \left(N_{WZ\to l\nu ll}^{MC}(\Delta g_1^Z, \Delta\kappa^Z, \lambda^Z) + N_{WZ\to\tau+X}^{MC}(\Delta g_1^Z, \Delta\kappa^Z, \lambda^Z) \right) \times (1 + \sum_{k=1}^{n} x_k S_k^i) \tag{5.23}$$

where $N_{WZ\to l\nu ll}^{MC}(\Delta g_1^Z, \Delta\kappa^Z, \lambda^Z)$ and $N_{WZ\to\tau+X}^{MC}(\Delta g_1^Z, \Delta\kappa^Z, \lambda^Z)$ are the number of events predicted with aTGC parameters $(\Delta g_1^Z, \Delta\kappa^Z, \lambda^Z)$. As in the cross section fit each systematic uncertainty in a channel i, is assumed to change following a normal distribution with zero mean and unit variance ($x_k \sim N(0,1)$). The parameters S_k^i are the standard deviation representing the k^{th} systematic uncertainty in channel i.

Using the reweighting procedure described in the previous section, it is possible to write the number of expected signal events $N_{\rm s}^i$ as a function of aTGC parameters, and in p_T^Z bins. The background estimation, the observed events and the systematics were also calculated in p_T^Z bins, see Tables 5.16 and 5.14.

To set limits on the aTGC parameters, a frequentist limit approach [93] was adopted. The 95% confidence interval (C.I) was determined for each anomalous coupling. Limits on one coupling or on two coupling parameters at the same time were set; to do this, one parameter was fitted and the other couplings were set to their SM values, which yields to the so called one-dimentional limit (1D). For the two dimensional limit (2D) two couplings are simultaneously fitted, so the best-fit value can have non-zero couplings in two parameters. The p-value of the aTGC values which yield anomalous cross-sections inside the 95% C.I. of the cross-section, determines the 95% C.I. of the anomalous couplings.

The procedure for determining the one dimensional 95% C.I. is as follows.

1. The likelihood function $L(n|\sigma,\beta)$ presented in Equation 5.18 of Section 5.7.4, can be modified by replacing the number of expected signal events N_s^i by a quadratic function of $\alpha = \Delta g_1^Z$, $\Delta\kappa^Z$, or λ^Z and using the reweighting method described in the previous section. Additionally, the sum over flavor bins is replaced by a sum over the seven p_T^Z bins ([0-30], [30-60], [60-90], [90-120], [120-150], [150-180], [180-2000] GeV).

   The symbol n stands for the observed numbers of data events, and β are the nuisance parameters which represent the Gaussian constrained systematics.

2. A test statistic $q(\alpha)$ is constructed by taking minus the natural logarithm of the ratio of the profile maximum likelihood at a test aTGC parameter value α to the

full maximum likelihood. That is

$$q(\sigma) = -ln\frac{L(n|\alpha,\hat{\hat{\beta}})}{L(n|\hat{\alpha},\hat{\beta})} \tag{5.24}$$

where $\hat{\hat{\beta}}$ is the ML estimator of β that maximizes the numerator for the fixed test value of α, and $\hat{\alpha}$ and $\hat{\beta}$ are the values of α and β which maximize the denominator. For the denominator this means that the minimization is done with α and β free $L(n|\hat{\alpha},\hat{\beta})$, and for the numerator different values of α are tried and β is minimized, $L(n|\alpha,\hat{\hat{\beta}})$.

3. The observed value of the test statistic, $q_{\rm obs}(\alpha)$, is found using the observed data $n = n_{\rm obs}$ for each value of the test cross-section. This is done by scanning a range of values of α and determining the value of the test statistic for each α and those give us how many times more likely the data are under one model than the other.

4. The limits can be set using two methods :

   - **Standard frequentist method:** which determines how often an outcome at least as unlikely as the actual observation is expected. A large number of pseudo experiments is generated for different test values of α, the test statistic for each pseudo experiment $q_{\rm pe}(\alpha)$ is computed, and compared with the observed $q_{\rm obs}(\alpha)$. Since the generation of pseudo experiments is a CPU time consuming procedure, the $q_{\rm pe}(\alpha)$ are built only for values of α around the ones corresponding to the 95% C.L on observed data.

     To generate each pseudo experiment, first, the nuisance parameters β were Gaussian fluctuated around the mean value of $\hat{\hat{\beta}}(\alpha)$. The numbers of "observed" events $N^i_{\rm pe}$ was then drawn randomly from a Poisson distribution whose mean was computed from the value of α and β.

     The p-value at each value of α is calculated as the fraction of pseudo experiments whose test statistic $q_{\rm pe}(\alpha)$ is smaller than the observed value $q_{\rm obs}(\alpha)$:

     $$p = \frac{N_{pe}(q_{\rm pe}(\alpha) < q_{\rm obs}(\alpha))}{N_{pe}} \tag{5.25}$$

     The number of pseudo experiments, is chosen to be 10.000, this choice is made in order to ensure that a p-value of 5% can be determined to a reasonable statistical precision of $\pm 0.2\%$.

   - **Asymptotic profile log-likelihood method:** It is an asymptotic regime of frequentist method, that can also be used to compute confidence intervals, defining:

     $$1 - p = 1 - \chi^2(q_{obs}(\alpha), NDF = 1), \tag{5.26}$$

and computing $q_{\rm obs}(\alpha)$ for different values of α and minimizing in β.

5. By scanning α, all values of the aTGC parameter for which $p(\alpha) \geq 5\%$ can be determined and these define the 95% C.I. of α for the observed data.

6. To find the expected sensitivity, the SM expectations for the signal and background were used ($n_{\rm obs} = n_{\rm SM}$). In the frequentist approach those yields are used to generate a large number of toy MC observed data sets, $n_{\rm obs}^{\rm toy}$. Using these sets, the distribution of the 95% C.I. for the aTGC parameters can be studied.

The baseline method used in this analysis is the standard frequentist, the results from the asymptotic profile likelihood method will be also given below.

Figure 5.19 shows the $1-p$ distribution as a function of each of the anomalous couplings Δg_1^Z, $\Delta\kappa^Z$, and λ^Z, obtained by using the profile likelihood method and no cut-off; the horizontal line shows the 95% C.I. The expected limits are on the left and the observed limits on the right. The observed limits are shown bin by bin (in different colors) and the combination of all the bins (black line). Because the expected number of signal events N_s^i is a quadratic function the parameter α, $N_s^i(\alpha)$ has a minimum near (but not exactly at) the SM point $\alpha = 0$, and increases in both positive and negative directions of α. As a result, there may be either one or two optimum values of α that best describe the observed data. This effect can be seen for some bins in Fig. 5.19, depending on whether $N_{\rm obs}$ is smaller or larger than the minimum expected value. This can result in two possibilities for the 95% C.I. of α, it may be a single continuous region as will be in our case or two disjoint regions.

As mentioned before the limits 1D and 2D are obtained in different ways. In the 1D case the limits are set on each parameter by setting the value of the other two aTGC parameters to the SM values. In the 2D case, only one aTGC parameter is set to zero, and the 95% confidence contour for the other two parameters are fit simultaneously, so the best-fit value can have non-zero couplings in two parameters.

The 2D limits are extracted following the same method as for the 1D limits. First, the best-fit value in the 2D aTGC parameter space is found. From that point, 1D limits are extracted along radial lines moving out from the best-fit value. The 95% confidence contour is the contour connecting the set of points which correspond to the 95% limits on the many radial spokes.

Results

The observed 95% C.I. on the anomalous couplings Δg_1^Z, $\Delta\kappa^Z$, and λ^Z are summarized in Tables 5.23, 5.24 and 5.25. Two different cut-off scale were used $\Lambda = 2$ TeV (in order to compare with the Tevatron results), and no form-factor (equivalent to setting $\Lambda \to \infty$). These limits are 1D limits obtained by setting the other aTGC parameters to the SM

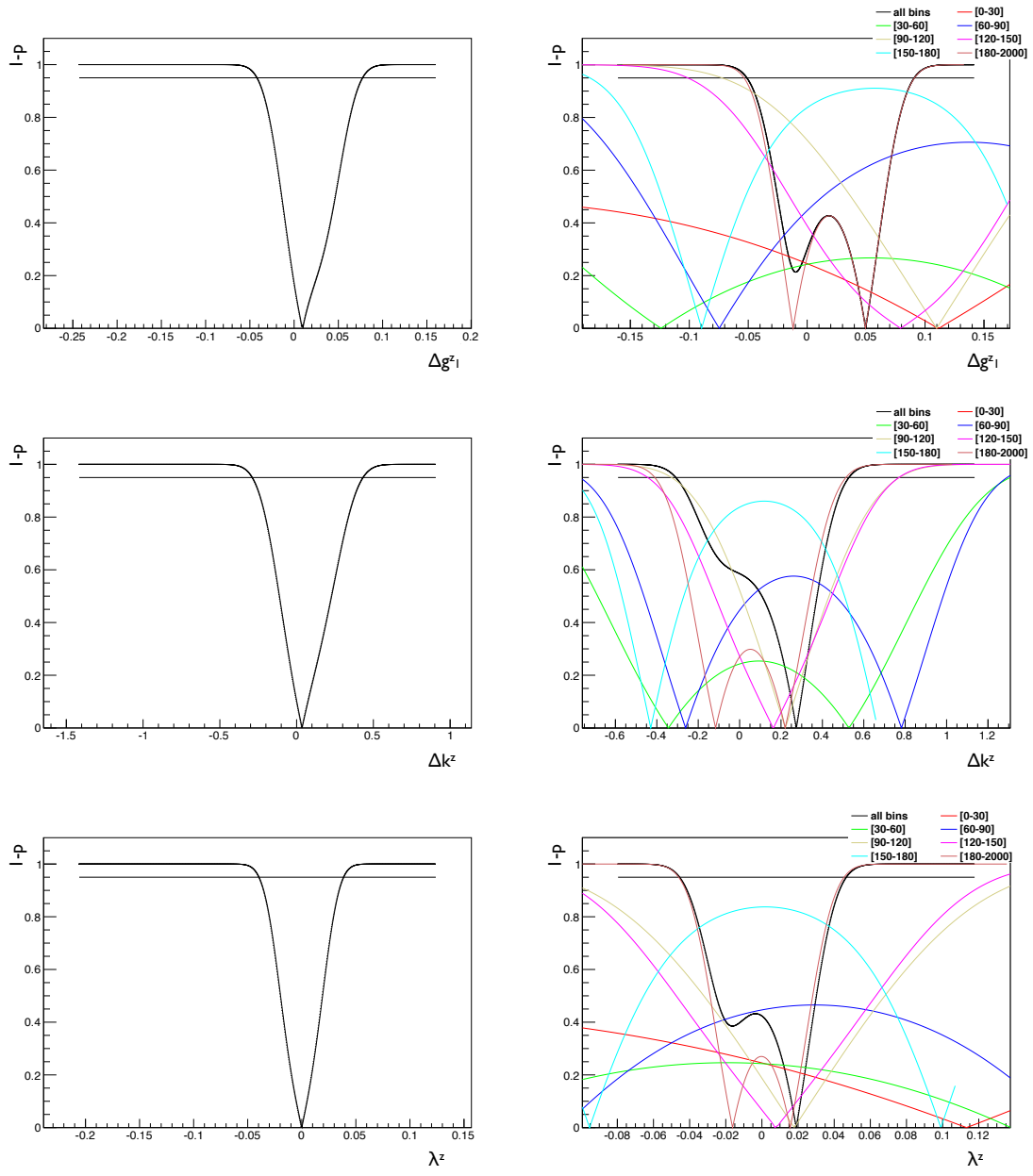

Figure 5.19: Using the profile log-likelihood approach, the $1-p$ distribution in function of each one of the anomalous couplings Δg_1^Z (top row), $\Delta\kappa^Z$(medium row), and λ^Z (bottom row) is shown. The expected limits for each coupling are on the left and the observed limits on the right, no cut-off scale used. The 95% C.I. limits are pointed by the horizontal line, the observed limit for each p_T^Z bin is shown in different colors, and also the combined fit result. The last bin [180-2000] in brown have the highest sensitivity to the presence of aTGC, this bin give us smallest limits and is the one driving the fit.

value. The limits in Table 5.23 were calculated using the frequentist approach, the ones on Tables 5.24 and 5.25 were calculated using the profile log-likelihood approach.

The expected and observed limits without form-factor shown in Table 5.24, correspond to the 95% C.I. limits are pointed by the horizontal line in Fig. 5.19. Since the last bin

	Observed 95% C.I. $\Lambda = 2$ TeV	Expected 95% C.I. $\Lambda = 2$ TeV	Observed 95% C.I. no cut-off	Expected 95% C.I. no cut-off
Δg_1^Z	[-0.075,0.134]	[-0.06,0.119]	[-0.058,0.093]	$[-0.046, 0.080]$
$\Delta\kappa^Z$	[-0.43,0.70]	[-0.38,0.58]	[-0.37,0.57]	[-0.33,0.47]
λ^Z	[-0.069,0.070]	[-0.059,0.059]	[-0.050,0.050]	[-0.042,0.043]

Table 5.23: Observed 1D 95% C.I. and expected 95% C.I. on the anomalous couplings Δg_1^Z, $\Delta\kappa^Z$, and λ^Z, calculated using the frequentist method.

	Observed 95% C.I. $\Lambda = 2$ TeV	Expected 95% C.I. $\Lambda = 2$ TeV	Observed 95% C.I. no cut-off	Expected 95% C.I. no cut-off
Δg_1^Z	[-0.063,0.130]	[-0.053,0.108]	[-0.051,0.091]	[-0.042,0.079]
$\Delta\kappa^Z$	[-0.34,0.65]	[-0.33,0.53]	[-0.31,0.53]	[-0.29,0.44]
λ^Z	[-0.062,0.065]	[-0.053,0.053]	[-0.045,0.047]	[-0.039,0.039]

Table 5.24: Observed 1D 95% C.I. and expected 95% C.I. on the anomalous couplings Δg_1^Z, $\Delta\kappa^Z$, and λ^Z, calculated using the profile likelihood method.

[180-2000] in brown have the highest sensitivity to the presence of aTGC, Table 5.25 shows the expected and observed limits extracted using only the information of this bin, as expected it gives the smallest limits and is the one driving the combined fit. Figure 5.20 compares the observed 1D limit obtained using the frequentist approach with the Tevatron results. ATLAS results are already competitive with those from the Tevatron.

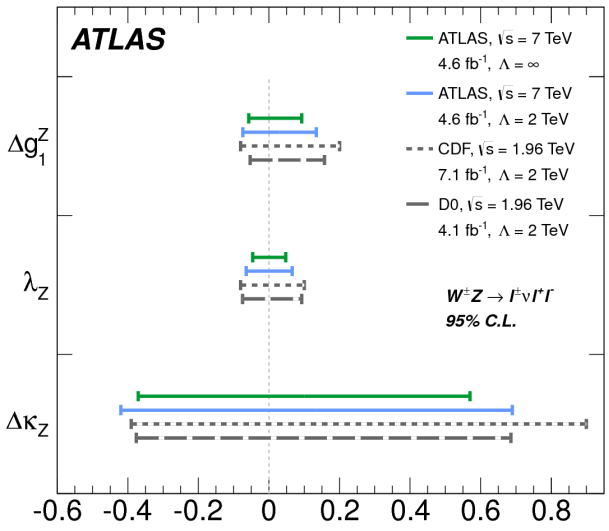

Figure 5.20: aTGC limits from ATLAS and Tevatron experiments. Luminosities, centre of mass energy and cut-off Λ for each experiment are shown and the limits are for 95% C.I.

	Observed 95% C.I.	Expected 95% C.I.
	no cut-off	no cut-off
Δg_1^Z	[-0.051,0.091]	[-0.041,0.077]
$\Delta\kappa^Z$	[-0.41,0.51]	[-0.35,0.45]
λ^Z	[-0.046,0.046]	[-0.040,0.039]

Table 5.25: Observed 1D 95% C.I. and expected 95% C.I. on the anomalous couplings Δg_1^Z, $\Delta\kappa^Z$, and λ^Z, calculated using the profile likelihood method and only the information of the last p_T^Z bin [180-2000] GeV.

The 95% C.I. for the 2D fitting scenario are shown as contours in Fig.s 5.21 and 5.22 with a 2 TeV cut-off scale and with no form factor $\Lambda \to \infty$ respectively. The 2D limits were obtained using the profile likelihood approach by fitting to parameter and setting the other aTGC parameter to the SM value.

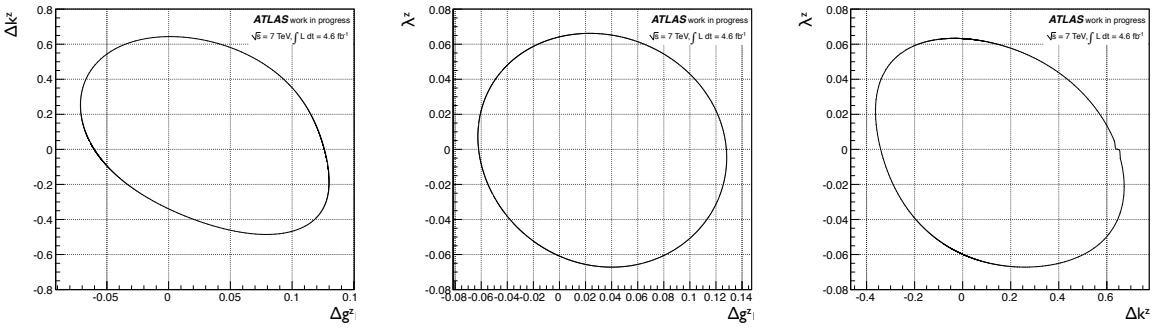

Figure 5.21: Observed 2D 95% Confidence Contours. The cut-off scale is 2 TeV, the limits shown with a thick line are calculated using the profile likelihood method.

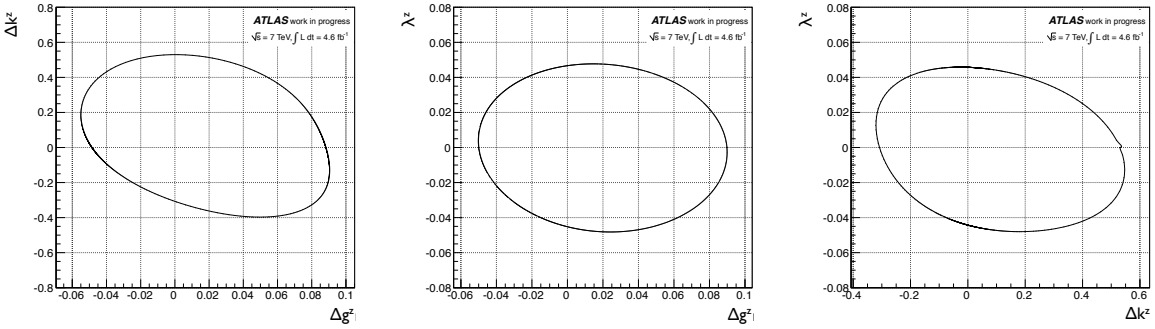

Figure 5.22: Observed 2D 95% Confidence Contours. No form-factor is used (equivalent to setting $\Lambda \to \infty$). The limits shown with a thick line are calculated using the profile likelihood method.

5.9 Conclusion

A measurement of the $W^{\pm}Z$ production cross-section using electrons and muons in the final state has been performed. In a dataset of proton-proton collisions at $\sqrt{s} = 7$ TeV with an integrated luminosity of 4.64 fb^{-1} a total of 317 candidates were observed with a background expectation of $68.1 \pm 2.1(\text{stat}) \pm 8.2(\text{sys})$. The Standard Model expectation for the number of signal events is $231.2 \pm 1.1(\text{stat}) \pm 7.8(\text{sys})$.

The combined fiducial and total cross-sections were determined to be

$$\sigma^{fid}_{WZ\to l\nu ll} = 92.31^{+6.66}_{-6.33}(\text{stat})\ ^{+4.31}_{-4.26}(\text{syst})\ ^{+1.85}_{-1.79}(\text{lumi})\ \text{fb}$$

$$\sigma^{tot}_{WZ} = 19.00^{+1.38}_{-1.30}(\text{stat})\ ^{+0.92}_{-0.90}(\text{syst})\ ^{+0.38}_{-0.37}(\text{lumi})\ \text{pb}$$

The precision of the measurement is dominated by the statistical uncertainty ($\sim 7\%$), while its systematic uncertainty accounts for $\sim 5\%$, and the luminosity $\sim 2\%$. Among the systematics errors the dominant one is the one coming from the data driven background estimation $\sim 4\%$, followed by the electron identification $\sim 1.6\%$. The theoretical errors in the total cross section $\sim$ 1.3%, are smaller than the experimental sources.

The result is in good agreement with the SM total cross section of $17.6^{+1.1}_{-1.0}$ pb calculated using MCFM [18].

Limits on the anomalous triple gauge couplings Δg_1^Z,$\Delta\kappa^Z$ and λ^Z, were extracted using the transverse momentum spectrum of Z bosons. The limits are compatible with the SM, and no sign of New Physics is observed. ATLAS and Tevatron limits are compatible and ATLAS results are already competitive. The WZ analysis using the 20 fb^{-1} of 8 TeV data is currently undergoing, the measurement will benefit greatly from increased size of the dataset and will provide much better limits on the anomalous triple gauge couplings and possibly surpass the Tevatron results. Nevertheless the aTGC studies will still be limited by statistics and this is a motivation for combination between the different channels, with CMS and to continue updating the analysis with the increasing integrated luminosity.

Chapter 6

$W^{\pm}Z$ Analysis at 8 TeV

For 2012 data taking, the LHC centre-of-mass energy was increased to 8 TeV. This results in an increase in both the signal cross section, of about 15%, and also the number of background events, depending on the process and reaching up to 68.5% for $t\bar{t}$ production. The LHC parameters during 2012 have resulted in an increase of the instantaneous luminosity delivered to ATLAS, with respect to the 2011 data taking. The higher luminosity was due in part to an increase in the number of protons per bunch. As a consequence the mean number of interactions per bunch crossing was also higher by approximately a factor of two, as shown in Fig. 6.1. The increase of this event pileup imposes stringent conditions on the trigger thresholds and affects the performance for identifying and measuring physics objects.

The $W^{\pm}Z$ cross section measurement presented in this chapter was made using 13 fb^{-1} of the 8 TeV data. As mentioned before, the data taking conditions were different for the 7 TeV and 8 TeV datasets; in order to cope with the new conditions, some changes in the analysis which were introduced are sumarized in Section 6.1. Nevertheless the analysis still follows the same general steps as in the cross section measurement described in Chapter 5.

The signature of the $W^{\pm}Z$ signal consist of three high transverse momentum (p_{T}), isolated leptons plus a significant amount of missing transverse energy ($E_{\mathrm{T}}^{\mathrm{miss}}$). A cut-based approach was chosen with a simple set of cuts. The cuts were based on those used for the 7 TeV analysis and adapted to the new conditions (see Section 6.3 for details).

The background estimation is described in Section 6.5. Both data driven methods and MC samples are used. Backgrounds with at least one fake lepton are estimated from data (fake leptons include pion, kaon, and heavy quark decays to real leptons in addition to jets that pass the lepton identification). The estimates are cross-checked with MC.

The acceptance is calculated using the MC simulation and thus it is important to know the level of agreement between the MC simulation and the data. We rely on measurements done by the trigger and combined performance groups for calculating the correction factors. Systematics related to each reconstructed physical object are discussed in Section 6.6.

The number of observed and expected events for the 8 TeV dataset as well as some

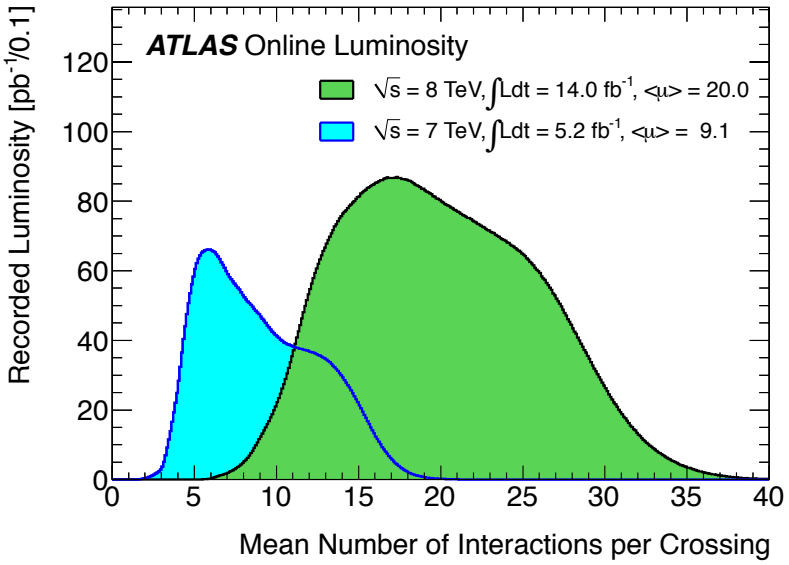

Figure 6.1: Luminosity-weighted distribution of the mean number of interactions per bunch crossing for the 2011 and 2012 data. This shows the full 2011 run and 2012 data taken between April and September. The integrated luminosities and the mean μ values are given in the figure. Details about how the mean number of interactions per crossing is calculated can be found in [63].

kinematic distributions are presented in Section 6.7. And finally, with all those inputs the cross section is calculated using a maximum likelihood technique to combine different decay channels. In Section 6.8, the cross section results are presented.

6.1 8 TeV analysis versus 7 TeV analysis

Some changes were made in the 8 TeV analysis compared to the 7 TeV analysis. The major changes are the following :

- $W^{\pm}Z$ **MC generator**: PowHeg replaced the MC@NLO generator.
- **Trigger**: the thresholds were increased to cope with the pile-up conditions.
- Z **selection for the electrons**: The electrons forming the Z candidate must satisfy the medium++ quality definition instead of loose++. This requirement reduces the Z+jets background.
- **Isolation**: the isolation for the leptons from the Z uses a cone of $\Delta R = 0.2$ and for the third lepton forming the W is tightened to a cone of $\Delta R = 0.3$. The smaller cone size for the Z allows to select high p_T Z, for which leptons are more collinear. At the same time the tight isolation for the W lepton ensures a good background rejection.
- ZZ **veto requirement**: reduces the background from ZZ; events with four or more leptons passing the selection criteria listed in Section 6.3 are discarded.

- **Background estimation**: new data driven methods are introduced to estimate the backgrounds from Z+jets and top ($t\bar{t}$ and single top).

6.2 Data and MC simulation samples

6.2.1 Data samples

The data samples corresponds to the data collected between April and September 2012, at $\sqrt{s} = 8$ TeV collisions. During these data taking periods, the instantaneous luminosity varied from about 10^{33} cm^{-2}s^{-1} to 6.8×10^{33} cm^{-2}s^{-1}. Figure 6.1 shows the distribution of the mean number of interactions per bunch crossing for the 2011 and the 2012 datasets. On average, the mean number of interactions per bunch crossing at 8 TeV is about twice the number at 7 TeV. The bunch-to-bunch time spacing has been kept at 50 ns in all data taking periods.

After the data-quality conditions, the integrated luminosity in the 8 TeV sample used in this analysis is estimated to be 13 fb^{-1}, with a relative uncertainty of 2.8% [65].

6.2.2 Monte Carlo samples

The $W^{\pm}Z$ production processes and subsequent pure leptonic decays were modeled by the POWHEG [94] generator. This MC generator uses a parton density function set CT10, which incorporates the next-to-leading-order (NLO) QCD matrix elements into the parton shower by interfacing to the PYTHIA [77] program.

As mentioned before in a $W^{\pm}Z$ selection, the major backgrounds come from jets associated with Z gauge bosons, diboson production of ZZ pairs, diboson production of a W or Z in association with a photon, and top events ($t\bar{t}$ and single top). The W/Z+jets is estimated using ALPGEN/JIMMY. The diboson processes WW, ZZ are modeled with MC@NLO, JIMMY [73] and POWHEGPYTHIA8 [94]. The $W/Z+\gamma$ is modeled with ALPGEN and SHERPA. MC@NLO, MADGRAPH and AcerMCPythia are used to model the $t\bar{t}$ and single top events. The different generators used to model the signal and the background are listed in Table 6.1. In appendix A, the full list of MC signal and background samples used for the 8 TeV analysis, including generator names, total number of MC events produced, k-factor, generator level filter efficiencies and corresponding cross sections are given.

The simulated beam spot in 2012 MC is too wide in the z-direction, this can have up to $\sim$2% effect on the electron. This can cause discrepancies in the rapidity related variables and in the estimation of the number of vertices, affecting then the track-cluster-matching (in η), the number of TRT hits and the isolation. In order to correct the z vertex position, MC events are reweighted in order to match the real data distribution.

To solve the differences of pileup as well as efficiency and resolution modeling, the same procedure as for the 2011 MC was followed. Including all these corrections to the MC, we make sure that the simulations correctly describe our data.

Process	Generator
$W^{\pm}Z \to \ell\nu\ell\ell$	PowhegPythia8
Z+jets$\to \ell\ell$+jets	Alpgen/Jimmy
$Z + b\bar{b}$+jets	Alpgen/Jimmy
Z+jets filter 10$< m_{\ell\ell} <$60 GeV	Alpgen/Jimmy
$W^{\pm}$+jets	Alpgen/Jimmy
$W^+W^- \to \ell\nu\ell\nu$	MC@NLO
$gg \to W^+W^- \to \ell\nu\ell\nu$	Jimmy
$ZZ \to \ell\ell\ell\ell$	PowhegPythia8
$gg \to ZZ \to \ell\ell\ell\ell$	PowhegPythia8
$Z\gamma$	Sherpa
$W\gamma$+jets	Alpgen/Jimmy
$t\bar{t} + W^{\pm}$	MadGraph
$t\bar{t} + Z$	MadGraph
$t\bar{t}$	MC@NLO
top t-channel$\to \ell$	AcerMCPythia
top s-channel$\to \ell$	MC@NLO

Table 6.1: MC samples/processes and generators used to model signal and backgrounds on the 8 TeV analysis.

6.3 $W^{\pm}Z$ selection

The requirements applied in the 8 TeV analysis follow the event selection in 2011, described in Section 5.2. But to cope with the increased pileup conditions some optimizations have been made; the 13 event selection steps are described below:

1. **Good Run List:** Events must be in the Good Run List (GRL), reflecting luminosity blocks with fully functional sub-detectors during data taking (data only).

2. **Trigger:** Single lepton triggers were used, but the transverse energy thresholds were increased with respect to the 7 TeV dataset. The threshold increase was done in order to reduce the event rate, and to cope with the high luminosity conditions. The single lepton triggers for the 8 TeV data require an isolated lepton with a p_T >24 GeV or an electron (muon) with p_T larger than 60 (36) GeV, with no isolation requirement.

3. **Primary vertex:** The primary vertex must be reconstructed using at least 3 good tracks.

4. **Lepton selection:** A similiar to 7 TeV analysis muon and electron selection was used in the 8 TeV analysis. The different thresholds used in this selection, for muon and electron isolation, and the impact parameter criterion, have been optimized to provide the best compromise between sensitivity and robustness of the analysis.

   Muon Selection: Basically the same muon selection as for the 7 TeV analysis is used: the muons must be reconstructed either Combined or Segment-Tagged, be inside the acceptance of the inner detector $|\eta| < 2.5$, and have p_T >15 GeV. Nevertheless, to cope with the increased pileup conditions, the number of required hits in each silicon sub-detector for each track was adapted [78]. The

changes with respect to the previous hit requirements are in the number of pixel hits, at least one hit in the pixels including the B-layer hit, and in the number of SCT hits at least five, including the number of crossed dead sensors.

To ensure that the candidates come from the primary vertex, the transverse impact parameter significance ($\frac{|d_0|}{\sigma_{d_0}}$) with respect to the primary vertex must be less than 3 and the absolute distance in the $z \times \sin(\theta)$-direction with respect to the primary vertex, $|z \times \sin(\theta)|$, to be within 0.5 *mm*.

Finally for the muon track isolation, the ΔR distance was reduced to 0.2, so the fraction ($\frac{p_T Cone20}{p_T}$) is asked to be less than 0.15. A smaller cone size was introduced in order to reduce the contribution to the isolation from pileup. Also the smaller cone size for the Z leptons allows to select high p_T Z, for which leptons are more collinear. A comparison of the muon selection criterias used in the 7 TeV and 8 TeV analysis is presented in Table 6.2.

Description	$\sqrt{s} = 7$ TeV	$\sqrt{s} = 8$ TeV
Reconstruction Combined or Segment-Tag staco muons	✔	✔
Kinematic Acceptance $p_T > 15$ GeV	✔	✔
Pixel B-layer hit $\geqslant 2$	✔	✔
Number of pixel hits	$N_{\text{pixel hits}} \geqslant 2$	$N_{\text{pixel hits}} \geqslant 1$
Number of SCT hits	$N_{\text{SCT hits}} \geqslant 6$	$N_{\text{SCT hits}} \geqslant 5$
Less than 3 holes in all silicon layers	✔	✔
$\|\eta\| < 1.9$, TRT hits + outliers $\geqslant 6$ and outliers/(outliers+hits) < 0.9.	✔	✔
$\|\eta\| > 1.9$, TRT hits + outliers > 6 and outliers/(outliers+hits) < 0.9.	✔	✔
Geometrical Acceptance $\|\eta\| < 2.5$	✔	✔
Longitudinal Impact parameter	$\|z_0\| < 1$ *mm*	$\|z_0 \times \sin(\theta)\| < 0.5$ *mm*
Transverse Impact parameter $\|d_0/\sigma_{d_0}\| < 3$	✔	✔
Track isolation	$\frac{p_T Cone30}{p_T} < 0.15$	$\frac{p_T Cone20}{p_T} < 0.15$

Table 6.2: Summary of the Muon definition used for the 7 TeV compared to the 8 TeV $W^{\pm}Z$ analysis.

Electron Selection: For this analysis the electrons are required to pass the egamma "*loose++*" electron identification requirements, must be reconstructed using a cluster with $|\eta| < 1.37$ or $1.52 < |\eta| < 2.47$, and to have $E_{\mathrm{T}} > 15$ GeV.

The electrons must also come from a primary vertex, in order to ensure that, the candidates have a requirement on the longitudinal distance with respect to the primary vertex $|z_0 \times \sin(\theta)| < 0.5$ *mm* and the tranverse impact parameter significance d_0 must be less than 6.

The final electron requirement applied is the isolation calorimetric and track-based. The transverse energy or momenta deposited in a cone in $\Delta R = 0.2$ around the electron candidate was used. The different choice of cone size with respect to the 7 TeV analysis is mainly motivated by the increased pileup conditions, a smaller cone size providing good rejection power and being less sensitive to the fake contribution from pileup events. Also the smaller cone size for the Z allows to select high p_T Z, for which leptons are more collinear.

The track-based isolation must be less than 13% of the electron candidate p_{T}. The calorimeter isolation must be less than 14% of the electron candidate E_{T}. For the 8 TeV analysis, calorimeter topological cluster were used. A summary of the electron requirements for the 7 TeV and 8 TeV analyses is presented in Table 6.3.

Description	$\sqrt{s} = 7$ TeV	$\sqrt{s} = 8$ TeV
Identification Criteria loose++	✔	✔
Kinematic Acceptance $p_T > 15$ GeV	✔	✔
Object Quality : outside regions with LAr readout problems (OTx/OQ flag)	✔	✔
Geometrical Acceptance $\|\eta\| < 1.37$ or $1.52 < \|\eta\| < 2.47$	✔	✔
Longitudinal Impact parameter	$\|z_0\| < 1\ mm$	$\|z_0 \times \sin(\theta)\| < 0.5\ mm$
Transverse Impact parameter	$\|d_0/\sigma_{d_0}\| < 10$	$\|d_0/\sigma_{d_0}\| < 6$
Track isolation	$\frac{p_T Cone30}{p_T} < 0.13$	$\frac{p_T Cone20}{p_T} < 0.13$
Calorimeter isolation $\frac{E_T Cone30}{E_T} < 0.14$	✔	
Topocluster isolation $\frac{topoE_T Cone20}{E_T} < 0.14$		✔

Table 6.3: Summary of the Electron definition used for the 7 TeV and 8 TeV $W^{\pm}Z$ analyses.

5. **Overlap removal** As in the 2011 analysis, objects are removed from the event using ΔR overlap criteria to avoid double counting, electrons are removed if they are within $\Delta R < 0.1$ of any selected muon; if two selected electrons overlap within $\Delta R < 0.1$, the lower-p_{T} electron is removed; and the jets within $\Delta R < 0.3$ of any selected muon or electron are removed.

6. $E_{\mathrm{T}}^{\mathrm{miss}}$ **cleaning** Jets with $\mathrm{p}_T > 20$ GeV are tested for the "looser bad" jet criteria. If any of the aforementioned jets is tagged as "looser bad", the event is rejected. These criteria assess the quality of jets by examining some of the common sources of spurious or out-of-time energy in the calorimeters.

7. **Event cleaning: LAr/Tile noise and corrupted events** Events with Liquid Argon or Tile Calorimeter data integrity errors are vetoed. During the 2012 data-taking when a sub-detector was recovering from a busy condition, events where saved with some detector information missing, there is also a special flag used to detect and remove those corrupted events.

8. ZZ **veto**: The ZZ events in which both Z bosons decay leptonically are a major background to the $W^{\pm}Z$ signal. A fully leptonic ZZ event will have four real leptons that can pass the lepton selection. For a ZZ event to pass the $W^{\pm}Z$ selection, the event must have large $E_{\mathrm{T}}^{\mathrm{miss}}$. The source of this $E_{\mathrm{T}}^{\mathrm{miss}}$can be mismeasured jets or a lepton from a Z decay outside the fiducial acceptance of the detector. In order to decrease this background in the 8 TeV analysis, events with four or more leptons passing the selection criteria previously described are discarded.

9. Z **candidate**: The event must have two leptons of the same flavor and opposite charge, with an invariant mass that is consistent with the Z mass : $|M_{ll} - 91.1876| <$

10 GeV. If more than one pair of leptons form a Z candidate, as can be the case in the $\mu\mu\mu$ and eee channels, the candidate with invariant mass closest to the Z PDG mass (91.1876 GeV) is taken. In order to reduce the posibility of mispairing, the identification quality is tightened, requiring the electrons forming the Z to satisfy the $medium++$ quality definition.

10. **Third lepton**: The lepton that is not associated with the Z boson candidate must satisfy the combined (tight++) quality definition for muons (electrons). The third lepton must have $p_{\mathrm{T}} > 20$ GeV and satisfy the same relative isolation requirement but in a cone of $\Delta R = 0.3$.

11. **Missing transverse energy**: The $E_{\mathrm{T}}^{\mathrm{miss}}$ in the event must be larger than 25 GeV.

12. **W transverse mass**: The transverse mass of the system (lepton identified as coming from $W^{\pm}$and $E_{\mathrm{T}}^{\mathrm{miss}}$) must be larger than 20 GeV.

13. **Trigger matching**: One of the offline reconstructed muons or electrons associated with the W or Z decay, and with p_{T} at greather than 25 GeV (for both muons and electrons), must match the online reconstructed muon (electron) that triggered the event.

6.4 Event Selection

The expected signal and background contributions to the final sample are modeled either with MC simulation or data-driven methods.

Using the set of cuts described above, the expected number of events in the 8 TeV sample ($\mathcal{L} = 13$ fb^{-1}) selected after each cut for the $W^{\pm}Z$ MC signal, with all corrections applied, are summarized in Table 6.4. At each step, the number of events is shown for each considered channel. In addition the relative acceptance of each cut are given in Table 6.5.

Cutflow 8 TeV	Events			
	eee	$ee\mu$	$\mu\mu e$	$\mu\mu\mu$
All	32274.4			
Muon or electron trigger	12943.5			
Primary vertex	12906.0			
$E_{\mathrm{T}}^{\mathrm{miss}}$ cleaning	12892.3			
ZZ veto	12889.9			
Z candidate	801.33		1034.48	
Three leptons	196.94	254.67	263.07	343.09
$E_{\mathrm{T}}^{\mathrm{miss}}$ cut	156.32	209.22	210.77	283.03
$W^{\pm}M_T$ cut	146.25	198.98	196.55	266.40
Trigger match	146.25	198.88	196.10	264.91
Scale factors	137.21	188.81	190.63	259.97

Table 6.4: Expected number of MC events after each cut for $W^{\pm}Z \to \ell\nu\ell'\ell'$ for $\mathcal{L} = 13$ fb^{-1}. Boson decays to τ's are not included.

Cutflow 8 TeV	Acceptance %			
	eee	$ee\mu$	$\mu\mu e$	$\mu\mu\mu$
All	100.0			
Muon or electron trigger	40.10			
Primary vertex	99.71			
$E_{\mathrm{T}}^{\mathrm{miss}}$ cleaning	99.89			
ZZ veto	99.98			
Z cut	6.22		8.03	
Three leptons	24.58	31.78	25.43	33.17
$E_{\mathrm{T}}^{\mathrm{miss}}$ candidate	79.38	82.15	80.12	82.50
$W^{\pm}M_T$ cut	93.56	95.11	93.25	94.12
Trigger match	100.0	99.95	99.77	99.44
Scale factors	93.82	94.93	97.21	98.14

Table 6.5: Relative acceptance of MC events after each cut for $W^{\pm}Z \to \ell\nu\ell'\ell'$ for $\mathcal{L} = 13$ fb^{-1}. Boson decays to τ's are not included.

Cutflow 8 TeV	Events			
	eee	$ee\mu$	$\mu\mu e$	$\mu\mu\mu$
All	9493.14			
Muon or electron trigger	2883.26			
Primary vertex	2878.16			
$E_{\mathrm{T}}^{\mathrm{miss}}$ cleaning	2870.56			
ZZ veto	2870.18			
Z cut	393.12		495.59	
Three leptons	13.11	17.39	16.59	25.34
$E_{\mathrm{T}}^{\mathrm{miss}}$ candidate	10.82	14.38	13.69	21.21
$W^{\pm}M_T$ cut	7.10	10.78	10.03	16.52
Trigger match	7.10	10.78	9.99	16.32
Scale factors	6.63	10.23	9.66	15.96

Table 6.6: Expected number of MC events after each cut for $W^{\pm}Z \to \ell\nu\ell'\ell'$, where at least ℓ or ℓ' is a τ going to μ or e, for $\mathcal{L} = 13$ fb^{-1}.

As expected the absolute acceptance increases with the number of muons in the final state because the reconstruction efficiency for muons is higher than for electrons. The contribution from $W^{\pm}Z \to \ell\nu\ell'\ell'$, where at least ℓ or ℓ' is tau, is dominated by $W^{\pm}Z \to \tau\nu\ell'\ell'$ where the τ decays into an electron or a muon. This contribution of the order of 5% is added to the signal for the cross-section extraction; the cutflow for this MC sample is shown in Table 6.6.

6.5 Background Estimation

The expected background yield is estimated using MC simulation normalized to the theoretical cross section for ZZ and $W/Z+\gamma$ production and using data-driven methods for the Z+jets and $t\bar{t}$ processes. The techniques and results used for the background estimation are presented in the following sections.

6.5.1 MC-based Estimations

The ZZ, $W/Z+\gamma$, WW and $t\bar{t}$+V ($V = Z, W$) are estimated using the generated MC samples and the previously described selection criteria (Sec 6.3). Table 6.7 summarizes the expected background event yields from MC estimations, at the end of the cut flow. The contribution of WW and $t\bar{t}$+V samples were found negligible and are not included in the Table. The yields were normalized to a luminosity of 13 fb^{-1}. The first error on the yields is statistical and the second error is the systematic. The systematic error includes the uncertainties on theoretical cross-sections used to normalize the MC samples (see table 5.9), and the uncertainties for each object used in the event reconstruction. These values, with the corresponding uncertainties, are included in the background estimation for the cross-section calculation.

8 TeV MC Sample	Events			
	eee	$ee\mu$	$e\mu\mu$	$\mu\mu\mu$
$W/Z+\gamma$	13.4±3.0±0.8	1.3±0.6±0.1	17.2±3.2±0.9	–
ZZ	10.3±0.2±0.6	14.7±0.3±0.8	12.8±0.2±0.7	18.8±0.2±1.0

Table 6.7: Expected number of events passing all 8 TeV selection cuts for signal and MC based background estimation, normalized to an integrated luminosity of $\mathcal{L} = 13$ fb^{-1}. The first error is statistical while the second is systematic.

6.5.2 Data-Driven Estimations

For the 8 TeV analysis, new data driven methods were developed. The new methods are more robusts against systematics problems that affected the previous methods used in the 7 TeV analysis.

Among the systematic problems affecting the data driven estimation described in Section 5.4.2:

- The control regions were defined using the $E_{\mathrm{T}}^{\mathrm{miss}}$ requirements. However the low $E_{\mathrm{T}}^{\mathrm{miss}}$ region is not well understood, data/MC discrepancies could lead to an overestimation of the background.

- The requirement on the W transverse mass is applied in the low $E_{\mathrm{T}}^{\mathrm{miss}}$ region; forcing then p_T of the W lepton to be high to compensate. The control region will then be enriched in high p_T leptons and will not cover all the p_T spectrum of our signal.

- The control regions contain an important contamination of signal events, that could go up to 40% in some regions.

The following sections describe the new techniques and the checks performed in different control regions of data. The Z+jet and top ($t\bar{t}$ and single top) are the main contributions in the signal region from backgrounds with at least one "fake" lepton. The general

Figure 6.2: Data Driven principle. A Control Region enriched with background is built the amount of background in this region is estimated. Then Transfer Factor from the Control Region to the Signal Region is defined, and used to estimate the Final Yield.

concept of the data driven techniques used for backgrounds containing jets, is illustrated in Fig. 6.2. The idea is to build background enriched Control Regions (CR) by reversing analysis cuts (ex. isolation, $E_{\mathrm{T}}^{\mathrm{miss}}$, impact parameter significance). The background is estimated in the control region. The final yield is obtained by extrapolating from the control region to the signal region using a Transfer Factor (TF).

Since the background sources for electrons and muons are of different nature, the $Z + \mu$ and the $Z + e$ processes, are studied separately. In the case of a "fake" muon, the contribution is estimated using a sideband fit to the m_{ll} distribution in a Z+jet and top enriched control region, subsequently a tranfer factor obtained from MC is used to extrapolate to the signal region. An alternative method was implemented using a $e^{\pm}\mu^{\mp}+\mu$ control region, to cross check the top results obtained with the sideband fit.

To estimate the amount of background with at least one "fake" electron, we used the matrix method. A control region enriched with W+jet events was defined to estimate the probability of a jet faking a lepton. The various control samples and resulting background estimations will be discussed in the following sections.

6.5.3 Estimation of the background in the $Z + \mu$ final states

1. **Estimate of the $t\bar{t}$ background using the $e^{\pm}\mu^{\mp} + \mu$ control region :**

   In the $W^{\pm}Z$ selection, opposite charge same flavor dilepton pairs are selected, in order to form a Z boson. The control region must be enriched with $t\bar{t}$ events,

and is therefore constructed by selecting events with an $e^{\pm}\mu^{\mp}$ dilepton pair, with an invariant mass in a window of 10 GeV around the Z PDG mass ($m_Z = 91.1876$ GeV), and one additional muon.

In order to avoid Z contamination, events $e^{\pm}\mu^{\mp} + \mu$ in which the pair of muons have opposite charge and m_{ll} is within 10 GeV from m_Z are eliminated from the selection. The leptons in the $e^{\pm}\mu^{\mp}$ pair must satisfy all the good lepton requirements usually used for Z identification. For the additional muon (the one usually associated with the W) no isolation requirements or impact parameter criteria are applied, but all the other W selection criteria are applied. In Fig. 6.3, the corresponding $e^{\pm}\mu^{\mp}$ dilepton pair invariant mass distributions is presented. The distribution is flat and dominated by top events as expected. The contamination from other backgrounds (Z+jets, $Z+\gamma$, ZZ, WW and WZ) is small (less than 10%) and is subtracted using MC. In Table 6.8 the observed and expected yields in this control region are presented for 13 fb^{-1}, the last row of the table corresponds to the data after subtracting the contamination from other backgrounds.

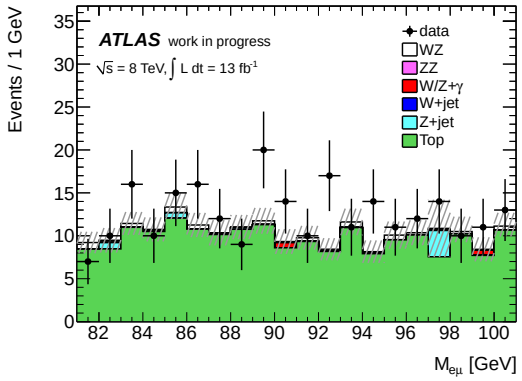

Figure 6.3: Distribution of the $e^{\pm}\mu^{\mp}$ dilepton pair invariant mass for data and corresponding MC for $Z + \mu$ channels. The statistical uncertainty is shown by shaded bands.

Table 6.8: Composition of the $e^{\pm}\mu^{\mp}$ control region, the errors are statistical. The contamination from other backgrounds (Z+jets, $Z + \gamma$, ZZ, WW and WZ) is subtracted from data using MC, the result is presented in the last row of the table.

Data	254
$t\bar{t}$ MC	195.9 ± 6.2
Z+jets MC	4.6 ± 3.2
$Z + \gamma$ MC	1.4 ± 0.9
ZZ MC	0.66 ± 0.05
WW MC	0.51 ± 0.26
WZ MC	6.4 ± 0.7
Data - MC contamination	240.4 ± 16.3

Extrapolation to the signal region To estimate the amount of $t\bar{t}$ events in the signal region, the number of events in the control region is extrapolated using

a transfer factor obtained from $t\bar{t}$ MC simulation. The transfer factor presented in Equation. 6.1 is built using the ratio of the corresponding yields in the control region of $ee\mu$ and $\mu\mu\mu$ events to the $\mu e\mu$ yield, and the efficiency of the isolation and impact parameter requirements (since these two selection criteria were relaxed on the additional muon to build the control region).

$$f_{\text{transfer}} = \frac{N^{\mu\mu\mu/ee\mu}}{N^{\mu e\mu}} \times \epsilon_{iso} \times \epsilon_{d_0} \tag{6.1}$$

Since the tranfer factor is estimated using MC simulations, it is important to verify that the $t\bar{t}$ MC correctly describes the efficiencies used. Figure 6.4 compares the efficiency of the isolation and impact parameter significance in data and MC. The efficiency of these two variables is derived for the additional muons in the $e^{\pm}\mu^{\mp} + \mu$ control region. The efficiency is calculated as the number of muons passing the isolation and the impact parameter significance requirements over the total number of events. The efficiencies calculated in data and MC are in good agreement as illustrated in Fig. 6.4. The difference between data and MC (up to 10%) is taken into account in the systematics.

Final result Table 6.9 summarizes the different ingredients used in the transfer factor computation. And, the final expectations in the signal region are given in Table 6.10. These are computed from the product of the $t\bar{t}$ with $(e\mu)\mu$ from Table 6.8 and the transfer factors. The systematic uncertainty on the final yields originates from the difference between data and MC efficiencies and also take into account the statistical error on the transfer factor.

Table 6.9: The transfer factor decomposition, the errors are statistical.

	$\mu\mu\mu$	$ee\mu$
$\frac{N^{\ell\ell\mu(\ell=e,\mu)}}{N^{\mu e\mu}}$	0.561 ± 0.030	0.462 ± 0.026
ϵ_{d_0}	0.525 ± 0.009	
ϵ_{iso} after ϵ_{d_0} cut	0.169 ± 0.007	
$f_{\text{transfer}} = \frac{N^{\mu\mu\mu/ee\mu}}{N^{\mu e\mu}} \times \epsilon_{iso} \times \epsilon_{d_0}$	$(4.96 \pm 0.35).10^{-2}$	$(4.08 \pm 0.30).10^{-2}$

Table 6.10: Estimated number of $t\bar{t}$ events in the signal region using the $e^{\pm}\mu^{\mp}$ method.

	$\mu\mu\mu$	$ee\mu$	Total
Top from data	$11.9 \pm 0.8 \pm 2.2$	$9.8 \pm 0.7 \pm 1.8$	$21.7 \pm 1.0 \pm 2.8$
Top from MC	7.1 ± 1.3	6.3 ± 1.0	13.4 ± 1.6

2. **Estimate of the Z+jets and Top background using sideband fit** The main idea is to perform a fit to measure the Z+jets and top-quark ($t\bar{t}$ and single top)

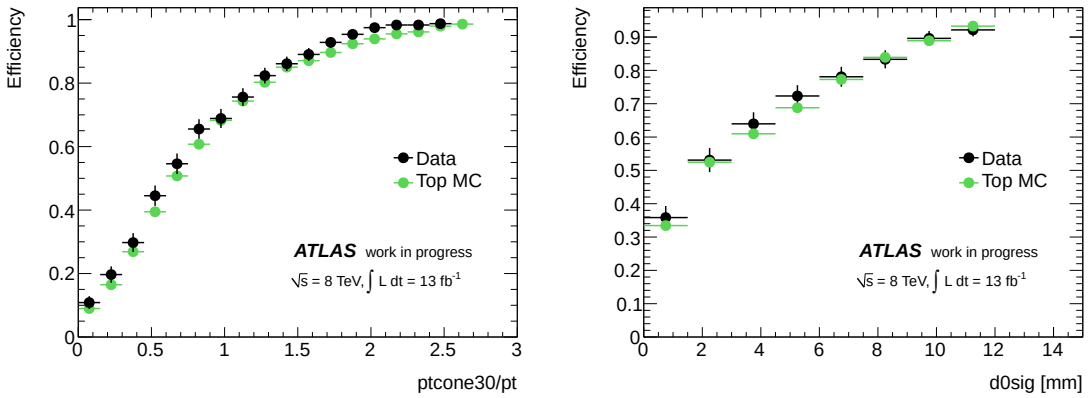

Figure 6.4: Distribution of isolation and IP significance efficiencies in the $t\bar{t}$ control region defined using the $e^{\pm}\mu^{\mp}$ selection as described in the text. The analysis cut on isolation is 0.15 and 3 for the d_0 significance.

backgrounds at the same time. This method is extensively discussed in Ref. [95]. As mentioned before both Z+jets and top events contain two real leptons plus an additional "fake" lepton. In the first case, the fake leptons arise either from decays of hadrons with b or c-quark content or from misidentified light jets. In the second case, as seen in the previous section, each top quark decays to a W boson and a b quark.

The amount of top and Z+jets backgrounds can be estimated using a control region with enhanced hadronic jet contribution. In this region the cut on the Z invariant mass is relaxed, in order to have larger sidebands around the peak. Thus the invariant mass of the opposite charge and same flavor di-leptons, will have a peak at the Z-mass due to Z+jets along with a flat distribution of top events. The estimated number of Z+jets events in the control region can then be extrapolated to the signal region using a transfer factor obtained from MC which has been verified with data.

The control region is defined by applying all the $W^{\pm}Z$ analysis selection cuts except, for the muon coming from the W, that no isolation requirement is applied and the impact parameter significance cut is reversed to remove the ZZ contributions. Figure 6.5 illustrates the composition of this control region: as expected the sideband regions are dominated by top events and the peak at the Z-mass is dominated by Z+jets background. This particular shape lead us to estimate the top and Z + jets backgrounds using a second order Chebychev polynomial for the top component, and a Breit-Wigner line-shape convoluted with a Crystal-Ball resolution function for the Z + jets component. The data/MC discrepancies seen in Fig. 6.5, can be explained by the predicted Z+jets in the MC. This is the main reason why a data driven method is used to estimate this background contribution.

In order to test the validity of the fit, a "closure test" using simulated samples was

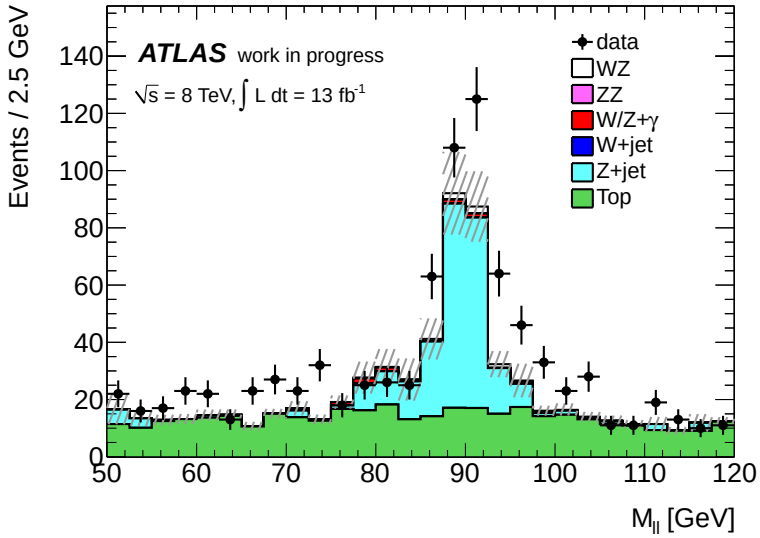

Figure 6.5: Distribution of opposite charge and same flavor di-lepton invariant mass in the control region, where the isolation requirement is not applied to the muon coming from the W, and the impact parameter significance requirement is reversed. In this plot the $Z \to ee$ and $Z \to \mu\mu$ channels are summed together.

performed. In Fig. 6.6 the result of the fit performed on the MC distribution for the $ee\mu$ and $\mu\mu\mu$ channels separately are presented. The input events of top and Z+jets as well as the results of the fit are given in the Table 6.11. The fit results and the input MC background are compatible, whithin uncertainties.

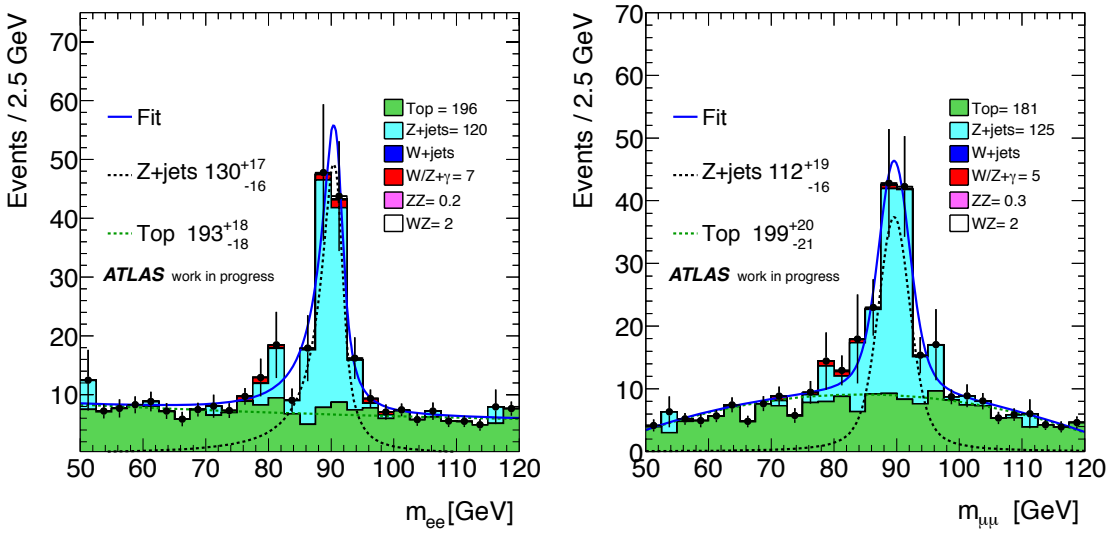

Figure 6.6: Monte Carlo distribution of opposite charge and same flavor di-lepton invariant mass in the control region for closure test. The two decays channels are shown separately $ee\mu$ (left) and $\mu\mu\mu$ (right) channel. The fit used to obtain the yields for top and Z + jets is presented. The MC input events of top and Z+jets are given in the legend for comparison and the results of the fit on MC are given near the dashed lines.

Table 6.11: Closure test results, the amount of top and Z+jets events is estimated using the sideband fit on the MC samples. The fit results and the input MC background are compatible.

	$\mu\mu\mu$	$ee\mu$
Z+jet from fit	112^{+19}_{-16}	130^{+17}_{-16}
Z+jet from MC	125 ± 17	120 ± 18
Top from fit	199^{+20}_{-21}	193^{+18}_{-18}
Top from MC	181 ± 6	195 ± 7

To fit the data distribution the input parameters are obtained from the closure test, and are allowed to fluctuate within 10% of their nominal values. In Fig. 6.7, the results of the fit on data for the two channels $ee\mu$ and $\mu\mu\mu$ are presented. The small contamination from the signal and other electroweak processes are subtracted.

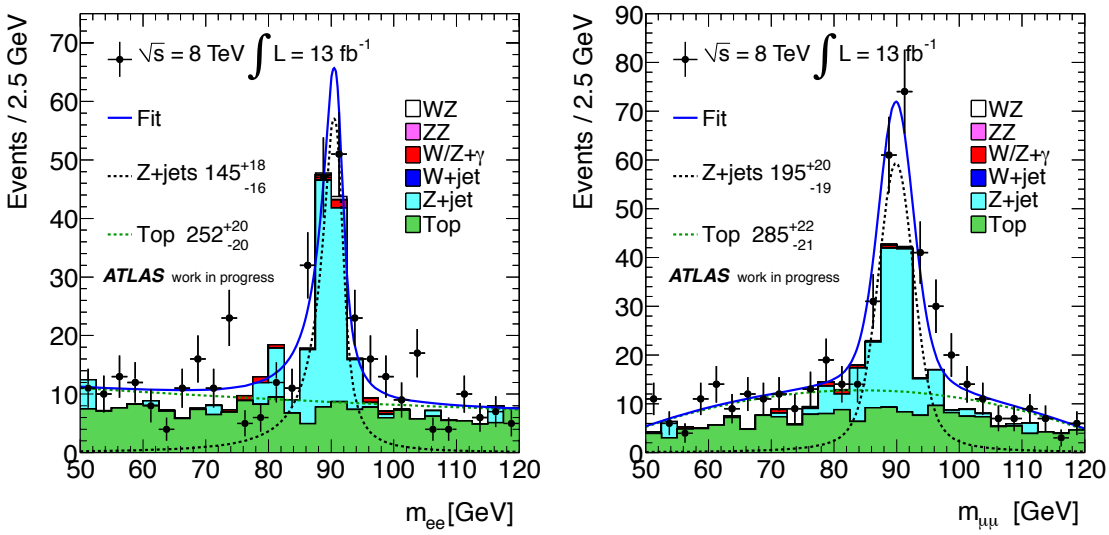

Figure 6.7: Data and MC distributions of opposite charge and same flavor di-leptons in the control region for the $ee\mu$ (left) and $\mu\mu\mu$ (right) channel. The fit used to obtain the yields from data for top and Z + jets is presented and the results of the fit on data are given near the dashed lines.

Template fit : As a cross-check to the sideband fit results, a template fit was performed as shown in Fig. 6.8. The shape templates for the Z+jets and top are obtained from MC. The yields are calculated by fitting templates to data. Table 6.12 shows the obtained yiels for the two methods. The results obtained with the template are compatible with those estimated from the sideband fit with a parametrization. Although due to the lack of the MC statistics, it is difficult to build smooth templates from the MC, so the sideband fit result is chosen as baseline.

Once the top and Z+jets contributions have been estimated in the control region, they can be extrapolated to the signal region using a transfer factor. The transfer factor is obtained from MC and has been verified with data [95].

Table 6.12: Results for Z+jets and top background contributions in the control region. The yields are estimated using the sideband fit and the template fit .

	$ee\mu$	$\mu\mu\mu$
Z+jet from sideband fit	145^{+18}_{-16}	195^{+20}_{-19}
Z+jet from template fit	134^{+16}_{-15}	209^{+19}_{-16}
Top from sideband fit	252^{+20}_{-20}	285^{+22}_{-21}
Top from template fit	263^{+20}_{-19}	271^{+23}_{-22}

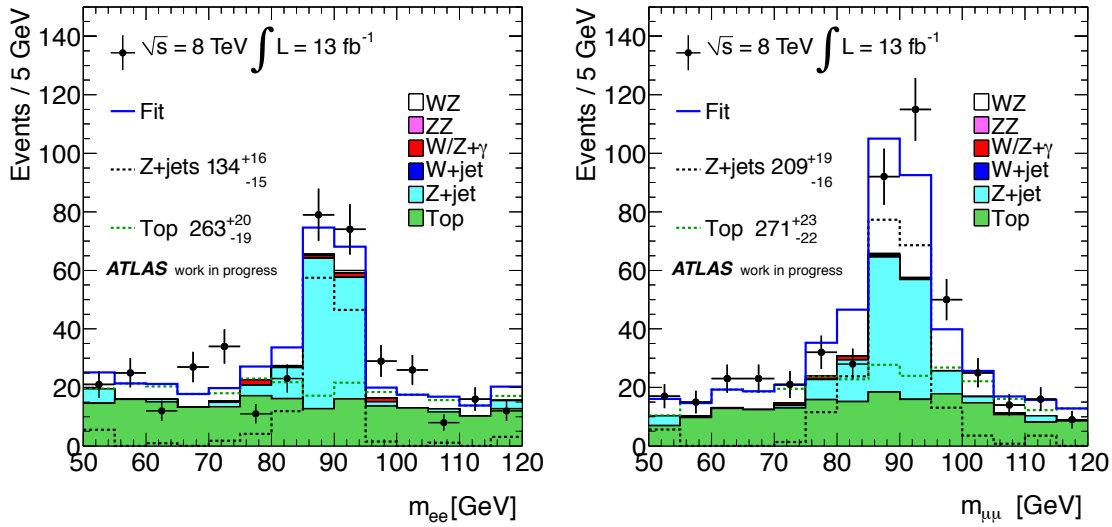

Figure 6.8: Distribution of opposite charge and same flavor di-leptons invariant mass in the control region for the $ee\mu$ (left) and $\mu\mu\mu$ (right) channel. The template fit used to obtain the yields from data for top and Z + jets is presented, and the results of the fit on data are given near the dashed lines.

Extrapolation to the signal region In order to estimate the amount of background in the signal region, we need to extrapolate the yields obtained using the sideband fit in the control region. Since we enlarge the Z mass window cut to built the control region, the first step is to integrate the yields in this 10 GeV window around the Z mass ($|m_{ll} - 91.1876| < 10$ GeV), then a transfer factor obtained from the MC is used. Two methods are used: in the first, the transfer factor is calculated as the ratio of the MC expectation in the signal region to the control region:

$$f_{\text{transfer}} = \frac{N_{SR}}{N_{CR}} \tag{6.2}$$

In the second method we consider the efficiency of the two cuts used to built the control region, the following formula is used:

$$f_{\text{transfer}} = \frac{\epsilon_{iso} \times \epsilon_{d_0}}{(1 - \epsilon_{d_0})} \tag{6.3}$$

where ϵ_{d_0} and ϵ_{iso} are the p_{T}-dependent efficiencies for the muon coming from the W to satisfy the impact parameter significance and the isolation selection criteria. In Table 6.13, the transfer factors computed using the two methods are presented. The p_{T}-dependence of the efficiencies is taken into account in the calculation.

Table 6.13: Transfer factors for top and Z+jets obtained from the MC and used for the extrapolation from the control region to the signal region. The errors on the transfer factors are statistical.

Transfer factor f_{transfer}	$f_{\mathrm{transfer}} = \frac{\epsilon_{iso} \times \epsilon_{d_0}}{(1-\epsilon_{d_0})}$	$\frac{N_{SR}}{N_{CR}}$
Z+jets	0.29 ± 0.03	0.26 ± 0.07
Top	0.14 ± 0.01	0.10 ± 0.02

However, since the transfer factor is calculated using simulation, it is important to verify that the Z+jets and top MC correctly describe the variables involved in the extrapolation namely isolation and impact parameter significance requirements on muons.

To test the top MC, we built a control region enriched with top events, using the $e^{\pm}\mu^{\mp}\mu$ control region described previously. The isolation and impact parameter significance efficiencies are shown in Fig. 6.4 where good agreement between data and MC is observed.

Another control region enriched in Z+jets events is formed by reversing the W transverse mass ($M_T^W < 20$ GeV) cut applied in the WZ analysis selection and where no isolation or impact parameter significance requirement are applied to the muon coming from the W. The diboson contamination in this control region is subtracted using MC. Figure 6.9 compares the efficiency of these two variables in data and in MC, where a good agreement is found.

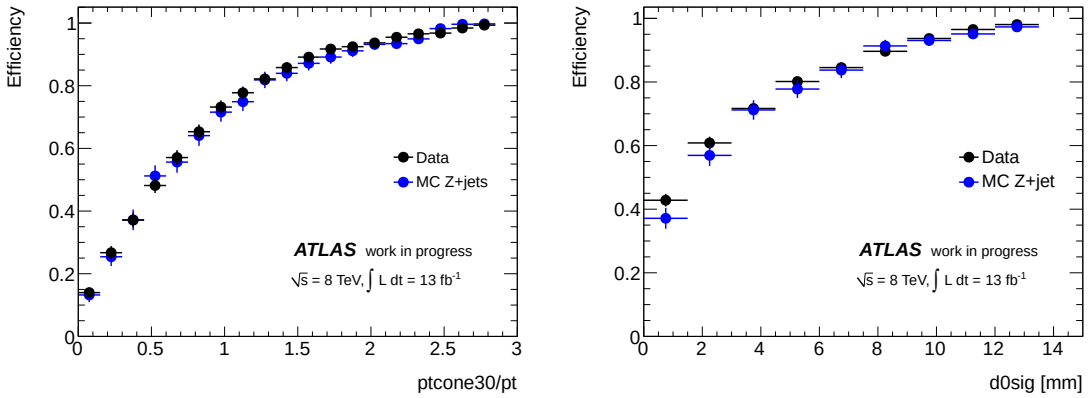

Figure 6.9: Distribution of isolation and IP significance efficiencies in the Z+jets control region defined in the text.

Final results The final estimated numbers of top and Z+jets events in the signal region are given in Table 6.14 using the transfer factor of Eq. 6.2. The systematic

uncertainties are calculated taking into account the statistical error on the transfer factor and the discrepancies between the two transfer factor methods. The top background estimated with this method is compatible with the one obtained with the $e^{\pm}\mu^{\mp}+\mu$ control region. Since this method allows both the Z+jets and top-quark background to be determined simultanously, this method is chosen as the baseline for the analysis.

Table 6.14: Estimated numbers of top and Z+jets events in the signal region using the sideband method.

	$\mu\mu\mu$	$ee\mu$	Total
Z+jets from data fit	$46.8 \pm 4.8 \pm 14.3$	$32.8 \pm 3.9 \pm 10.2$	$79.6 \pm 6.2 \pm 17.5$
Z+jets from MC	34.9 ± 9.0	19.7 ± 8.9	54.6 ± 12.7
top from data fit	$9.1 \pm 0.7 \pm 4.9$	$6.3 \pm 0.5 \pm 3.4$	$15.4 \pm 0.9 \pm 6.0$
top from MC	7.1 ± 1.3	4.3 ± 0.8	11.4 ± 1.6

6.5.4 Estimation of the background in the $Z + e$ final states

The matrix method is used in the $Z + e$ channels. It allows us to measure the combined contribution of Z+jets and top-quark events ($t\bar{t}$ and single top) entirely from data. Those background events will contain two "real" prompt leptons plus a "fake" non-prompt electron coming mainly from misidentified jets.

As illustrated in Fig. 6.10, in a data sample there are "real" and "fake" electrons, the $W^{\pm}Z$ selection uses a set of requirements to identify the "real" leptons in the data sample. Using those selection requirements two groups of events can be defined:

- **Tight-cut sample (N^{tight})** : events passing all signal extraction cuts ($W^{\pm}Z$ selection)

- **Loose-cut sample (N^{loose})** : events passing all selection cuts, except for the isolation cuts and the electron identification requirement on the W daughter lepton.

So the tight events are actually a subset of loose events that pass additional quality requirements. However, as illustrated in Fig. 6.10, there may be "fake" electrons that are able to pass all the selection requirements, and are considered as part of the tight selection ($N^{\text{tight}}_{\text{fake}}$), this contribution need to be quantified.

The number of events in the tight and loose samples (N^{tight} and N^{loose}) can be broken down into contributions from "real" electrons produced in W and Z decays, and "fake" electrons from all other sources:

$$N^{\text{loose}} = N^{\text{loose}}_{\text{real}} + N^{\text{loose}}_{\text{fake}}, \tag{6.4}$$

$$N^{\text{tight}} = N^{\text{tight}}_{\text{real}} + N^{\text{tight}}_{\text{fake}}. \tag{6.5}$$

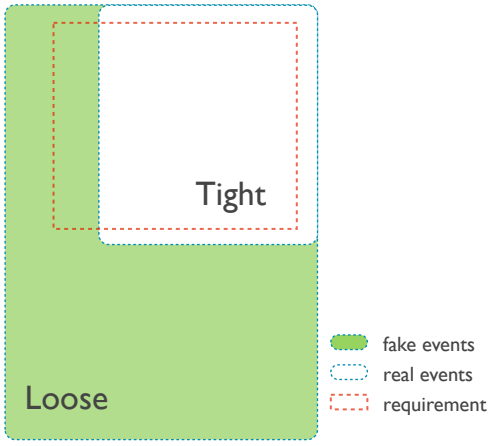

Figure 6.10: The data sample contains real and fake electrons. The matrix method is based on the probabilities of real and fake events to pass a number of requirements. Using those requirements two groups of events are defined: loose and tight, where tight events (N^{tight}) are a subset of loose events (N^{loose}) that also pass the additional requirements.

Efficiencies for tight requirements are defined as the fractions of loose real and fake electrons that also satisfy the tight lepton identification criteria (ϵ_{real} and ϵ_{fake}). Therefore, these efficiencies are defined as:

$$\epsilon_{\text{real}} = \frac{N^{\text{tight}}_{\text{real}}}{N^{\text{loose}}_{\text{real}}}, \tag{6.6}$$

$$\epsilon_{\text{fake}} = \frac{N^{\text{tight}}_{\text{fake}}}{N^{\text{loose}}_{\text{fake}}} \tag{6.7}$$

using the ϵ_{real} and ϵ_{fake}, N^{tight} can be defined as :

$$N^{\text{tight}} = \epsilon_{\text{real}} N^{\text{loose}}_{\text{real}} + \epsilon_{\text{fake}} N^{\text{loose}}_{\text{fake}}. \tag{6.8}$$

This system of equations can be solved to yield the number of fake events $N^{\text{tight}}_{\text{fake}}$ in the tight sample:

$$N^{\text{tight}}_{\text{fake}} = \frac{\epsilon_{\text{fake}}}{\epsilon_{\text{real}} - \epsilon_{\text{fake}}} (N^{\text{loose}} \epsilon_{\text{real}} - N^{\text{tight}}). \tag{6.9}$$

Equation 6.9 expresses the number of fake electrons that are able to pass the tight selection criteria, in terms of the number of loose events N^{loose}, the number of tight events N^{tight}, and two efficiencies ϵ_{real} and ϵ_{fake}. This is the basic matrix method formula.

The N^{tight} and N^{loose} are obtained from the signal region, either by applying all the $W^{\pm}Z$ selection requirements or relaxing the isolation and electron identification requirements. The tag and probe method is applied in independent samples of data as described below to determine ϵ_{real} and ϵ_{fake} for electrons.

Isolation and electron identification efficiency for "fake" electrons (ϵ_{fake}):

The non-prompt electrons are mainly originating from misidentified jets. The ϵ_{fake} represents the rate at which a jet that satisfies the relaxed electron cuts can also satisfy the tight requirements. To measure ϵ_{fake}, a sample enriched with jets is needed. A W + jets data sample is used, since those events have a similar spectrum of jets when compared to Z+jets events.

The W+jets data sample, is selected requiring events to have a good muon (serving as a tag), which satisfy the identification and isolation criteria required for candidates for the W lepton decay, along with $E_{\text{T}}^{\text{miss}} > 20$ GeV, $M_{\text{T}}(\mu, \text{E}_{\text{T}}^{\text{miss}}) > 40$ GeV, and exactly one additional electron candidate with the same charge as the muon, in order to reject Z, WW, and top contamination.

The loose and tight regions are defined with respect to the electron. In the loose control region, the electron must pass all the $W^{\pm}Z$ selection cuts required for the W lepton, except for the isolation cuts and the $tight{+}{+}$ identification. In the tight region all the selection cuts are required. The transverse momentum of the jet faking an electron in the W+jets sample is shown in Fig. 6.11, the left and right plots show the fake electrons passing respectively the loose and tight requirements. The control region is dominated by W+jets events and a reasonable data and MC agreement is observed, as can be seen from the left plot of Fig. 6.11, on the other hand the right plot shows the expected disagreement between the data and MC predictions for the tight fake events.

The residual contaminations from SM backgrounds are estimated using the MC simulation and are subtracted from the data. The ϵ_{fake} is finally calculated as the ratio of the data events passing the tight requirements to the number of selected events in the W + jets control region. The ϵ_{fake} was calculated as a function of p_T and η as shown in Fig. 6.12.

Isolation and electron identification efficiency for "real" electrons (ϵ_{real}):

The efficiency for an electron to pass the isolation and identification requirements is also measured using data with the tag and probe method in a Z+jets enriched region. This region is formed by reversing the W transverse mass cut ($M_T^W < 20$ GeV) applied in the WZ analysis, the third lepton must be a muon and no isolation or impact parameter significance requirement is applied. The tag and probe technique is applied on the electrons from the Z. The selection requires the presence of a tag electron, satisfying the tight identification criteria and matching the trigger object and a loose electron candidate (probe). The efficiency is calculated as the ratio of the number of probes passing the isolation and identification requirement divided by the total number of probes. The overall efficiency was found to be around 60% for electrons with p_T between 20-40 GeV, and ∼70% for electrons above 40 GeV.

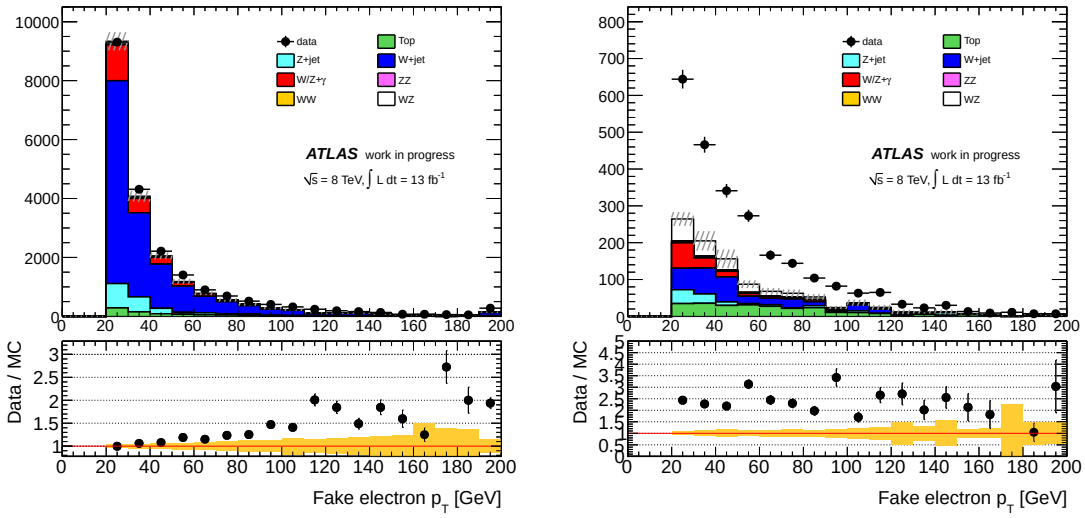

Figure 6.11: The transverse momentum of the jet faking an electron in the W + jets loose region (left) and after passing the isolation and the electron identification selection (right). The statistical uncertainty is shown by shaded bands.

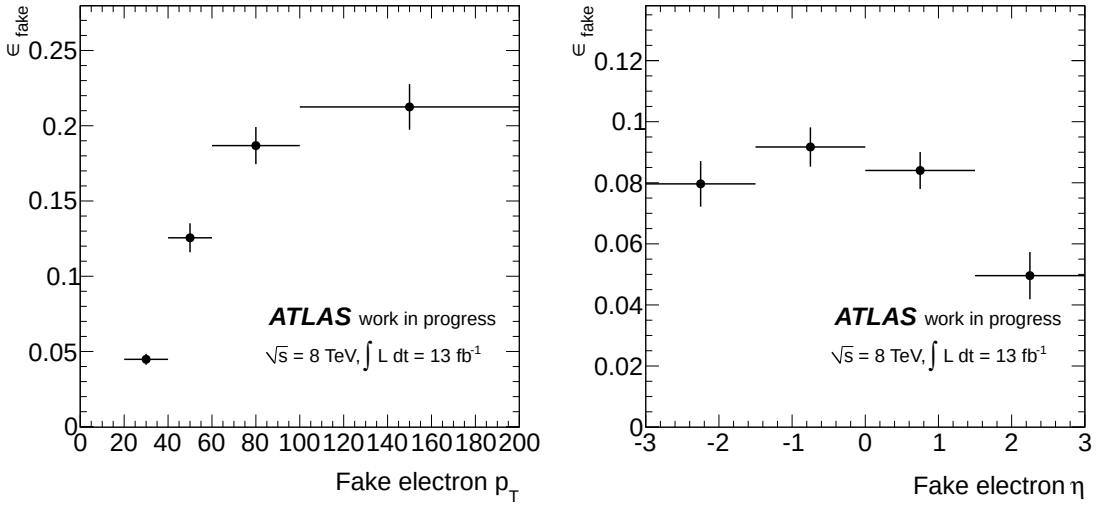

Figure 6.12: Distribution of the electron ϵ_{fake} as a function of p_T and η in data using 13 fb^{-1}.

Final background estimate:

Using the measured ϵ_{real} and ϵ_{fake}, and from the signal region the N^{loose} and N^{tight} the final yield is derived with the Equation 6.9. Table 6.15 shows the final yield.
For the statistical uncertainty on the final yield, the formula (6.9) has four terms as input (N^{loose}, N^{tight}, ϵ_{real} and ϵ_{fake}), but the purely statistical uncertainty on the $N^{\text{tight}}_{\text{fake}}$ prediction comes from the uncertainty on N^{loose}, and N^{tight}. Since N^{tight} is a subset of N^{loose}, N^{tight} and N^{loose} are correlated. If we define $N^{\Delta} = N^{\text{loose}} - N^{\text{tight}}$ then the relative

uncertainty is computed as :

$$\frac{\sigma(N_{\text{fake}}^{\text{tight}})}{N_{\text{fake}}^{\text{tight}}} \sim \frac{1}{\sqrt{N}^{\Delta}} \tag{6.10}$$

For the fake electron estimation, the following sources of systematic uncertainty are considered:

- Statistical errors on ϵ_{real} and ϵ_{fake} are considered as systematics.
- The bias due to the $E_{\text{T}}^{\text{miss}}$ cut: this cut is applied to select the W + jets control region, but it could introduce a bias on the jet kinematic. To verify the effect of this requirement, the $E_{\text{T}}^{\text{miss}}$ cut is loosened to 15 GeV and the difference between the new measured ϵ_{fake} and the nominal one is taken as the systematic uncertainty.
- The bias due to the $M_{\text{T}}(\mu, \text{E}_{\text{T}}^{\text{miss}})$ requirement is treated similarly to the $E_{\text{T}}^{\text{miss}}$ cut.
- The systematics due to the substraction of other background contamination is obtained by varying the amount of estimated background by 10%, and the difference with the measured ϵ_{fake} is taken as systematic uncertainty.

Table 6.15: Estimated number of top and Z+jets events in the signal region in the eee and $\mu\mu e$ channels.

	$\mu\mu e$	eee	Total
top and Z+jets from data	$56.7 \pm 3.7 \pm 11.2$	$36.6 \pm 2.9 \pm 10.8$	$93.3 \pm 4.7 \pm 15.6$
top and Z+jets from MC	32.4 ± 9.0	28.5 ± 7.5	60.9 ± 11.7

6.6 Systematic Uncertainties

All the systematic uncertainties taken into account in the $W^{\pm}Z$ cross section measurement are summarized in Table 6.16. The uncertainties on the Data-Driven background estimates are discussed in Section 6.5.2, were the data driven methods were presented.

For all systematics, the uncertainties of different channels resulting from the same underlying source variation are treated as fully correlated. The same relative uncertainties calculated using the signal MC samples have been assigned to the corresponding MC background processes.

6.7 Observed and Expected Events

After applying the selection criteria of the $W^{\pm}Z$ analysis, described in Section 6.3, on the 8 TeV data set corresponding to an integrated luminosity of 13 fb^{-1}, we observe 1094 $W^{\pm}Z$ candidates in data with 819.2 signal and 277.1 background events expected. The number of expected and observed events after applying all selection cuts are summarized in Table 6.17, with both statistical and systematic uncertainties. The W/Z+jets and $t\bar{t}$ backgrounds are estimated using data-driven methods and all other predictions come from MC simulation.

Uncertainties per channel [%]	$\mu\mu\mu$	$e\mu\mu$	$ee\mu$	eee
μ reconstruction efficiency	0.87	0.57	0.3	-
μ p_{T} scale & resolution	0.05	0.08	0.04	-
μ isolation & impact parameter efficiency	1.73	1.25	0.53	-
e reconstruction efficiency	-	0.7	1.4	2.0
e identification efficiency	-	1.1	2.0	3.2
e isolation & impact parameter efficiency	-	0.18	0.38	0.57
e energy scale	-	0.2	0.4	0.6
e energy resolution	-	0.1	0.2	0.2
$E_{\mathrm{T}}^{\mathrm{miss}}$ cluster energy scale	0.42	0.58	0.24	0.31
$E_{\mathrm{T}}^{\mathrm{miss}}$ jet energy scale	0.44	0.73	0.18	0.35
$E_{\mathrm{T}}^{\mathrm{miss}}$ jet energy resolution	0.51	0.97	0.12	0.13
$E_{\mathrm{T}}^{\mathrm{miss}}$_CellOut_Res	0.58	0.55	0.15	0.48
Trigger - μ	0.37	0.13	0.03	-
Trigger - e	-	0.09	0.09	0.06
Generator	1.2	1.2	1.2	1.2
PDF	1.6	1.6	1.6	1.6
Scale	0.9	0.9	0.9	0.9
Luminosity	2.8	2.8	2.8	2.8

Table 6.16: Summary of all relative acceptance uncertainties in the cross-section calculation.

Final State	eee	$ee\mu$	$e\mu\mu$	$\mu\mu\mu$	Combined
Observed	192	270	298	334	1094
ZZ	10.3±0.2±0.6	14.7±0.3±0.8	12.8±0.2±0.7	18.8±0.2±1.0	56.6±0.4±1.6
W/Z+jets	36.6±2.9±10.8	32.8±3.9±10.2	56.7±3.7±11.2	46.8±4.8±14.3	188.4±7.9±23.5
Top		6.3±0.5±3.4		9.1±0.7±4.9	
$W/Z+\gamma$	13.4±3.0±0.8	1.3±0.6±0.1	17.2±3.2±0.9	–	31.9±4.5±1.3
Bkg (total)	60.3±4.2±10.8	55.4±4.1±10.3	86.7±4.9±11.3	74.7±4.9±14.3	277.1±9.1±23.6
Expected signal	143.9±2.5±12.2	199.1±2.5±15.9	200.3±2.7±15.5	275.9±3.2±20.8	819.2±5.6±32.8
Expected S/B	2.4	3.7	2.3	3.7	3.0

Table 6.17: Summary of observed events and expected signal and background contributions in the four tri-lepton channels and combined. The first error is statistical while the second is systematic. The $t\bar{t}$ and Z+jets numbers are normalized the data-driven estimate. The background from top in the eee and $\mu\mu e$ channels is included in the corresponding W/Z+jets one.

6.7.1 Kinematic Distributions

The kinematic distributions for inclusive $W^{\pm}Z$ candidate events are plotted in Figures 6.13 - 6.15. The $E_{\mathrm{T}}^{\mathrm{miss}}$ distributions in the four channels, after applying all the $W^{\pm}Z$ analysis selection except the $E_{\mathrm{T}}^{\mathrm{miss}}$ cut, are shown in in Fig. 6.13. The $E_{\mathrm{T}}^{\mathrm{miss}}$ and $W^{\pm}$ transverse mass after $E_{\mathrm{T}}^{\mathrm{miss}}$ cut are shown in Fig. 6.13 as well as the W charge, the invariant mass of the three leptons, the jet multiplicity and the jet η distributions in Fig. 6.14. Figure 6.15 shows the kinematic distributions for inclusive $W^{\pm}Z$ candidate events after applying all the $W^{\pm}Z$ analysis selections. In all these distributions the $t\bar{t}$ and Z+jets backgrounds are normalized to the data-driven estimate. Overall a good data/MC agreement is obtained.

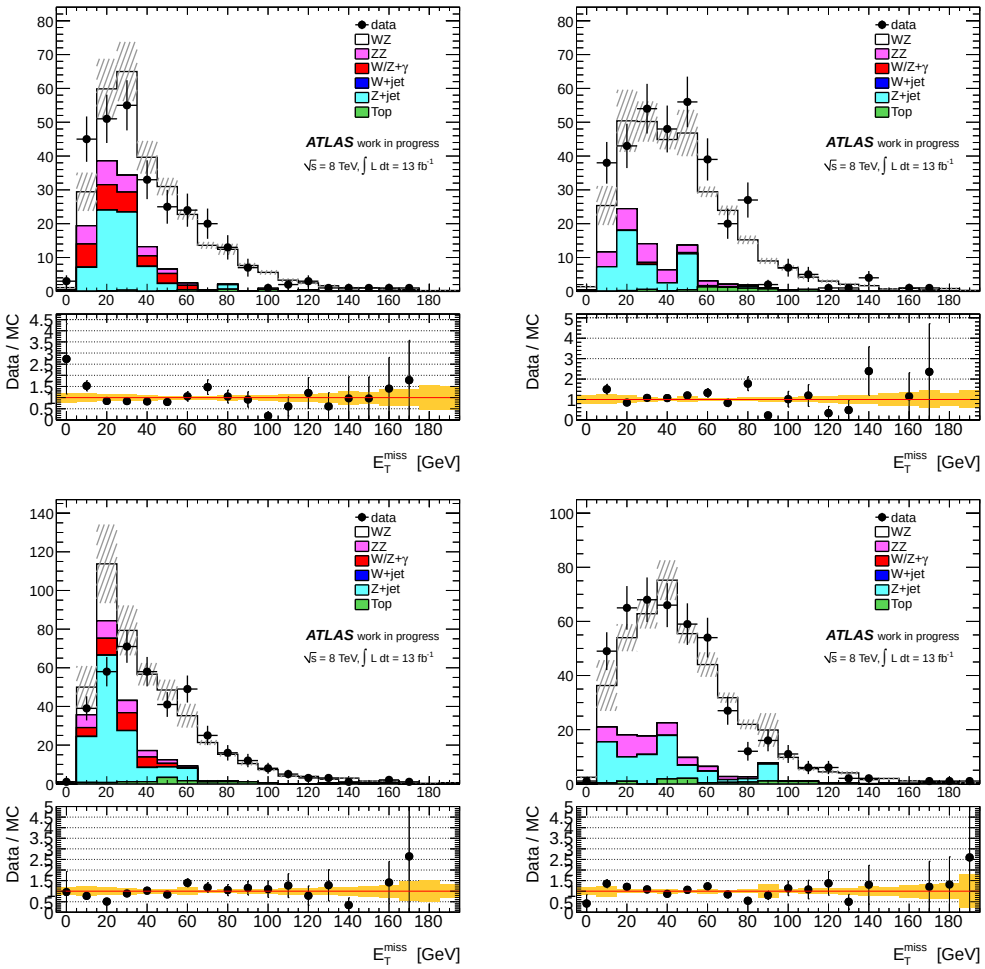

Figure 6.13: $E_{\mathrm{T}}^{\mathrm{miss}}$ distribution after applying all the WZ analysis selection except the $E_{\mathrm{T}}^{\mathrm{miss}}$ cut for eee (top left), $ee\mu$ (top right), $e\mu\mu$ (bottom left) and $\mu\mu\mu$ (bottom right) events. The statistical uncertainty is shown by shaded bands.

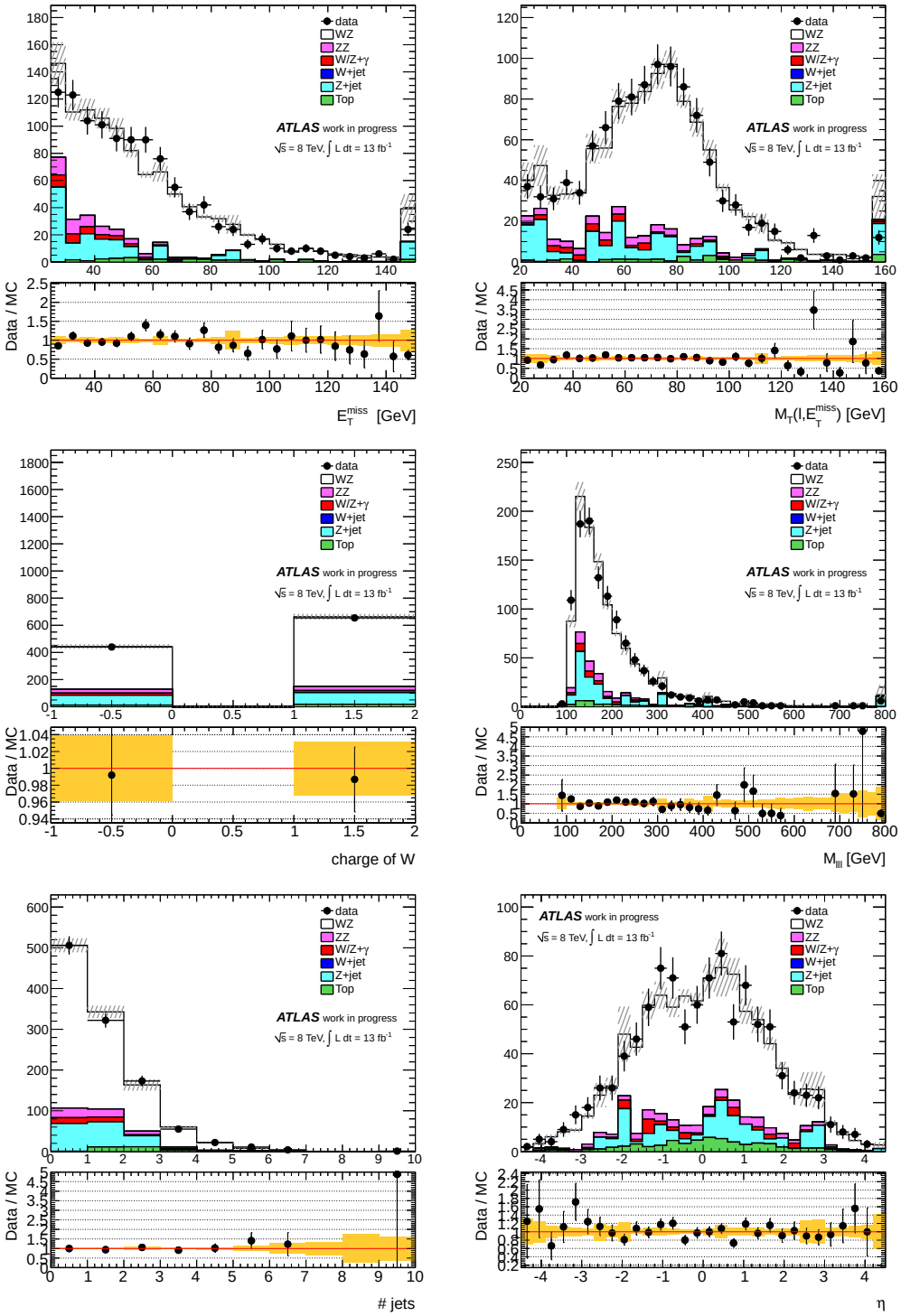

Figure 6.14: $E_{\mathrm{T}}^{\mathrm{miss}}$ (left) and W transverse mass(right) in the top row, W charge (left) and the invariant mass of the three leptons (right) in the second row and in the last row the jet multiplicity (left) and jet η distribution (right) after applying all the WZ analysis selection. The statistical uncertainty is shown by shaded bands.

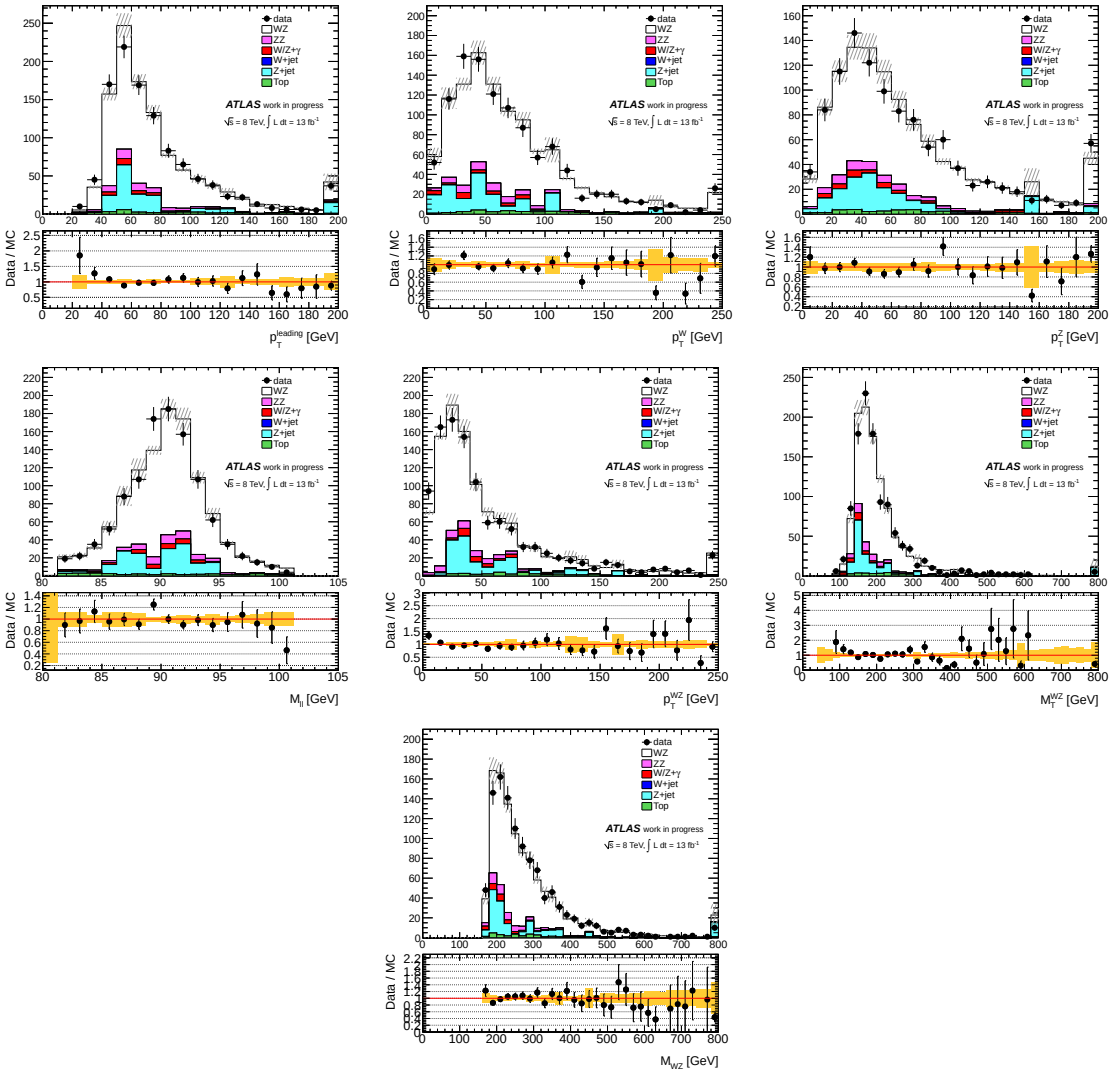

Figure 6.15: Kinematic distributions after all cuts for WZ candidates including p_{T} of leading lepton, and p_{T} of W and p_{T} of Z in the top row, invariant mass of Z, p_{T} of WZ and transverse mass of WZ in the second row. Invariant mass of WZ at the bottom. The shaded bands indicate the total statistical and systematic uncertainties of the MC prediction. Prediction distributions come from MC; but for $t\bar{t}$ and Z+jets, the yields are scaled up according to data-driven estimation. The statistical uncertainty is shown by shaded bands.

6.8 Cross Section Extraction

The WZ cross-section measurements for the 8 TeV analysis, are obtained using the same technique explained previously in Section. 5.7.4. For the fiducial cross section measurement, and a further total cross section extrapolation, a fiducial volume needs to be defined, corresponding to the 8 TeV selection. In this volume the efficiency correction term C_{WZ} (defined in Section 5.7.1) is calculated, as well as the total acceptance correction needed to extrapolate from the truth level fiducial volume to the full phase space of truth (details in Section 5.7.2). In the following sections the fiducial volume corresponding to the 8 TeV selection will be defined, and efficiency correction terms and the total acceptance values will be calculated. Finally the fiducial and total cross section results are presented.

6.8.1 Fiducial Volume and Acceptance Values

Since the selections for electrons and muons for the 8 TeV analysis have changed, they have different detector acceptances, a common phase space region between the channels needs to be defined, in which a fiducial cross section can be extracted. The common fiducial volume for the 8 TeV analysis is defined as:

- $p_T^\ell > 15$ GeV for the two charged leptons from the Z decay
- $p_T^\ell > 20$ GeV for the charged lepton from the W decay
- $|\eta^\ell| < 2.5$ for the three charged leptons
- $p_T^\nu > 25\,\text{GeV}$ for the neutrino
- $|m_{\ell\ell} - m_Z| < 10\,\text{GeV}$ for the Z candidate
- $m_T^W > 20\,\text{GeV}$ for the W candidate
- $\Delta R(l, l') > 0.3$ between W and Z leptons and $\Delta R(l, l') > 0.2$ between Z leptons

Using the definitions of the $A_{WZ\to l\nu l'l'}$ and $C_{WZ\to l\nu l'l'}$ from sections 5.7.1 and 5.7.2, and the 8 TeV fiducial volume, we have calculated these values using the signal MC. The $A_{WZ\to l\nu l'l'}$ for the 8 TeV analysis is calculated using POWHEG with PYTHIA showering, after dressing the final state leptons with all final state photons within $\Delta R < 0.1$. The A_{WZ}'s for all four channels are shown in Table 6.18 and compared with the results from MCFM, referred as A_{WZ}(MCFM) in the table. $C_{WZ\to l\nu l'l'}$ is calculated using the POWHEG signal MC. The calculated values are also summarized in Table 6.18. The difference in the A_{WZ} computed using MCFM generator and POWHEG with showering are taken as the systematic uncertainty of the generator and is found to be 1.2%.

6.8.2 Cross-Section Results

The WZ cross-section measurement for the 8 TeV analysis, is obtained using the maximum likelihood fit explained in Section. 5.7.4. The final results for the fiducial and total cross-section measurement in each channel and for the combined measurement are shown in

	$\mu\mu\mu$	$e\mu\mu$	$ee\mu$	eee
A_{WZ}(MCFM)	0.336	0.336	0.336	0.336
A_{WZ}(POWHEG showering)	0.333	0.329	0.329	0.336
C_{WZ}	0.828	0.604	0.572	0.429
$A_{WZ} \times C_{WZ}$	0.276	0.199	0.188	0.144

Table 6.18: Fiducial and total acceptance corrections per channel.

Tables 6.21 and 6.22. The systematic uncertainties including all sources except luminosity, which is listed separately, are shown in tables 6.19 and 6.20.

The expected cross-section from MCFM using as re-normalization and factorization scales $\mu_r = \mu_f = mWZ$ and the CT10 NLO PDF is 20.3 pb.

Source	$\mu\mu\mu$	$e\mu\mu$	$ee\mu$	eee	Combined
μ - Rec. efficiency	$^{+0.99}_{-0.94}$	$^{+0.69}_{-0.68}$	$^{+0.32}_{-0.32}$	$^{+0.00}_{-0.00}$	$^{+0.59}_{-0.67}$
μ -p_T smearing	$^{+0.12}_{-0.09}$	$^{+0.11}_{-0.11}$	$^{+0.00}_{-0.00}$	$^{+0.00}_{-0.00}$	$^{+0.08}_{-0.12}$
μ - isolation & IP efficiency	$^{+1.88}_{-1.77}$	$^{+1.39}_{-1.35}$	$^{+0.54}_{-0.53}$	$^{+0.00}_{-0.00}$	$^{+1.12}_{-1.24}$
e - Rec. Efficiency	$^{+0.00}_{-0.00}$	$^{+0.79}_{-0.79}$	$^{+1.51}_{-1.50}$	$^{+2.40}_{-2.33}$	$^{+0.79}_{-0.91}$
e - Id. Efficiency	$^{+0.00}_{-0.00}$	$^{+1.27}_{-1.24}$	$^{+2.24}_{-2.06}$	$^{+3.90}_{-3.67}$	$^{+1.27}_{-1.39}$
e - Energy Smearing	$^{+0.00}_{-0.00}$	$^{+0.11}_{-0.11}$	$^{+0.21}_{-0.21}$	$^{+0.23}_{-0.25}$	$^{+0.11}_{-0.16}$
e - Energy Scale	$^{+0.00}_{-0.00}$	$^{+0.23}_{-0.23}$	$^{+0.43}_{-0.43}$	$^{+0.70}_{-0.72}$	$^{+0.19}_{-0.30}$
e - iso IP	$^{+0.00}_{-0.00}$	$^{+0.23}_{-0.23}$	$^{+0.43}_{-0.43}$	$^{+0.70}_{-0.72}$	$^{+0.19}_{-0.30}$
$E_{\mathrm{T}}^{\mathrm{miss}}$ - jes	$^{+0.44}_{-0.42}$	$^{+0.79}_{-0.79}$	$^{+0.21}_{-0.21}$	$^{+0.47}_{-0.47}$	$^{+0.43}_{-0.51}$
$E_{\mathrm{T}}^{\mathrm{miss}}$ - jer	$^{+0.55}_{-0.52}$	$^{+1.04}_{-1.01}$	$^{+0.11}_{-0.11}$	$^{+0.12}_{-0.12}$	$^{+0.45}_{-0.53}$
$E_{\mathrm{T}}^{\mathrm{miss}}$ - cluster	$^{+0.44}_{-0.42}$	$^{+0.69}_{-0.68}$	$^{+0.21}_{-0.21}$	$^{+0.36}_{-0.35}$	$^{+0.40}_{-0.47}$
$E_{\mathrm{T}}^{\mathrm{miss}}$ - CellOut Res	$^{+0.65}_{-0.63}$	$^{+0.69}_{-0.68}$	$^{+0.21}_{-0.21}$	$^{+0.55}_{-0.59}$	$^{+0.52}_{-0.60}$
μ - Trigger	$^{+0.44}_{-0.42}$	$^{+0.11}_{-0.11}$	$^{+0.00}_{-0.00}$	$^{+0.00}_{-0.00}$	$^{+0.20}_{-0.26}$
e - Trigger	$^{+0.00}_{-0.00}$	$^{+0.11}_{-0.11}$	$^{+0.11}_{-0.11}$	$^{+0.12}_{-0.12}$	$^{+0.01}_{-0.12}$
Signal stat. (MC)	$^{+1.19}_{-1.13}$	$^{+1.37}_{-1.33}$	$^{+1.26}_{-1.25}$	$^{+1.75}_{-1.72}$	$^{+0.58}_{-0.78}$
Bkg stat. (MC)	$^{+0.09}_{-0.08}$	$^{+1.52}_{-1.52}$	$^{+0.31}_{-0.31}$	$^{+2.27}_{-2.30}$	$^{+0.50}_{-0.56}$
Bkg stat. (Data Driven)	$^{+1.89}_{-1.89}$	$^{+1.76}_{-1.75}$	$^{+1.86}_{-1.86}$	$^{+2.19}_{-2.21}$	$^{+0.93}_{-1.06}$
Data Driven methods	$^{+5.52}_{-5.48}$	$^{+5.31}_{-5.29}$	$^{+4.80}_{-4.80}$	$^{+8.18}_{-8.20}$	$^{+4.46}_{-4.57}$
Total (no lumi)	$^{+6.44}_{-6.34}$	$^{+6.58}_{-6.52}$	$^{+6.05}_{-5.98}$	$^{+10.15}_{-10.07}$	$^{+5.12}_{-5.41}$

Table 6.19: Relative systematic uncertainties (%) on the fiducial cross-section for each channel.

Figure 6.16 shows measurements of the total $W^{\pm}Z$ production cross section as a function of center-of-mass energy, from the ATLAS and CMS experiments at the LHC, and from the CDF [30] and D0 [32] experiments at the Tevatron, as well as the theoretical predictions.

Source	$\mu\mu\mu$	$e\mu\mu$	$ee\mu$	eee	Combined
μ - Rec. efficiency	$^{+0.97}_{-0.95}$	$^{+0.65}_{-0.70}$	$^{+0.32}_{-0.32}$	$^{+0.00}_{-0.00}$	$^{+0.63}_{-0.62}$
μ -p_T smearing	$^{+0.11}_{-0.11}$	$^{+0.11}_{-0.12}$	$^{+0.00}_{-0.00}$	$^{+0.00}_{-0.00}$	$^{+0.08}_{-0.06}$
μ - isolation & IP efficiency	$^{+1.85}_{-1.78}$	$^{+1.34}_{-1.38}$	$^{+0.54}_{-0.53}$	$^{+0.00}_{-0.00}$	$^{+1.20}_{-1.18}$
e - Rec. Efficiency	$^{+0.00}_{-0.00}$	$^{+0.76}_{-0.81}$	$^{+1.52}_{-1.48}$	$^{+2.39}_{-2.29}$	$^{+0.86}_{-0.85}$
e - Id. Efficiency	$^{+0.00}_{-0.00}$	$^{+1.23}_{-1.26}$	$^{+2.18}_{-2.10}$	$^{+3.95}_{-3.62}$	$^{+1.33}_{-1.33}$
e - Energy Smearing	$^{+0.00}_{-0.00}$	$^{+0.11}_{-0.12}$	$^{+0.21}_{-0.21}$	$^{+0.24}_{-0.23}$	$^{+0.11}_{-0.10}$
e - Energy Scale	$^{+0.00}_{-0.00}$	$^{+0.22}_{-0.24}$	$^{+0.43}_{-0.43}$	$^{+0.71}_{-0.69}$	$^{+0.25}_{-0.24}$
e - iso IP	$^{+0.00}_{-0.00}$	$^{+0.22}_{-0.24}$	$^{+0.43}_{-0.43}$	$^{+0.71}_{-0.69}$	$^{+0.25}_{-0.24}$
$E_{\mathrm{T}}^{\mathrm{miss}}$ - jes	$^{+0.43}_{-0.42}$	$^{+0.76}_{-0.81}$	$^{+0.21}_{-0.21}$	$^{+0.47}_{-0.46}$	$^{+0.48}_{-0.46}$
$E_{\mathrm{T}}^{\mathrm{miss}}$ - jer	$^{+0.54}_{-0.53}$	$^{+1.00}_{-1.04}$	$^{+0.11}_{-0.11}$	$^{+0.12}_{-0.11}$	$^{+0.50}_{-0.49}$
$E_{\mathrm{T}}^{\mathrm{miss}}$ - cluster	$^{+0.43}_{-0.42}$	$^{+0.65}_{-0.70}$	$^{+0.21}_{-0.21}$	$^{+0.35}_{-0.35}$	$^{+0.44}_{-0.42}$
$E_{\mathrm{T}}^{\mathrm{miss}}$ - CellOut Res	$^{+0.64}_{-0.63}$	$^{+0.65}_{-0.70}$	$^{+0.21}_{-0.21}$	$^{+0.59}_{-0.58}$	$^{+0.56}_{-0.54}$
μ - Trigger	$^{+0.43}_{-0.42}$	$^{+0.11}_{-0.12}$	$^{+0.00}_{-0.00}$	$^{+0.00}_{-0.00}$	$^{+0.21}_{-0.20}$
e - Trigger	$^{+0.00}_{-0.00}$	$^{+0.11}_{-0.12}$	$^{+0.11}_{-0.11}$	$^{+0.12}_{-0.11}$	$^{+0.07}_{-0.06}$
Generator	$^{+1.21}_{-1.18}$	$^{+1.17}_{-1.21}$	$^{+1.21}_{-1.18}$	$^{+1.20}_{-1.17}$	$^{+1.22}_{-1.17}$
PDF	$^{+1.62}_{-1.56}$	$^{+1.58}_{-1.60}$	$^{+1.62}_{-1.57}$	$^{+1.61}_{-1.56}$	$^{+1.62}_{-1.56}$
Scale	$^{+0.90}_{-0.89}$	$^{+0.87}_{-0.91}$	$^{+0.90}_{-0.89}$	$^{+0.90}_{-0.88}$	$^{+0.91}_{-0.88}$
Signal stat. (MC)	$^{+1.17}_{-1.14}$	$^{+1.32}_{-1.35}$	$^{+1.27}_{-1.23}$	$^{+1.75}_{-1.69}$	$^{+0.69}_{-0.68}$
Bkg stat. (MC)	$^{+0.08}_{-0.08}$	$^{+1.47}_{-1.54}$	$^{+0.31}_{-0.31}$	$^{+2.26}_{-2.25}$	$^{+0.50}_{-0.48}$
Bkg stat. (Data Driven)	$^{+1.88}_{-1.87}$	$^{+1.71}_{-1.78}$	$^{+1.85}_{-1.86}$	$^{+2.18}_{-2.17}$	$^{+1.02}_{-0.98}$
Data Driven method	$^{+5.48}_{-5.49}$	$^{+5.26}_{-5.35}$	$^{+4.77}_{-4.77}$	$^{+8.16}_{-8.14}$	$^{+4.49}_{-4.45}$
Total (no lumi)	$^{+6.75}_{-6.71}$	$^{+6.80}_{-6.97}$	$^{+6.40}_{-6.34}$	$^{+10.38}_{-10.20}$	$^{+5.70}_{-5.62}$

Table 6.20: Relative systematic uncertainties (%) on the total cross-section for each channel.

Channel	Cross-Section [fb]
$\mu\mu\mu$	$23.29^{+1.69}_{-1.59}(\mathrm{stat})\ ^{+1.50}_{-1.48}(\mathrm{syst})\ ^{+0.74}_{-0.68}(\mathrm{lumi})$
$e\mu\mu$	$26.16^{+2.22}_{-2.07}(\mathrm{stat})\ ^{+1.72}_{-1.71}(\mathrm{syst})\ ^{+0.86}_{-0.81}(\mathrm{lumi})$
$ee\mu$	$26.76^{+2.12}_{-1.98}(\mathrm{stat})\ ^{+1.62}_{-1.60}(\mathrm{syst})\ ^{+0.83}_{-0.78}(\mathrm{lumi})$
eee	$22.71^{+2.51}_{-2.28}(\mathrm{stat})\ ^{+2.31}_{-2.29}(\mathrm{syst})\ ^{+0.77}_{-0.73}(\mathrm{lumi})$
Combined	$99.24^{+3.77}_{-2.95}(\mathrm{stat})\ ^{+5.09}_{-5.37}(\mathrm{syst})\ ^{+3.09}_{-3.04}(\mathrm{lumi})$

Table 6.21: Measured fiducial cross-sections for each channel and combined.

Channel	Cross-Section [pb]
$\mu\mu\mu$	$19.07^{+1.41}_{-1.30}(\mathrm{stat})\ ^{+1.29}_{-1.28}(\mathrm{syst})\ ^{+0.59}_{-0.55}(\mathrm{lumi})$
$e\mu\mu$	$21.42^{+1.85}_{-1.67}(\mathrm{stat})\ ^{+1.46}_{-1.49}(\mathrm{syst})\ ^{+0.69}_{-0.67}(\mathrm{lumi})$
$ee\mu$	$21.90^{+1.76}_{-1.60}(\mathrm{stat})\ ^{+1.40}_{-1.39}(\mathrm{syst})\ ^{+0.68}_{-0.64}(\mathrm{lumi})$
eee	$18.59^{+2.07}_{-1.88}(\mathrm{stat})\ ^{+1.93}_{-1.90}(\mathrm{syst})\ ^{+0.63}_{-0.59}(\mathrm{lumi})$
Combined	$20.30^{+0.77}_{-0.65}(\mathrm{stat})\ ^{+1.16}_{-1.14}(\mathrm{syst})\ ^{+0.65}_{-0.61}(\mathrm{lumi})$

Table 6.22: Measured total cross-sections for each channel and combined.

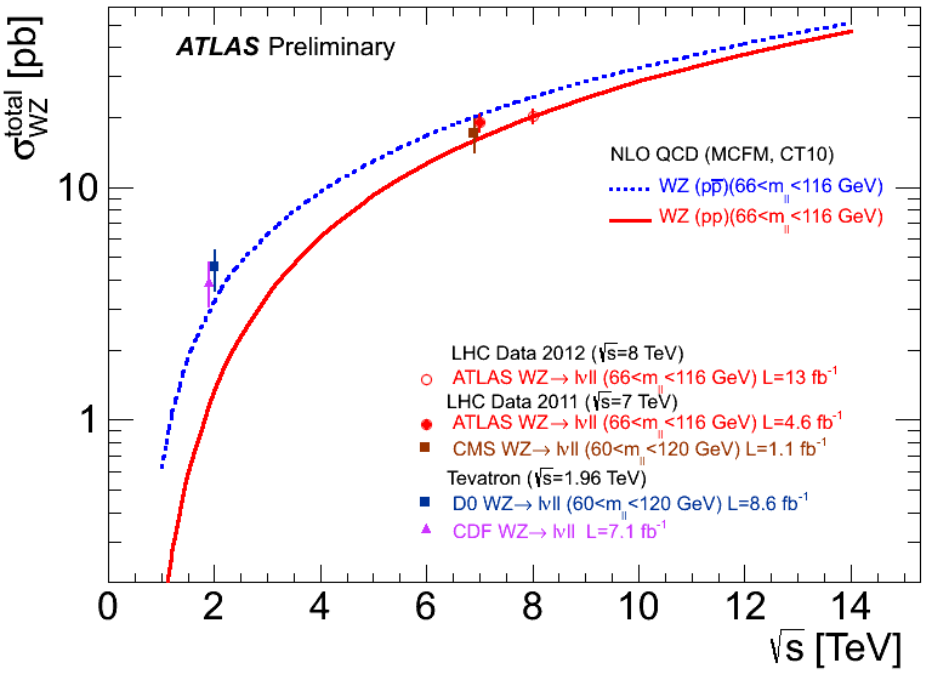

Figure 6.16: Measurements and theoretical predictions of the total $W^{\pm}Z$ production cross section as a function of center-of-mass energy. Experimental measurements from CDF and D0 in proton antiproton collisions at the Tevatron at $\sqrt{s} = 1.96$ TeV, and experimental measurements from ATLAS and CMS in proton-proton collisions at the LHC at $\sqrt{s} = 7$ TeV and at $\sqrt{s} = 8$ TeV are shown. The blue dashed line shows the theoretical prediction for the $W^{\pm}Z$ production cross section in proton anti-proton collisions, calculated at NLO using MCFM with PDF set CT10. The solid red line shows the theoretical prediction for the $W^{\pm}Z$ production cross section in proton-proton collisions, calculated in the same way. The ATLAS results at 8 TeV define the total cross section with a Z boson with mass between 66 GeV and 116 GeV. The results from CDF define the total cross section assuming zero-width for the Z boson and neglecting the γ^* contribution. The results from D0 define the total cross section with a Z boson with mass between 60 GeV and 120 GeV.

6.9 Conclusion

A measurement of the $W^{\pm}Z$ production cross-section with the ATLAS detector in LHC proton-proton collisions at $\sqrt{s} = 8$ TeV has been performed using electrons and muons in the final state. In a dataset with an integrated luminosity of 13 fb^{-1}(Table 6.17) a total of 1094 candidates were observed with a background expectation of 277.1 $\pm$ 9.1(stat)$\pm$23.6(sys). The Standard Model expectation for the number of signal events is 819.2 $\pm$ 5.6(stat)$\pm$32.8(sys). The fiducial[1] and total cross-sections were determined to be

$$\sigma^{fid}_{WZ\to l\nu l'l'} = 99.24^{+3.77}_{-2.95}(\text{stat})\ ^{+5.09}_{-5.37}(\text{syst})\ ^{+3.09}_{-3.04}(\text{lumi})\ \text{fb}$$

$$\sigma^{tot}_{WZ} = 20.30^{+0.77}_{-0.65}(\text{stat})\ ^{+1.16}_{-1.14}(\text{syst})\ ^{+0.65}_{-0.61}(\text{lumi})\ \text{pb}$$

The result is in good agreement with the SM total cross section of 20.3 ± 0.8 pb. calculated using MCFM [18] with parton density function set CT10 and $66 < M_{\ell\ell} < 116$ GeV cut.

The $W^{\pm}Z$ analysis is currently underway using the full 20 fb^{-1} of data collected in 2012. The goal is to produce:

- inclusive WZ cross-section measurement. The increased data set will also allow for precise studies of data control regions, thus allowing a reduction in the systematic uncertainties associated with the data driven systematics.
- Differential cross-section as a function of m_{WZ}, p_T^Z or jet multiplicity (N_j).
- The TGC measurement. This study will benefit greatly from increased size of the dataset and will provide much better limits on the anomalous triple gauge couplings and possibly surpass the Tevatron results. Nevertheless the aTGC studies will still be limited by statistics and this is a motivation for combination between the different channels and with CMS. The two experiments are aiming at developing a coherent approach, and combination framework.
- The interpretation of the $W^{\pm}Z$ production of the $\geq$ 2-jet bin in the context of Vector Boson Scattering (VBS) and extracting exlusion limits in anomalous Quartic Gauge Couplings (aQGC).
- Polarization/spin correlation: angular measurements of the Z (or W) boson.

With such an ambitious program, there is still a lot of interesting work to do.

[1] The fiducial volume is defined in Section 6.8.

Chapter 7

Micromegas study for HL-LHC environment

The upgrade of the LHC will lead to a luminosity increase of a factor 10 compared to the nominal of 10^{34} cm^{-2}s^{-1}. The luminosity increase will mean ten times higher particle rates in the detectors. While in most of the ATLAS muon system the detectors can handle these rates [53], this is not the case for the first forward station (Small Wheel). Furthermore, the upgraded Small Wheel is expected to take part in the Level 1 trigger decision, something that the current detectors are not able to do.

The idea to use Micromegas detectors for muon triggering and tracking over large areas was proposed in 2007. At that time Micromegas were already used in several High Energy Particle Physics experiments, like, COMPASS [96] and Kabes [97] and had shown to operate with very high particle rates with excellent spatial resolution. However, Micromegas chambers were not produced in large quantities and the largest surface of Micromegas detectors constructed at that time were the ones for COMPASS with an active area of 40×40 cm^2 and the ones developed for the T2K TPC readout [98] with dimension 35×36 cm^2.

An R&D activity was started and the Muon ATLAS Micromegas Activity (MAMMA) created to develop large detectors based on the bulk-Micromegas technology for use in the ATLAS Muon Spectrometer. Many studies were done to prove the Micromegas capability of triggering and high precision tracking in the HL-LHC environment. The work presented in this chapter is part of this R&D effort.

Finally the Micromegas were proposed for the New Small Wheel (NSW) and in early 2012, the ATLAS Muon Collaboration decided to follow the MAMMA proposal. In total, eight planes of Micromegas detectors covering the full NSW should be installed, corresponding to a total detector area of 1200 m^2. The Micromegas in the NSW will share space with eight planes of thin-gap multi-wire detectors (sTGC), in order to create a redundant system of sTGCs and Micromegas, both for triggering and tracking. The NSW is expected to be installed during the LHC shutdown beginning in 2018. The main re-

quirements for the detectors are:

- High counting rate capability, including dense ionization.
- High single plane detection efficiency, ($\geqslant$98%).
- Spatial resolution better than 100 μm, possibly up to large incident angles of 45°.
- Second coordinate measurement, with a few mm precision.
- Two-track discrimination at a distance of $\sim$1-2 mm.
- Good time resolution, $\sim$5 ns, to allow bunch-crossing identification.
- Level-1 triggering capability, within $\sim$1 μsec.
- Good aging properties.

In this chapter, following a short introduction of the Micromegas detector basic operation principles and the resistive technology, the results from the analysis of the autumn 2010 beam test data are presented. At the end of the chapter, a short summary of the current situation on Micromegas development will be presented.

7.1 The Micromegas detector

The Micromegas (MICROMEsh GAseous Structure) [99] is a gaseous particle detector coming from the development of wire chambers, to overcome the technical limitations like the wire spacing limit, the rate capability and aging problems. This technology was introduced in 1996 and has been successfully used in nuclear and high energy particle physics experiments during the past years [96, 97] when good spatial resolution at high rates was required.

The Micromegas detectors are made light weight in order to minimize the perturbation to the crossing particles. They are made of three parallel planes as seen in Fig. 7.1. The first plane is a drift electrode, which is followed by a gas gap of a few millimeters thickness that acts as conversion and drift region. Then there is a thin metallic mesh (micro-mesh) at 100 μm typical distance from the readout that creates the amplification region. And finally the anode plane with printed conductive strips.

The strips can be printed to obtain a spacing of the order 500 μm, providing a spatial resolution better than 100 μm, in the right conditions (gas, high voltage settings). The amplification gap of Micromegas is obtained by suspending a mesh over the anode strips. The precise gap, usually of the order of 50 μm to 100 μm is obtained by using adequate insulating spacers (pillars) printed on top of the anode plane by conventional lithography of a photo-resistive film [100]. The pillars are typically of 400 μm diameter arranged in a regular matrix with a distance between neighboring pillars of 2.5 mm in x and y. The small amplification gap assures excellent gain properties, and also provides fast signals of the order of 100 ns.

The drift electrode and the amplification mesh are at high voltage potentials, and the readout electrode is at ground potential. The HV are chosen to produce an electric field in

the drift region of a few 100 V/cm and in the amplification region of a few tens of kV/cm [99]

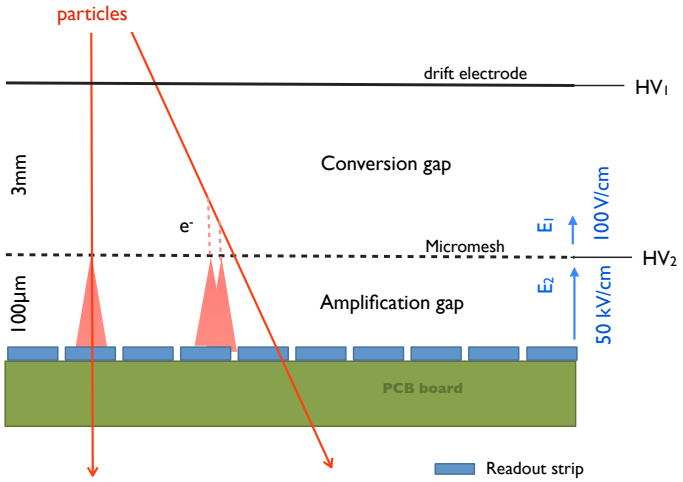

Figure 7.1: Operating principle of a Micromegas detector. Sparks can occur between the anode and the micro-mesh.

7.1.1 Working principle

In a Micromegas detector, as in every gaseous detector, the detection of the particles is made by amplifying the charges that are created by ionization in the gas volume. As mentioned before, in a Micromegas the gas volume is divided in two by a metallic micro-mesh placed at a typical distance of 100 μm from the readout strips.

When a charged particle passes through, it ionizes the gas volume in the drift space creating electron/ion pairs. Due to the electric field (of the order of 100 V/cm) the electron will drift toward the micro-mesh and the ion toward the cathode. When the electron arrives close to the micro-mesh, it enters an intense electric field (typically of the order of a few tens of kV/cm in the amplification gap). Accelerated by this field, the electron reaches enough energy to ionize atoms that will also ionize the gas, creating pairs; this is the avalanche effect. In this way, several thousand pairs are created from a hundred of primary charges, enough to create a significant signal. The electronic signal is read by a charge amplifier. The amplitude and the shape of the signal, read via the electronics on the readout electrode, that provide information on the time and energy of the particle.

The electric field configuration of Micromegas detectors are illustrated in Fig. 7.2. Due to the field gradient at the entrance of the micro-mesh hole, the field lines are compressed resulting in this characteristic funnel shape. The electrons liberated in the conversion gap by the ionizing radiation follow these lines and are focused into the multiplication gap where amplification process takes place. The ratio between the electric field in the amplification gap and that in the conversion gap must be set at large values (> 5) to

permit a full electron transmission, and to reduce a part of ion cloud, produced in the avalanche, to escape into the conversion gap. This ensures a good transmission of the electrons from the drift to the amplification region and a collection on the grid of more than 99 % of the ions produced in the avalanche [99] for correct working condition.

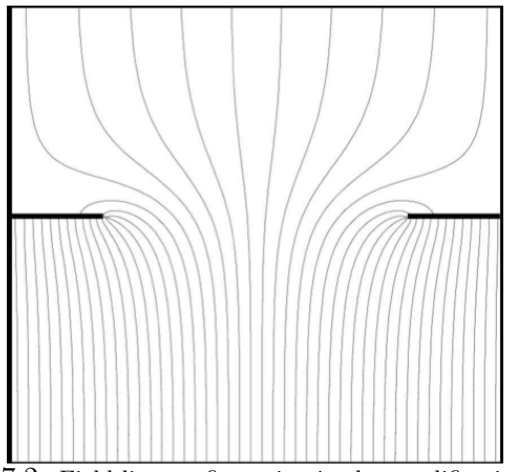

Figure 7.2: Field line configuration in the amplification region.

For a given grid voltage and gas mixture, a flat maximum of the gas gain as a function of the amplification gap size is predicted. The maximum should occur for gaps between 10 and 100 μm depending on the gas mixture. With a careful choice of the gas and the gap, the detector should be insensitive to small gap variations. This property, together with the uniform amplification field, explain the very good energy resolution of Micromegas detectors.

Due to the small size of the amplification gap, electrons and ions produced in the gas amplification are collected in 1 *ns* and 30-100 *ns* respectively. This allows the operation of the detector up to very high rates.

The spark issue

The principle of operation of Micromegas detectors with a very high electric field in the amplification region, make them particularly vulnerable to sparking. Sparks occur when the total number of electrons in the avalanche reaches the Raether limit [101], originating a discharge (or "spark") between the micro-mesh and the readout strips. The sparks are electric arcs between the mesh and the anode at ground potential.

The use of Micromegas in ATLAS calls for high detection efficiency for minimum ionizing muons, a gas with amplification factors (gain) of the order of 10^4 is needed. Ionization processes producing more than a few thousand electrons over a short amplification gap distance implies the risk of sparking. Such ionization levels could be reached in the most unfavorable regions of the ATLAS muon system where less than 10% of this rate is expected to come from muons, approximately 20% from protons and pions, the rest, from photon and neutron interactions [53]. The latter are of concern since neutrons interact-

ing in the chambers create slowly moving recoils from elastic scattering and low-energy hadronic debris from nuclear breakup. They both are heavily ionizing and lead to large energy deposits with the risk of sparking [102].

Sparks are not destructive and are not a problem concerning the detector robustness or the electronics on which it is possible to have a suitable protection, but the discharge of the whole micro-mesh induces a dead time up to 1 or 2 *ms* to recover the nominal voltage. Most of the R&D work in 2010 was dedicated to the spark problem. Many different approaches were tried, including pre-amplification in the drift region or using foils used in GEM detectors, a segmented micro-mesh, resistive layers, resistive strips, among others, in order to make Micromegas detectors spark resistant while maintaining their ability to measure minimum-ionizing particles with excellent precision in high-rate environments.

7.2 Resistive Micromegas

As mentioned before in a standard Micromegas detector, a high amplification field is applied in a thin gap, as represented on the Fig. 7.1. This feature makes them particularly vulnerable to sparking. One of the suggested solutions to reduce the effect of sparks in Micromegas, is to use resistive coatings on top of the read-out strips.

In a standard Micromegas detector the movement of the charges in the avalanche induces a signal directly on the readout strips. When a continuous resistive layer and insulator is present between the gas gap and the readout strips, the charge movement in this layer results in an "RC-type" differentiation of the signal. It also causes a spread of the signal to neighboring strips, obtaining good resolution with wider (fewer) strips. If, however, the resistive layer is segmented, the spread of the signal across neighboring strips is avoided, since only the charge induced on the readout strips below the resistive strip is "seen". One of the advantage of resistive strips rather than a continuous resistive layer is to keep the area affected by a discharge as small as possible, avoiding the charge spreading across several readout strips.

It should be noted that the discharge probability is the same for a resistive and for a standard chamber. The sparks can appear between the mesh and the anode at ground potential, be it resistive strips or metallic readout strips. The purpose of this spark protection layer is to limit, in the event of a spark, the discharge current to a level such that the drop of the mesh HV becomes insignificant.

7.3 2010 Test beam

As part of the R&D program of the MAMMA collaboration, the performances of four resistive chambers (with different read-out strip pitches) were studied, using 120 GeV momentum pions with rates from 25 up to 250 kHz/cm^2, at the H6 CERN Super Proton Synchrotron (SPS) beam line. The data was collected during the autumn of 2010, with

the main objective being to study the spatial resolution and efficiency of the resistive detectors. The tested detectors were built using various configurations, in terms of pitch, amplification gap and resistive coating.

7.3.1 Characteristics of the resistive detectors under study

One of the suggested solutions for sparks is to place a resistive coating on top of the anode read-out strips. The Micromegas structure is then built on top of the resistive strips or layer. The mesh is supported by small pillars (typically of 400 μm diameter) arranged in a regular matrix with a distance between neighboring pillars of 2.5 mm in x and y. During this test three different resistive configuration were studied:

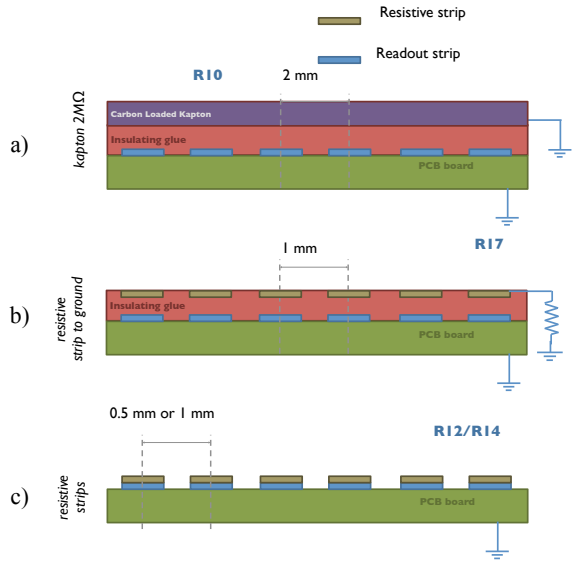

Figure 7.3: Fabrication techniques of resistive Micromegas.

a) Kapton 2 $M\Omega/\square$ layer: In a standard Micromegas the avalanche electrons induces a signal directly on the readout strips. In this case on top of the readout strips an insulating layer of 70μm thickness is placed, followed by a 2 $M\Omega/\square$ continuous Carbon-loaded Kapton resistive layer, (see Fig. 7.3a), the charge movement in this layer results in an RC-type differentiation of the signal [103]. It also causes a spread of the signal to neighboring strips and this effect helps in obtaining good resolution with wider (fewer) strips. A picture of the detector can be seen in Fig. 7.4.

b) Resistive strip to ground: In this type of detector the protection consists of a thin layer of insulator on top of which resistive strips are pasted. The resistivity of the strip is a few M$\Omega/\square$, see Fig. 7.3b. The resistive strips match the same geometry of the readout strips and each resistive strip is grounded at one extremity through a resistor [104].

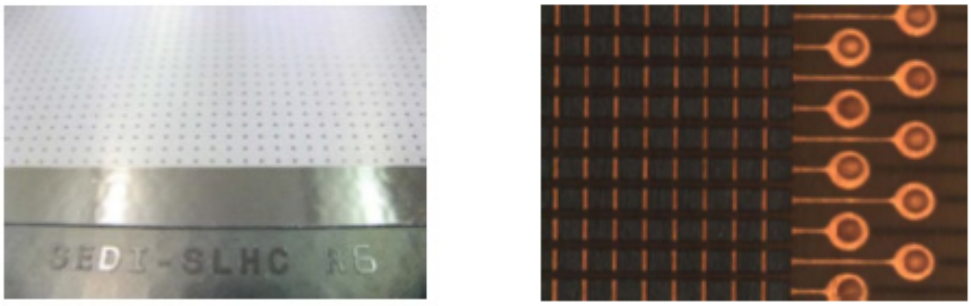

(a) R10 (b) R12/R14

Figure 7.4: Picture of the resistive Micromegas detectors tested. The R10 chamber has a kapton layer 2 MΩ/□, and chambers R12 and R14 have resistive strips of 300 kΩ/□. More details can be found in Table 7.1.

c) Resistive strips: In this case a resistive coating following the readout geometry is directly glued on the readout strips, and no insulating layer is present. The charges are evacuated through the readout strip, Fig. 7.3c. A picture of the resistive detector tested can be seen in Fig. 7.4.

More characteristics and specifications of the detectors under test can be found in Table 7.1.

Chamber	pitch	N° strips	Circuit type	Capacitance	Energy resolution ^{55}Fe	Gain max
R10	2.0 *mm*	48	kapton layer 2 MΩ/□	1.67 nF	22.1% (310 V)	7829 (410 v)
R17	1.0 *mm*	96	resistive strip to ground	943 pF	29.8% (310 V)	10236 (410 v)
R14	1.0 *mm*	96	resistive strips 300 kΩ/□	943 pF	36.3% (350 V)	10023 (410 v)
R12	0.5 *mm*	96	resistive strips 300 kΩ/□	637 pF	24.4% (320 V)	9835 (410 v)

Table 7.1: Characteristics of the four resistive chambers tested.

7.3.2 The test beam setup

The resistive chambers described above, were subsequently exposed to pions of ∼120 GeV, at the CERN SPS H6 beam line, during two weeks in autumn of 2010. An external reference measurement, on the plane normal to the beam direction was given by a telescope consisting of 3 (x and y) planes of standard Micromegas. Four resistive detectors were tested.

The goal of the test was to evaluate the influence of the resistive technology on the spatial resolution and efficiency of the prototypes. The experimental set-up is illustrated in Fig. 7.5. The beam entered from the right of the figure, passed through one scintillator,

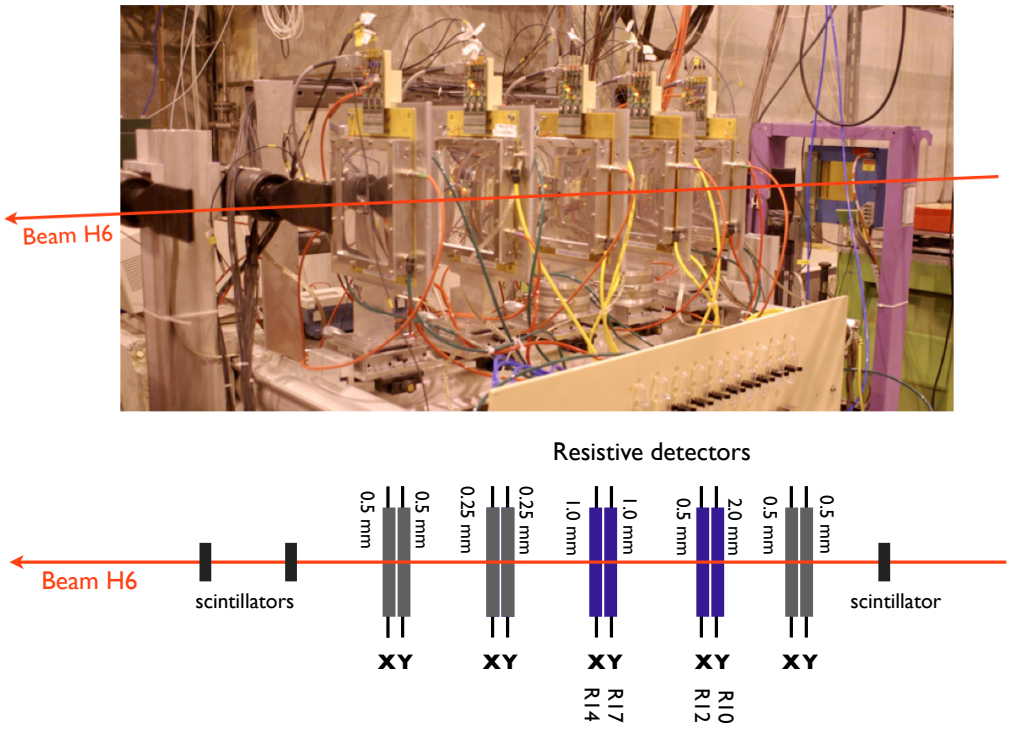

Figure 7.5: Picture and scheme of the test beam setup. The red arrow show the beam direction. In black the 3 trigger scintillators and the five planes of chambers (x and y direction) i.e 10 Micromegas chambers in total.

then the Micromegas and finally through two more scintillators. The trigger was defined by the coincidence of these three scintillators.

The telescope detectors were manufactured at Saclay, whereas the resistive detectors were manufactured at CERN. The main characteristics of the resistive detectors are summarized in Table 7.1. During the test beam, two different gas mixtures were used: Ar + 2%C_4H_{10}+3%CF_4 for the resistive detectors and Ar + 2%C_4H_{10} for the telescope. The resistive detectors were tested with different high voltage values and mounted on a rotating structure, in order to collect data with different beam angle.

7.3.3 Signal acquisition system

The three scintillators coincidence signal is used to trigger the acquisition of an event. For each trigger, the charge on the strips of all the Micromegas is read out with the help of electronic boards based on the Gassiplex chip [105]. Each board has 6 Gassiplex chips as illustrated in Fig. 7.6, for a total of 96 channels, the peaking time is 1.2 μs and is controlled by a CAEN sequencer with four C-RAM modules [106]. The data acquisition, storage management and online monitoring system were achieved with LabView acquisition software developed by NCSR Demokritos (Athens, Greece). Fig. 7.6 shows a schematic view of the Micromegas data acquisition setup, a picture of the Gassiplex board and a picture

of one of the Micromegas pointing the position were the Gassiplex board is placed.

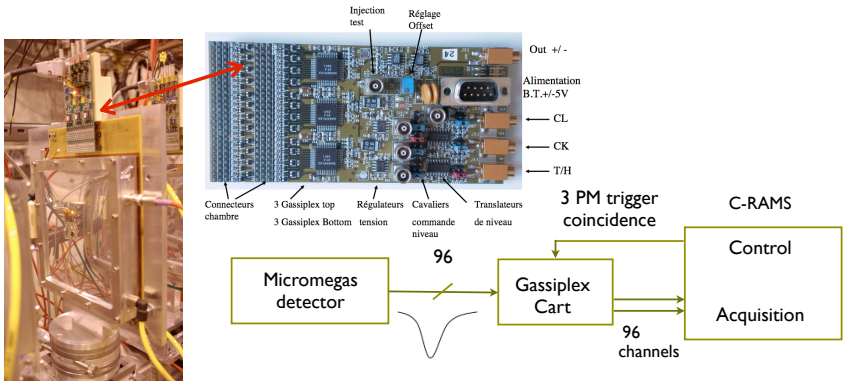

Figure 7.6: Picture of a Micromegas detector and a Gassiplex board [105]. A scheme of the signal acquisition system is also shown.

7.4 Data Analysis

During the test beam, runs with different beam and detector conditions were taken:

- high rate exposures: pions of $\sim$ 80 to 120 GeV at rates from 25 to 250 kHz/cm^2.
- Resistive detectors were tested with different High Voltages settings, and
- detectors rotated with respect to the beam (0°, 20°, 30°).

The data analysis started immediatly after the test beam and covered data cleaning, detectors alignment, and track reconstruction, to efficiency and resolution measurements. In the following sections, an overview of the study of different resistive Micromegas performances is presented.

7.4.1 Data preparation and Common mode noise rejection

The first step in the analysis chain was to make sure that the data could be exploited. The data had to satisfy a set of data quality criteria, based on proper operation of the telescope detectors, the signal acquisition system, gas supply and trigger. The analysis was restricted to the remaining datasets.

When a event is triggered the information of all the strips in the Micromegas is readout by the Gassiplex board. The data of each strip needs to be organized to follow the real strip position in the detector, called the detector mapping. Figure 7.7a shows a Gassiplex read-out of each one of the 96 channels, in a run without beam and before mapping. The concentration of measurements that gives the dark shadowed area in each channel corresponds to the pedestal level of each channel (the zero level when no particle has left information). Figure 7.7b shows a run with beam after the mapping is done; the beam

can be seen as high ADC counts: in the region around the strip 25. Once the mapping is done, the pedestals need to be aligned across the channels, in order to have a common level across the different channels.

The pedestals are aligned for each run using the data. To do the pedestal adjustment, the information of the fifteen strips with the highest signal, was removed. Doing that the beam signal is cleaned and only the pedestals remains. Then on this data a gaussian fit is made, strip by strip. The mean value of the fit is used to correct for pedestal alignment and the sigma is the pedestal widths (σ_{ped}). Figure 7.7c shows the result of the pedestal alignment.

Once the pedestals are aligned a continuous dark shadow can be seen around 100 ADC counts, this line correspond to the so called "common mode noise" which essentially are pedestals shifts correlated across the channels. To correct for the common mode noise the mean value of ADC counts was calculated event by event and used to bring the measurements to the pedestal level. Figure 7.7d shows the data after the common mode noise cleaning.

Finally the noisy or dead channels are identified and masked for the rest of the analysis. Figure 7.7e shows in a histogram of the beam profile for one detector, the first ten strips are constantly fired, and are considered as noisy; they are masked for the rest of the run, as can be seen in Fig. 7.7f. All this cleaning process is made run by run, since the pedestal levels can change depending on the run conditions.

Before combining the measurements of the separate Micromegas modules, the relative internal alignment of the telescope and resistive detectors should be established. To define the reference frame for the internal alignment, the plane of the first telescope detector in association with the beam direction was used. It is noted that this is possible due to the very narrow angular profile of the beam. Relative translations in the $x - y$ planes of the detectors are accounted for by requiring the same beam center position for all planes. When clusters and tracks are reconstructed, the tracks are used to improve the alignment.

7.4.2 Cluster and track reconstruction

As previously mentioned when a charged particle goes through a Micromegas detector, it creates an avalanche of electrons that are going to induce a signal on the readout strips. Depending on the ionizing particle, the size of the avalanche, the gas dispersion, the resistive coating and strip pitch, the avalanche can reach one or several strips.

The first step in the reconstruction is to identify groups of fired strips with charge above a given threshold, those groups are called "clusters". The threshold is defined by 3.5 σ_{ped} of electronics noise, which is usually $\sim$ 2-3 ADC counts.

The particle position is then reconstructed combining the strip information in simple Center Of Gravity (COG),

$$x_{\text{hit}} = \frac{\Sigma_i w_i \cdot x_i}{\Sigma_i w_i} \tag{7.1}$$

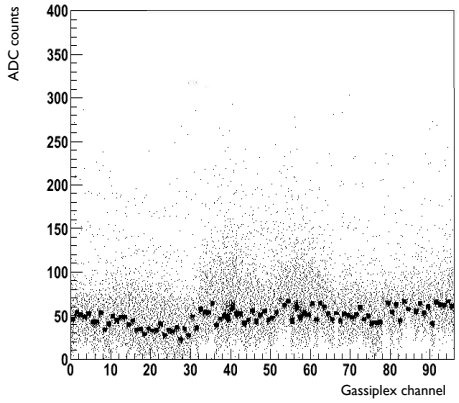

(a) Pedestal run without beam.

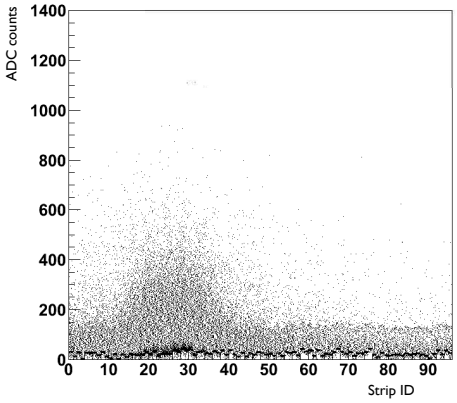

(b) Run with beam before pedestal adjustment.

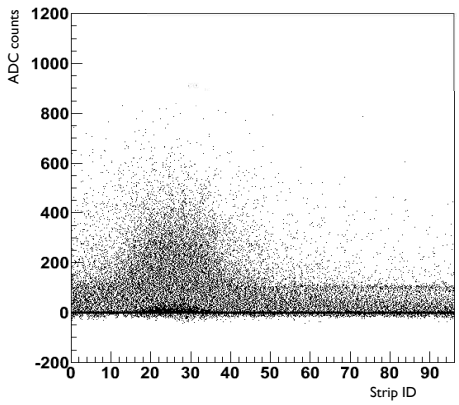

(c) After pedestal adjustment common mode noise (pedestals shifts) can be seen.

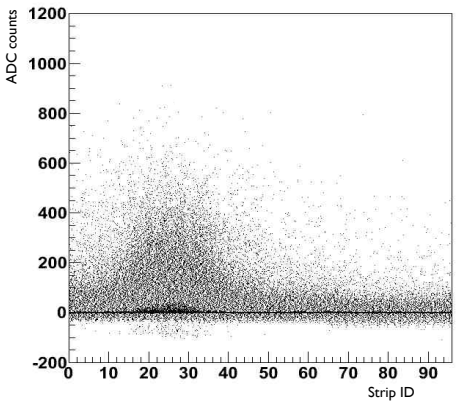

(d) Clean data after common mode noise correction.

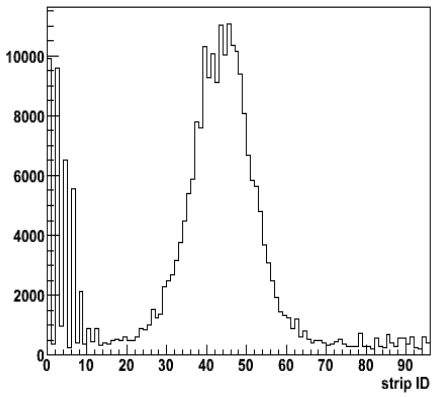

(e) Noisy channels can be seen on the left.

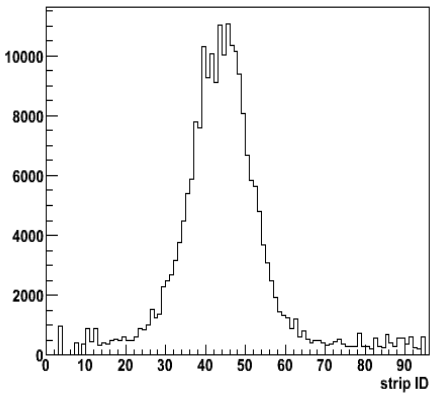

(f) The noisy channels are removed.

Figure 7.7: Data preparation steps, (a) shows the readout of the Gassiplex board before the mapping in a run without beam, (b) shows a run with beam before pedestal level adjustment, (c) shows the data after pedestal adjustment, some common mode noise is remaining. Plot (d) shows the data after the common mode noise correction. Plots (e) and (f) are beam profiles, the first ten strips on (e) are clearly noisy, therefore there are masked for the rest of the analysis as illustrated in (f).

where w_i is the charge on the strip, x_i is the coordinate of the strip in the cluster, and x_{hit} is the coordinate of the cluster COG. Using this algorithm it is possible to estimate the particle hit position, in each one of the Micromegas.

The hit position information of each Micromegas telescope is combined using a fit to form the particle track. The track information is then used to estimate the hit position in the resistive Micromegas. Figure 7.8 (top left) shows the residual distribution $x_{\text{hit}} - x_{\text{track}}$, where x_{hit} the reconstructed position given by the resistive Micromegas and x_{track} its corresponding extrapolated value from the fit of the track using the telescope detectors. A residual distribution is expected to follow a Gaussian shape, and the resolution is the width σ. However in some of the tested detectors the residual distribution was not a Gaussian as shown in Fig. 7.8.

In order to understand the origin of the bias, on Fig. 7.8 (bottom left), the x_{hit} position was traced with respect to the central strip position (x_{strip}); a zero value means that x_{hit} is in the border of the central strip and a value of one at its other end. The vertical line exactly at $x_{\text{strip}} = 0.5$ corresponds to the one strip cluster signal, where the impact point is reconstructed by default on the middle of the strip. The data points follow an S-shape distribution. This distribution was made for all detectors and it was found that this bias was present only for those strips with large pitch (i.e larger or equal to 1 mm). The bias was attributed to the discretization of the signal created by large strip pitches with respect to the avalanche size [107].

In order to correct for this bias, a new way of giving weight to the strips was proposed. The idea is to calculate the impact point as a center of gravity, but with logarithmic weights. So w_i in Equation 7.1 will be:

$$w_i = w_0 + log(\frac{Q_i}{\Sigma_j Q_j}), \tag{7.2}$$

$$w_0 = -log(\frac{Q_{min}}{Q_{tot}}) \rightarrow w_0 > 0 \tag{7.3}$$

were Q_i is the charge on the strip and $\Sigma_j Q_j$ is the total charge of the cluster. The weight w_i is constrained to be positive (otherwise set to zero). The w_0 can be interpreted as a charge threshold above which a strip will be taken into account for the center of gravity calculation. Using this technique the relative weights of the strips surrounding the central strip is increased. In the calculation of the reconstructed position this will avoid giving most of the weight to the central strip, reducing the discretization effect induced by large strip size.

The result of this reconstruction technique can be seen on the right plots of Fig. 7.8. The agreement of the gaussian fit is clearly better and the S-shape disappeared. Since this technique works properly, it was used for the resistive detectors with large strip pitch (R10, R17 and R14) and the normal COG's for the rest.

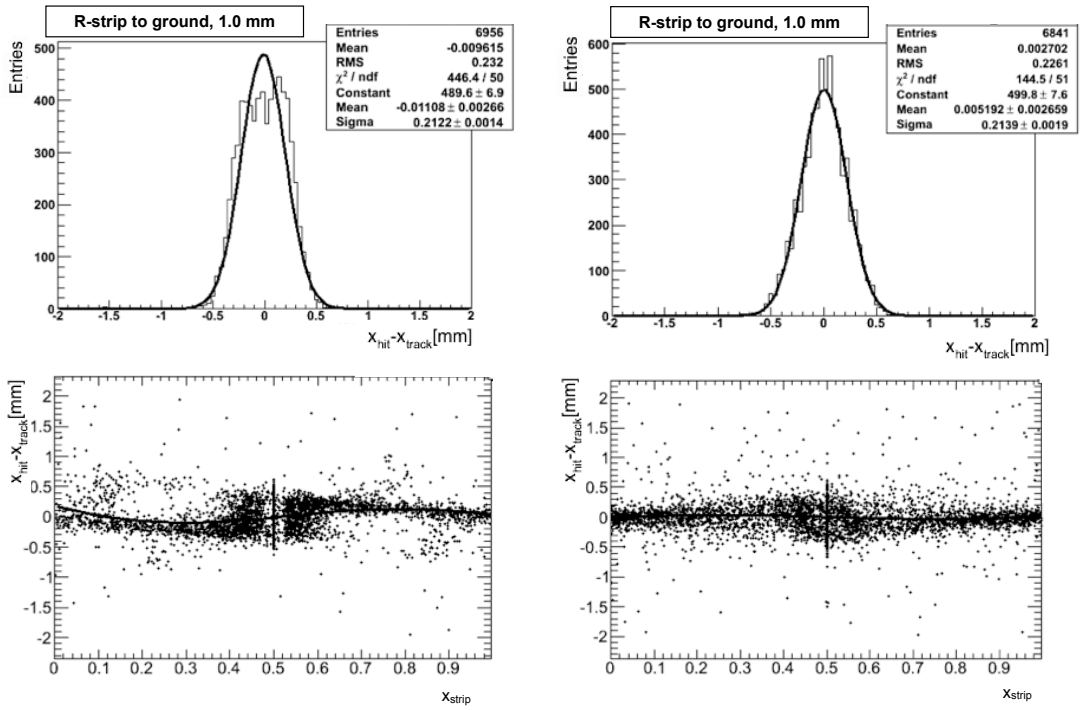

Figure 7.8: On top the residuals distribution, and on the bottom the residual distribution vs the x_{strip}. The plots on the left are done using the COG technique and the right ones using logarithmic weight technique.

Once the hit position for each chamber is estimated, a track is reconstructed by fitting all the $(x_{\text{hit}}, y_{\text{hit}})$ points with a straight line. Since the telescope chambers as well as the resistive chambers have different resolutions (different strip pitch, gas etc..). The fit considers the contribution of each j chamber with a weight related to the chamber resolution σ_j.

Using the reconstructed tracks, misalignments of individual chambers have been corrected and a final position precision below $< 100\ \mu m$ is achieved as shown in the following section.

7.5 Efficiency and resolution results

The efficiency and resolution study of the resistive detectors was done using as reference the measurements of the telescope. To ensure that a particle traversed the detectors, the following selection is applied :

- A cluster must be reconstructed in all telescope detectors.

- The reconstructed charge of the cluster should be below a maximum threshold, in order to avoid being in the tail of the charge distribution. Figure 7.9 shows the reconstructed cluster total charge for one of the telescope detectors. As expected the charge is a landau distribution, the contributions of clusters of different multiplicity are show in colors.
- The cluster size should be smaller than 3 *mm*. To avoid counting as signal noise events like pedestal shifts.
- The cluster used to build the telescope track should be compatible with the track direction within the mean beam dispersion in x and y.

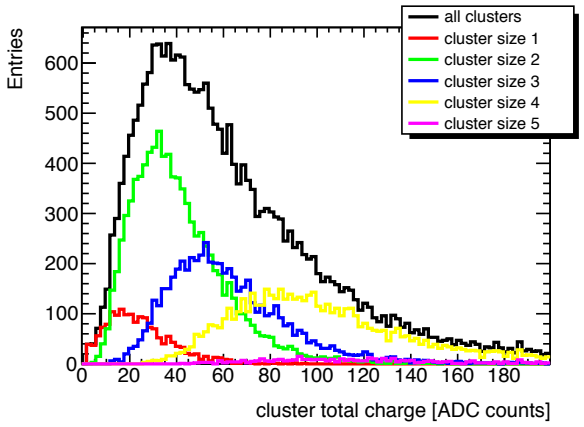

Figure 7.9: Total reconstructed cluster charge for one of the telescope detectors. The total cluster charge of all multiplicities is shown in black, and the contribution for clusters from one to five strips are in different colors. As expected the global histogram shape follows a Landau distribution.

7.5.1 Spatial Resolution

The method to measure a detector resolution (σ_{Mm}), is to compare the impact point reconstructed by the detector (x_{det}) to the expected one from the track fit (x_{track}). The resolution is then the standard deviation of the gaussian fit of the residuals $\delta = x_{\mathrm{det}} - x_{\mathrm{track}}$ distribution.

An important issue to consider is that the uncertainties on the reconstructed track will affect x_{track} and so the residual distribution. The uncertainties in track reconstruction are related to the resolution of the detectors and to the number of points available. Since our telescope gives us a limited number of points, two approaches can be taken to reconstruct the track:

- the chamber of interest is included in the fit of the track, or
- the track fit is made using only the telescope information.

The resolutions obtained in those two cases are shown for one run in Fig. 7.10. The resolutions when the chamber of interest is included on the fitted track (red fit) are overestimated, since the point for which the resolution is to be determined was included in the line fit, and those obtained by excluding it (blue fit) gives resolutions which are worse than the real ones since the line is determined from the telescope points which themselves have an uncertainty.

A compromise is a geometric-mean of the two track fitting methods. Combining the information it is possible to get a better estimate of the true detector resolution [108]. Let us assume a track consisting of N measurements with known values y_j, $j = 1..N$. The corresponding measured values x_j are distributed around the expected mean $x_j = a + by_j$ with the standard deviations σ_j, a and b being the track parameters. To determine the resolution of a measurement i a coordinate system so that $y_i = 0$, for simplicity is chosen. So the residual distribution will be given by $\delta_i = a - x_i$, a can be determined from the track fit by either including (a_i^{in}) or excluding (a_i^{ex}) the measurement i. The residual δ_i will be distributed with a standard deviation σ_i, wich depends on the coordinates (x_j, y_j) and weights $w_j = 1/\sigma_j^2$ of all measurements.

Minimizing the χ^2 gives an estimate for a:

$$a_i^{\text{in}} = \frac{\sum_j w_j x_j . \sum_k w_k y_k^2 - \sum_k w_k y_k . \sum_j w_j x_j y_j}{D^{\text{in}}} \tag{7.4}$$

where

$$D^{\text{in}} = \sum_j w_j . \sum_j w_j y_j^2 - (\sum_j w_j y_j)^2 \tag{7.5}$$

and

$$a_i^{\text{ex}} = \frac{\sum_{j\neq i} w_j x_j . \sum_{k\neq i} w_k y_k^2 - \sum_{k\neq i} w_k y_k . \sum_{j\neq i} w_j x_j y_j}{D_i^{\text{ex}}} \tag{7.6}$$

where

$$D_i^{\text{ex}} = \sum_{j\neq i} w_j . \sum_{j\neq i} w_j y_j^2 - (\sum_{j\neq i} w_j y_j)^2 \tag{7.7}$$

And since $y_{(j=i)} = 0$

$$D_i^{\text{ex}} = D^{\text{in}} - w_i \sum_j w_j y_j^2 \tag{7.8}$$

The residual δ_i^{in} of point i is :

$$\delta_i^{\text{in}} = a^{\text{in}} - x_i = \frac{\sum_j w_j x_j (\sum_k w_k y_k^2 - y_j \sum_k w_k y_k) - D^{\text{in}} x_i}{D^{\text{in}}} \tag{7.9}$$

$$= \frac{\sum_{j\neq i} w_j x_j (\sum_k w_k y_k^2 - y_j \sum_k w_k y_k) - D_i^{\text{ex}} x_i}{D^{\text{in}}} \tag{7.10}$$

Assuming that the N measurements are independent, the variance of the residual distri-

R-strip 300 $k\Omega$, 0.5 mm

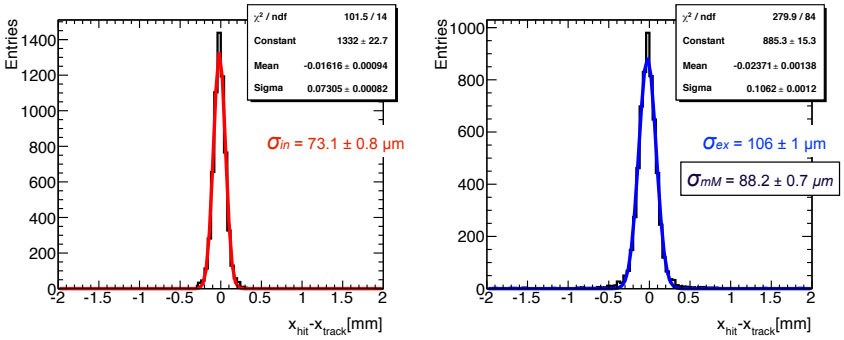

R-strip 300 $k\Omega$, 1.0 mm

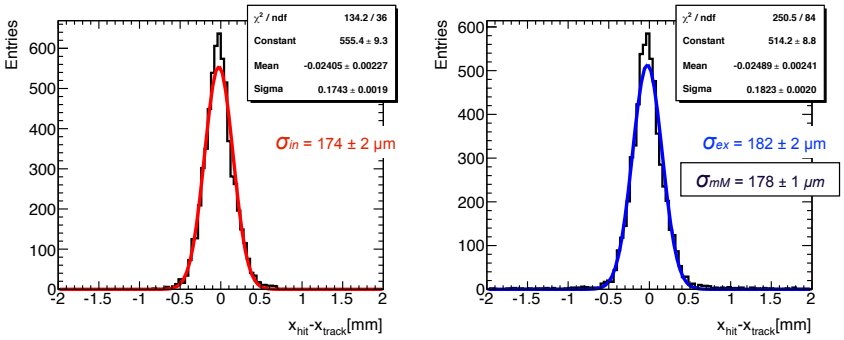

R-strip to ground, 1.0 mm

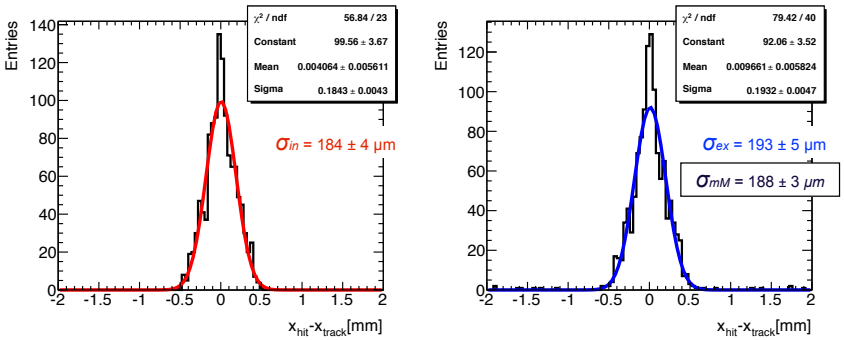

R-layer kapton 2 $M\Omega$, 2.0 mm

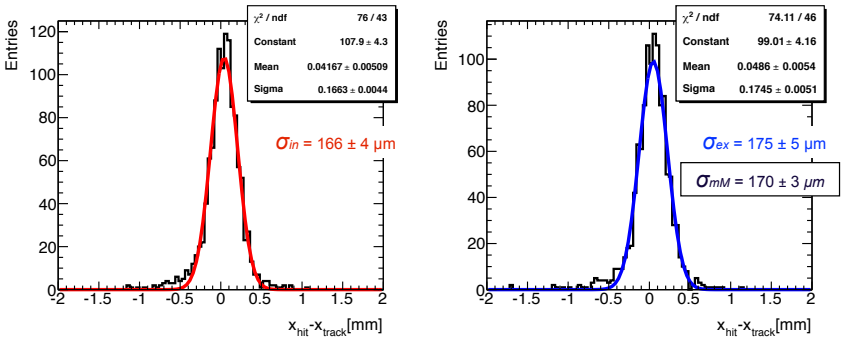

Figure 7.10: Difference between the position measured by the Micromegas and the extrapolated telescope track for the four resistive chambers under study. The red and blue right panels show the results for σ_{in} and σ_{ex}, σ_{Mm} is considered the resolution of the detector.

bution can be written approximately:

$$\sigma^2_{\text{in}_i} = \sum_j \left(\frac{\partial \delta_i^{\text{in}}}{\partial x_j} \sigma_j \right)^2 \tag{7.11}$$

The partial differentiation removes the x_j terms leaving:

$$\sigma^2_{\text{in}_i} = \frac{\sum_{j \neq i} w_j^2 \sigma_j^2 (\sum_k w_k y_k^2 - y_j \sum_k w_k y_k)^2 - (D_i^{\text{ex}} \sigma_i)^2}{(D^{\text{in}})^2} \tag{7.12}$$

Rearranging some terms:

$$\sigma^2_{\text{in}_i} = \sigma_i^2 \frac{D_i^{\text{ex}}}{D^{\text{in}}} \qquad \text{and} \qquad \sigma^2_{\text{ex}_i} = \sigma_i^2 \frac{D^{\text{in}}}{D_i^{\text{ex}}} \tag{7.13}$$

The quantities D^{in} and D_i^{ex} are fixed for a given layout and can be calculated to correct the resolution measured, however it is simpler to combine the last two expressions:

$$\sigma_i^2 = \sigma_{\text{in}_i} \cdot \sigma_{\text{ex}_i} \tag{7.14}$$

So finally we can write the resolution of our Micromegas under study like:

$$\sigma_{\text{Mm}} = \sqrt{\sigma_{\text{in}} \cdot \sigma_{\text{ex}}} \tag{7.15}$$

where σ_{in} and σ_{ex} are the obtained resolutions by respectively including and excluding the chamber of interest from the track fit.

Using this technique σ_{Mm} was estimated for all detectors and for different HV values. Figure 7.11 shows σ_{Mm} as a function of the mesh HV. It was found that the resolution is degraded if the strip pitch is too wide with respect to the avalanche size due to insufficient charge sharing between readout strips. And also that for higher HV_{mesh} the resolution is better because of higher gain. A resolution of 88.1 μm for 500 μm strip pitch (R12) was achieved.

7.5.2 Efficiency

The efficiency is defined as the fraction of tracks for which the residual between the extrapolated impact point and the closest cluster mean position is less than 5 σ_{Mm}. The efficiency and the respective uncertainty can be expressed as:

$$\epsilon = \frac{n_+}{n} \qquad \delta\epsilon = \sqrt{\frac{n_+ n_-}{n^3}} \tag{7.16}$$

where n is the total number of tracks reconstructed by the telescope, n_+ are tracks seen by the detector under study inside the 5 σ_{Mm} window around the expected point, and n_-

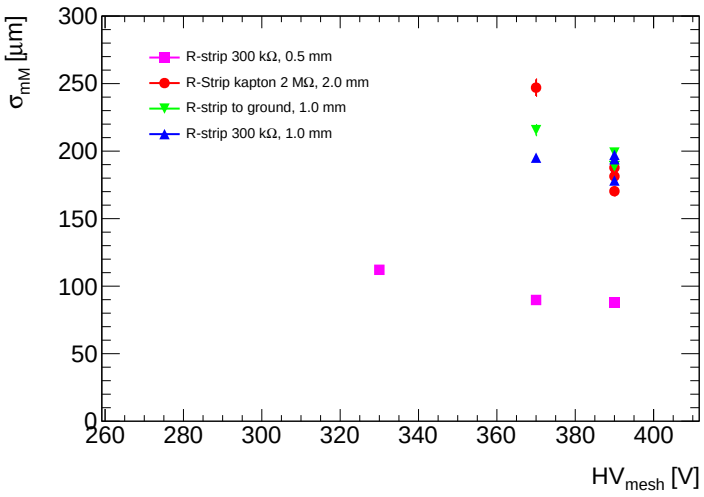

Figure 7.11: Resolution σ_{Mm} as a function of the mesh HV for three of the technologies tested.

are the tracks seen by the telescope and missing in the detector under study. For efficiency studies, tracks are reconstructed using only telescope chambers information. When the extrapolated track intercepts the studied detector near a known dead strip or a noisy region, the event is rejected. The efficiencies were calculated for different run conditions. Figure 7.12 shows, for the three resistive detectors, the efficiency as a function of the distance between the measured hit and the expected position (ΔX or ΔY), for a run with $\mathrm{HV_{mesh}} = 350$ V. An efficiency better than 95% is reached in all cases at $\pm 5\ \sigma_{\mathrm{Mm}}$.

(a) R-strip 300 $k\Omega$, 0.5 mm (b) R-strip 300 $k\Omega$, 1.0 mm (c) R-strip to ground, 1.0 mm

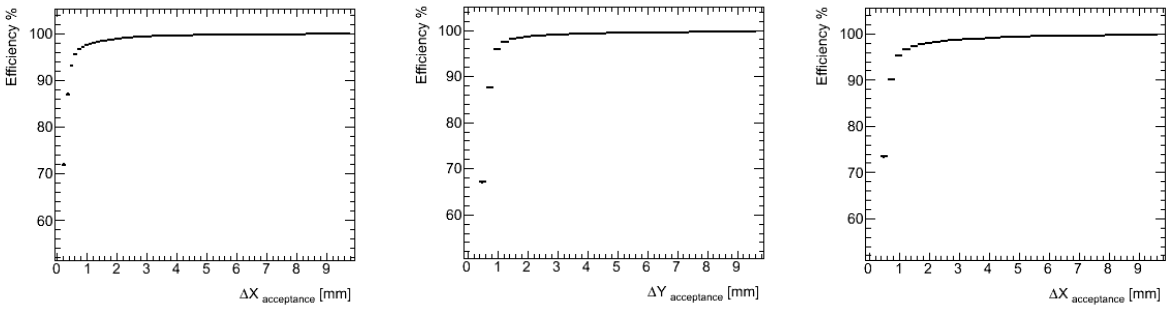

Figure 7.12: The reconstruction efficiency of the Micromegas as a function of the distance requirement between the reference and the reconstructed track. The efficiencies for all three detectors are grater than 95% at 5 σ_{Mm}

Figure 7.13 summarizes the efficiency results as a function of the mesh HV ($\mathrm{HV_{mesh}}$). The detection efficiency increases with the $\mathrm{HV_{mesh}}$ until a value close to ~98% is reached. The detector with resistive strips connected to the ground provides the best efficiency

results.

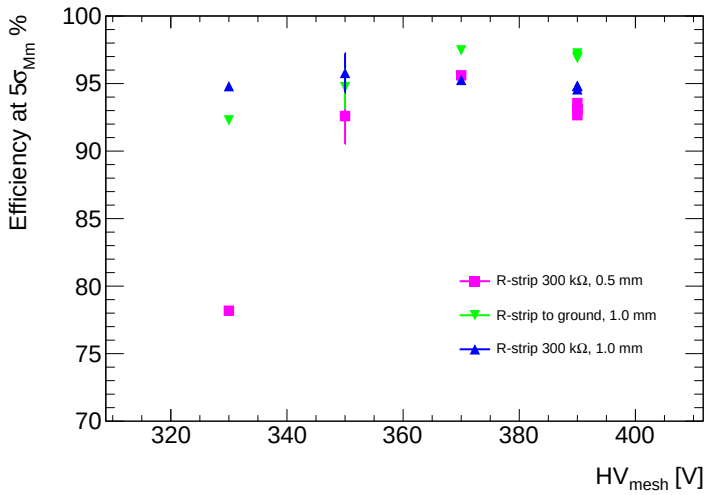

Figure 7.13: Efficiency at $\pm 5\ \sigma_{\mathrm{Mm}}$ as a function of the micro-mesh high voltage for three of the technologies tested. The detection efficiency increases with the micro-mesh voltage set until a value close to 98% is reached.

The efficiency results for all tested detectors have shown a dependence on the operating conditions and even at high gain it depends on the track position with respect to the pillars. Figure 7.14 shows the expected impact point for the "R-strip to ground" (R17) detector, when a track is reconstructed by the detector inside a $\pm 5\ \sigma_{\mathrm{Mm}}$ window around the expected point. This is an efficiency map where the dead areas can be clearly identified as white spots. The regular white spots structure corresponds to the pillars supporting the mesh, which are arranged in a regular matrix with a neighboring pillars distance of $\sim$2.5 *mm* in x and y.

Since the usual case in ATLAS is to have inclined tracks traversing the detectors, for some runs the resistive Micromegas were rotated in order to get tracks with different incidence angles. As illustrated in Fig. 7.15 for inclined tracks, the charged particle will traverse a larger gas volume creating more primary electrons. The shower in the amplification region will be wider and the charge will be spread over a larger number of strips. The total number of strips contributing to a track signal depends on the track angle, strip pitch, and drift gap thickness.

Figure 7.16 shows for the "R-strip to ground" R17 detector, the efficiency for different $\mathrm{HV_{mesh}}$ values and incidence track angle. For perpendicular tracks (0° angle) the efficiency is of the order of $\sim$98%. The main inefficiency is due to dead areas coming from pillars supporting the mesh. For inclined tracks the measured efficiency is around $\sim$98%. So the efficiency for inclined tracks measured remains almost the same and can be even better for some HV values. For the three detectors tested the "R-strip to ground" (R17) has shown to have the best efficiency results.

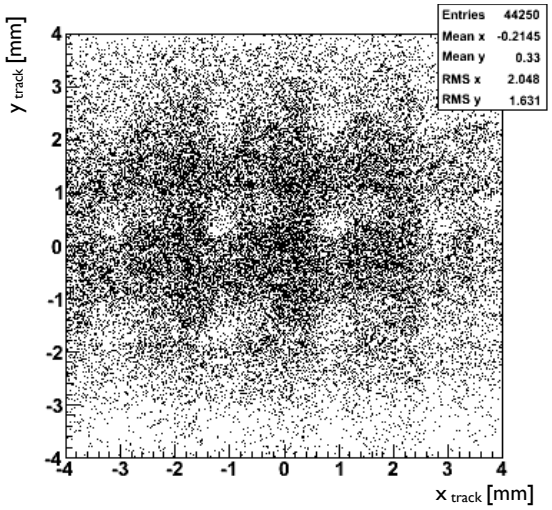

Figure 7.14: Efficiency map for the "R-strip to ground" (R17) detector. The regular white spots are dead areas and correspond to the pillars supporting the mesh. They are arranged in a regular matrix with a distance between pillars of ∼2.5 *mm* in x and y.

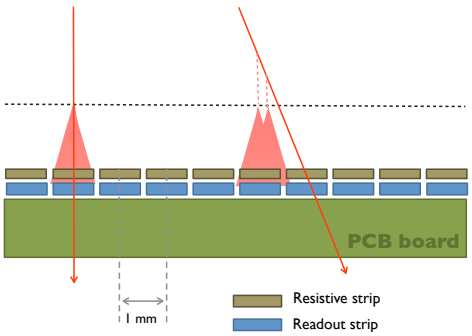

Figure 7.15: Example of the shower induced by a perpendicular and an inclined track. Since the inclined track traverse a larger gas volume, it can create more primary electrons creating larger showers.

7.5.3 Sparking behavior

As already mentioned, sparks are a major concern for Micromegas applications at the LHC. A resistive protection was implemented in order to limit the spark discharge currents, to a level such that the drops of the mesh HV becomes insignificant.

The HV and the currents were monitored and recorded whenever a HV or current value changed. Figure 7.17 shows the monitored HV and currents for one standard chamber on the left, and for the "R-strip to ground" resistive chamber (R17) on the right. Both chambers had same beam exposure and different mesh HV settings (both with a gain $\sim 10^4$). The resistive chamber worked correctly up to the highest gas gains, while the

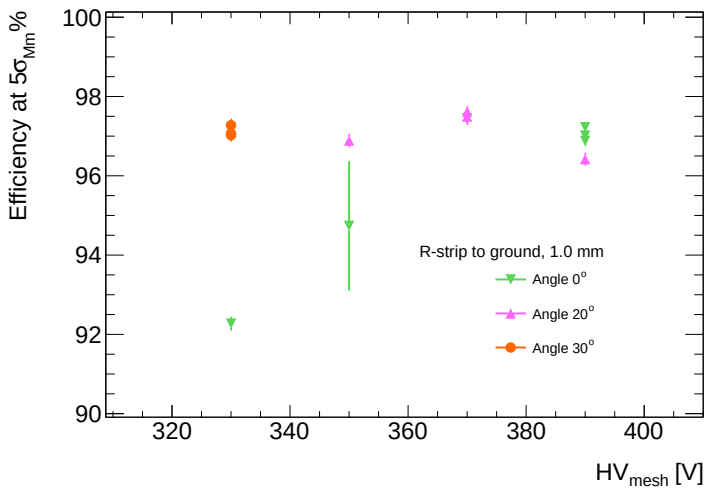

Figure 7.16: For the "R-strip to ground" detector the efficiency at $\pm 5\ \sigma_{\mathrm{Mm}}$ is shown as a function of the mesh High Voltage for different particle incidence angle.

non-resistive chamber shows very often HV breakdowns. For the standard Micromegas a discharge induces HV drops (as current leakage) and for the resistive detector, no HV drops were seen and neither was a current leakage. The occasional current spikes seen for the resistive detector are related to the HV setting, and not to sparks.

All four resistive chambers produced clean data, and had no HV breakdowns, while the spark currents did not exceed a few 100 nA [109].

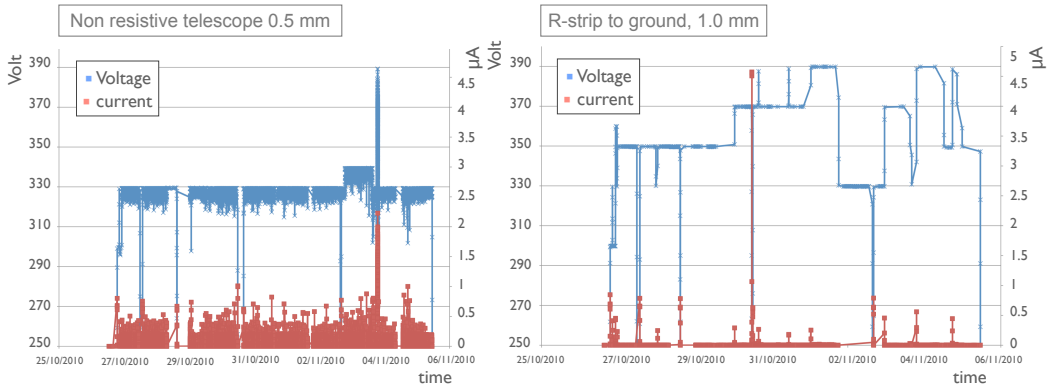

Figure 7.17: The monitored HV and currents as a function of the mesh HV during the test beam of autumn 2010 for a non-resistive Micromegas (left) and the chamber with resistive strips to ground R17 (right). The continuous line shows the HV, while points represent the current. A spark induce a HV drop and a current will be recorded.

7.6 Conclusion

The performance of four resistive bulk-Micromegas detectors have been studied using a ∼120 GeV pion beam of the CERN SPS. The data were collected during the autumn of 2010, with the main objective of studying the spatial resolution and efficiency of these detectors.

Four different strip pitch have been tested (see Table 7.1) . It was found that the resolution degrades if the strip pitch is too wide with respect to the avalanche size due to insufficient charge sharing between readout strips. In order to reduce the systematic errors, a different cluster reconstruction algorithm was implemented which takes into account the discretization problem. Therefore for the 0.5 mm strip pitch, this kind of systematic errors are not seen and it is possible to achieve a resolution of 88 μm, with a ∼98% of efficiency.

Three different resistive techniques were tested, inducing no degradation on the efficiency neither on the resolution with respect to the standard Micromegas. During the test beam the HV and currents were monitored. All four resistive chambers produced clean data, had no HV breakdowns, and the spark currents did not exceed a few 100 nA. This proves that the resistive coating is able to contain or even suppress the spark signal and therefore avoid deadtime.

For the three technologies tested the "R-strip to ground" detector has the best efficiency (∼98% at 5 σ_{mM}). This technology has also undergone extensive tests with hadron beams at the CERN-SPS, X-rays, as well as in a neutron beam. In addition, four 10×10 cm^2 Micromegas chambers have been installed in the ATLAS cavern and are taking data under LHC conditions.

The "R-strip to ground" technology shows excellent rate capability, spatial resolution, and efficiency. A resolution of the order of 100 μm is achieved [110], allowing pattern recognition and track reconstruction. The spark protection system with resistive strips is efficient, sparks are no longer an issue [104, 110]. Large-area resistive-strip chambers have been successfully built and show excellent performance. Aging tests with a beam of thermal neutrons and also with an X-ray beam, showed no deterioration of the detector after an exposure far above the levels that will be reached at the HL-LHC during 5 years of operation [111, 112].

After all those studies, the resistive Micromegas technology "R-strip to ground" is able to fulfill all of the ATLAS requirements [113], and was proposed for the ATLAS upgrade to equip the new Small Wheel (NSW).

At the beginning of 2012, after discussions and reviews, the ATLAS Muon Collaboration decided to follow the proposal. The NSW will be built with a total of eight planes of Micromegas detectors, corresponding to a total detector area of 1200 m^2. In addition to the Micromegas, the NSW will also be equipped with eight planes of thin-gap multi-wire detectors, called sTGC, such as to create a fully redundant system of sTGCs and Micromegas, both for triggering and tracking. The NSW is expected to be installed during

the LHC shutdown planned for 2018.

Conclusions and Perspectives

A measurement of the $W^{\pm}Z$ diboson production has been performed, using the fully leptonic decay channel, $W^{\pm}Z \to \ell\nu\ell\ell$ with $\ell = \mu$ and e. Two different LHC datasets of proton-proton collisions were used, 4.64 fb^{-1} at a center-of-mass energy of 7 TeV and 13 fb^{-1} at 8 TeV. The total production cross section, as well as the fiducial cross section inside the ATLAS detector fiducial volume were measured. These measurements were found to be in good agreement with the Standard Model predictions. In the 8 TeV data, for the first time, systematic errors on the cross-section were dominant, the Data-Driven background estimation being the dominant one.

On the 7 TeV dataset one-dimensional and two-dimensional limits at 95% confidence level on the anomalous triple gauge couplings Δg_1^Z, $\Delta\kappa^Z$ and λ were extracted using the transverse momentum spectrum of Z bosons. The limits, compared with Tevatron results, are already competitive.

The $W^{\pm}Z$ analysis is currently underway using the full 20 fb^{-1} of data collected in 2012. The increased dataset will allow for precise studies of data control regions, thus allowing a reduction in the systematic uncertainties associated with the Data-Driven methods. The aTGC analysis will also benefit greatly from increasing the size of the dataset. Nevertheless the sensitivity $W^{\pm}Z$ analysis with the full 8 TeV dataset is still low. The charged couplings are also accessible through the $W\gamma$ channel, this is the channel with the highest statistics, even thought the sensitivity with the 20 fb^{-1} is still low. It will be possible to start probing the "interesting" range ($\Delta\kappa_\gamma \sim 0.01$ and $\lambda_\gamma \sim 0.001$), with $\gtrsim 100$ fb^{-1} at the design energy of 14 TeV.

In March 2013 the LHC was stopped in order to prepare the machine for the next step: reaching the design energy of 14 TeV (or close to it) and the design luminosity 10^{34} cm^{-2}s^{-1}. This will make possible to collect an integrated luminosity of about 40 fb^{-1} per year of run. The plans for the HL-LHC and ATLAS upgrade are already advancing, and it is expected that by the end of Phase-II ($\sim$ 2023) the accelerator will reach an instantaneous luminosity of 10^{35} cm^{-2}s^{-1}. The goal is to accumulate 3000 fb^{-1} of data by 2030.

Precision tests of the SM will benefit from the high statistics of data that might be collected. The anomalous parameters also have an $\sqrt{s}$ dependence, so higher center-of-mass energies can greatly enhance the sensitivity to anomalous triple-gauge-boson couplings.

Finally in the last part of the thesis I presented my contribution on the R&D activity of the MAMMA (Muon Atlas MicroMegas Activity) group. My work was part of a large number of studies done to prove the Micromegas capability of high precision tracking in the HL-LHC environment. That effort lead Micromegas detectors to be proposed for the New Small Wheel (NSW) .Early 2012, the ATLAS Muon Collaboration decided to follow the MAMMA proposal. In total, eight planes of Micromegas detectors covering the full NSW should be installed during the LHC shutdown foreseen in 2018.

The LHC experiments have already entered new territory with their first measurements. The results so far have included the validation of many aspects of the Standard Model of particles and the discovery of the Higgs boson. Furthermore, the LHC experiments are sensitive to a broad spectrum of signatures that may indicate phenomena whose explanation lies beyond the Standard Model. We thus have reasons to be excited about the possible discoveries that ATLAS and CMS will make in the coming years.

In parallel the LHC and its detectors, are being prepared for a luminosity upgrade which means that a significant amount of work is still needed to prepare the detector and the analysis tools for the future. In conclusion I must say that this is “a great time to do physics” .

Appendix A

MC Samples

A.0.1 Monte Carlo samples for the 7 TeV analysis

The $W^{\pm}Z$ production processes and subsequent pure leptonic decays were modeled by the MC@NLO 4.0 [69]. The MC@NLO MC generator uses a parton density function (PDF) set CT10, which incorporates the next-to-leading-order (NLO) QCD matrix elements into the parton shower by interfacing to the HERWIG/JIMMY [71] program. The $W^{\pm}Z$ decays into τ leptons are included in dedicated MC samples and these τ leptons decay to all known final states.

Two sets of $W^{\pm}Z$ MC samples were generated, one with the SM couplings and the other with anomalous coupling $\Delta g = 0$, $\Delta\kappa = 0$, $\lambda = 0.13$. The SM samples are used in the cross section analysis to calculate the acceptance and efficiency of the selection, while the samples including anomalous couplings are used in the aTGC analysis.

Table A.1 lists the signal samples used in the 7 TeV analysis, the generator names, the total number of MC events produced, k-factors, the generator level filter efficiencies and corresponding cross sections. In the case a filter efficiency is listed in the table, the cross section is the unfiltered one, and the final filtered cross section is the product of the filter efficiency and the unfiltered cross section.

In the $W^{\pm}Z$ selection the major backgrounds come from jets associated with W or Z gauge bosons, diboson production of ZZ pairs, diboson production of a W or Z in association with a photon, and top events. ($t\bar{t}$, $t\bar{t}$ + W/Z and single top). We use MC@NLO to model the $t\bar{t}$ and single top events and ALPGEN/JIMMY [72] (Table A.5) to model the W/Z+jets background (Z+jets, Tables A.3; W+jets Table A.2). Whenever LO event generators are used, the cross sections are corrected by linearly scaling the LO cross section to NLO or NNLO (if available) matrix element calculations. The scaling factors are denoted k-factors, and are listed in the tables. The diboson processes WW, ZZ are modeled with HERWIG and PYTHIA respectively. The $W/Z + \gamma$ is modeled with Sherpa (Table A.4).

$\sqrt{s}$	Process	Generator	Events	k-factor	ϵ_{filter}	Cross-section [pb]
7 TeV	$W^+Z \to e\nu ee$	MC@NLO	49999	1.0	1.0	0.04114
	$W^-Z \to e\nu ee$	MC@NLO	50000	1.0	1.0	0.02243
	$W^+Z \to e\nu\mu\mu$	MC@NLO	49999	1.0	1.0	0.04114
	$W^-Z \to e\nu\mu\mu$	MC@NLO	49900	1.0	1.0	0.02243
	$W^+Z \to e\nu\tau\tau$	MC@NLO	50000	1.0	1.0	0.04114
	$W^-Z \to e\nu\tau\tau$	MC@NLO	49950	1.0	1.0	0.02243
	$W^+Z \to \mu\nu ee$	MC@NLO	49999	1.0	1.0	0.04114
	$W^-Z \to \mu\nu ee$	MC@NLO	50000	1.0	1.0	0.02243
	$W^+Z \to \mu\nu\mu\mu$	MC@NLO	49950	1.0	1.0	0.04114
	$W^-Z \to \mu\nu\mu\mu$	MC@NLO	50000	1.0	1.0	0.02243
	$W^+Z \to \mu\nu\tau\tau$	MC@NLO	49950	1.0	1.0	0.04114
	$W^-Z \to \mu\nu\tau\tau$	MC@NLO	50000	1.0	1.0	0.02243
	$W^+Z \to \tau\nu ee$	MC@NLO	49999	1.0	1.0	0.04114
	$W^-Z \to \tau\nu ee$	MC@NLO	49949	1.0	1.0	0.02243
	$W^+Z \to \tau\nu\mu\mu$	MC@NLO	50000	1.0	1.0	0.04114
	$W^-Z \to \tau\nu\mu\mu$	MC@NLO	50000	1.0	1.0	0.02243
	$W^+Z \to \tau\nu\tau\tau$	MC@NLO	49950	1.0	1.0	0.04114
	$W^-Z \to \tau\nu\tau\tau$	MC@NLO	50000	1.0	1.0	0.02243
	aTGC $W^+Z \to \ell\nu\ell\ell$	MC@NLO	$\approx$ 49995	1.0	1.0	0.05516
	aTGC $W^-Z \to \ell\nu\ell\ell$	MC@NLO	$\approx$ 49995	1.0	1.0	0.02849

Table A.1: The $W^{\pm}Z$ signal production processes, cross-sections and numbers of fully simulated MC events used in the 7 TeV analysis. The MC simulation "filter" is an event selection at the generator level. The corresponding filter efficiencies are given in the table. The listed cross sections do not include k-factors nor filter efficiencies. We also indicate the MC generators used to produce the MC events. For the last two signal samples ℓ denotes e, μ and τ, those samples were produced at aTGC values $\Delta g = 0$, $\Delta\kappa = 0$, $\lambda = 0.13$

$\sqrt{s}$	Process	Generator	Events	k-factor	ϵ_{filter}	Cross-section [pb]
7 TeV	W$e\nu$Np0	Alpgen	6952874	1.2	1.0	6921.60
	W$e\nu$Np1	Alpgen	4998487	1.2	1.0	1304.30
	W$e\nu$Np2	Alpgen	3768632	1.2	1.0	378.29
	W$e\nu$Np3	Alpgen	1008947	1.2	1.0	101.43
	W$e\nu$Np4	Alpgen	250000	1.2	1.0	25.87
	W$e\nu$Np5	Alpgen	69999	1.2	1.0	7.0
	W$\mu\nu$Np0	Alpgen	3462942	1.2	1.0	6919.60
	W$\mu\nu$Np1	Alpgen	4998236	1.2	1.0	1304.20
	W$\mu\nu$Np2	Alpgen	3768737	1.2	1.0	377.83
	W$\mu\nu$Np3	Alpgen	1008446	1.2	1.0	101.88
	W$\mu\nu$Np4	Alpgen	254950	1.2	1.0	25.75
	W$\mu\nu$Np5	Alpgen	70000	1.2	1.0	6.92
	W$\tau\nu$Np0	Alpgen	3418296	1.2	1.0	6918.60
	W$\tau\nu$Np1	Alpgen	2499194	1.2	1.0	1303.20
	W$\tau\nu$Np2	Alpgen	3750986	1.2	1.0	378.18
	W$\tau\nu$Np3	Alpgen	1009946	1.2	1.0	101.51
	W$\tau\nu$Np4	Alpgen	249998	1.2	1.0	25.64
	W$\tau\nu$Np5	Alpgen	65000	1.2	1.0	7.04

Table A.2: MC samples/processes used to model W+jets in the 7 TeV analysis. For each process the corresponding generator names, total numbers, k-factors, generator level filter efficiencies and cross-sections of events are shown. The listed cross sections do not include k-factors nor filter efficiencies.

$\sqrt{s}$	Generator	Events	k-factor	ϵ_{filter}	Cross-section [pb]	
7 TeV	ZeeNp0	Alpgen	6618284	1.25	1.0	668.32
	ZeeNp1	Alpgen	1334897	1.25	1.0	134.36
	ZeeNp2	Alpgen	2004195	1.25	1.0	40.54
	ZeeNp3	Alpgen	549949	1.25	1.0	11.16
	ZeeNp4	Alpgen	149948	1.25	1.0	2.88
	ZeeNp5	Alpgen	50000	1.25	1.0	0.83
	Z$\mu\mu$Np0	Alpgen	6615230	1.25	1.0	668.68
	Z$\mu\mu$Np1	Alpgen	1334296	1.25	1.0	134.14
	Z$\mu\mu$Np2	Alpgen	1999941	1.25	1.0	40.33
	Z$\mu\mu$Np3	Alpgen	549896	1.25	1.0	11.19
	Z$\mu\mu$Np4	Alpgen	150000	1.25	1.0	2.75
	Z$\mu\mu$Np5	Alpgen	50000	1.25	1.0	0.77
	Z$\tau\tau$Np0	Alpgen	10613179	1.25	1.0	668.40
	Z$\tau\tau$Np1	Alpgen	3334137	1.25	1.0	134.81
	Z$\tau\tau$Np2	Alpgen	1004847	1.25	1.0	40.36
	Z$\tau\tau$Np3	Alpgen	509847	1.25	1.0	11.25
	Z$\tau\tau$Np4	Alpgen	144999	1.25	1.0	2.79
	Z$\tau\tau$Np5	Alpgen	45000	1.25	1.0	0.77
	ZeebbNp0_nofilter	Alpgen/Jimmy	409999	1.25	1.0	6.57
	ZeebbNp1_nofilter	Alpgen/Jimmy	160000	1.25	1.0	2.48
	ZeebbNp2_nofilter	Alpgen/Jimmy	60000	1.25	1.0	0.89
	ZeebbNp3_nofilter	Alpgen/Jimmy	30000	1.25	1.0	0.39
	Z$\mu\mu$bbNp0_nofilter	Alpgen/Jimmy	409949	1.25	1.0	6.56
	Z$\mu\mu$bbNp1_nofilter	Alpgen/Jimmy	155000	1.25	1.0	2.47
	Z$\mu\mu$bbNp2_nofilter	Alpgen/Jimmy	60000	1.25	1.0	0.89
	Z$\mu\mu$bbNp3_nofilter	Alpgen/Jimmy	29999	1.25	1.0	0.39
	ZeeNp0 M10to40 pt20	Alpgen/Jimmy	994949	1.22	1.0	3051.62
	ZeeNp1 M10to40 pt20	Alpgen/Jimmy	299998	1.22	1.0	87.87
	ZeeNp2 M10to40 pt20	Alpgen/Jimmy	999946	1.22	1.0	41.10
	ZeeNp3 M10to40 pt20	Alpgen/Jimmy	149998	1.22	1.0	8.38
	ZeeNp4 M10to40 pt20	Alpgen/Jimmy	40000	1.22	1.0	1.85
	ZeeNp5 M10to40 pt20	Alpgen/Jimmy	10000	1.22	1.0	0.46
	Z$\mu\mu$Np0 M10to40 pt20	Alpgen/Jimmy	999849	1.22	1.0	3051.62
	Z$\mu\mu$Np1 M10to40 pt20	Alpgen/Jimmy	300000	1.22	1.0	87.87
	Z$\mu\mu$Np2 M10to40 pt20	Alpgen/Jimmy	999995	1.22	1.0	41.45
	Z$\mu\mu$Np3 M10to40 pt20	Alpgen/Jimmy	150000	1.22	1.0	8.38
	Z$\mu\mu$Np4 M10to40 pt20	Alpgen/Jimmy	39999	1.22	1.0	1.85
	Z$\mu\mu$Np5 M10to40 pt20	Alpgen/Jimmy	10000	1.22	1.0	0.46

Table A.3: MC samples/processes used to model Z+jets samples on the 7 TeV analysis. For each process the corresponding generator names, total numbers, k-factors, generator level filter efficiencies and cross-sections of events are shown. The listed cross sections do not include k-factors nor filter efficiencies.

$\sqrt{s}$	Process	Generator	Events	k-factor	ϵ_{filter}	Cross-section [pb]
7 TeV	WW	Herwig	2489244	1.52	0.38863	29.592
	ZZ	Pythia	149999	1.40	0.6235	0.07494
	Z$ee\gamma$_1jet	Sherpa	199899	1.0	1.0	14.7
	Z$\mu\mu\gamma$_1jet	Sherpa	199950	1.0	1.0	14.7
	Z($\tau\tau$) γ	Pythia,MadGraph	49949	1.41	0.15	9.41
	W$e\nu\gamma$_1jet	Sherpa	399899	1.0	1.0	75.5
	W$\mu\nu\gamma$_1jet	Sherpa	399948	1.0	1.0	75.5
	$W^+(\tau)$ γ	Pythia,MadGraph	49999	1.75	1.0	25.4
	$W^-(\tau)$ γ	Pythia,MadGraph	50000	1.83	1.0	16.8

Table A.4: MC samples/processes used to model diboson backgrounds, including WW, ZZ, $W\gamma$ and $Z\gamma$, in the 7 TeV and 8 TeV analysis. For each process the corresponding generator names, total numbers, k-factors, generator level filter efficiencies and cross-sections of events are shown. The listed cross sections do not include k-factors nor filter efficiencies.

$\sqrt{s}$	Process	Generator	events	k-factor	ϵ_{filter}	Cross-section [pb]
7 TeV	$t\bar{t}$	MC@NLO	14983835	1.0	0.55551	166.8
	$t\bar{t} + W^{\pm}$	MadGraph	100000	1.3	1.0	0.12444
	$t\bar{t} + Z$	MadGraph	99997	1.3	1.0	0.095581
	$t\bar{t}$	MC@NLO	199861	1.0	0.5562	1.6457E+2
	t-channel→e	MC@NLO	299998	1.0	1.0	7.1522
	t-channel→ μ	MC@NLO	299999	1.0	1.0	7.1767
	t-channel→ τ	MC@NLO	299999	1.0	1.0	7.1277
	s-channel→e	MC@NLO	299948	1.0	1.0	0.46856
	s-channel→ μ	MC@NLO	299998	1.0	1.0	0.46837
	s-channel→ τ	MC@NLO	299899	1.0	1.0	0.46978
	Wt	MC@NLO	899694	1.0	1.0	13.102

Table A.5: MC samples/processes used to model top (including $t\bar{t}$ and single top) and dijet backgrounds in the 7 TeV analysis. For each process the corresponding generator names, total numbers, k-factors, generator level filter efficiencies and cross-sections of events are shown. The listed cross sections do not include k-factors nor filter efficiencies.

A.0.2 Monte Carlo samples for the 8 TeV analysis

The Monte Carlo samples used on the 8 TeV analysis, are listed in the following Tables. Table A.6 lists the signal samples, the generator names, the total number of MC events produced, k-factor, the generator level filter efficiencies and corresponding cross sections. In the case a filter efficiency is listed in the table, the cross section is the unfiltered one, and the final filtered cross section is the product of the filter efficiency and the unfiltered cross section. The different generators used to model the W/Z+jets background are presented in Table A.7 for W+jets; and Table A.9 for Z+jets. The diboson processes WW, ZZ are modeled with MC@NLO and PowhegPythia8. The $W/Z + \gamma$ is modeled with Alpgen and Sherpa (Table A.10). MC@NLO is used to model the $t\bar{t}$ and single top events (Table A.8).

$\sqrt{s}$	Process	Generator	Events	k-factor	ϵ_{filter}	Cross-section [pb]
8 TeV	$W^+Z \to e\nu ee$	PowhegPythia8	190000	1.0	0.29456	1.4070
	$W^+Z \to e\nu\mu\mu$	PowhegPythia8	190000	1.0	0.35211	0.9382
	$W^+Z \to e\nu\tau\tau$	PowhegPythia8	76000	1.0	0.16682	0.1746
	$W^+Z \to \mu\nu ee$	PowhegPythia8	189999	1.0	0.29351	1.3990
	$W^+Z \to \mu\nu\mu\mu$	PowhegPythia8	190000	1.0	0.35132	0.9537
	$W^+Z \to \mu\nu\tau\tau$	PowhegPythia8	76000	1.0	0.16863	0.1746
	$W^+Z \to \tau\nu ee$	PowhegPythia8	75400	1.0	0.14289	1.3990
	$W^+Z \to \tau\nu\mu\mu$	PowhegPythia8	76000	1.0	0.18256	0.9382
	$W^+Z \to \tau\nu\tau\tau$	PowhegPythia8	19000	1.0	0.05851	0.1719
	$W^-Z \to e\nu ee$	PowhegPythia8	189899	1.0	0.29694	0.9795
	$W^-Z \to e\nu\mu\mu$	PowhegPythia8	190000	1.0	0.35302	0.6390
	$W^-Z \to e\nu\tau\tau$	PowhegPythia8	76000	1.0	0.15969	0.1125
	$W^-Z \to \mu\nu ee$	PowhegPythia8	190000	1.0	0.29766	0.9359
	$W^-Z \to \mu\nu\mu\mu$	PowhegPythia8	190000	1.0	0.35414	0.6488
	$W^-Z \to \mu\nu\tau\tau$	PowhegPythia8	76000	1.0	0.16023	0.1125
	$W^-Z \to \tau\nu ee$	PowhegPythia8	76000	1.0	0.14803	0.9359
	$W^-Z \to \tau\nu\mu\mu$	PowhegPythia8	76000	1.0	0.18657	0.6390
	$W^-Z \to \tau\nu\tau\tau$	PowhegPythia8	19000	1.0	0.05665	0.1107

Table A.6: The $W^{\pm}Z$ signal production processes, cross-sections and numbers of fully simulated MC events used on the 8 TeV analysis. The MC simulation "filter" is an event selection at the generator level. The corresponding filter efficiencies are given in the table. The listed cross sections do not include k-factors nor filter efficiencies. We also indicate the MC generators used to produce the MC events.

$\sqrt{s}$	Process	Generator	Events	k-factor	ϵ_{filter}	Cross-section [pb]
8 TeV	W$e\nu$Np0	ALPGEN/JIMMY	3459894	1.19	1.0	8037.1
	W$e\nu$Np1	ALPGEN/JIMMY	2499491	1.19	1.0	1579.2
	W$e\nu$Np2	ALPGEN/JIMMY	3769487	1.19	1.0	477.20
	W$e\nu$Np3	ALPGEN/JIMMY	1009997	1.19	1.0	133.93
	W$e\nu$Np4	ALPGEN/JIMMY	249999	1.19	1.0	35.622
	W$e\nu$Np5	ALPGEN/JIMMY	70000	1.19	1.0	10.553
	W$\mu\nu$Np0	ALPGEN/JIMMY	3469692	1.19	1.0	8040.0
	W$\mu\nu$Np1	ALPGEN/JIMMY	2499694	1.19	1.0	1580.3
	W$\mu\nu$Np2	ALPGEN/JIMMY	3764886	1.19	1.0	477.50
	W$\mu\nu$Np3	ALPGEN/JIMMY	1006698	1.19	1.0	133.94
	W$\mu\nu$Np4	ALPGEN/JIMMY	254999	1.19	1.0	35.636
	W$\mu\nu$Np5	ALPGEN/JIMMY	69900	1.19	1.0	10.571
	W$\tau\nu$Np0	ALPGEN/JIMMY	3419992	1.19	1.0	8035.8
	W$\tau\nu$Np1	ALPGEN/JIMMY	2499793	1.19	1.0	1579.8
	W$\tau\nu$Np2	ALPGEN/JIMMY	3765989	1.19	1.0	477.55
	W$\tau\nu$Np3	ALPGEN/JIMMY	1009998	1.19	1.0	133.79
	W$\tau\nu$Np4	ALPGEN/JIMMY	249998	1.19	1.0	35.583
	W$\tau\nu$Np5	ALPGEN/JIMMY	65000	1.19	1.0	10.540

Table A.7: MC samples/processes used to model W+jets on the 8 TeV analysis. For each process the corresponding generator names, total numbers, k-factors, generator level filter efficiencies and cross-sections of events are shown. The listed cross sections do not include k-factors nor filter efficiencies.

$\sqrt{s}$	Process	Generator	events	k-factor	ϵ_{filter}	Cross-section [pb]
8 TeV	$t\bar{t}$	MC@NLO	9977338	1.0	0.105	238.06
	$t\bar{t} + W^{\pm}$	MADGRAPH	400000	1.18	1.0	0.1041
	$t\bar{t} + Z$	MADGRAPH	400000	1.34	1.0	0.06769
	t-channel→e	AcerMCPythia	299999	1.0	1.0	9.48
	t-channel→ μ	AcerMCPythia	299999	1.0	1.0	9.48
	t-channel→ τ	AcerMCPythia	299999	1.0	1.0	9.48
	s-channel→e	MC@NLO	199899	1.0	1.0	0.606
	s-channel→ μ	MC@NLO	199799	1.0	1.0	0.606
	s-channel→ τ	MC@NLO	999699	1.0	1.0	0.606

Table A.8: MC samples/processes used to model top (including $t\bar{t}$ and single top) and dijet backgrounds on the 8 TeV analysis. For each process the corresponding generator names, total numbers, k-factors, generator level filter efficiencies and cross-sections of events are shown. The listed cross sections do not include k-factors nor filter efficiencies.

$\sqrt{s}$	Generator	Events	k-factor	ϵ_{filter}	Cross-section [pb]	
8TeV	ZeeNp0	Alpgen/Jimmy	6604283	1.23	1.0	711.77
	ZeeNp1	Alpgen/Jimmy	1329994	1.23	1.0	155.17
	ZeeNp2	Alpgen/Jimmy	404798	1.23	1.0	48.745
	ZeeNp3	Alpgen/Jimmy	109998	1.23	1.0	14.225
	ZeeNp4	Alpgen/Jimmy	30000	1.23	1.0	3.7595
	ZeeNp5	Alpgen/Jimmy	10000	1.23	1.0	1.0945
	Z$\mu\mu$Np0	Alpgen/Jimmy	6609982	1.23	1.0	712.11
	Z$\mu\mu$Np1	Alpgen/Jimmy	1334897	1.23	1.0	154.77
	Z$\mu\mu$Np2	Alpgen/Jimmy	404897	1.23	1.0	48.912
	Z$\mu\mu$Np3	Alpgen/Jimmy	110000	1.23	1.0	14.226
	Z$\mu\mu$Np4	Alpgen/Jimmy	29999	1.23	1.0	3.7838
	Z$\mu\mu$Np5	Alpgen/Jimmy	10000	1.23	1.0	1.1148
	Z$\tau\tau$Np0	Alpgen/Jimmy	6605586	1.23	1.0	711.81
	Z$\tau\tau$Np1	Alpgen/Jimmy	1334896	1.23	1.0	155.13
	Z$\tau\tau$Np2	Alpgen/Jimmy	404900	1.23	1.0	48.804
	Z$\tau\tau$Np3	Alpgen/Jimmy	110000	1.23	1.0	14.160
	Z$\tau\tau$Np4	Alpgen/Jimmy	28999	1.23	1.0	3.7744
	Z$\tau\tau$Np5	Alpgen/Jimmy	10000	1.23	1.0	1.1163
	ZeebbNp1_nofilter	Alpgen/Jimmy	80000	1.0	1.0	3.25
	ZeebbNp2_nofilter	Alpgen/Jimmy	45000	1.0	1.0	1.19
	ZeebbNp3_nofilter	Alpgen/Jimmy	5000	1.0	1.0	0.50
	Z$\mu\mu$bbNp0_nofilter	Alpgen/Jimmy	150000	1.0	1.0	8.37
	Z$\mu\mu$bbNp1_nofilter	Alpgen/Jimmy	80000	1.0	1.0	3.25
	Z$\mu\mu$bbNp2_nofilter	Alpgen/Jimmy	45000	1.0	1.0	1.18
	Z$\mu\mu$bbNp3_nofilter	Alpgen/Jimmy	5000	1.0	1.0	0.51
	Z$\tau\tau$bbNp0_nofilter	Alpgen/Jimmy	150000	1.0	1.0	8.38
	Z$\tau\tau$bbNp1_nofilter	Alpgen/Jimmy	80000	1.0	1.0	3.24
	Z$\tau\tau$bbNp2_nofilter	Alpgen/Jimmy	45000	1.0	1.0	1.19
	Z$\tau\tau$bbNp3_nofilter	Alpgen/Jimmy	5000	1.0	1.0	0.50
	ZeeNp0 M10to60	Alpgen/Jimmy	1000000	1.19	1.0	3477.2
	ZeeNp1 M10to60	Alpgen/Jimmy	300000	1.19	1.0	108.72
	ZeeNp2 M10to60	Alpgen/Jimmy	400000	1.19	1.0	52.77
	ZeeNp3 M10to60	Alpgen/Jimmy	150000	1.19	1.0	11.30
	ZeeNp4 M10to60	Alpgen/Jimmy	40000	1.19	1.0	0.26
	ZeeNp5 M10to60	Alpgen/Jimmy	110000	1.19	1.0	0.69
	Z$\mu\mu$Np0 M10to60	Alpgen/Jimmy	1000000	1.19	1.0	3477.1
	Z$\mu\mu$Np1 M10to60	Alpgen/Jimmy	300000	1.19	1.0	108.75
	Z$\mu\mu$Np2 M10to60	Alpgen/Jimmy	400000	1.19	1.0	52.73
	Z$\mu\mu$Np3 M10to60	Alpgen/Jimmy	150000	1.19	1.0	11.33
	Z$\mu\mu$Np4 M10to60	Alpgen/Jimmy	40000	1.19	1.0	2.59
	Z$\mu\mu$Np5 M10to60	Alpgen/Jimmy	120000	1.19	1.0	0.69

Table A.9: MC samples/processes used to model Z+jets samples on the 8 TeV analysis. For each process the corresponding generator names, total numbers, k-factors, generator level filter efficiencies and cross-sections of events are shown. The listed cross sections do not include k-factors nor filter efficiencies. The NpX (X = 0...5) in the process name refers to the number of additional partons in the final state.

$\sqrt{s}$	Process	Generator	Events	k-factor	ϵ_{filter}	Cross-section [pb]
8 TeV	$W^+W^- \to e\nu e\nu$	MC@NLO	199900	1.0	1.0	0.631
	$W^+W^- \to e\nu\mu\nu$	MC@NLO	199899	1.0	1.0	0.631
	$W^+W^- \to e\nu\tau\nu$	MC@NLO	199998	1.0	1.0	0.631
	$W^+W^- \to \mu\nu e\nu$	MC@NLO	200000	1.0	1.0	0.631
	$W^+W^- \to \mu\nu\mu\nu$	MC@NLO	198000	1.0	1.0	0.631
	$W^+W^- \to \mu\nu\tau\nu$	MC@NLO	199500	1.0	1.0	0.631
	$W^+W^- \to \tau\nu e\nu$	MC@NLO	199500	1.0	1.0	0.631
	$W^+W^- \to \tau\nu\mu\nu$	MC@NLO	199999	1.0	1.0	0.631
	$W^+W^- \to \tau\nu\tau\nu$	MC@NLO	199999	1.0	1.0	0.631
	$gg \to W^+W^- \to e\nu e\nu$	Jimmy	30000	1.0	1.0	0.018
	$gg \to W^+W^- \to e\nu\mu\nu$	Jimmy	30000	1.0	1.0	0.018
	$gg \to W^+W^- \to e\nu\tau\nu$	Jimmy	30000	1.0	1.0	0.018
	$gg \to W^+W^- \to \mu\nu e\nu$	Jimmy	30000	1.0	1.0	0.018
	$gg \to W^+W^- \to \mu\nu\mu\nu$	Jimmy	30000	1.0	1.0	0.018
	$gg \to W^+W^- \to \mu\nu\tau\nu$	Jimmy	29900	1.0	1.0	0.018
	$gg \to W^+W^- \to \tau\nu e\nu$	Jimmy	30000	1.0	1.0	0.018
	$gg \to W^+W^- \to \tau\nu\mu\nu$	Jimmy	30000	1.0	1.0	0.018
	$gg \to W^+W^- \to \tau\nu\tau\nu$	Jimmy	30000	1.0	1.0	0.018
	$ZZ \to eeee$	PowhegPythia8	599998	1.0	0.90765	0.0735
	$ZZ \to ee\mu\mu$	PowhegPythia8	599799	1.0	0.82724	0.1708
	$ZZ \to ee\tau\tau$	PowhegPythia8	599899	1.0	0.82724	0.1708
	$ZZ \to \mu\mu\mu\mu$	PowhegPythia8	600000	1.0	0.91241	0.0735
	$ZZ \to \mu\mu\tau\tau$	PowhegPythia8	600000	1.0	0.58725	0.1708
	$ZZ \to \tau\tau\tau\tau$	PowhegPythia8	300000	1.0	0.10604	0.0735
	$ZZ \to ee\nu\nu$	PowhegPythia8	298400	1.0	1.0	0.168
	$ZZ \to \mu\mu\nu\nu$	PowhegPythia8	300000	1.0	1.0	0.168
	$ZZ \to \tau\tau\nu\nu$	PowhegPythia8	299999	1.0	1.0	0.168
	$ggZZ \to eeee$	PowhegPythia8	90000	1.0	1.0	0.00075
	$ggZZ \to \mu\mu\mu\mu$	PowhegPythia8	89699	1.0	1.0	0.00075
	$ggZZ \to ee\mu\mu$	PowhegPythia8	89899	1.0	1.0	0.0015
	$Z(ee)\gamma$	Sherpa	1199795	1.0	1.0	32.261
	$Z(\mu\mu)\gamma$	Sherpa	1199596	1.0	1.0	32.317
	$W\gamma$Np0	Alpgen/Jimmy		1.15	1.0	230.09
	$W\gamma$Np1	Alpgen/Jimmy		1.15	1.0	59.343
	$W\gamma$Np2	Alpgen/Jimmy		1.15	1.0	21.469
	$W\gamma$Np3	Alpgen/Jimmy		1.15	1.0	7.1032
	$W\gamma$Np4	Alpgen/Jimmy		1.15	1.0	2.1224
	$W\gamma$Np5	Alpgen/Jimmy		1.15	1.0	0.4661

Table A.10: MC samples/processes used to model diboson backgrounds, including WW, ZZ, $W\gamma$ and $Z\gamma$, on the 8 TeV analysis. For each process the corresponding generator names, total numbers, k-factors, generator level filter efficiencies and cross-sections of events are shown. The listed cross sections do not include k-factors nor filter efficiencies.

Bibliography

[1] ATLAS Collaboration, *Measurement of WZ Production in Proton-Proton Collisions at* $\sqrt{s} = 7$ TeV *with the ATLAS detector*, Eur. Phys. J. C **72** (2012) 2173, arXiv:1208.1390 [hep-ex].

[2] ATLAS Collaboration, *A Measurement of WZ Production in Proton-Proton Collisions at* $\sqrt{s} = 8$ TeV *with the ATLAS Detector*, ATLAS-CONF-2013-021 (2013) , https://cds.cern.ch/record/1525557.

[3] F. Englert and R. Brout, *Broken Symmetry and the Mass of Gauge Vector Mesons*, Phys. Rev. Lett. **13** (1964) no. 9, 321–323.

[4] P. W. Higgs, *Broken Symmetries, Massless Particles and Gauge Fields*, Phys. Rev. Lett. **12** (1964) 132–133.

[5] S. Weinberg, *A Model of Leptons*, Phys. Rev. Lett. **19** (Nov, 1967) 1264–1266. http://link.aps.org/doi/10.1103/PhysRevLett.19.1264.

[6] S. L. Glashow, *Partial Symmetries of Weak Interactions*, Nucl. Phys. **22** (1961) 579–588.

[7] J. Goldstone, A. Salam, and S. Weinberg, *Broken Symmetries*, Phys. Rev. **127** (Aug, 1962) 965–970.

[8] S. L. Glashow, J. Iliopoulos, and L. Maiani, *Weak Interactions with Lepton-Hadron Symmetry*, Phys. Rev. **D2** (1970) 1285–1292.

[9] G. 't Hooft, *Renormalization of Massless Yang-Mills Fields*, Nucl. Phys. **B33** (1971) 173–199.

[10] G. 't Hooft and M. Veltman, *Regularization and renormalization of gauge fields*, Nuclear Physics B **44** (1972) no. 1, 189 – 213.

[11] D. J. Gross and F. Wilczek, *Asymptotically Free Gauge Theories. I*, Phys. Rev. D **8** (Nov, 1973) 3633–3652.

[12] H. D. Politzer, *Reliable Perturbative Results for Strong Interactions?*, Phys. Rev. Lett. **30** (Jun, 1973) 1346–1349.

[13] H. D. Politzer, *Asymptotic Freedom: An Approach to Strong Interactions*, Phys. Rept. **14** (1974) 129–180.

[14] M. E. Peskin and D. V. Schroeder, *An Introduction to Quantum Field Theory; 1995 ed.* Westview, Boulder, CO, 1995.

[15] Particle Data Group Collaboration, J. Beringer et al., *Review of Particle Physics* , Phys.Rev. **D86** (2012) 010001.

[16] ATLAS Collaboration, *Observation of a new particle in the search for the Standard Model Higgs boson with the ATLAS detector at the LHC*, Phys.Lett. **B716** (2012) 1–29, arXiv:1207.7214 [hep-ex].

[17] CMS Collaboration, S. Chatrchyan et al., *Observation of a new boson at a mass of 125 GeV with the CMS experiment at the LHC*, Phys.Lett. **B716** (2012) 30–61, arXiv:1207.7235 [hep-ex].

[18] J. M. Campbell, R. K. Ellis, and C. Williams, *Vector boson pair production at the LHC*, JHEP **1107** (2011) 018, arXiv:1105.0020 [hep-ph].

[19] P. Langacker, *The standard model and beyond*. High Energy Physics, Cosmology and Gravitation. Taylor and Francis, Boca Raton, FL, 2010.

[20] H. Baer, C.-h. Chen, F. Paige, and X. Tata, *Trileptons from chargino-neutralino production at the CERN Large Hadron Collider*, Phys. Rev. D **50** (Oct, 1994) 4508–4516. http://link.aps.org/doi/10.1103/PhysRevD.50.4508.

[21] ATLAS Collaboration, *Search for resonant $WZ \to l\nu ll$ production using $\sqrt{s}$ = 8 TeV pp collisions with ATLAS*, https://cds.cern.ch/record/1525522.

[22] CMS Collaboration, *Search for W' (or techni-rho) to WZ*, https://cds.cern.ch/record/1377329/.

[23] R. Foadi, M. T. Frandsen, T. A. Ryttov, and F. Sannino, *Minimal walking technicolor: Setup for collider physics*, Phys. Rev. D **76** (Sep, 2007) 055005. http://link.aps.org/doi/10.1103/PhysRevD.76.055005.

[24] K. Agashe, R. Contino, and A. Pomarol, *The minimal composite Higgs model*, Nuclear Physics B **719** (2005) no. 1-2, . http://www.sciencedirect.com/science/article/pii/S0550321305003445.

[25] M. Perelstein, *Little Higgs models and their phenomenology*, Progress in Particle and Nuclear Physics **58** (2007) no. 1, . http://www.sciencedirect.com/science/article/pii/S0146641006000469.

[26] G. Altarelli, B. Mele, and M. Ruiz-Altaba, *Searching for mew heavy vector bosons in $p\bar{p}$ collliders*, Z.Phys. **C45** (1989) 109.

[27] K. Hagiwara, R. D. Peccei, and D. Zeppenfeld, *Probing the Weak Boson Sector in $e^+e^- \to W^+W^-$*, Nucl. Phys. B **282** (1987) 253.

[28] J. Ellison and J. Wudka, *Study of Trilinear Gauge Boson Couplings at the Tevatron Collider*, Ann. Rev. Nucl. Part. Sci. **48** (1998) 33, arXiv:9804322 [hep-ph].

[29] J. Harvey and J. Polchinski, *Recent Directions in Particle Theory: From Superstrings and Black Holes to the Standard Model.* Proceedings of the 1992 Theoretical Advanced Study Institute in Elementary Particle Physics, Boulder, Colorado, 1992 (World Scientific, Singapore, 1993).

[30] CDF Collaboration, T. Aaltonen et al, *Measurement of the WZ cross section and triple gauge couplings in $p\overline{p}$ collisions at* $\sqrt{s}$=1.96 TeV, Phys. Rev. D **86** (2012) 031104.

[31] D0 Collaboration, V. M. Abazov et al., *Measurement of the $WZ \to \ell\nu\ell\ell$ Cross Section and Limits on Anomalous Triple Gauge Couplings in $p\bar{p}$ Collisions at $\sqrt{s}$ = 1.96 TeV*, Phys. Lett. B **695** (2011) 67, arXiv:1006.0761 [hep-ex].

[32] The D0 Collaboration, V. M. Abazov et al, *Measurement of the WZ and ZZ production cross sections using leptonic final states in* 8.6 fb^{-1} *of $p\overline{p}$ collisions*, Phys. Rev. D **85** (2012) 112005.

[33] The LEP Collaborations ALEPH, DELPHI, L3, OPAL and the LEP TGC Working Group, *A Combination of Charged Triple Gauge Boson Couplings Measured by the LEP Experiments*, LEPEWWG/TGC/2005-01 (2005) .

[34] ATLAS Collaboration, *Measurement of the WZ production cross section and limits on anomalous triple gauge couplings in proton-proton collisions at $\sqrt{s} = 7$* TeV *with the ATLAS detector*, Phys.Lett. **B709** (2012) 341–357, arXiv:1111.5570 [hep-ex].

[35] CMS Collaboration, *Measurement of the WW, WZ and ZZ cross sections at CMS*, CMS-PAS-EWK-11-010 (2011) , http://cds.cern.ch/record/1370067.

[36] L. Evans and P. Bryant, *LHC Machine*, JINST **3** (2008) S08001.

[37] ATLAS Collaboration, *The ATLAS Experiment at the CERN Large Hadron Collider*, JINST **3** (2008) S08003.

[38] CMS Collaboration, *The CMS experiment at the CERN LHC*, JINST **3** (2008) S08004.

[39] ALICE Collaboration, *The ALICE experiment at the CERN LHC*, JINST **3** (2008) S08002.

[40] LHCb Collaboration, *The LHCb Detector at the LHC*, JINST **3** (2008) S08005.

[41] TOTEM Collaboration, *The TOTEM experiment at the CERN Large Hadron Collider*, JINST **3** (2008) S08007.

[42] LHCf Collaboration, *The LHCf detector at the CERN Large Hadron Collider*, JINST **3** (2008) S08006.

[43] J. M. Campbell, J. W. Huston, and W. J. Stirling, *Hard interactions of quarks and gluons: a primer for LHC physics*, Reports on Progress in Physics **70** (2007) no. 1, 89. http://stacks.iop.org/0034-4885/70/i=1/a=R02.

[44] Website: LHC Commissioning with Beam, http://lhc-commissioning.web.cern.ch/lhc-commissioning/.

[45] ATLAS's website with luminosity related public results, https://twiki.cern.ch/twiki/bin/view/AtlasPublic/-LuminosityPublicResults.

[46] *CERN press releases*, http://press.web.cern.ch/press/. PR08.08, PR09.08, PR17.09, PR18.09, PR07.10.

[47] ATLAS Collaboration, *Expected Performance of the ATLAS Experiment - Detector, Trigger and Physics*. 2009. arXiv:0901.0512 [hep-ex].

[48] ATLAS Collaboration, *The ATLAS Experiment at the CERN Large Hadron Collider*, JINST **3** (2008) S08003.

[49] J.-F. Arguin, M. Elsing, and B. Heinemann, *ATLAS Tracking Performance in the Presence of Pile-up*, ATL-INDET-INT-2010-001 (2010) , https://cds.cern.ch/record/1240260?

[50] ATLAS Collaboration, *ATLAS: Detector and physics performance technical design report.*, CERN-LHCC-99-14 **1** (1999) , https://cds.cern.ch/record/391176?

[51] ATLAS Collaboration, *ATLAS muon spectrometer: Technical Design Report*, ATLAS-TDR-10, CERN-LHCC-97-022 (1997) , https://cds.cern.ch/record/331068?

[52] ATLAS Collaboration, *ATLAS technical proposal for a general-purpose pp experiment at the Large Hadron Collider at CERN*, CERN-LHCC-94-43, LHCC-P-2 (1994) , https://cds.cern.ch/record/290968?

[53] S. Baranov et al, *Estimation of Radiation Background, Impact on Detectors, Activation and Shielding Optimization in ATLAS*, ATL-GEN-2005-001 (2005) , http://cds.cern.ch/record/814823.

[54] P. Rinard, *Neutron Interaction with Matter, in Passive Nondestructive Assay of Nuclear Materials*. U.S. Nuclear Regulatory Commission, NUREG/CR-5550, chap 12, 1991.

[55] S. Borzakov, et al, *Response of the MDT filled with Ar+5%CO2+3%CH4 to thermal neutrons*, ATL-MUON-96-116. ATL-M-PN-116 , http://cds.cern.ch/record/683715/.

[56] W. Lampl, S. Laplace, D. Lelas, P. Loch, H. Ma, S. Menke, and S. Rajagopalan, D. Rousseau, S. Snyder, and G. Unal, *Calorimeter Clustering Algorithms: Description and Performance*, ATL-LARG-PUB-2008-002. ATL-COM-LARG-2008-003 , http://cds.cern.ch/record/1099735.

[57] ATLAS Collaboration, *Electron performance measurements with the ATLAS detector using the 2010 LHC proton-proton collision data*, European Physical Journal C **72** (2012) 1909, arXiv:1110.3174 [hep-ex].

[58] ATLAS Collaboration, *Expected electron performance in the ATLAS experiment*, ATL-PHYS-PUB-2011-006 (2011) , http://cds.cern.ch/record/1345327.

[59] ATLAS Collaboration, *Electron performances measurements using the 2011 LHC proton-proton collisions*, ATL-COM-PHYS-2012-1024 , https://cds.cern.ch/record/1461219/.

[60] R. Nicolaidou, L. Chevalier, S. Hassani, J. F. Laporte, E. L. Menedeu, and A. Ouraou, *Muon identification procedure for the ATLAS detector at the LHC using Muonboy reconstruction package and tests of its performance using cosmic rays and single beam data*, Journal of Physics: Conference Series **219** (2010) . http://stacks.iop.org/1742-6596/219/i=3/a=032052.

[61] L. Dixon, Z. Kunzst, and A. Signer, *Vector Boson Pair Production in Hadronic Collisions at $O(\alpha_s)$: Lepton Correlation and Anomalous Couplings*, Phys. Rev. D **60** (1999) 114037, arXiv:9907305v1.

[62] ATLAS twiki Good Runs Lists Tutorial, https://twiki.cern.ch/twiki/bin/viewauth/Atlas/GoodRunsListsTutorial.

[63] ATLAS Collaboration, *Luminosity determination in pp collisions at $\sqrt{s}$ = 7 TeV using the ATLAS detector at the LHC*, The European Physical Journal C **71** (2011) .

[64] ATLAS Luminosity Calculator website, https://atlas-lumicalc.cern.ch/.

[65] ATLAS Collaboration, *Improved luminosity determination in pp collisions at $\sqrt{s}$ = 7 TeV using the ATLAS detector at the LHC*, arXiv:1302.4393 [hep-ex].

[66] ROOT - *An Object Oriented Data Analysis Framework*, http://root.cern.ch.

[67] Athena Core software's website, http://atlas-computing.web.cern.ch/atlas-computing/packages/-athenaCore/athenaCore.php.

[68] *Geant4: A toolkit for the simulation of the passage of particles through matter*, . http://geant4.cern.ch/.

[69] S. Frixione, F. Stoeckli, P. Torrielli, B. R. Webber, and C. D. White, *The MC@NLO 4.0 Event Generator*, arXiv:1010.0819 [hep-ph].

[70] H.-L. Lai, M. Guzzi, J. Huston, Z. Li, P. M. Nadolsky, et al., *New parton distributions for collider physics*, Phys.Rev. **D82** (2010) 074024, arXiv:1007.2241 [hep-ph].

[71] G. Corcella et al., *HERWIG 6.5 release note*, arXiv:0210213 [hep-ph].

[72] M. L. Mangano, M. Moretti, F. Piccinini, R. Pittau, and A. D. Polosa, *ALPGEN, a generator for hard multiparton processes in hadronic collisions*, JHEP **0307** (2003) 001, arXiv:0206293 [hep-ph].

[73] J. M. Butterworth, J. R. Forshaw, and M. H. Seymour, *Multiparton interactions in photoproduction at HERA*, Z. Phys. **C72** (1996) 637–646, arXiv:9601371 [hep-ph].

[74] J. Alwall et al., *MadGraph/MadEvent v4: The New Web Generation*, JHEP **09** (2007) 028, arXiv:07062334 [hep-ph].

[75] T. Sjostrand et al., *A brief introduction to PYTHIA 8.1*, Comput. Phys. Commun. **178** (2008) 852, arXiv:0710.3820 [hep-ph].

[76] T. Gleisberg, S. Hoeche, F. Krauss, M. Schonherr, S. Schumann, et al., *Event generation with SHERPA 1.1*, JHEP **0902** (2009) 007, arXiv:0811.4622 [hep-ph].

[77] T. Sjostrand et al., *High-Energy Physics Event Generation with PYTHIA 6.1*, Comput. Phys. Commun. **135** (2001) 238, arXiv:0010017 [hep-ph].

[78] ATLAS Muon Combined Performance, https://twiki.cern.ch/twiki/bin/viewauth/AtlasProtected/MuonPerformance.

[79] ATLAS Collaboration, *Muon Reconstruction Efficiency in Reprocessed 2010 LHC Proton-Proton Collision Data Recorded with the ATLAS Detector*, ATLAS-CONF-2011-063 , http://cds.cern.ch/record/1345743.

[80] ATLAS Energy scale and resolution recommendations, https://twiki.cern.ch/twiki/bin/viewauth/AtlasProtected/EnergyScaleResolutionRecommendations.

[81] ATLAS Collaboration, *Reconstruction and Calibration of Missing Transverse Energy and Performance in W and Z Events in ATLAS Proton-Proton Collisions at* $\sqrt{s} = 7\ TeV$, ATLAS-CONF-2011-080 , https://cds.cern.ch/record/1355703?ln=en.

[82] ATLAS Collaboration, *Performance of missing transverse momentum in ATLAS with 2011 proton-proton collisions at* $\sqrt{s} = 7\ TeV$, ATLAS-CONF-2012-101 , https://cds.cern.ch/record/1463915.

[83] ATLAS Collaboration, *Selection of jets produced in proton-proton collisions with the ATLAS detector using 2011 data*, ATLAS-CONF-2012-020 , http://cds.cern.ch/record/1430034.

[84] J. Butterworth, et al., *Single Boson and Diboson Production Cross Sections in pp Collisions at* $\sqrt{s} = 7\ TeV$, ATL-COM-PHYS-2010-695 , https://cds.cern.ch/record/1287902.

[85] ATLAS Collaboration, *Measurement of the Top Quark-Pair Production Cross Section with ATLAS in pp Collisions at* $\sqrt{s} = 7$ TeV, Eur. Phys. J. C **71** (2011) 1577, arXiv:1012.1792 [hep-ex].

[86] ATLAS and CMS Collaboration, J. Nielsen, *W/Z+Jet Cross Section Measurements at the Large Hadron Collider*, ATLAS proceedings ATL–COM–PHYS–2009–324, https://cds.cern.ch/record/1184475.

[87] M. Groll and the ATLAS Collaboration, *Associated Production of Weak Bosons at the LHC with the ATLAS Detector*, J. Phys. Conf. Ser. **171** (2009) 012086, http://stacks.iop.org/1742-6596/171/i=1/a=012086.

[88] T. Melia, P. Nason, R. Rontsch, and G. Zanderighi, *W+W-, WZ and ZZ production in the POWHEG BOX*, arXiv:1107.5051 [hep-ph].

[89] ATLAS Electron Gamma Performance, https://twiki.cern.ch/twiki/bin/viewauth/AtlasProtected/ElectronGamma.

[90] ATLAS Collaboration, *Performance of Missing Transverse Momentum Reconstruction in Proton-Proton Collisions at 7 TeV with ATLAS*, arXiv:1108.5602 [hep-ex].

[91] Chakravarti, Laha, and Roy, *Handbook of Methods of Applied Statistics*, John Wiley and Sons **volume I** (1967) 392–394.

[92] F. James, *MINUIT - Function Minimization and Error Analysis.* CERN Program Library entry D506, Geneva, 1998.

[93] G. Cowan, K. Cranmer, E. Gross, and O. Vitells, *Asymptotic Formulae for Likelihood-Based Tests of New Physics*, Eur. Phys. J. C **71** (2011) 1554, arXiv:1007.1727v2 [hep-ph].

[94] T. Melia, P. Nason, R. Rontsch, and G. Zanderighi, *W^+W^-, WZ and ZZ production in the POWHEG BOX*, JHEP **078** (2011) 1111, arXiv:1107.5051 [hep-ph].

[95] ATLAS Collaboration, *Observation of an excess of events in the search for the Standard Model Higgs boson in the $H \to ZZ^{(*)} \to 4\ell$ channel with the ATLAS detector*, ATLAS-CONF-2012-092 , https://cds.cern.ch/record/1460411.

[96] C. Bernet et al, *The 40 × 40 cm^2 gaseous microstrip detector Micromegas for the high-luminosity COMPASS experiment at CERN*, Nucl. Instr. and Meth **A536** (2005) 61.

[97] B. Peyaud, *KABES: a novel beam spectrometer for NA48*, Nucl. Instr. and Meth **A535** (2004) 247.

[98] S. Awar et al, *Large bulk Micromegas detectors for TPC applications*, Nucl. Instr. and Meth **A602** (2009) 415–420.

[99] I. Giomataris et al, *Micromegas: A high granularity position sensitive gaseous detector for high particle flux environments*, Nucl. Instr. Meth **A376** (1996) 29–35.

[100] I Giomataris et al, *Micromegas in a bulk*, Nucl. Instr. and Meth **A560** (2006) , arXiv:physics/0501003.

[101] H. Raether Z. Phys **112** (1939) 464.

[102] S. Procureur et al, *Discharge studies in micromegas detectors in a 150-GeV/c pion beam*, Nucl. Instr. and Meth **A659** (2011) .

[103] W. Riegler, *Extended theorems for signal induction in particle detectors VCI*, Nucl. Instr. and Meth **A535** (2004) 287.

[104] T. Alexopoulos et al, *A spark-resistant bulk-Micromegas chamber for high-rate applications*, Nucl. Instr. and Meth **A640** (2011) , arXiv:1011.5370 [physics.ins-det].

[105] J. Santiard, *Gassiplex, a low noise analog signal processor for readout of gaseous detectors*, Nucl. Instrum. Meth **A360** (1995) .

[106] V551 C.A.E.N. Sequencer User Guide.

[107] G. Landi, *Properties of the center of gravity as an algorithm for position measurements*, Nucl. Instr. and Meth **485** (2002) .

[108] R. K. Carnegie, et al., *Resolution studies of cosmic ray tracks in a TPC with GEM readout*, Nucl. Instr. and Meth **A538** (2005) 372.

[109] F. Jeanneau et al, *Performances and Ageing Study of Resistive-Anodes Micromegas Detectors for HL-LHC Environment*, IEEE Transactions on Nuclear Science,1 **59** (2012) , `arXiv:1201.1843 [physics.ins-det]`.

[110] J Manjarrés et al, *Performances of anode-resistive Micromegas for HL-LHC*, Journal of Instrumentation **7** (2012) no. 03, C03040. `http://stacks.iop.org/1748-0221/7/i=03/a=C03040`.

[111] J Galén et al, *Aging studies of Micromegas prototypes for the HL-LHC*, Journal of Instrumentation **7** (2012) no. 01, C01041. `http://stacks.iop.org/1748-0221/7/i=01/a=C01041`.

[112] J Galán et al, *An ageing study of resistive micromegas for the HL-LHC environment*, Journal of Instrumentation **8** (2013) no. 04, P04028. `http://stacks.iop.org/1748-0221/8/i=04/a=P04028`.

[113] S Vlachos et al, *New Small Wheel Technical Design Report*, `https://cds.cern.ch/record/1542447?`

Acknowledgements

I would like to express my sincere gratitude to Samira Hassani and Philippe Schune, my supervisors, for their patient guidance, enthusiastic encouragement and teaching. I would also like to thank F. Jeanneau, for the introduction to the Micromegas detectors and for his advice and assistance.

I am grateful to the ATLAS group and the SEDI at CEA Saclay for hosting me during my PhD studies. It has been a great pleasure for me to work with David Attie, Esther Ferrer Ribas, Ioannis Giomataris, Jean-Francois Laporte, Ahmimmed Ouraou, Claude Guyot, Laurent Chevalier and Pierre-Francois Giraud. I owe them my deepest gratitude for their valuable advices and teaching.

I would like to particularly thank Jean Ernwein for going through my thesis, I really appreciate his detailed comments and the interesting discussions.
I would like to express my gratitude to C. Petridou, D. Bloch, U. Bassler, S. Lavignac, and G. Mikenberg for accepting to be in my examining committee. I am especially grateful to my rapporteurs, Chara and Daniel, for the evaluation of this thesis and their useful comments.

I thank all the doctoral and postdoctoral fellows Bernardo Resende, Henso Abreu, Homero Martinez, Camilla Maiani, Meng Xiao, Sofia Protopapadaki, Dimitra Tsionou, Michael Macaire and Flor Blaszczyk for all the interesting discussions that we had and friendship. Many thanks to my Venezuelan friends Diego, Jonas, Antonio, Camila, Homero and Henso who supported me all the time.

I would like to thank the ATLAS collaboration for allowing me to participate in this great experiment. I thank many people I had the opportunity to work with in the Standard Model group and the WZ group. I acknowledge particularly the support of Dinos Bachas and Chara Petridou.

I acknowledge the HELEN project (High Energy Physics Latinamerican-European Network) for a training internship, which was the bridge between my undergraduate studies

and my doctoral studies in particle physics. I thank Luis Nuñez, Alejandra Melfo and Jose Ocariz for their support and to care about my present and my future.

Finally I thank my family and Heberth, for all of your love, support and encouragement, and for always taking the time to listen. I couldn't have done this without you.

Mesure des dibosons WZ avec le détecteur ATLAS auprès du LHC et Etude des performances des Micromegas resistif en vue de leur application auprès du HL-LHC

Joany Manjarrés Ramos

Cette thèse comporte deux parties: la première porte sur la mesure de la production des paires de deux bosons de jauge $W^{\pm}Z$ en utilisant les données collectées par le détecteur ATLAS auprès du grand collisionneur de proton-proton (LHC) au CERN. La deuxième partie de la thèse est dédiée à l'étude des propriétés des Micromegas résistives, en vue de leur installation dans la partie avant du spectromètre à muons du détecteur ATLAS, durant la première phase de haute luminosité du LHC (HL-LHC).

La mesure de production des paires $W^{\pm}Z$ permet de tester le secteur électrofaible du Modèle Standard à haute énergie et de rechercher de la nouvelle physique au-delà du Modèle Standard. Toute déviation par rapport aux prédictions du Modèle Standard serait l'indication de nouvelle physique. L'étude présentée dans cette thèse est basée sur les données des collisions proton-proton à une énergie de centre de masse de 7 et 8 TeV. Elles correspondent à une luminosité intégrée de 4.8 et 13 fb^{-1} enregistrées respectivement durant l'année 2011 et durant le premier semestre de 2012. Les états finals de paires $W^{\pm}Z$ se désintégrant en électrons, muons et énergie transverse manquante, sont sélectionnés. Les bruits de fond $t\bar{t}$ et Z+jets sont estimés à partir des données avec des méthodes développées dans le cadre de cette thèse. La section efficace fiducielle et totale de production des paires $W^{\pm}Z$ sont calculées et les limites sur les couplages à trois bosons de jauge WWZ en sont extraites.

La deuxième partie de cette thèse est dédiée à l'amélioration du spectromètre à muons d'ATLAS en vue de son fonctionnement à haute luminosité auprès du HL-LHC. La très haute luminosité atteinte à l'horizon 2018 impose de prévoir des modifications substantielles sur l'ensemble des sous-détecteurs constituant ATLAS. L'efficacité, la résolution et la robustesse de Micromegas résistives sont étudiées dans le cadre d'un projet de R&D visant à la construction de chambres à muons vers l'avant à l'aide de la technologie Micromegas résistives.

WZ diboson measurements with the ATLAS experiment at the LHC and Performance of resistive Micromegas in view of HL-LHC applications

Joany Manjarrés Ramos

During the past two years, the CERN Large Hadron Collider (LHC) has performed exceptionally. The data collected by ATLAS made possible the first Standard Model physics measurements and produced a number of important experimental results. In the first part of this document the measurement of the $W^{\pm}Z$ production with the ATLAS detector is presented and the second part is devoted to the study of resistive Micromegas properties, in view of the installation in the ATLAS spectrometer forward regions for the first phase of High Luminosity LHC (HL-LHC).

The measurement of the $W^{\pm}Z$ production probes the electroweak sector of the Standard Model at high energies and allows for generic tests for New Physics beyond the Standard Model. Two datasets of LHC proton-proton collisions were analyzed, 4.8 fb^{-1} of integrated luminosity at center-of-mass energy of $\sqrt{s} = 7$ TeV, and 13 fb^{-1} at $\sqrt{s} = 8$ TeV, collected in 2011 and the first half of 2012 respectively. Fully leptonic decay events are selected with electrons, muons and missing transverse momentum in the final state. Different data-driven estimates of the background were developed in the context of this analysis. The fiducial and total cross section of $W^{\pm}Z$ production are measured and limits on anomalous triple gauge boson couplings are set.

The second part of the document is devoted to the upgrade of the ATLAS detector. The conditions at the High Luminosity LHC calls for detectors capable of operating in a flux of collisions and background particles approximately ten times larger compared to today's conditions. The efficiency, resolution and robustness of resistive Micromegas were studied, as part of the R&D project aimed at the construction of large-area spark-resistant muon chambers using the micromegas technology.